High frequency quantum noise of mesoscopic systems and current-phase relation of hybrid junctions

Julien Basset

To cite this version:

Julien Basset. High frequency quantum noise of mesoscopic systems and current-phase relation of hybrid junctions. Other [cond-mat.other]. Université Paris Sud - Paris XI, 2011. English. NNT : 2011PA112199 . tel-00635825

HAL Id: tel-00635825
https://theses.hal.science/tel-00635825

Submitted on 26 Oct 2011

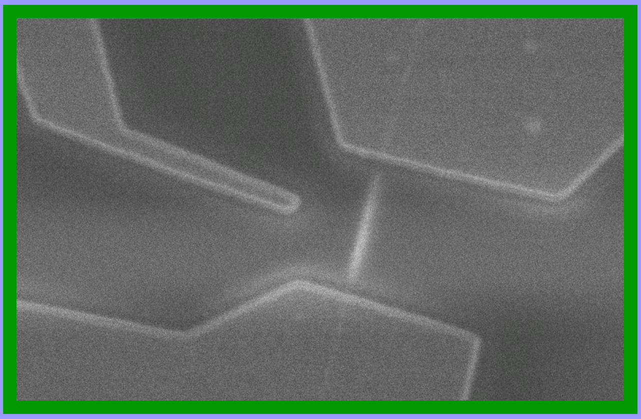

Université
Paris Sud
XI

High frequency quantum noise of mesoscopic systems and current-phase relation of hybrid junctions

Laboratoire de
Physique des
Solides

Julien BASSET

Mesoscopic Physics Group

Orsay

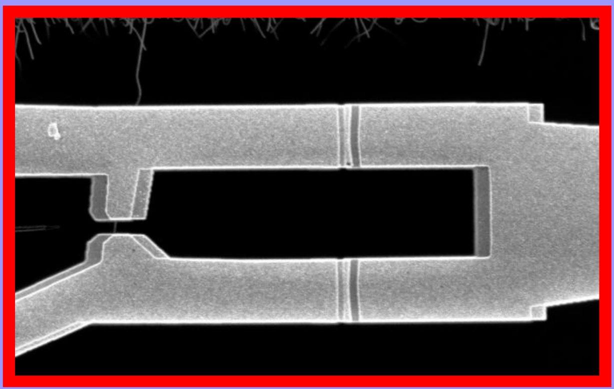

Abstract : This thesis discusses two experiments of mesoscopic physics regarding the high frequency quantum noise and the superconducting proximity effect. We nevertheless focused on a single model system: the carbon nanotube.

The first experiment aims to measure the high frequency quantum noise of the tube. In order to measure those fluctuations we have designed an original on-chip detection scheme in which the noise source and the detector, a Superconductor/Insulator/Superconductor junction, were coupled through a resonant circuit. This first allowed us to measure the equilibrium noise of the resonator. It exhibits a strong asymmetry between emission and absorption related to zero point fluctuations. We have then measured the out-of-equilibrium emission noise of quasiparticles tunneling of a Josephson junction. It exhibits a strong frequency dependence in agreement with theoretical predictions and allowed us to validate the detection scheme. Finally, the out-of-equilibrium emission noise associated to the Kondo effect (characteristic energy k_BT_K with T_K the Kondo temperature) in a carbon nanotube quantum dot was measured. We find a strong singularity at voltage $V=h\nu/e$ (ν is the measurement frequency) for frequency $\nu\sim k_BT_K/h$. This singularity is related to resonances in the density of states of the dot pinned at the Fermi energy of the leads. At higher frequency $h\nu\sim 3k_BT_K$ the singularity vanishes and understood in terms of decoherence effects induced by the bias voltage.

In the second experiment, we have developed a technique allowing to measure in the same experiment the current-phase relation and the current-voltage characteristic of a weak link separating two superconductors. We have characterized a carbon nanotube based junction through which a gate tunable current-phase relation was observed. Jointly to a high critical current amplitude, an anharmonic current-phase relation was measured.

Keywords: *mesoscopic physics, quantum noise, Kondo effect, superconducting proximity effect, carbon nanotube, quantum dot.*

Résumé : Cette thèse est consacrée à l’étude de deux aspects de la physique mésoscopique que sont le bruit quantique haute fréquence et l'effet de proximité supraconducteur en se focalisant toutefois sur un système modèle: le nanotube de carbone.

Ainsi la première partie de cette thèse est dédiée à la mesure de bruit quantique haute fréquence. Afin de mesurer ces fluctuations nous avons développé un système de détection "on-chip" original dans lequel la source de bruit et le détecteur, une jonction Supraconducteur/Isolant/Supraconducteur, sont couplés par un circuit résonant. Cela nous a permis dans un premier temps de mesurer le bruit à l'équilibre du résonateur. Son bruit comporte une forte asymétrie entre émission et absorption reliée aux fluctuations de point zéro. Une seconde étape a été de mesurer le bruit hors équilibre d’émission du passage tunnel de quasi-particules dans une jonction Josephson. Ce bruit comporte une forte dépendance en fréquence en accord avec les prédictions théoriques et nous a permis de valider le principe de détection. Finalement, nous avons pu mesurer le bruit associé au régime Kondo hors équilibre d'une boîte quantique à nanotube de carbone (énergie caractéristique k_BT_K avec T_K la température Kondo). Ce bruit d’émission à $k_BT_K\sim h\nu$ possède une forte singularité à la tension $V=h\nu/e$ (ν étant la fréquence de mesure). Cette singularité est reliée aux résonances Kondo dans la densité d’états de la boîte associés aux niveaux de Fermi de chaque réservoir. A plus haute fréquence $h\nu\sim 3k_BT_K$, la singularité disparaît, ce qui est compris par des effets de décohérence induits par la tension.

Dans la seconde partie, nous avons développé une technique permettant de mesurer à la fois la relation courant/phase et la caractéristique courant/tension d'un lien faible séparant deux supraconducteurs. Nous avons ainsi caractérisé une jonction à base de nanotube de carbone au travers de laquelle une relation courant-phase modulable par une tension de grille a été observée. Cette relation courant/phase exhibe une forte anharmonicité lorsque le supercourant présente une relativement grande amplitude.

Mots clefs: *physique mésoscopique, bruit quantique, effet Kondo, supraconductivité de proximité, nanotube de carbone, boîte quantique.*

Université Paris Sud

Laboratoire de Physique des Solides

Thèse

pour obtenir le grade de

Docteur en Sciences

Spécialité: Physique des Solides

Julien BASSET

High frequency quantum noise of mesoscopic systems and current-phase relation of hybrid junctions

Soutenue le 14 octobre 2011 devant la commission d'examen:

Norman Birge	**Rapporteur**
Hélène Bouchiat	**Directrice de thèse**
Richard Deblock	**Co-directeur de thèse**
Silvano De Franceschi	**Rapporteur**
Benoît Douçot	**Examinateur**
Christian Glattli	**Examinateur**
Pascal Simon	**Président**

Remerciements

Alors étudiant à Grenoble, c'est débût 2008 que j'ai rencontré pour la première fois le groupe de physique mésoscopique à Orsay. A l'époque j'avais fait le choix d'effectuer mon stage de Master 2 aux Etats-unis tout en voulant continuer en thèse sur Paris. Je me trouvais alors dans la situation délicate de devoir trouver un groupe voulant bien m'accueillir en thèse et ce sans me connaître. Qu'à cela ne tienne, Hélène Bouchiat m'a fait confiance, dégôté une bourse et accueilli dans son groupe. Pour cela je ne dirais qu'un mot: merci! Puis vient le premier jour de ma thèse, le 01/10/2008. Je fais alors plus ample connaissance avec le groupe, ses pauses café, ses discussions informelles et biensûr mon projet. Projet mené avec Richard Deblock, qui a été tout pour moi pendant ses 3 années: un mentor, un modèle, un confident. J'ai tout appris à ses côtés: la lithographie électronique, la fabrication des nanotubes, les évaporations, la cryogénie, la physique du bruit, des nanotubes, la supraconductivité de proximité... Il a su faire face à toutes mes questions, mes arrivées inopinées dans son bureau, mes sautes d'humeurs et bien plus encore. Je le remercie sincèrement et profondément. Merci Richard! Je tiens à re-remercier Hélène qui en co-encadrant cette thèse a toujours su remettre en question chaque point de mon argumentation. A chaque fois que je pensais avoir compris un point important, Hélène me faisait douter me forçant à rentrer plus en profondeur dans le sujet d'intérêt. Je la remercie pour ça et tout le reste. Bien entendu, un groupe ne se limite pas à 2 personnes et je souhaite à cet effet remercier l'ensemble du groupe méso. Les permanents d'abord: Sophie Guéron, pour sa bonne humeur contagieuse et son entrain de tous les instants, Meydi Ferrier pour être le Léonard de son disciple, Alik Kasumov pour les pauses café, agrémentées de chocolat, dehors au soleil (ou pas) et Sandrine Autier-Laurent pour ses conseils avisés dans les moments de stress. Les non-permanents ensuite: Claudia Ojeda pour son affection, les pique-niques en bordure de Seine, les happy-hours à Denfert, être venu découvrir l'Ardèche et accessoirement avoir partagé mon bureau (et donc mon humeur) pendant presque deux ans. Alexei Chepelianskii pour son génie, Francesca Chiodi pour sa jovialité, Katsuyoshi Komatsu pour avoir supporté toute ma période de rédaction en tant qu'officemate, Bastien (ou Basile) Dassonneville pour être un bon disciple dévoué corps et âme à la science, Miguel Monteverde pour les discussions à propos de graphène en montant la rue de la colline. Je remercie également Julien Gabelli pour les discussions,

ses avis bien tranchés envers toute situation scientifique, politique, économique,... Marco Aprili pour les discussions de couloir et le temps passé avec lui pour entretenir son bâti d'évaporation. Je remercie grandement Raphaël Weil qui m'a bien aidé pendant cette thèse en fabriquant de supers échantillons "courant-phase". Je remercie encore dans le désordre, Jean-Yves Chauleau, Stanislas Rohart, Amandine Bellec, Bertrand Reulet, Charis Quay, André Thiaville, Chuan Li,... ainsi que les services techniques et administratifs. Je remercie cordialement Françoise Hippert, Joël Chevrier et Laurent Saminadayar à Grenoble sans qui mon aventure parisienne n'aurait jamais vu le jour, le président de l'Université Paris Sud pour m'avoir octroyé une bourse, Jean-Paul Pouget et Dominique Chandesris, les directeurs successifs du Laboratoire de Physique des Solides pour m'y avoir accueilli. Finalement, je remercie cordialement Norman Birge, Silvano De Franceschi, Benoît Douçot, Christian Glattli, Pascal Simon, Hélène et Richard d'avoir fait partie de mon jury. Je remercie ma famille, mes amis et Claire pour avoir été là au cours de ces années et avoir organisé un pot ardèchois inoubliable.

Paris, October 2011 Julien Basset

Contents

Chapter i

Résumé de la thèse

i.1 Introduction

Les progrès important de l'électronique moderne permettent à ce jour de fabriquer et manipuler des dispositifs dont les dimensions pertinentes sont de l'ordre de la dizaine de nanomètres. On parle alors de nano-électronique. Cette miniaturisation progressive alliée à la possibilité de refroidir ces échantillons à des températures de l'ordre du mK permet de sonder des régimes dans lesquels la mécanique classique n'est plus valable et où la mécanique quantique prend le relais. C'est le coeur de la physique mésoscopique qui tend à rendre compte des propriétés électroniques à des échelles intermédiaires entre l'atome et le monde macroscopique. Ces systèmes sont suffisamment petits pour être quantiquement cohérents, c'est à dire que leur taille est inférieure à la longueur sur laquelle les fonctions d'onde électroniques conservent une phase bien définie. De ce fait leurs propriétés sont profondément affectées par les interférences quantiques au sein du matériau. La nanoélectronique quantique se propose de fonder une nouvelle électronique basée sur les phénomènes quantiques de la matière et plus particulièrement sur la nature quantique des électrons. Il devient alors possible d'utiliser les niveaux d'énergies quantiques pour coder l'information et optimiser son traitement [1].

Un des systèmes les plus étudié dans ce domaine est la boîte quantique [2] artificiel consistant en une région de l'espace où un nombre bien défini d'électrons est confiné. Le spectre d'énergie découlant de ce confinement est, à l'image des atomes, discret. Ces systèmes peuvent être considérés comme des atomes artificiels. Un des grands avantages que l'on a à fabriquer ces atomes artificiels est la possibilité de les connecter à des réservoirs d'électrons. Dans ce cas selon le régime atteint de couplage avec la boîte on observe des phénomènes multiples et variés. Parmi ceux-ci, l'effet Kondo dans les boîtes quantiques [3] est un sujet central de ce manuscrit. Nous voulons en étudier deux aspects complémentaires que sont sa dynamique haute fréquence [4] et sa compétition avec la supraconductivité de proximité [5]. Cette thèse s'articule donc autour de deux axes de recherches, distincts, complémentaires et appliqué à un seul et même objet: la boîte quantique à base de nanotubes de carbone.

i.2 Bruit quantique haute fréquence de systèmes mésoscopiques

La première partie de ce manuscrit est dédiée à l'étude des fluctuations de courant, ou bruit, dans un régime dit "quantique" ou "haute fréquence".

En effet, bien que le bruit électrique ait été étudié de manière extensive à basse fréquence dans de nombreux systèmes [6] de tailles variées et présentant ou non de la cohérence quantique, son étude haute fréquence est relativement nouvelle.

Dans ce régime particulier où l'énergie thermique à laquelle est menée l'expérience est bien plus faible que l'énergie correspondant à la fréquence de mesure, les fluctuations de courant acquièrent une forte dépendance en fréquence. Le bruit comporte alors des signatures des échelles d'énergie pertinentes dans le système telles que la tension (énergie eV) ou la température (énergie k_BT).

Plus encore, ce bruit quantique peut être décrit en terme d'échanges de photons d'énergie $h\nu$ entre la source et le détecteur de bruit. Selon que les photons soient émis ou absorbés par la source on mesure le bruit en émission (correspondant aux fréquences négatives) ou le bruit en absorption (correspondant aux fréquences positives) [7] (voir figure i.1). Cette différence entre procédés d'émission et absorption est bien connue dans le domaine de l'optique quantique mais est difficile à observer dans des systèmes électroniques puisque la plupart des amplificateurs utilisés dans la mesure du bruit échangent de l'énergie avec le système mesuré. Il s'ensuit que le résultat des mesures est une combinaison non triviale des bruits en émission et en absorption [8].

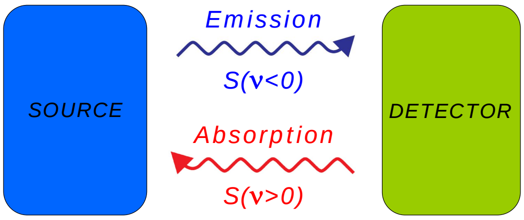

Figure i.1: Schématisation du procédé d'échange de photons entre la source de bruit et le détecteur. Pour mesurer le bruit en émission, le détecteur doit être passif alors que pour mesurer le bruit en absorption, il doit être actif.

D'un autre côté un détecteur quantique [7, 9], tel que la jonction Supraconducteur/ Isolant/ Supraconducteur (SIS) permet de mesurer indépendamment le spectre de bruit en émission et en absorption. Cependant, due à la difficulté d'extraire la contribution du bruit à l'équilibre, ce type de mesure n'a été mené que dans le cadre de mesures de bruit en excès. Le bruit en excès correspondant à la différence entre le bruit à une tension donnée et le bruit à l'équilibre.

Pour comprendre cela, il peut être intéressant d'introduire en quelques mots le principe de détection ainsi que le spectre de bruit à fréquence finie d'un système à l'équilibre.

i.2.1 Asymétrie du bruit quantique

La différence entre le bruit en émission et le bruit en absorption intervient dès lors que l'on considère une description quantique du circuit électrique auquel on s'intéresse [10]. Une forte conséquence est alors que le spectre de bruit de tout élément dissipatif est fortement asymétrique vis-à-vis des processus d'émission ($\nu < 0$) et d'absorption ($\nu > 0$) à l'équilibre thermique. C'est le théorème de fluctuation-dissipation [7]:

$$S_V(\nu) = \frac{2Re\,[Z(\nu)]\,h\nu}{[1 - e^{-\beta h\nu}]}. \tag{i.1}$$

avec $\beta = 1/k_B T$. Cette formule décrit la transition entre le bruit thermique à basse fréquence et le régime quantique relié aux fluctuations de point zéro du champ électromagnétique à fréquence finie. Nous avons représenté en figure i.2 la dépendence en fréquence attendue du spectre de bruit en tension d'une résistance R pour différentes températures. Ces courbes montrent clairement la forte asymétrie entre émission et absorption. A basse température le système ne présente pas de bruit en émission bien qu'il présente toujours du bruit en absorption. En augmentant la température, du bruit en émission apparaît et le bruit en absorption augmente.

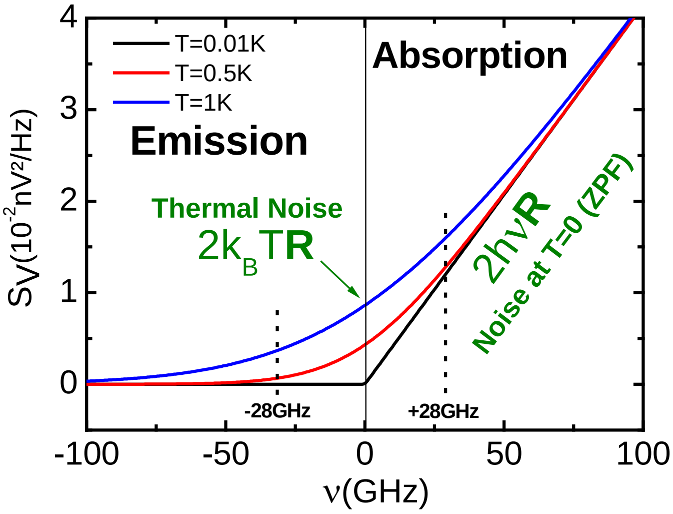

Figure i.2: Dépendence en fréquence attendue du bruit en tension à l'équilibre d'une résistance $R = 300\Omega$ à trois températures (formule i.1) . A température nulle $T = 0$, il n'y a pas de bruit en émission alors que le bruit en absorption augmente linéairement avec la fréquence. Ce bruit à température nulle est une signature directe des fluctuations de point zéro.

Nous avons conçu au cours de cette thèse une expérience originale permettant la mesure de bruit en émission et en absorption d'un circuit résonant à l'équilibre thermique basée sur l'utilisation d'un détecteur de bruit embarqué: la jonction SIS.

i.2.2 Principe de détection avec une jonction SIS

Le principe de détection de bruit haute fréquence avec une jonction SIS est basée sur la modification de la caractéristique courant/tension dc induite par le bruit en tension haute fréquence $S_V(\nu)$ présent à ses bornes. Le traitement quantitatif du principe de détection peut être dérivée dans le cadre de la théorie $P(E)$ [11] (cf. chapitre 4). Dans cette théorie l'environnement bruyant de la jonction SIS présente une certaine probabilité $P(E)$ d'échanger l'énergie E avec la jonction. Cette probabilité est directement reliée au spectre de bruit en tension $S_V(\nu)$ de l'environnement. On dit alors que le courant dc généré par la présence de bruit aux bornes de la jonction est un courant photo-assisté I_{PAT}. Ce courant prend la forme, lorsque la jonction est polarisée à la tension V_D:

$$\begin{aligned}
I_{PAT}(V_D) &= \underbrace{\int_0^{\infty} d\nu \left(\frac{e}{h\nu}\right)^2 S_V(-\nu) I_{QP,0}(V_D + \frac{h\nu}{e})}_{Emission} \\
&+ \underbrace{\int_0^{eV_D/h} d\nu \left(\frac{e}{h\nu}\right)^2 S_V(\nu) I_{QP,0}(V_D - \frac{h\nu}{e})}_{Absorption} \\
&- \underbrace{\int_{-\infty}^{+\infty} d\nu \left(\frac{e}{h\nu}\right)^2 S_V(\nu) I_{QP,0}(V_D)}_{Renormalization} . \qquad \text{(i.2)}
\end{aligned}$$

où $I_{QP,0}(V_D)$ est la caractéristique courant/tension de la jonction SIS détectrice sans environnement. Le premier terme de l'équation i.2 est relié au bruit en émission, le second au bruit en absorption et le troisième à la renormalisation du courant élastique.

La figure i.3 montre une caractéristique courant/tension typique de la jonction SIS avec (courbe verte) et sans environnement bruyant (courbe noire = $I_{QP,0}(V_D)$). Selon que l'on est polarisé en dessous ou en dessus du gap supraconducteur, différents scénarios sont possibles.

Région sensible au bruit en émission: $|V_D| < 2\Delta/e$ Cette situation correspond à une polarisation sous la gap. Dans ce cas, le courant élastique de quasi-particules au travers la jonction tunnel est bloqué. En revanche sous irradiation, du fait du bruit émis par l'environnement, les quasi-particules peuvent absorber des photons d'énergie $h\nu = (2\Delta - e|V_D|)$ leur permettant de passer par effet tunnel au travers la jonction. On a alors un courant photo-assisté dont l'amplitude et la position sont respectivement reliées à la puissance de bruit en émission de l'environnement et à la fréquence ν (formule i.3).

Région sensible au bruit en absorption: $|V_D| > 2\Delta/e$ La jonction est désormais polarisée au delà du gap. Dans ce cas un courant fini, essentiellement dû à la traversée par effet tunnel élastique de quasi-particules, s'écoule au travers de la jonction. Il est pourtant possible pour une quasi-particules de traverser la jonction de manière inélastique en émettant un photon d'énergie $h\nu = e|V_D| - 2\Delta$. Cela est possible si et seulement si l'environnement du détecteur est capable de l'absorber (cf. insert de droite dans la figure i.3). On sonde alors la capacité de l'environnement à absorber des photons, c'est à dire son spectre de bruit en absorption. Si tel est le cas, la caractéristique courant/tension exhibe une marche négative dont l'amplitude et la position sont respectivement reliées à la puissance de bruit en absorption de l'environnement et à la fréquence ν.

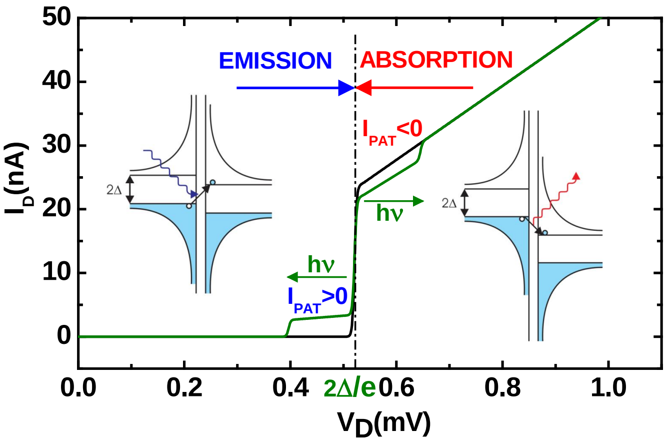

Figure i.3: Courbe noire: caractéristique courant/tension I(V) d'une jonction SIS typique. Courbe verte: courbe I(V) calculée du détecteur sous irradiation donnant lieu au courant photo-assisté I_{PAT}. En dessous du gap, le détecteur est sensible au bruit en émission; au delà du gap au bruit en absorption. L'amplitude du courant photo-assisté est exagérée pour des raisons de clarté. La figure montre également des représentations de type semi-conducteur de la jonction SIS polarisée en dessous et en dessus du gap. En dessous du gap, un photon émis par l'environnement permet le passage tunnel d'un électron au travers de la jonction (courant photo-assisté positif). En dessus du gap un photon absorbé par l'environnement réduit le taux de passage tunnel des quasi-particules (courant photo-assisté négatif).

Dans cette thèse nous avons couplé de manière résonante deux sources différentes de bruit au détecteur SIS. Cela nous a permis de mesurer le bruit quantique à l'équilibre du circuit de couplage résonant ainsi que le bruit hors-équilibre de deux sources différentes: une jonction Josephson et une boite quantique, constituée par un nanotube de carbone, dans le régime Kondo.

i.2.3 Circuit de couplage

Le circuit de couplage est composé de deux lignes de transmissions coplanaires en aluminium toutes deux connectées à un plan de masse soit via la jonction SIS soit via la source de bruit (cf. Fig. i.4). Chaque ligne est composée de deux sections de même longueur mais de largeurs différentes afin d'assurer une rupture d'impédance responsable de la résonance. On a alors un résonateur quart d'onde avec comme première fréquence de résonance $\nu \sim 30GHz$ et des facteurs de qualité inférieur à 10. Ces lignes sont placées proches l'une de l'autre afin d'assurer un bon couplage source/détecteur aux fréquences de résonance et terminées par des résistances on-chip au travers desquelles sont polarisées indépendamment la source et le détecteur.

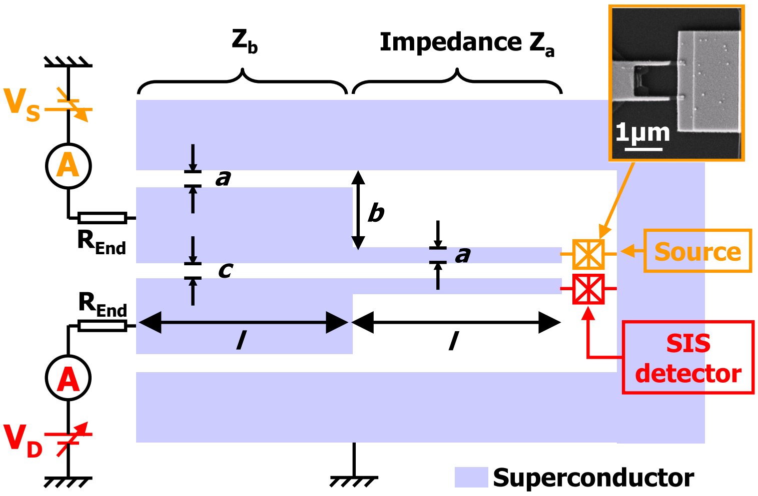

Figure i.4: Desin de l'échantillon avec $a = 5\mu m$, $b = 100\mu m$, $c = 5\mu m$ and $l = 1mm$. Les deux lignes de transmission sont terminées par deux résistances de platine on-chip. La jonctions SIS est réalisée par évaporation sous angle et a une géométrie de SQUID pour moduler le supercourant.

i.2.4 Mesure de bruit dans le régime quantique à l'équilibre d'un résonateur

En négligeant la source sur laquelle aucune tension de polarisation n'est appliquée, nous avons sondé le bruit à l'équilibre du résonateur. Pour ce faire nous avons étudié la forme particulière de la caractéristique courant/tension du détecteur ou plutôt de sa dérivée dI/dV (cf.i.5a) en fonction de la température. A basse température, en plus de la caractéristique attendue de la jonction, nous voyons des pics (dénoté par des flèches sur la figure i.5a) aux tensions $eV_D = 2\Delta + h\nu_n$ avec ν_n les fréquences de résonances du circuit de couplage ($\nu_1 = 28.4GHz$ et $\nu_3 = 80.2GHz$). Ces pics ne sont pas visibles en dessous du gap. Ce n'est plus vrai à haute température où un pic à $eV_D = 2\Delta - h\nu_1$ apparaît et croit avec la température. Nous attribuons ces pics à la sensibilité de la jonction SIS aux fluctuations de tension du circuit résonant.

De l'aire sous la courbe des pics à $V_D = (2\Delta - h\nu_1)/e$ nous avons extrait la dépendance en température du bruit en émission du résonateur à 28GHz. De l'aire sous les pics à $V_D = (2\Delta + h\nu_1)/e$ et $V_D = (2\Delta + h\nu_3)/e$ c'est le bruit en absorption à 28 et 80 GHz que nous extrayons. Les résultats sont montrés en Fig.i.5b et comparés aux prédictions théoriques prenant en compte les valeurs calibrées de $Re[Z]$. Un accord quantitatif a été trouvé.

L'expérience que nous avons menée est la première à avoir détecté indépendamment la puissance de bruit en émission et en absorption d'un circuit mésoscopique à l'équilibre.

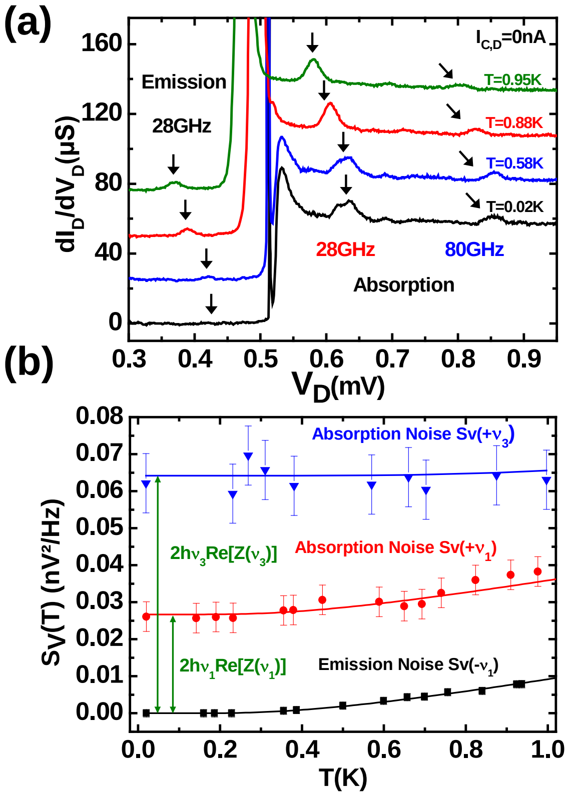

Figure i.5: (a) Conductance différentielle dI/dV_D du détecteur à différentes températures. Les courbes sont décalées verticalement par soucis de clarté. Les pics correspondant à la détection du bruit en émission et en absorption sont montrés par des flèches. (b) Dépendance en température du bruit en tension à $\nu_1 = 28.84GHz$ et $\nu_3 = 80GHz$ en émission et en absorption. Les lignes pleines correspondent aux prédictions théoriques avec $Re[Z(\nu_1)] = 714\Omega$ et $Re[Z(\nu_3)] = 604\Omega$. Seul le bruit en absorption, correspondant aux fluctuations de point zéro, est détecté en dessous de 0.4 K.

i.2.5 Mesure de bruit en émission hors-équilibre d'une jonction Josephson

Le circuit de couplage permet de coupler une source de bruit au détecteur via le circuit résonant. Cela nous a permis de mesurer le bruit émis lors du passage de quasi-particules au travers une jonction Josephson à deux fréquences.

Dans ce contexte, le bruit en courant $S_I(\nu)$ généré par la source de bruit se couple au détecteur via le circuit de couplage caractérisé par sa transimpédance $Z_t(\nu)$. Cette transimpédance quantifie le lien entre le bruit en tension $S_V(\nu)$ apparaissant aux bornes du détecteur et le bruit en courant généré par la source:

$$S_V(\nu) = |Z_t(\nu)|^2 S_I(\nu). \tag{i.3}$$

Pour mesurer le bruit émis par la jonction source, on polarise le détecteur à une tension fixe sous le gap $eV_D \leq 2\Delta$ (région sensible à l'émission), balaye la tension de la source au niveau de la branche de quasi-particules et mesure simultanément le courant photo-assisté créé au niveau du détecteur. La valeur de la tension appliquée au détecteur permet de remonter à la dépendance en fréquence du bruit. De la mesure du courant photo-assisté et de la calibration, on est capable de remonter au bruit de quasi-particules émis par la jonction Josephson à $\nu_1 = 28.4GHz$ et $\nu_3 = 80GHz$ (cf. Fig.i.6b).

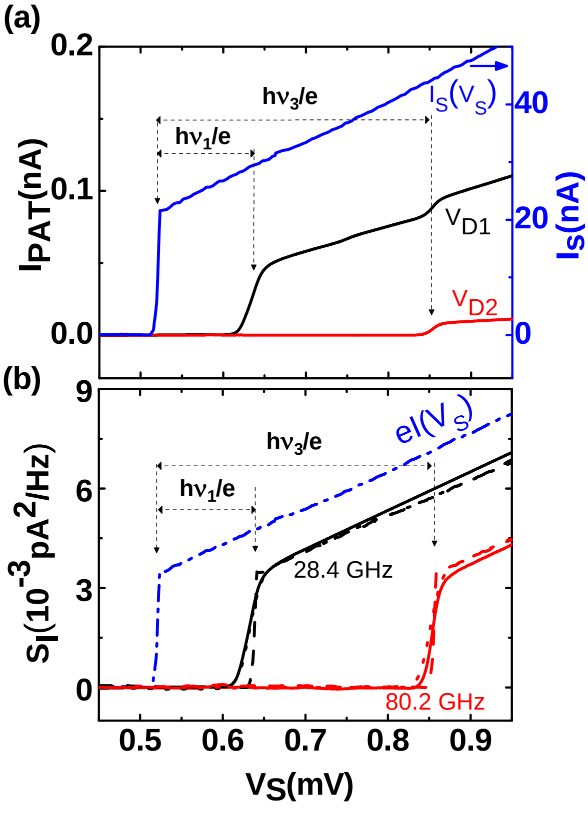

Figure i.6: (a) Axe de gauche: courant photo-assisté au travers du détecteur en fonction de la tension source V_S. Quand le détecteur est polarisé en V_{D1} il est sensible à la fois au bruit à ν_1, ν_2,ν_3... Quand il est polarisé en V_{D2} il n'est plus sensible au bruit à ν_1 et ν_2 mais uniquement à ν_3 et ... Axe de droite: courant dc au travers de la source I_S sur la même échelle de tension source (b) Bruit en émission extrait à $\nu_1 = 28.4$GHz et à $\nu_3 = 80.2$GHz. Pour comparaison, le bruit attendu est tracé en tirets. Le bruit attendu à fréquence nulle est tracé en bleu.

Les résultats s'accordent parfaitement avec la théorie prédisant que pour qu'une jonction Josephson émette du bruit de quasi-particules à la fréquence ν il est nécessaire de la polariser à $h\nu/e$ au delà du gap. Cela se comprend parfaitement au regard des transitions inélastiques nécessaires pour émettre un tel photon. L'amplitude du bruit mesuré est également en accord avec les prédictions théoriques.

i.2.6 Mesure de bruit en émission hors-équilibre d'une boîte quantique à nanotube de carbone dans le régime Kondo.

En adaptant légèrement notre circuit de couplage nous avons été capable de remplacer la jonction Josephson par une autre source de bruit: la boîte quantique à nanotube de carbone (cf. Fig.i.7). La transparence des barrières obtenue était telle que nous avons pu observer l'effet Kondo et mesurer pour la première fois les fluctuations de courant haute fréquence associées. Les fréquences sondés $\nu_1 \approx 30GHz$ et $\nu_3 \approx 80GHz$ sont du même ordre de grandeur que l'échelle caractéristique de l'effet Kondo donné par la température Kondo T_K. Nous avons donc sondé le bruit d'une impureté Kondo à l'échelle de temps donnée par sa dynamique propre.

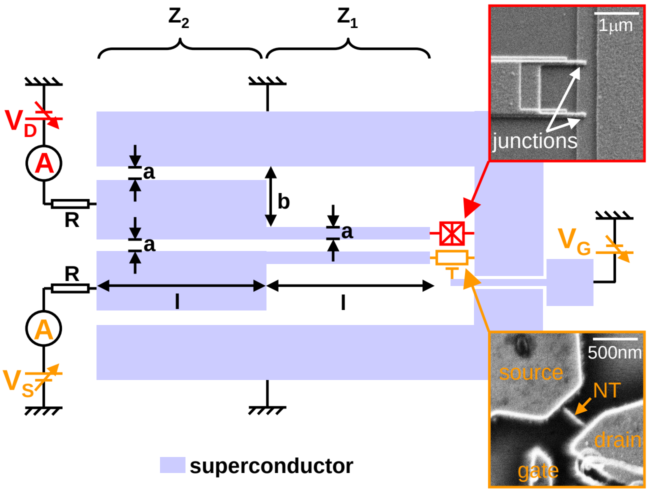

Figure i.7: Dessin de l'échantillon: un nanotube de carbone (image en microscopie électronique du bas) est couplé à une jonction SIS (image en microscopie électronique du haut), utilisée comme détecteur quantique de bruit, par un circuit résonant. Le nanotube de carbone est fabriqué par CVD, connecté avec des électrodes de Palladium et une grille latérale contrôle son potentiel électrostatique.

Pour $h\nu_1 \approx k_B T_K$, le bruit en émission haute fréquence du nanotube dans le régime Kondo montre une singularité quand la tension est de l'ordre de la fréquence à laquelle est mesurée le bruit. A plus haute fréquence $h\nu_3 \approx 3k_B T_K$, elle n'est plus visible.

Nous attribuons cette singularité à l'existence de deux résonances Kondo associées aux niveaux de Fermi des contacts (cf. Fig.i.8). Les transitions inélastiques entre chaque résonance donne lieu à un fort niveau de bruit aux fréquences correspondants à l'énergie les séparant $h\nu \approx eV_S$.

Des calculs de type groupe de renormalisation effectués par C.P. Moca *et al.* [4] permettent de reproduire quantitativement nos données expérimentales compte tenu d'un taux de décohérence additionnelle du spin dans la boîte. Cette décohérence de l'effet Kondo induite par la tension est un phénomène bien connue et a déjà été étudié expérimentalement [12, 13] et théoriquement [14–16]. La tension engendre une réduction de la résonance Kondo due à des procédés inélastiques.

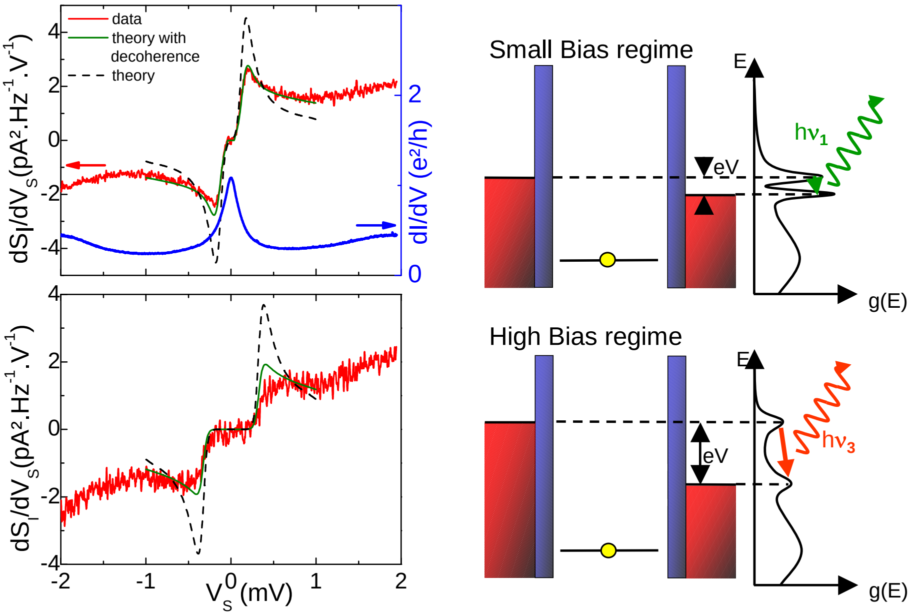

Figure i.8: (a) Dérivée du bruit en courant (courbe rouge) et conductance différentielle (courbe bleu) du nanotube de carbone en fonction de la tension V_S à ses bornes au centre de l'arête Kondo. Axe de gauche : dS_I/dV_S à 29.5GHz en fonction de la tension V_S. La courbe verte correspond aux courbes calculées avec le groupe de renormalisation et en tenant compte d'une décohérence additionnelle. Axe de droite: Conductance différentielle dI/dV du nanotube en unité de e^2/h. (b) Même données à 78GHz. La courbe verte correspond aux courbes calculées avec le groupe de renormalisation dS_I/dV_S en utilisant la même dépendance en tension du taux de décohérence.(c) Représentation schématique d'une boîte quantique dans le régime Kondo hors-équilibre et sa densité d'états associée à deux tensions différentes. Quand la boîte quantique est polarisée en tension, la résonance Kondo se sépare en deux résonances séparées de la tension appliquée. Il en découle une augmentation du bruit en émission à la fréquence $eV_S = h\nu$. L'amplitude des pics de résonances, et par conséquent le bruit en émission à $eV_S = h\nu$ sont réduits par la décohérence introduite par la tension finie appliquée à la boîte.

Le schéma de détection utilisé permet de tracer une carte complète du bruit dans la région de l'arête Kondo. Nous avons ainsi défini la fonction F(V) permettant de comparer le bruit mesuré au bruit d'une jonction tunnel normal:

$$F(V) = \frac{dS_I/dV_S}{e\,dI/dV_S(V_S - h\nu/e)}. \tag{i.4}$$

Il s'agit du rapport entre la dérivée du bruit mesuré et la conductance différentielle décalée de la tension correspondant à la fréquence de mesure. Pour un sytème linéaire ou pour un système non linéaire avec une transmission qui ne dépend pas de l'énergie, cette quantité est égale au facteur de Fano. Nous avons tracé cette fonction $F(V)$ pour $\nu_1 = 29.5$GHz (Fig. i.9a) et $\nu_3 = 78$GHz (Fig. i.9b). Pour $|eV_S| < h\nu$, où le bruit en émission est nul, $F(V)$ est arbitrairement fixée à zéro. Quelque soit la fréquence le bruit est sous-poissonien avec $F(V)$ proche de l'unité dans les régions faiblement conductrices et une forte diminution de $F(V)$ aux abords des régions plus fortement conductrices. Ce comportement est consistant qualitativement avec la réduction du facteur de Fano pour des canaux de conduction bien transmis.

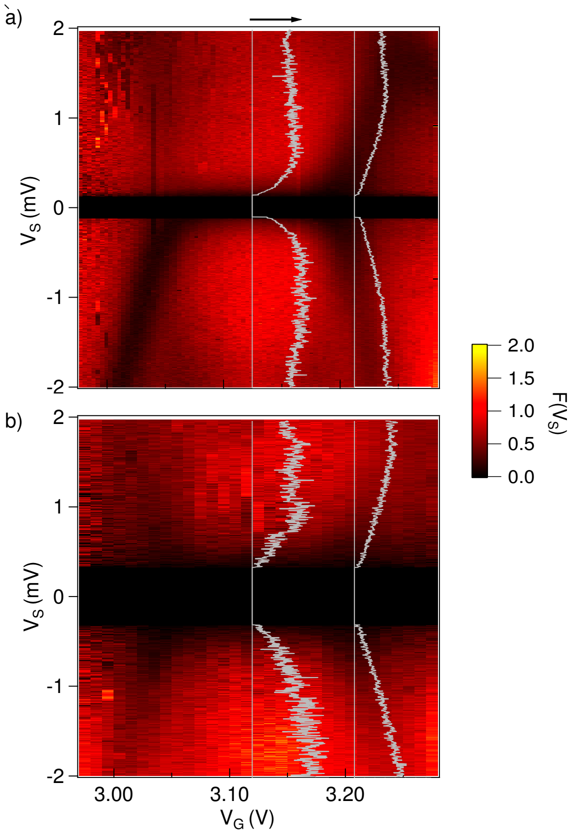

Figure i.9: Facteur de Fano effectif $F(V)$ en fonction de la tension source V_S et la tension de grille V_G à $\nu_1 = 29.5$GHz (a) et $\nu_3 = 78$GHz (b). F est arbitrairement fixé à zéro dans l'intervalle $e|V_S| < h\nu$. Les courbes grises en dessus du graphique en couleur correspondent à la dépendance en tension de F à $V_G = 3.12$V et $V_G = 3.21$V. La flèche noire indique $F(V) = 1$.

i.2.7 Conclusion

Nous avons développé un schéma de détection original permettant de coupler de manière résonante une source de bruit au détecteur choisi, la jonction SIS. Cela nous a permis de mesurer, aux fréquences de résonance du circuit de couplage, le bruit à l'équilibre du résonateur, le bruit hors équilibre d'une jonction Josephson et enfin le bruit associé au régime Kondo hors équilibre. Ce nouveau schéma de couplage est applicable à tous types de source de bruit haute impédance.

i.3 Mesures de relations courant/phase

La deuxième partie de ce manuscrit est dédiée à la mesure de relations courant/phase au travers d'une jonction hybride supraconducteurs/nanotube de carbone.

Dès lors qu'un conducteur normal est connecté à un supraconducteur, il est influencé par les corrélations induites par le supraconducteur. C'est l'effet de proximité [17]. Le mécanisme responsable de cet effet est la réflection d'Andreev [18] à l'interface normal/supraconducteur. Dans ce procédé, un électron du métal normal est réfléchi en un trou créant une paire de Cooper dans le supraconducteur. Grâce à ce phénomène un transport non dissipatif de courant, un supercourant, peut avoir lieu entre deux supraconducteurs séparés par un métal normal (lien faible) tant que la cohérence de phase dans la partie normale est préservée. Le supercourant est alors porté, dans la partie normale, par des états intriqués de paires électron/trou, les états liés d'Andreev, dépendants de la différence de phase entre les deux supraconducteurs. Une mesure de la relation courant/phase (RCP) renseigne alors sur les propriétés de cohérence de la partie normale.

Dans la suite, la partie normale est constituée par un nanotube de carbone se comportant comme une boîte quantique. Dans ce cas particulier, l'effet de proximité est fortement modifié par les interactions électroniques. Par exemple, il a été démontré que dans le cadre de contacts à transparence intermédiaire, le supercourant dépend du nombre d'électrons dans la boîte [12]. Si le nombre d'électron est impair, la RCP est décalée de π et on a une jonction $'\pi'$. Toujours dans un mode de transmission intermédiaire, l'effet Kondo peut aussi entrer en jeu. Dans ce cas le singulet de spin entre les électrons des réservoirs et le spin dans la boite d'énergie caractéristique $k_B T_K$ entre en compétition avec le singulet de spin des électrodes BCS d'énergie caractéristique Δ. Dans ce régime de compétition $\Delta \approx k_B T_K$, des RCP très particulières sont attendues montrant en particulier des transitions entre les états $'0'$ et $'\pi'$ de la boîte induites par la différence de phase entre les supraconducteurs.

Un des objectifs de cette thèse était de mesurer ces RCP particulières. Pour ce faire nous avons mis au point une technique de mesure de RCP permettant de mesurer à la fois la conductance de l'objet dans l'état supraconducteur et sa RCP associée. Cette technique est basée sur une adaptation du SQUID asymétrique présenté dans la référence [19]. Nous avons d'abord vérifié son principe de fonctionnement sur une petite jonction Josephson puis nous l'avons appliqué au nanotube de carbone.

i.3.1 Un SQUID asymétrique pour étudier les relations courant/ phase et courant/ tension d'un lien faible

Nous avons réalisé un SQUID *dc* fortement asymétrique comme schématisé sur la figure i.10. Les contacts A et C sont respectivement la source et le drain du SQUID. Un bras contient le lien faible à caractériser (petite jonction Josephson, boîte quantique,...) alors que l'autre possède deux grandes jonctions Josephson en série séparées par un contact central B.

L'intérêt d'un tel SQUID est triple. Premièrement, l'asymétrie entre les branches du SQUID permet de mesurer simplement la relation courant/phase (cf. [19]). Deuxièmement, les trois contacts permettent de mesurer les résistances des jonctions et du lien faible à température ambiante. Troisièmement, on peut utiliser le contact B pour mesurer la conductance du lien faible dans l'état supraconducteur.

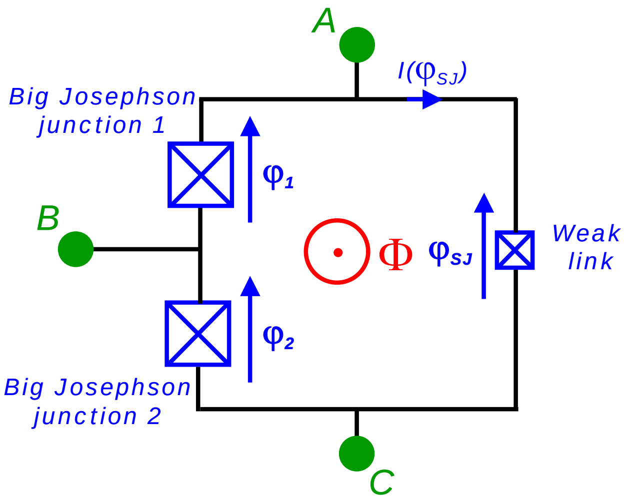

Figure i.10: Schéma du SQUID asymétrique. Les phases φ_1, φ_2 and φ_{SJ} sont reliées au flux magnétique dans la boucle ϕ par la relation $\varphi_{SJ} - (\varphi_1 + \varphi_2) = -2\pi\phi/\phi_0 + 2n\pi$ avec $\phi_0 = h/2e$.

Principe de la mesure de la relation courant/phase

En notant φ_1, φ_2 les différences de phase entre les deux grandes jonctions et φ_{SJ} la différence de phase aux bornes de la petite jonction, on a la relation $\varphi_{SJ} - (\varphi_1 + \varphi_2) = -2\pi\phi/\phi_0 + 2n\pi$ avec $\phi_0 = h/2e$ le quantum de flux, ϕ le flux magnétique appliqué et n un entier, permettant de relier le flux appliqué à la différence de phase aux bornes du lien faible.

Désormais, si I_0 est le courant critique des grandes jonctions et $I_{SJ,0}$ celui du lien faible, dû à la forte asymétrie du SQUID $I_0 >> I_{SJ,0}$, le SQUID passera d'un état non dissipatif à un état dissipatif (le SQUID switche) lorsque $\varphi_1 \cong \varphi_2 \cong \pi/2$ et donc $\varphi_{SJ} \cong$

$-2\pi\phi/\phi_0 + \pi + 2n\pi$. Il s'en suit que la mesure du courant critique du SQUID en fonction du flux magnétique appliqué obéit à la relation:

$$I_C(2\pi\phi/\phi_0) \cong I_0 + I_{SJ,0}f(\pi - 2\pi\phi/\phi_0), \tag{i.5}$$

avec $I_{SJ,0}f(x)$ la relation courant/phase du lien faible. Le courant critique du SQUID est donc modulé en fonction du champ magnétique appliqué avec une modulation entièrement dû à la relation courant/phase du lien faible. En pratique, on ne mesure jamais le courant critique, à cause de la température finie de l'environnement, mais un courant de switching plus faible. Cet élément important ne change en revanche pas le principe de l'expérience.

Principe de la mesure de la relation courant/tension

On utilise le contact C pour fixer V_{BC} à une tension en dessous du gap supraconducteur où le transport de quasi-particules est prohibé. Cette tension fait que la jonction 2 agit comme un interrupteur ouvert. Il ne reste plus qu'à mesurer la relation courant tension de la petite jonction en appliquant une tension entre A et C tout en mesurant le courant qui sort en C (cf. Fig.i.10).

i.3.2 Test du schéma de mesure appliqué à une jonction Josephson

Nous avons testé ce principe de détection en l'appliquant en premier lieu à une petite jonction Josephson pour laquelle la relation courant/phase est bien connue. Les résultats de la mesure de la relation courant/phase et courant/tension sont montrés sur la figure i.11.

On conclut de ces mesures que notre technique est complètement adaptée à l'étude de liens faibles de relativement haute impédance ($Re[Z] \in [10-50]k\Omega$). Elle permet de mesurer le caractère harmonique de la relation courant/phase testée et, de manière non ambiguë, la conductance différentielle du lien faible dans l'état supraconducteur.

i.3.3 Relation courant/ phase d'une jonction hybride Supraconducteur/ Nanotube de carbone

Nous considérons maintenant un nanotube de carbone en lieu et place de la petite jonction Josephson utilisée lors de la mise au point de la technique. Une image de l'échantillon en microscopie électronique est montrée sur la figure i.12. Le nanotube est couplé capacitivement à une grille arrière en silicium dopé afin de pouvoir moduler son potentiel électrostatique.

L'expérience permet de tracer des cartes de relations courant/phase en fonction de la tension de grille appliquée. On peut alors relier ces informations aux cartes de conductance en fonction des tensions source/drain et de grille à la fois dans l'état normal et dans l'état supraconducteur. Le nanotube est dans un régime de couplage fort avec les électrodes. La conductance différentielle monte jusqu'à $4e^2/h$ sans pour autant montrer des signes clairs

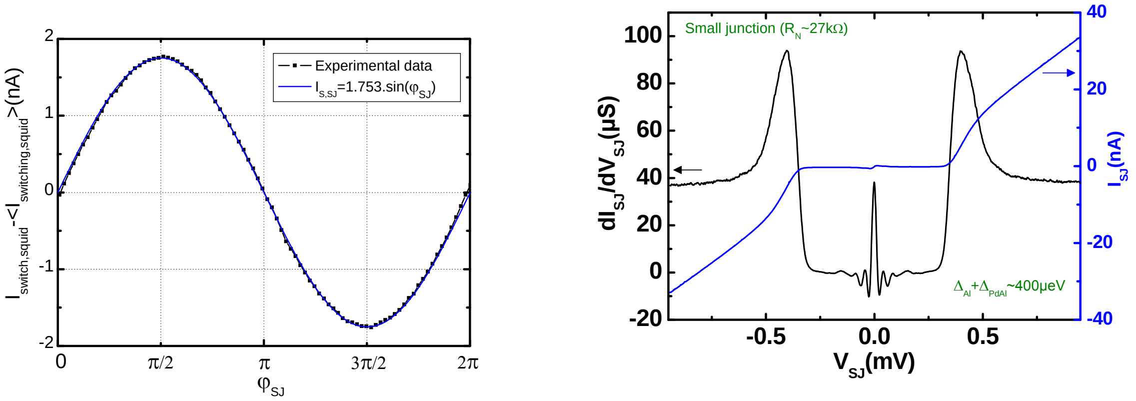

Figure i.11: (a) Relation courant/phase expérimentale d'une petite jonction Josephson. Les données reproduisent parfaitement l'évolution sinusoïdale attendue. (b) Conductance différentielle dI_{SJ}/dV_{SJ} et caractéristique courant/tension $I_{SJ}(V_{SJ})$ d'une petite jonction Josephson extraites de l'expérience. Ces courbes sont obtenues en fixant V_{BC} à une tension en dessous du gap supraconducteur où le transport de quasi-particules est prohibé, et avec un champ magnétique $B = 8.5$ Gauss pour éliminer le supercourant dans les grandes jonctions. On trouve $\Delta_{PdAl} + \Delta_{Al} = 400\mu eV$ et la résistance normale $R_{N,SJ} = 27k\Omega$.

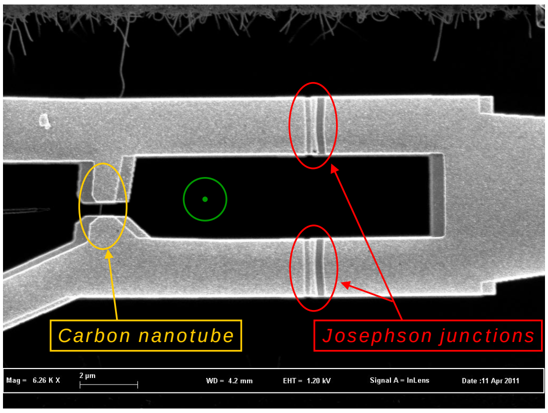

Figure i.12: Image en microscopie électronique du SQUID asymétrique utilisé dans l'expérience. Les jonctions et les contacts du nanotube sont composés de la séquence de matériaux $PdAl/Al_20_3/Al$. Les contacts du nanotube sont séparés de $\approx 450nm$.

du régime Fabry-Pérot. Comme attendue, les régions présentant une forte conductance montre des supercourants élevés. Des supercourants supérieurs à 10 nA ont ainsi été mesurés au travers du nanotube. Lorsque le supercourant est grand, la relation courant-phase est fortement anharmonique (cf.Fig.i.13a). Au contraire, quand le supercourant est faible, la relation redevient harmonique (cf.Fig.i.13b). Cela est consistant avec une analyse considérant un canal de conduction bien transmis. Une étude plus précise prenant en compte l'asymétrie des barrières ainsi que la dépendance en température de l'anharmonicité de la relation courant-phase est en cours.

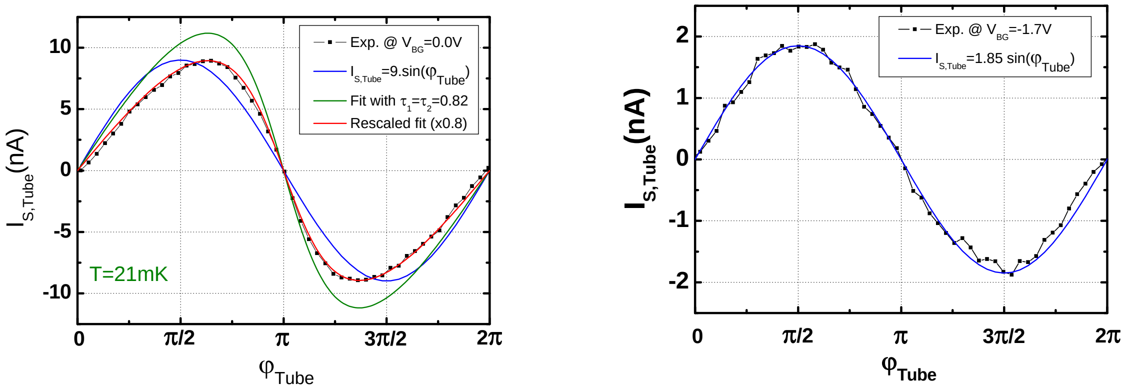

Figure i.13: (a) Relation courant/phase de la boîte quantique à nanotube de carbone dans une région de forte conductance (courbe noire). L'amplitude du supercourant est de 9.0nA et la RCP est anharmonique comme le suggère la comparaison avec la courbe bleue représentant une sinusoïde de même phase et même amplitude. La courbe verte correspond à un fit utilisant le formalisme des points contacts atomiques [20] à température nulle. Cela n'est pas suffisant pour reproduire les données. Nous avons donc renormalisé ce fit (courbe rouge) par le facteur 0.8 pouvant être expliqué par les incertitudes sur le gap supraconducteur des contacts, la conductance du tube dans l'état normal mais aussi par un effet de température finie. (b) Relation courant/phase dans une région de faible conductance (courbe noire). L'amplitude du supercourant est de 1.85nA et la RCP est harmonique comme suggéré par le fit sinusoïdal (courbe bleue).

i.3.4 Conclusion

Nous avons développé une extension de la technique introduite par le groupe Quantronique [19] permettant de mesurer à la fois la relation courant/phase et la relation courant/tension d'un lien faible. Nous l'avons testée sur une petite jonction Josephson et appliqué à une boîte quantique en nanotube de carbone. Le nanotube était dans un régime de couplage fort avec les électrodes permettant d'obtenir un supercourant maximum de 12 nA. La taille du supercourant est complètement reliée à l'importance de la conductance. Plus intéressant encore, quand le supercourant est fort la relation courant/phase est fortement anharmonique. Lorsqu'il est faible, la relation redevient harmonique. Le traitement théorique de ces données est toujours en cours.

i.4 Conclusion

Cette thèse a étudié deux aspects de la physique mésoscopique que sont le bruit quantique haute fréquence et l'effet de proximité supraconducteur en se focalisant toutefois sur un système modèle: la boîte quantique à nanotube de carbone.

Ainsi la première partie de cette thèse était dédiée à la mesure de bruit quantique haute fréquence. Afin de mesurer ces fluctuations nous avons imaginé un système de détection "on-chip" original dans lequel la source de bruit et le détecteur, une jonction SIS, sont couplés de manière résonante. Cela nous a permis de mesurer le bruit à l'équilibre du résonateur, le bruit hors équilibre d'une jonction Josephson et enfin le bruit associé au régime Kondo hors équilibre d'une boîte quantique à nanotube de carbone.

Dans la seconde partie, nous avons développé une technique permettant de mesurer à la fois la relation courant/phase et la relation courant/tension d'un lien faible séparant deux supraconducteurs. Après l'avoir testé sur une petite jonction Josephson, nous avons caractérisé la boîte quantique en nanotube de carbone au travers de laquelle un supercourant maximum de 12 nA a été observé. Conjointement à ce fort supercourant la relation courant/phase exhibe une forte anharmonicité.

Chapter 2

Introduction

The recent progress of modern electronics allows to build and manipulate devices at the nanoscale. This progressive miniaturization together with the possibility to cool down such devices at temperature of the order of mK's allows us to probe regimes in which classical mechanics is not valid anymore and quantum mechanics must be applied. This defines a sub-disciplin of condensed matter physics: *"the mesoscopic physics"*. It describes electronic properties at intermediate length scales between the atom and the macroscopic world. Mesoscopic physics study a large range of systems: insulators, semiconductors, metals, and superconductors. The systems studied are typically in the range of 100 nanometers to $1\mu m$. Thus mesoscopic physics has a close connection to the fields of nanofabrication and nanotechnology. Devices used in nanotechnology are examples of mesoscopic systems. The systems under interest are sufficiently small to be quantum mechanically coherent. This means their size is smaller than the length over which the electronic wave-functions keep a well defined phase, the phase coherence length L_φ. The properties of such systems are then strongly modified by quantum interferences.

Quantum nanoelectronics aims to use quantum phenomena for electronics [1]. One of the most studied system in this area is the artificial quantum dot. It consists in a designed region of space where a defined number of electrons is confined. The electronic spectrum is then discrete exactly like atoms. The first artificial quantum dots have been realized by electrostatic confinement in a two dimensional electron gas [2] and are nowadays routinely achieved. Opposingly, molecular electronics is much younger but has received quite a lot of interest these last years. It is now possible to access individual molecules such as C_60 molecules [21], Co nanoparticles [22], DNA [23], carbon nanotubes [24]...

One of the main advantage of fabricating such artificial atoms is the possibility to connect them to charge reservoirs to make transport experiments . Depending on the coupling strength between the dot and the reservoirs or the nature of the contacts, different physical phenomena arise such as the Coulomb blockade [25], the Kondo effect [26, 27] or the superconducting proximity effect [28–31].

In this thesis we have used carbon nanotubes (CNTs) to fabricate quantum dots. In the following, we then first present them and explicit how does transport through CNT quantum dot behave depending on the transparency of the contacts.

Contents

2.1 Single wall carbon nanotubes

Since their discovery in 1991 by Sumio Iijima [32], carbon nanotubes have attracted a lot of interest. The atomic structure of CNTs is that of a sheet of graphene rolled into a cylinder.

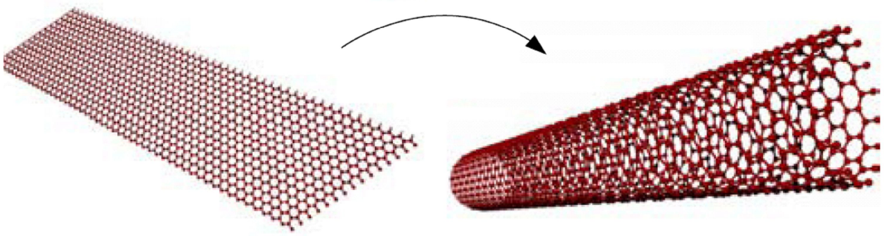

Figure 2.1: The atomic structure of CNTs is that of a sheet of graphene rolled into a cylinder.

From the mechanical point of view, this confers carbon nanotubes a high mechanical stiffness and a good flexibility at the same time. Despite their lightweight, they are one of the strongest materials known, with a Young modulus in the range of TPa [33]. Carbon nanotubes often grow in bundles, ropes or they appear nested within each other. They are consequently named multi-wall carbon nanotubes (MWCNTs). In the following, we will limit ourselves to the description of single-wall carbon nanotubes (SWCNTs).

Beyond those awesome mechanical properties, carbon nanotubes also have exceptional electrical properties. It is interesting to note that in theory metallic nanotubes can carry an electric current density of $4.10^9 A/cm^2$ which is more than 10^3 times greater than metals such as copper [34, 35]. Potential applications are studied in microelectronics to replace, as an example, *vias* in the back-end-of-line[1] of integrated circuits [36]. For more applications see for example [37].

Carbon nanotubes are among the most versatile model systems for electrical transport experiments in mesoscopic physics [38]. The precise roll-up direction and diameter determine whether it is metallic or semiconducting. In addition, metallic nanotubes are often considered as ideal one-dimensional conductors for the study of Luttinger liquid behavior [39].

In the following we first describe cristallographic and intrinsic electronic properties of SWCNTs. Afterwise, we show that a carbon nanotube connected to metallic leads may operate as a *quantum dot* in which electrons are confined. In this case electrons occupies well defined electronic states exactly like atoms.

2.1.1 Description

As already mentioned, a CNT is a sheet of graphene rolled into a cylinder. Graphene is derived from graphite in which carbon atoms are arranged in an hexagonal network. Depending on winding directions of the carbon nanotube with respect to the eigen vectors of graphene network, one obtains different kinds of nanotubes described by a certain helicity. To understand this, let us consider a graphene sheet as shown in figure 2.2. In this figure, a ribbon indicated by black lines is chosen to make the CNT . This choice is characterized by the vector C_h which can be decomposed on the eigen basis of the hexagonal network (a_1, a_2) so that

$$C_h = na_1 + ma_2. \tag{2.1}$$

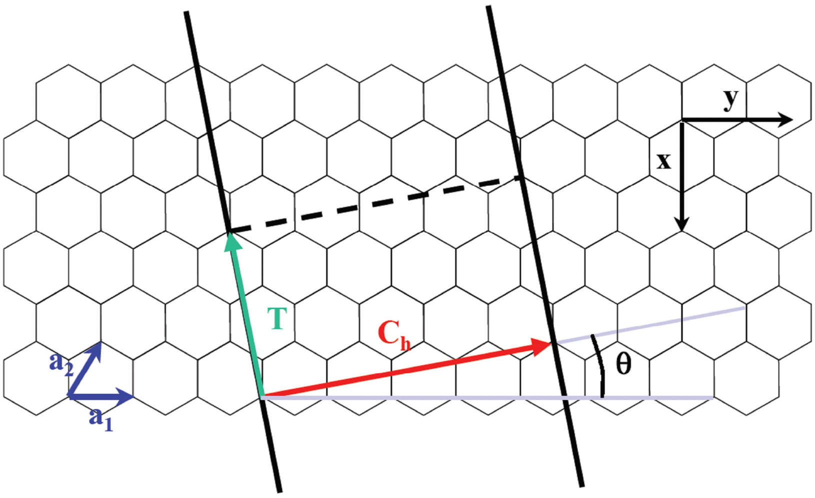

Figure 2.2: Graphene sheet. The two black lines define a ribbon from which a carbon nanotube is rolled. For this specific choice, a (4,1) carbon nanotube is obtained (see text).

---

[1] Back-end-of-line (BEOL) denotes the second portion of integrated circuits fabrication where the individual devices (transistors, capacitors, resistors, etc.) get interconnected with wiring on the wafer.

The couple of integers (n,m) classifies the nanotubes and determines their characteristics: diameter, helicity angle (θ on figure 2.2), eigen vectors of the nanotube (T)... From the cristallographic point of view, if helicity $\theta = 0^0$ tubes are called *zigzag* tubes corresponding to the set of couples (n,0). Opposingly, when $\theta = 30^0$ tubes are *armchair* and the set of couples is (n,n). Other kinds of nanotubes are *helicoidal* tubes. These different examples are illustrated in Fig.2.3.

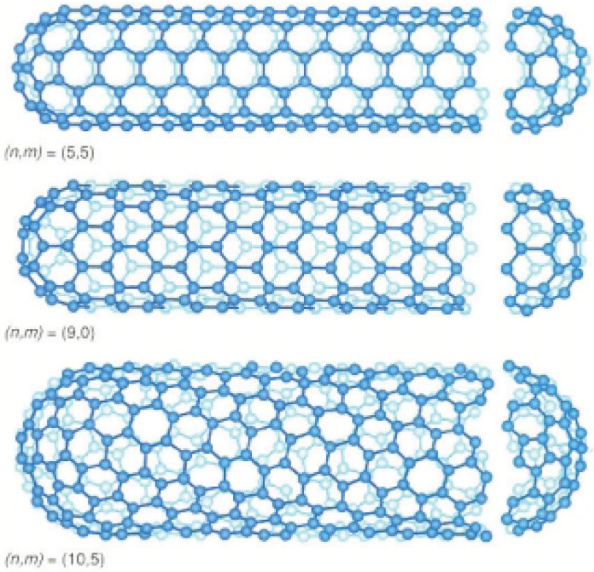

Figure 2.3: Different types of single wall carbon nanotubes: armchair (5,5), zigzag (9,0) and helicoidal (10,5).

2.1.2 Intrinsic electronic properties

The structure of a nanotube strongly affects its electrical properties. This comes from the peculiar band structure of the graphene sheet in which is introduced periodic boundary conditions to take into account the rolling. This limit condition highly depends on the particular rolling direction characterized by the couple (n,m).

A tight-binding model for π orbitals electrons in graphene allows to determine its dispersion relation and by extension the one of carbon nanotubes. It reads:

$$E^{\pm}(k_x, k_y) = \pm\gamma_0\sqrt{1 + 4cos\frac{\sqrt{3}k_x a_0}{2}cos\frac{k_y a_0}{2} + 4\left(cos\frac{k_y a_0}{2}\right)^2} \tag{2.2}$$

with the nearest-neighbor hopping energy $\gamma_0 = 2.8eV$ and the lattice constant $a_0 = 2.46$. Conduction and valence bands, respectively, correspond to the different signs in the above dispersion relation. As can be seen on Fig.2.4, they touch each other in six points, the *K-values* (Graphene is thus a semi-metal). However, only two of these six points are independent, whereas the rest is equivalent by symmetry. Those points are denoted K and

K'. In the vicinity of the K-points the energy depends linearly on the wave vector, similar to a relativistic particle.

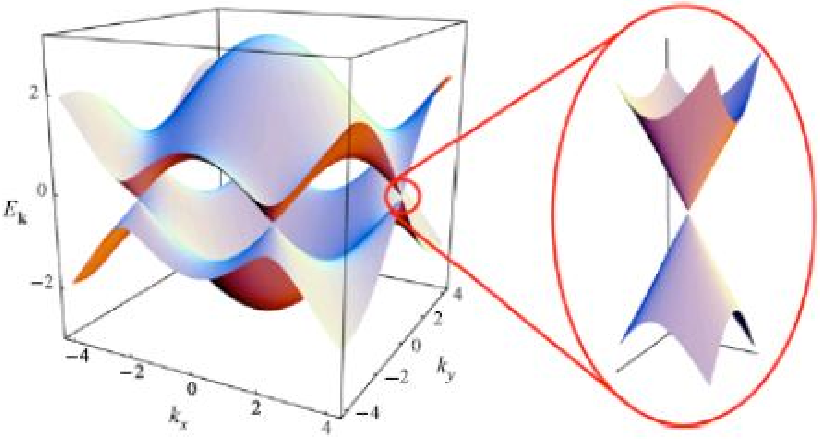

Figure 2.4: Dispersion relation of a graphene sheet from which is derived the band structure of carbon nanotubes. At half filling only six points touch each other: the K points.

Since a CNT is a graphene sheet rolled into a cylinder, this implies periodic boundary conditions for the electronic wave functions along the axis defined by the rolling vector C_h. As an example, let us consider the armchair tube (n,n). In this case the vector C_h only has a non zero component along the x axis[2]. The periodic boundary condition imposes that wave vector along x get quantized and reads:

$$k_x = \frac{2\pi q}{n\sqrt{3}a_0} \tag{2.3}$$

with q an integer number. As a consequence, the first Brillouin zone of the nanotube corresponds to interval $]-\pi/a_0, \pi/a_0]$. This is represented in figure 2.5a which highlights the metallic behaviour of the armchair carbon nanotube. At half-filling, two degenerate points touch the Fermi energy giving rise to 4 conduction channels if one takes into account the spin degree of freedom.

For a zig-zag tube (n,0) one can have different cases depending on n values. The quantization rule is here along the y axis:

$$k_y = \frac{2\pi q}{n a_0} \tag{2.4}$$

In the first Brillouin zone, the wavevector k falls within the interval $]-\pi/\sqrt{3}a_0, \pi/\sqrt{3}a_0]$. Consequently, depending on n values dispersion branches may or not include the point K as respectively represented in figure 2.5b and c. In the last case, the dispersion relation exhibits a bandgap which can reach hundreds of meV [40,41]. The tube is semiconducting.

---

[2] Note than the (x, y) basis is defined modulo a rotation of $2\pi/3$.

For a given (n,m) nanotube, if $n = m$, the nanotube is metallic; if $n - m$ is a multiple of 3, then the nanotube is semiconducting with a very small band gap, otherwise the nanotube is a moderate semiconductor. Thus all armchair ($n = m$) nanotubes are metallic, and nanotubes (6,4), (9,1), etc. are semiconducting. However, this rule has exceptions, because curvature effects in small diameter carbon nanotubes can influence strongly electrical properties. Thus, a (5,0) SWCNT that should be semiconducting is metallic according to the calculations. Likewise, vice versa zigzag and chiral SWCNTs with small diameters that should be metallic have a finite gap (armchair nanotubes remain metallic).

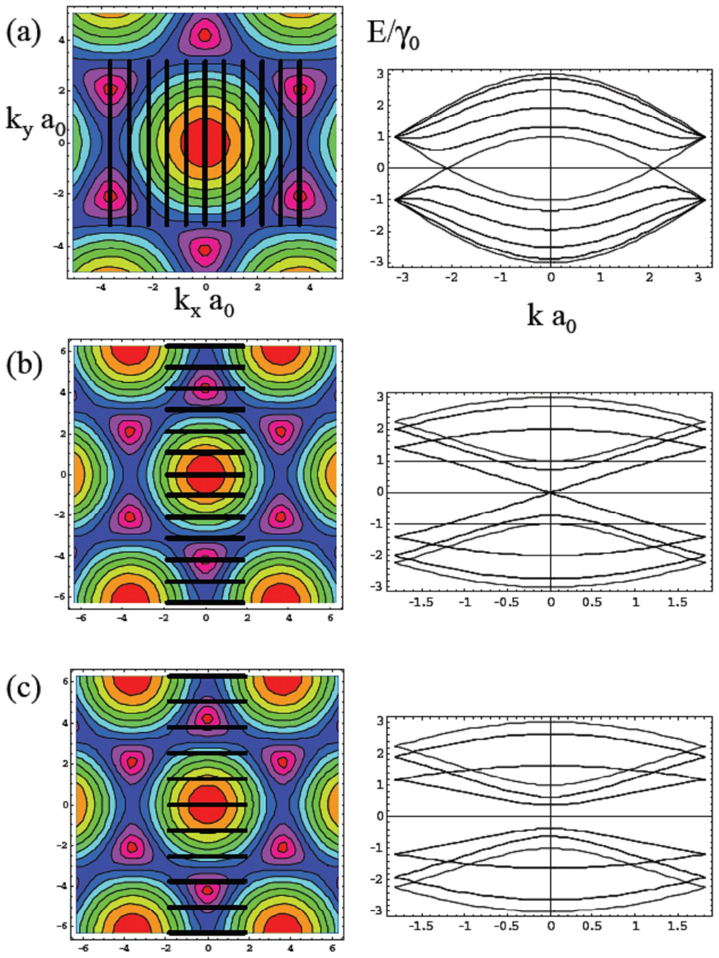

Figure 2.5: Dispersion relation of different single wall carbon nanotubes. On the left are represented the dispersion relation of a graphene sheet where black lines denote allowed values for the transverse wave vector imposed by boundary conditions. On the right are shown the deduced dispersion relations of the carbon nanotubes. (a) Metallic armchair tube (5,5). (b) Metallic zigzag tube (6,0). (c) Semiconducting zigzag tube (5,0).

2.2 Carbon nanotube quantum dots

The particular geometry of carbon nanotubes, few nanometers in diameter and several micrometers long, allows to remarkably easily connect them in a top-down approach[3]. By depositing two electrodes onto a previously selected SWCNT, a junction is created between source (S) and drain (D) electrodes, which in general can consist of a normal metal, a ferromagnet, or even a superconductor. Confinement is thus introduced in the remaining dimension and a quantum dot is formed between the barriers at the contacts. Indeed, when the distance between contacts is comparable to the wavelength of the electrons that occupy it, the system exhibits a discrete energy spectrum, resembling that of an atom. As a result, quantum dots behave in many respects as artificial atoms. A quantum dot is a general kind of system and many different sizes and materials can be used to realize it: single molecules trapped between electrodes [30, 42], metallic or superconducting nanoparticles, self-assembled quantum dots, semiconductor lateral or vertical dots [2, 43], semiconducting nanowires or carbon nanotubes [24, 44] between closely spaced electrodes (see Fig.2.6a). In this thesis, we study metallic carbon nanotubes based quantum dots.

2.2.1 Hamiltonian description

Hamiltonian of the dot

The hamiltonian of the isolated dot can be written as [45–47]:

$$H_{dot} = \sum_{ns} \epsilon_n d^+_{ns} d_{ns} + E_C(\hat{N} - N_0)^2 - E_S \hat{S}^2. \tag{2.5}$$

The first term of this hamiltonian describe the excitation spectrum of the dot with ϵ_n the energy of the single-particle level n. d^+_{ns} (d_{ns}) is the creation (respectively annihilation) operator of an electron with spin s in the single particle level ϵ_n. From this term, one can introduce the mean single-particle level spacing between two successive energy levels $< \epsilon_{n+1} - \epsilon_n >= \delta E$. This term takes into account the confinement potential together with the inherent physics of the carbon nanotube[4].

The second term describes the electrostatic energy of the dot. $E_C = e^2/2C$ is the charging energy of the dot with C the total capacitance which is the sum of the capacitances between the dot and the source, C_S, the drain, C_D, and the gate, C_G: $C = C_S + C_D + C_G$ (see Fig.2.6a). $\hat{N}$ is the operator of the number of electrons in the dot and $N_0 = C_G V_G/e$ is a tunable term via a nearby gate voltage V_G (coupling capacitance C_G) allowing to change the total number of electrons in the dot.

Finally, the last term of this expression correspond to intradot exchange interactions with energy exchange E_S and $\hat{S} = \sum_{nss'} d^+_{ns} \frac{\sigma_{ss'}}{2} d_{ns'}$ the spin operator of the dot. $\sigma =$

---

[3] The top-down approach uses the traditional workshop or microfabrication methods where externally-controlled tools are used to cut, mill, and shape materials into the desired shape and order. Micropatterning techniques, such as photolithography and inkjet printing belong to this category.

[4] Note than if orbital degenerascy of the carbon nanotube is lifted, this will be taken into account in this term.

$(\sigma^x, \sigma^y, \sigma^z)$ are the Pauli matrices. In the following we will neglect this last term assuming than $E_S << \delta E, E_C$.

A dot is thus a small box that can be arbitrarily filled with electrons making use of a nearby gate voltage.

Total hamiltonian

In practice, the dot is not fully isolated from the external world and is coupled via tunnel barriers to source and drain reservoirs, with which particles can be exchanged. By attaching current and voltage probes to these reservoirs electronic properties of the dot are measured and the nearby gate electrode is used to tune the electrostatic potential of the dot with respect to the reservoirs. The complete hamiltonian H of the system reservoirs, dot is decomposed in three terms:

$$H = H_{leads} + H_{dot} + H_{tunneling}. \tag{2.6}$$

The first term describes free electrons in metallic leads with a continuous spectrum ξ_k and a constant density of states ν[5]:

$$H_{leads} = \sum_{\alpha k s} \xi_k c^+_{\alpha k s} c_{\alpha k s} \ , \xi_k = -\xi_{-k}. \tag{2.7}$$

The operator $c^+_{\alpha k s}$ ($c_{\alpha k s}$) creates (respectively destroys) an electron with spin s in the state k of lead α ($\alpha = S, D$ for source/drain leads).

The second term is given by Eq.2.5 and the last term describes tunneling between the dot and the leads. It has the form:

$$H_{tunneling} = \sum_{\alpha k n s} t_{\alpha n} c^+_{\alpha k s} d_{ns} + H.c. \tag{2.8}$$

where $t_{\alpha n}$ is the tunneling amplitude connecting the state n in the dot with the state k in the lead α.

The tunneling between the dot and the leads induces a broadening of discrete levels in the dot. The width $\Gamma_{\alpha n}$ that level n acquires due to escape of an electron to lead α is given by

$$\Gamma_{\alpha n} = \pi \nu |t^2_{\alpha n}| \tag{2.9}$$

which by extension gives the total width of the level n:

$$\Gamma_n = \sum_{\alpha} \Gamma_{\alpha n} = \sum_{\alpha} \pi \nu |t^2_{\alpha n}| \tag{2.10}$$

---

[5] Note than the use of superconducting leads with a gapped density of states would be taken into account within this term.

Conclusion

We conclude by summarizing the relevant energy scales introduced by this hamiltonian description. First, due to electronic confinement and particular band structure in the dot, a discrete energy spectrum of single-particle levels is formed at energies ϵ_n with a mean level spacing δE. Second, due to the small size of the dot, capacitance between external gate and leads impose a strong charging energy $E_C = e^2/2C$ which has to be paid each time one needs to add an electron on the dot. Third, the tunnel coupling to external leads induce a broadening Γ of the single-particle levels as shown in Fig.2.6b.

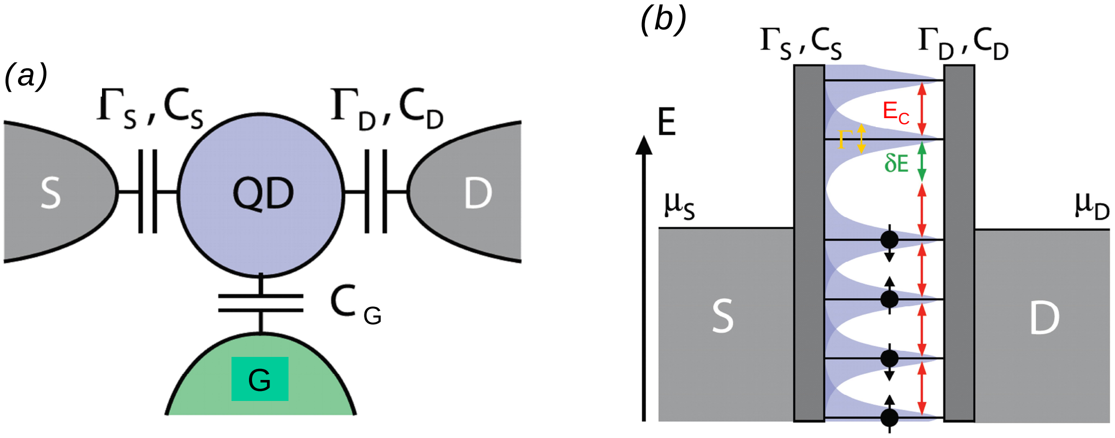

Figure 2.6: (a) Schematic of a quantum dot (QD) with source (S)/drain (D) leads and a capacitively coupled gate (G) .(b) The discrete energy levels of width $\Gamma = \Gamma_S + \Gamma_D$ on the QD are separated by the orbital energy δE and the charging energy E_C.

At low temperature, depending on the relative values of those different energy scales one encounters different transport regimes for the quantum dot. In the *weak coupling regime*, the tunneling hamiltonian can be taken as a small perturbation to the dot Hamiltonian and thus $\Gamma << E_C, \delta E$. The energy levels on the dot are clearly defined and Coulomb blockade is of primary importance. Opposingly, in the *strong coupling regime* the dot levels are strongly hybridized with the electronic wave functions of the reservoirs so that $\Gamma > E_C, \delta E$. In this case, the dot behaves as a constriction. Finally, in the *intermediate coupling regime* $\Gamma \approx E_C \approx \delta E$, the physics is very rich and complicated. In particular we will see how Kondo correlations may appear. We now detail those limits.

2.2.2 Strong coupling regime

In the strong coupling regime, the quantum dot levels are strongly hybridized with the electronic wave functions of the electrodes. Their width Γ are much larger than the charging energy and the mean single level spacing δE. The dot behaves as a constriction. In this case, by aligning the Fermi energy of the leads with the N degenerate energy level(s) in the dot, one reaches resonant conditions in which conductance is high. In the Landauer-

Büttiker formalism the conductance is essentially given by the formula[6] [6]:

$$G = e^2/h \sum_{i=1}^{N} T_i. \tag{2.11}$$

describing charge transport through N transport channels with transmission T ($0 \leq T \leq 1$). For one single orbital level aligned within the bias window, due to the spin degeneracy, conductance can go up to $2e^2/h$.

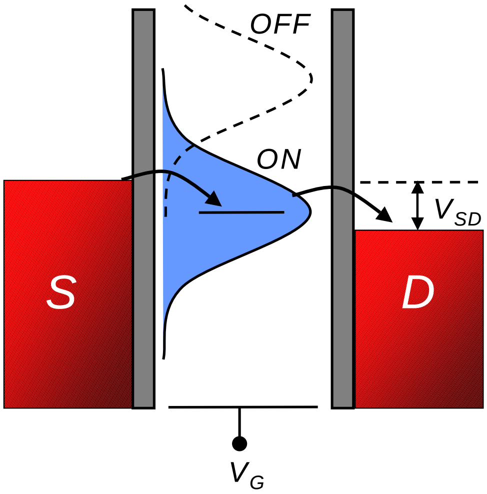

Figure 2.7: Schematic of electronic transport through a strongly coupled quantum dot. Due to the strong hybridization of the dot with the electronic wave functions of the electrodes the dot behaves more as a constriction. Every degenerate (spin and orbital) levels participate at the same time to the conductance of the system.

Carbon nanotube specificity 1 - The metallic nanotube is a one-dimensional conductor with two orbitally degenerate conducting channels. This orbital degeneracy can be intuitively understood by the two clockwise and anti-clockwise ways of propagating electrons along the nanotube [48]. As a consequence of the additional orbital degeneracy[7], the maximum conductance of a ballistic carbon nanotube with perfect barrier transparency is $G = 4G_0 = 4e^2/h$, corresponding to a resistance of $6.45k\Omega$. The factor 4 accounting for both spin and orbital degenerascy.

Carbon nanotube specificity 2 - Quantum interference between propagating electron waves may occur. The nanotube behaves as a coherent electron waveguide, with a resonant

---

[6] This formalism will be detailed in chapter 3

[7] In a real device, defects in the atomic structure often lifts this so called K-K' degeneracy and only one spin degenerate orbital level at a time aligns with the Fermi energy of the reservoirs.

cavity formed between the two nanotube/electrode interfaces (see figure 2.8). A Fabry-Perot electron resonator is formed. The vizualisation of these processes has been realized in carbon nanotubes [49–52] and two dimensional electron gases (2DEG) in a magnetic field [53]. The signature of this effect can be seen on the conductance which oscillates as a function of the nearby electrostatic gate voltage V_G and source-drain bias voltage V_{SD}. The oscillation period exhibits an inverse dependence on the nanotube length L and the characteristic energy scale is $E_{FP} = hv_F/L$ with v_F the Fermi velocity associated to the molecule.

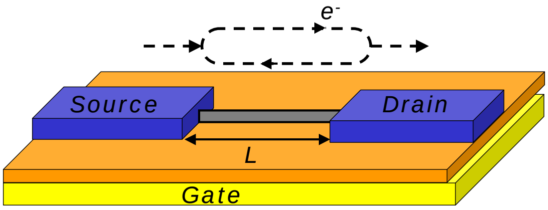

Figure 2.8: In the Fabry Perot regime the CNT, shown here in grey, acts as an electronic waveguide in which the two degenerate orbitals of the propagating electron waves interfere. Signatures on conductance are visible revealing the characteristic energy scale $E_{FP} = hv_F/L$ with v_F the Fermi velocity associated to the conductor and L the distance between contacts.

2.2.3 Weak coupling or Coulomb blockade regime

In the weak coupling regime, energy levels are very well defined and $\Gamma << E_C, \delta E$. This case is frequently reached in state of the art quantum dots due to their small dimensions. Indeed as the size falls down, the total capacitance to the external leads vanishes and charging energy becomes significant. It is common that charging energy reaches few meV[8] whereas in a dilution fridge, thermal energy k_BT is only few μeV[9]. As a consequence, thermally activated transport is strongly suppressed.

One conveniently introduces the electrochemical potential $\mu(N)$, which is by definition the energy required for adding the N^{th} electron to the dot:

$$\mu(N) = (N - N_0 - \frac{1}{2})E_C - \frac{E_C}{e}(C_S V_{SD} + C_G V_G) + \epsilon_N \tag{2.12}$$

The discrete levels are consequently spaced by the so-called addition energy:

$$\boxed{E_{add}(N) = \mu(N+1) - \mu(N) = E_C + \delta E} \tag{2.13}$$

which comports a purely electrostatic term meaning that every electrons approaching the QD feels a repulsion due to the charge of the electrons already present there, plus the energy

---

[8] The charging energy associated to a capacitance $C = 10aF$ is $E_C = 8meV$

[9] The thermal energy associated to a temperature $T = 10mK$ is $k_BT = 0.86\mu eV$

spacing between two discrete quantum levels, δE. Note that δE can be zero, when two consecutive electrons are added to the same spin-degenerate channel or a different orbitally degenerate channel. The addition energy spectrum of such weakly coupled quantum dot is shown in figure 2.9. It corresponds to a ladder of single particle levels that can be energetically shifted up and down with respect to the Fermi energies of the leads using a nearby gate voltage.

Zero bias regime If the single particle levels are below the Fermi energies of the leads (Fig. 2.9a), the energy provided to the dot at low temperatures and small bias voltage is too small to overcome the addition energy. Transport is exponentially suppressed. As a consequence, the number of electrons on the dot remains fixed and no current flows through it. This is the Coulomb blockade.

For transport to occur, a level of the dot must fall within the bias window between the electrochemical potential (Fermi energy) of the source (μ_S) and drain (μ_D) reservoirs, *i.e.* $\mu_S \geq \mu \geq \mu_D$ with $V_{SD} = (\mu_S - \mu_D)/e$. In this case, an electron can tunnel in and out of the dot carrying a finite current. This is done by changing the voltage applied to the gate electrode which shifts the whole *ladder* of electrochemical potential levels up or down. When a level falls within the bias window (see Fig. 2.9b), the current through the device is switched on. The electron number on the dot alternates between $N-1$ and N. Only after one electron tunnels off to the drain can another electron come onto the dot from the source. This cycle is known as sequential single-electron tunneling.

By sweeping the gate voltage and measuring the conductance, we obtain a trace as shown in Fig.2.9c. At the positions of the peaks, an electrochemical potential level is aligned with the source and drain Fermi energy and sequential tunneling occurs. Opposingly, in the valleys between the peaks, the number of electrons on the dot is fixed due to Coulomb blockade. The distance between the peaks corresponds to $E_{add} = E_C + \delta E$, and can therefore give information about the energy spectrum of the dot.

Carbon nanotube specificity- In figure 2.9 we show the case of a carbon nanotube with a fourfold degenerate energy level. Indeed, if one electron is already present on the first energy level of the dot, the addition energy of a second, third and fourth electron is E_C until the energy level is full (4 electrons for spin and orbit degenerascy in carbon nanotube). In this case, adding another electron to the dot requires to pay the charging energy plus the single energy level spacing δE.

Finite bias regime A second way to lift Coulomb blockade is to increase the source-drain voltage, V_{SD} (see Fig.2.9d). This increases the bias window in which an electronic level may stand. Again, a current flows when an electrochemical potential level falls within the bias window. When V_{SD} is increased so much that two levels of the dot fall within the bias window, there are two paths available for electrons tunneling through the dot. This leads to an increase of the current, enabling to perform the spectroscopy of the excited states. How exactly the current changes depends on the tunnel rates of the two paths.

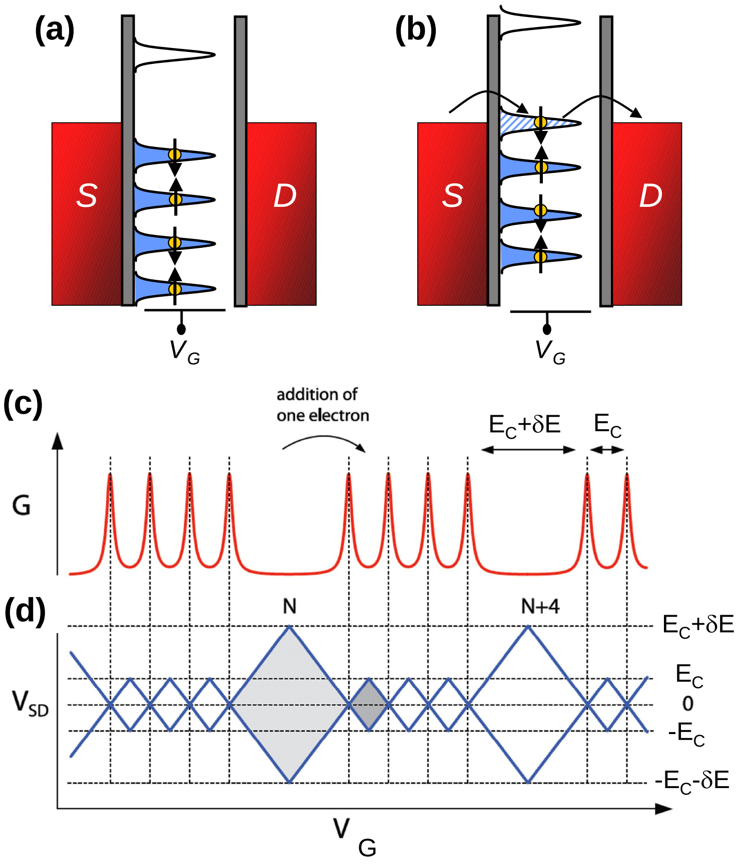

Figure 2.9: Transport through a metallic nanotube quantum dot in the Coulomb blockade regime. (a) No energy level in the dot aligns to the Fermi energies of the leads. Transport is energetically forbidden, no current flows through the dot. It is Coulomb blocked. (b) By tuning the gate voltage V_G, an energy level of the dot coincides with Fermi energy and resonant single electron tunneling occurs. The magnitude of the current depends on the tunnel rates between the dot and the reservoirs Γ_S and Γ_D. (c) Coulomb peaks in conductance versus gate voltage at zero bias. (d) Coulomb diamonds in differential conductance dI/dV_{SD}, versus V_{SD} and V_G. Each diamond corresponds to an integer number of electrons on the QD, and its size is determined by E_C and δE.

Stability diagram Usually, the current or differential conductance (the derivative of the current with respect to the source-drain bias) is measured while sweeping the bias voltage, for a series of different values of the gate voltage. Such a measurement is shown schematically in Fig. 2.9d. Inside the diamond-shaped region, the number of electrons is fixed due to Coulomb blockade, and no current flows. Outside the diamonds, Coulomb blockade is lifted and single-electron tunneling take place. The energy of excited states δE as well as the charging energy can be extracted directly from such *Coulomb diamonds*. It is important to note that a slightly asymmetric couplings to the two leads distort the diamonds so that they are no longer four-fold symmetric but appear slightly slanted. From the distortion of the diamonds, one can obtain the relative capacitive couplings of the two leads.

Limitations The simple model described above explains successfully how quantization of charge and energy leads to effects like Coulomb blockade and Coulomb oscillations. Nevertheless, it is too simplified in many respects. For instance, the model considers only first-order tunneling processes, in which an electron tunnels first from one reservoir onto the dot, and then from the dot to the other reservoir. Furthermore, this simple model does not take into account the spin of the electrons nor exchange effects.

2.2.4 Intermediate coupling regime

In the intermediate coupling regime, tunneling cannot be accurately accounted taking first order perturbation theory as done in the low coupling regime. In particular, going beyond this lowest-order allows one to consider processes in which states of the dot which are energetically not allowed participate in the tunneling process as *virtual states* [54, 55]. These processes are refered as co-tunneling processes. Indeed, even deep in a coulomb blockade valley where transport is energetically prohibited, quantum mechanically, as a direct consequence of time-energy uncertainty, it is allowed for an electron to tunnel in and out the dot.

Co-tunneling processes

Unlike the sequential tunneling, in the co-tunneling mechanism, the electron tunneling from one of the leads into the dot, and from the dot to the other lead occurs as a single quantum process[10].

Those co-tunneling processes can either be elastic or inelastic. In the inelastic co-tunneling mechanism (see Fig.2.10a), an electron tunnels from a lead into one of the vacant single-particle levels, while it is an electron occupying an other level in the dot which tunnels out of the dot. As a result, the charge transfer is accompanied by the creation of

---

[10] The co-tunneling effect leads, for sufficiently good tunnel coupling between dot and electrodes, to a non zero conductance in the Coulomb diamonds where transport is classically prohibited.

an electron/hole pair in the dot[11]. In the elastic co-tunneling mechanism (see Fig.2.10b), no pairs are created and the occupation numbers of single-particle energy levels of the dot in the initial and final states are the same. It is interesting to define the temperature $T_{el} = \sqrt{E_C \delta E}/k_B$. If $T \geq T_{el}$, inelastic co-tunneling is favored while for $T \leq E_C/k_B$ only elastic tunneling occurs.

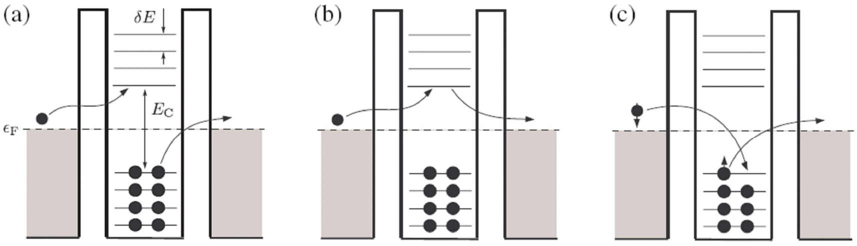

Figure 2.10: Taken from [47]. Examples of co-tunneling processes. (a) Inelastic co-tunneling. An electron-hole pair is left after tunneling process. (b) Elastic co-tunneling. (c) Elastic co-tunneling with a spin-flip.

Kondo regime

A dot which has a odd number of electrons in its ground state carries a spin 1/2. This opens a possibility of a co-tunneling process in which the transfer of an electron between the leads is accompanied by the simultaneous flip of the electron's spin of the dot (see Fig.2.10c and 2.11) [57]. This virtual process leads to a dynamical screening of the localized spin by the conduction electrons of the leads. The amplitude of such a process, calculated in fourth order tunneling theory diverges at zero energy. This logarithmic singularity in the transmission amplitude leads to an extraordinary enhancement of the conductance G accross the dot at zero bias and low temperature. This conductance enhancement can be understood in the light of Kondo physics [3,58] using renormalization group technique [59].

At this stage, it is important to note that Kondo theory originally explained the anomalous increase of the resistance at low temperature in dilute magnetic alloys. The physical interpretation is the screening of localized spins by the spin of conduction electrons. In such case the magnetic impurity forms with conduction electrons and at low temperature, a spin singlet ground state having a larger cross section: the *Kondo cloud*. As a consequence, resistance increases.

Anderson [57] also proposed that for the same reasons, a tunneling experiment should exhibit an increase of the zero bias conductance [60,61]. This effect was investigated later on with unpaired electrons in quantum dots both theoretically [62,63] and experimentally [26,64]. In this case the dot behaves as an $S = 1/2$ magnetic impurity between tunneling barriers separating two massive conductors.

---

[11] One signature of inelastic co-tunneling in quantum dot is an increase of the conductance at finite bias in the middle of a Coulomb blockade diamond [56]

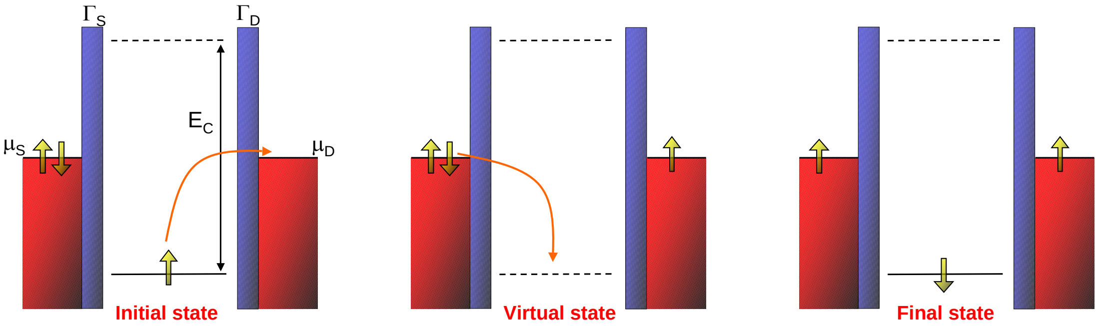

Figure 2.11: Elastic co-tunneling events responsible for Kondo type correlations between Fermi leads and single spin in the dot.

To understand this effect, it is interesting to write the effective low energy ($E < \Delta$ with Δ a cutoff energy) hamiltonian [12] in the form [47]:

$$H_{eff} = \sum_{\gamma ks} \xi_k \psi^{+}_{\gamma ks} \psi_{\gamma ks} + \sum_{\gamma} J_\gamma (s_\gamma . S). \tag{2.14}$$

The operators ψ_γ are linear combinations of operators $c_{S,D}$ describing electrons in the leads,

$$s_\gamma = \sum_{kk'ss'} \psi^{+}_{\gamma ks} (\frac{\sigma_{ss'}}{2}) \psi_{\gamma k's'} \tag{2.15}$$

is the local spin density of itinerant electrons in the channel $\gamma = 1, 2$ and S is the spin operator of the dot. The sum over k in Eq.2.14 is limited to a small energy strip $|\xi_k| < \Delta$. The second term of this hamiltonian represents the exchange between electrons in the leads and the spin of the dot. The exchange amplitudes J_γ are real and a simple expression, valid for $S = 1/2$, relates the exchange energy to the transmission amplitudes of the barriers:

$$tr(\hat{J}) = \frac{1}{E_C} \sum_n (|t_{Sn}|^2 + |t_{Dn}|^2). \tag{2.16}$$

In this context, the local spin of the dot together with the conduction electrons of the leads condense in a many-body spin-singlet ground state with a binding energy given by the critical Kondo temperature T_K. The Kondo temperature for $S = 1/2$ is related to the exchange couplings J_γ by

$$T_K \propto exp(-1/\nu tr(\hat{J})) \tag{2.17}$$

The manifestation of the spin singlet state is the formation of a Kondo resonance of width T_K at the Fermi energy of the leads in the quantum dot density of states. This resonance gives rise to a zero bias conductance peak whose amplitude depends on the barriers

---

[12] The range of energy considered must be small enough to conserve the charge state of the dot. To do so, a handmade cutoff $\Delta \approx min(\delta E, E_C)$ is necessary

transmissions:

$$G = \frac{2e^2}{h}\frac{4\Gamma_S\Gamma_D}{(\Gamma_S+\Gamma_D)^2}. \tag{2.18}$$

It is very interesting to note than G may reach a unitary limit as high as the spin degenerate quantum of conductance $2e^2/h$ [65, 66] if tunnel barriers are fully symmetric. The amplitude of the conductance only depends on the symmetry of the coupling to the electrodes and not of the strength[13]. The Kondo temperature is related to the charging energy E_C of the quantum dot, the total coupling $\Gamma = \Gamma_S + \Gamma_D$ to the electrodes and the position ϵ of the energy level measured from half filling[14], according to the Bethe-Ansatz [67, 68]:

$$T_K = \sqrt{E_C\Gamma/2}\exp\left[-\frac{\pi}{8E_C\Gamma}|4\epsilon^2 - E_C^2|\right]. \tag{2.19}$$

As a result of this many body singlet, the stability diagram of the quantum dot ($dI/dV = f(V_{SD}, V_G)$) exhibits a strong conductance increase at zero bias as long as there is an odd number of electrons in the dot (tunable *via* the nearby gate voltage): the so-called *Kondo ridge* (see Fig.2.12).

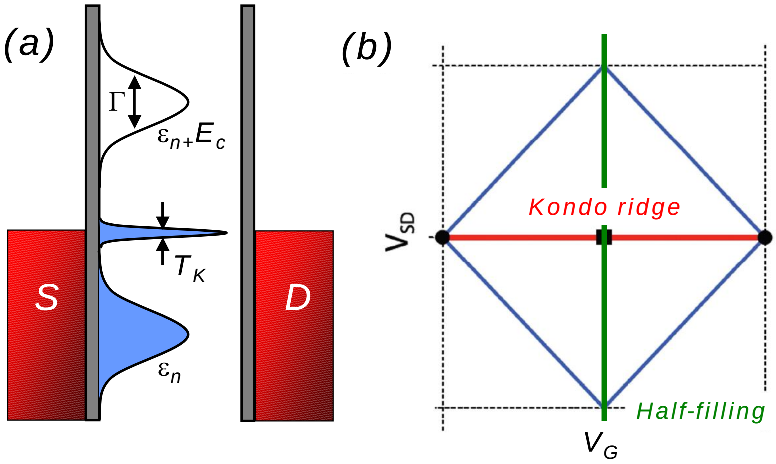

Figure 2.12: (a)Density of states of the dot exhibiting a Kondo resonance at Fermi energy of the leads. (b) Scheme of a stability diagram exhibiting Kondo effect. The zero bias conductance increase (Red line) is named Kondo ridge and survives as long as the number of electrons in the dot is odd. The green line corresponds to half-filling criteria (controlled with gate).

---

[13] At least as long as the coupling is strong enough for the Kondo effect to occur.

[14] Terminology to design an energy reference from which the absolute value of the energy difference between the last occupied state and the first unoccupied state is identical. In our case, this is exactly in the middle of two subsequent conductance peaks in a conductance trace versus gate voltage at zero bias (Fig.2.9c).

When the quantum dot is voltage biased, the Kondo resonance splits with a splitting given by the applied bias voltage. Conductance is suppressed and one recovers a low conductance characteristic of the Coulomb blockade. The maximum conductance of the Kondo peak is very sensitive to thermal fluctuations and its temperature dependence is well reproduced by the empirical formula given in reference [69]:

$$G = G_0/(1 + (2^{1/s-1}(T/T_K)^2))^s \tag{2.20}$$

with s a constant which depends on Kondo type correlations ($s = 0.22$ for spin $1/2$ kondo systems). This empirical formula derives from a fit to NRG calculations and is known to reasonably reproduce the temperature dependence of the zero bias peak. Typical Kondo temperatures that can be reached with a carbon nanotube range from 1 to $4K$, which is larger than the typical values in GaAs quantum dots [2].

2.3 Conclusion

Through this chapter we have introduced the main system of interest of this thesis: the carbon nanotube. We saw that depending on the transmission between metallic contacts and the tube many different transport regimes can be reached. One of them, the Kondo effect in quantum dots, will be a central topic of this thesis. In particular one wants to study two aspects of the Kondo effect that are its dynamics and the competition/interplay with superconductivity.

Dynamics - As already mentioned, Kondo effect is a dynamical process in which conduction electrons dynamically screen the dot's spin. It is known from the litterature that the relevant energy scale to describe such effect is the Kondo temperature T_K. This temperature for carbon nanotube quantum dots typically corresponds to frequencies in the $10 - 100GHz$ range. The question we ask then is: Can we probe the dynamics of the system at timescale shorter than h/k_BT_K? To answer this question we propose to look at the high frequency ($10 - 100GHz$) quantum noise of such Kondo impurity using an on chip quantum detector.

Competition/interplay with superconductivity - Another aspect of the Kondo effect we want to study is its capability to survive or not to superconducting correlations introduced by superconducting leads. Indeed, as was shown along this introduction chapter, the Kondo effect consists in a coupling between the spin of the dot and the electrons of the leads which together form a spin singlet ground state with characteristic energy k_BT_K. On the other hand superconductivity is also a spin singlet ground state where electrons condense in Cooper pairs with pairing energy Δ and phase θ. The competition between those two ground states is widely covered by theoretical litterature whereas only few experimental works exist in the regime $\Delta \approx k_BT_K$ where the two regime are in competition. In particular, looking at the current phase relation of such system is quite interesting since it could exhibit phase induced transitions between $'0'$ and $'\pi'$ state where the dot's spin is respectively screened or unscreened.

Part I

High Frequency Quantum Noise of Mesoscopic Systems

Introduction

Whereas electrical noise has been extensively studied at low frequency in various systems [6], going from macroscopic to mesoscopic scales, and is now relatively well understood, investigation of high frequency noise is much more recent. Of particular interest is the frequency range of the order of or higher than the applied voltage or temperature characteristic energy scales. Current fluctuations in this quantum regime acquire a frequency dependence with signatures of the relevant energy scales k_BT and eV (with T the temperature and V the bias voltage on the device). Thus current fluctuations has been found to increase linearly with frequency above k_BT/h [70, 71]. Similarly the excess noise, *i.e.* the difference between the noise at a given bias and the noise at equilibrium, measured in the limit $eV \gg k_BT$ has been found to decrease linearly with frequency and go to zero at frequency eV/h both in diffusive wires [72] and GaAs ballistic quantum point contacts [73].

As we will see in chapter 3, in the quantum regime noise can be described in terms of exchange of photons of energy $h\nu$ between the source and the noise detector. Depending on whether photons are emitted or absorbed by the source one measures emission noise (corresponding to negative frequencies) and absorption noise (corresponding to positive frequencies) [7]. This difference between emission and absorption processes is well known in the field of quantum optics but difficult to observe in electronic devices since most classical amplifiers exchange energy with the device measured and allow only the detection of a combination of emission and absorption noise [8]. On the other hand a quantum detector [7, 74], such as a superconductor-insulator-superconductor (SIS) tunnel junction [9, 75], allows to measure the non-symmetrized noise, *i.e.* distinguish between emission and absorption. This will be reviewed in chapter 4. Due to the difficulty to extract the equilibrium noise contribution, this type of measurement has only been done so far for the excess noise.

Chapter 5 considers an experiment in the quantum regime $h\nu \gg k_BT$ where are probed independently and quantitatively the emission and absorption noise of the resonator at equilibrium and the excess noise of the Josephson junction at the resonance frequencies. At the frequencies probed in the experiment and low temperature the resonator does not emit noise, whereas it shows absorption noise related to its zero point fluctuations. This technique also allows a direct extraction of the excess emission noise power of quasiparticles tunneling through the Josephson junction at 28.4 and 80.2 GHz, the resonance frequencies of the resonator.

Chapter 6 uses the same detection scheme presented in chapter 5. We measure for the first time the high frequency emission noise of a carbon nanotube quantum dot in the Kondo regime. We find a high frequency noise presenting a singularity at $h\nu \approx eV$, which is associated with the Kondo resonance, for frequency ν of the order of $k_B T_K/h$, and a strong reduction of this singularity in the noise for $h\nu \approx 3k_B T_K$.

Chapter 3

Noise in the Quantum Regime

In this introduction, we address the physics of noise in mesoscopic devices. After a short review of low frequency noise (section 3.1), we emphasize differences with the high frequency noise, the primary interest of this thesis (section 3.2). To do so a quantum treatment of electronic circuits is needed (section 3.2.1). In particular, we will present a quantum treatment of electronic circuits where the charge and the phase degree of freedom are quantum conjugate quantities. Within this formalism, we introduce the fluctuation dissipation theorem which relates the equilibrium noise properties of a system to the dissipative part of its impedance at the frequency of interest. A scattering approach of the noise is presented to take into account the out-of-equilibrium quantum noise properties of a coherent device characterized by an energy dependent scattering matrix. The particular case of the energy independent scattering matrix is discussed and an intuitive approach of finite frequency noise is given.

Contents

3.1 Classical description of noise

Let us consider a conducting system through which a current flows (see Fig.3.1). The measured current $I(t)$ fluctuates around its mean value $\langle I(t)\rangle$ and one can express the current as:

$$I(t) = \langle I(t) \rangle + \delta I(t). \tag{3.1}$$

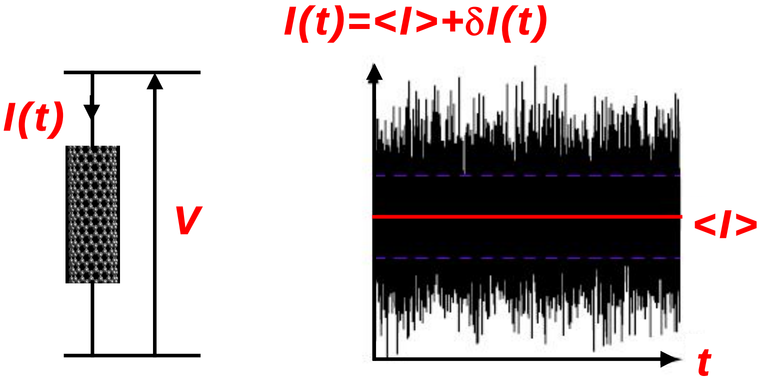

Figure 3.1: A voltage biased conductor exhibits a fluctuating current around its mean value $< I(t) >$. The value of the noise carry informations about correlations in the conductor.

It is always interesting to characterize those fluctuations. This is usually done by using the symmetrized version of the time dependent current-current correlator

$$C(\tau) = \rangle \delta I(t+\tau)\delta I(t) \rangle + \langle \delta I(t-\tau)\delta I(t) \rangle \tag{3.2}$$

where $<>$ designs an ensemble average. Assuming the ergodicity of the random process[1], one can identify this ensemble average to a time average over the realization of the quantity under concern. As a result, one has:

$$\begin{aligned} \langle I \rangle \quad &= lim_{T\to\infty} \tfrac{1}{2T} \textstyle\int_{-T}^{+T} I(t)dt; && (3.3) \\ \langle \delta I(t+\tau)\delta I(t) \rangle \quad &= lim_{T\to\infty} \tfrac{1}{2T} \textstyle\int_{-T}^{+T} \delta I(t+\tau)\delta I(t)dt && (3.4) \end{aligned}$$

The sign and magnitude of the function 3.2 tells us whether fluctuations of the current at time t and time $t+\tau$ are correlated, anticorrelated or statistically independent. Let us notice here that we assume that the noise process is stationary so that the statistical properties of the fluctuations δI are time translation invariant and thus only depend on τ. In practice it is convenient to work with the Fourier transform of this correlator

$$S_I(\nu) = \frac{1}{2\pi} \int_{-\infty}^{+\infty} d\tau e^{i2\pi\nu\tau} C(\tau), \tag{3.5}$$

---

[1] In mathematics, the term ergodic is used to describe a dynamical system which, broadly speaking, has the same behavior averaged over time as averaged over space. Here space would correspond to a large assembly of equivalent samples, where the uncorrelated current I would be measured at the same time t.

which defines the noise spectral density.

Most of the time, one wants to eliminate noise since it partly comes from parasitic effects in the electronic setup used to measure the sample of interest.

However quantum fluctuations due to electronic correlations in the system are unavoidable and leads to a finite amount of noise. For example, the $1/f$ noise or flicker noise may reveal the slow dynamics of impurities in mesoscopic systems [76–78]. For a system at equilibrium the thermal fluctuations leads to Johnson-Nyquist noise. Out of equilibrium, the discrete nature of the charge carriers leads to shot noise.

3.1.1 Johnson-Nyquist noise

The low frequency equilibrium current noise of an ergodic conducting system at temperature T is the Johnson-Nyquist noise [79,80]:

$$S_I(\nu = 0) = 4k_BTG, \tag{3.6}$$

with G the conductance of the system. Measuring the low frequency thermal shot noise does not bring more information than a conductance measurement.

3.1.2 Shot noise

When driven out-of-equilibrium, a conducting[2] system exhibits an excess amount of noise associated to the charge granularity: the shot noise. Its associated spectral density (Schottky formula) at zero frequency is, for uncorrelated events:

$$S_I(\nu = 0) = 2qI, \tag{3.7}$$

with q the charge carriers associated to the transport process and I the current flowing through the system. This prediction was verified in vacuum tube in 1925 [82] and allowed to experimentally highlight the fractional charge of Laughlin quasiparticles in the fractional quantum Hall regime [83,84] and the Cooper pairs charge [85,86].

For a mesoscopic system it can be shown that a conductor may be described by an assembly of N independent channels. An electron incident in channel i has a transmission probability T_i to be transmitted and $(1 - T_i)$ to be reflected [87] (see later in this chapter). This probabilistic process is responsible for the out-of equilibrium noise of the mesoscopic system. To each channel is associated a certain amount of noise leading to the zero frequency shot noise formula:

$$S_I(\nu = 0) = \sum_i 2qI(1 - T_i). \tag{3.8}$$

Finally, the Fano factor quantifies deviations from the poissonian value and is defined as:

---

[2] If the conducting system is a mesoscopic conductor, it has to be short enough to preserve its coherence [81].

$$F = \frac{S_I(\nu = 0)}{2qI} = \frac{\sum_n T_n(1 - T_n)}{\sum_n T_n} \tag{3.9}$$

3.2 Noise in the quantum regime

In this part, we study noise in the quantum regime where the energy associated to the frequency of interest is much higher than the thermal energy ($h\nu >> k_BT$). In those circumstances, the current must be considered as an operator and we need to ask ourself which current-current correlator should be used and is the symmetrized correlator still meaningful? Indeed, the symmetrized version of the correlator was introduced because the product $< \hat{I}(t + \tau)\hat{I}(t) >$ is generally not real, because the operators $\hat{I}(t + \tau)$ and $\hat{I}(t)$ do not commute, whereas the symmetrized version is. The use of the symmetrized correlator has been chosen in many books or publications but is not *a priori* justified [88, 89].

In the following, we will thus consider the non-symmetrized correlator and a quantum treatment of electronic circuits. It allows to introduce the fluctuation dissipation theorem (FDT) which identifies the equilibrium noise properties of a device of interest. We intuitively interpret noise in terms of emitted or absorbed photons during inelastic processes.

3.2.1 Quantum treatment of electronic circuits

In this part we present a quantum mechanical description of electrical circuits [10] in which the charge q (associated to the current) and the phase φ (associated to the voltage) are quantum conjugate variables $[\varphi, q] = ie$ as will be seen in the following. The phase-phase correlation function is introduced to extract the quantum fluctuation-dissipation theorem.

Generalities

In order to write the Hamiltonian of an electrical circuit, it is convenient to introduce two quantities related to the time dependent current $i(t)$ and voltage $v(t)$ associated to a conductor d. These are the charge $q(t)$ and the flux $\Phi(t)$ defined as:

$$\begin{cases} q(t) = \displaystyle\int_{-\infty}^{t} i(t')dt' \\ \varphi(t) = \dfrac{e}{\hbar} \displaystyle\int_{-\infty}^{t} v(t')dt' \end{cases} \tag{3.10}$$

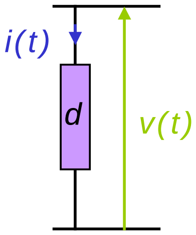

Within this formalism, the phase-phase time correlator reads:

$$\langle \varphi(t + \tau)\varphi(t) \rangle = \frac{e^2}{\hbar^2} \int_{-\infty}^{t+\tau} dt' \int_{-\infty}^{t} dt'' \, \langle v(t')v(t'') \rangle \tag{3.11}$$

We will see later how this correlator can be related to the noise spectral density of the element d under investigation. We will first consider a simple model circuit: the quantum harmonic oscillator.

Hamiltonian description of a quantum LC circuit

We consider a circuit constituted by an inductance L in parallel with a capacitance C. The energy of the quantum LC circuit is related to an electric term associated with the charge q^C accumulated accross the capacitor C: $H_Q = \frac{(q^C)^2}{2C}$ and a magnetic term related to the flux ϕ^L through the inductance L: $H_L = \frac{(\phi^L)^2}{2L}$. The hamiltonian of the circuit is thus:

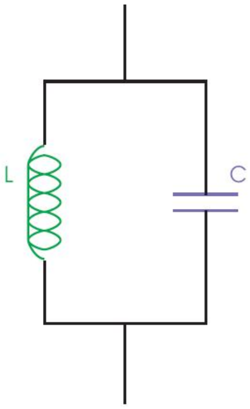

$$H_{LC} = H_Q + H_L = \frac{(q^C)^2}{2C} + \frac{(\phi^L)^2}{2L}.$$

This hamiltonian can be recast by introducing creation and annihilation operators a^+ and a:

$$H_{LC} = h\nu_0(a^+a + \frac{1}{2}) \text{ with } \begin{cases} a = \dfrac{\phi_0}{2\hbar Z_0}\left(\varphi^L + i\dfrac{Z_0}{\phi_0^2}q^C\right) \\ a^+ = \dfrac{\phi_0}{2\hbar Z_0}\left(\varphi^L - i\dfrac{Z_0}{\phi_0^2}q^C\right) \end{cases}$$

where $\nu_0 = 1/2\pi\sqrt{LC}$ and $Z_0 = \sqrt{L/C}$. One can conversely express the charge q^C and phase φ^L as a function of these operators:

$$\begin{cases} q^C = \dfrac{1}{i}\sqrt{\dfrac{\hbar}{2Z_0}}\left(a - a^+\right) \\ \varphi^L = \dfrac{1}{\phi_0}\sqrt{\dfrac{\hbar Z_0}{2}}\left(a + a^+\right) \end{cases}$$

By now applying formula 3.11, one obtains the phase-phase time correlator of the quantum LC circuit:

$$\langle\varphi(t+\tau)\varphi(t)\rangle = \frac{\hbar Z_0}{2\phi_0^2}\left\{\left\langle a^+a\right\rangle e^{i2\pi\nu_0\tau} + \left\langle aa^+\right\rangle e^{-i2\pi\nu_0\tau}\right\}. \tag{3.12}$$

The time average $< a^+a >$ corresponds to the mean number of occupied states of energy $h\nu_0$ at temperature T given by the Bose-Einstein occupation number $< n >$. It follows $\langle a^+a\rangle = \langle n\rangle = \frac{1}{e^{\beta h\nu_0}-1}$. The commutation relation between the creation and annihilation operators $[a, a^+] = 1$ allows to write $\langle aa^+\rangle = 1 + \langle a^+a\rangle = 1 + \langle n\rangle$. This relation can be injected in the phase-phase time correlator formula, which after performing a Fourier transform, becomes the Emission/Absorption spectrum of the quantum harmonic oscillator:

$$\boxed{S_\varphi(\nu) = \int_{-\infty}^{+\infty} d\tau \, \langle\varphi(t+\tau)\varphi(t)\rangle \, e^{i2\pi\nu\tau} = \frac{\hbar Z_0}{2\phi_0^2}\left\{\underbrace{\delta(\nu+\nu_0)\,\langle n\rangle}_{Emission} + \underbrace{\delta(\nu-\nu_0)(1+\langle n\rangle)}_{Absorption}\right\}.} \tag{3.13}$$

The noise spectrum of the quantum harmonic oscillator is not symmetric with respect to positive and negative frequencies. This point is related to the fact that the creation and annihilation operators do not commute according to the Heisenberg uncertainty principle. Especially, at $T = 0$ (fundamental state) one has $< n >= 0$. The system cannot emit photons (negative frequencies) in the environment while it can still absorb (positive frequencies) them, leading to absorption noise. These non zero fluctuations (in the ground state) of the considered system are called *Zero Point Fluctuations*. We will see later in this thesis how we have been able to measure them. At finite temperature ($T \neq 0$), higher energy states are thermally populated and emission becomes possible up to energies $\approx k_BT$. When the temperature is high ($k_BT >> h\nu$), one recovers the thermal limit ($< n > +1 \approx < n >$). The circuit emits as much as it absorbs and the fluctuations are dominated by thermal fluctuations.

The quantum fluctuation-dissipation theorem One can simply relate the spectrum of the quantum harmonic oscillator to its dissipative part of the impedance. To do so we write the impedance of the LC system:

$$Z_{LC}(\nu) = lim_{\eta\to 0} Z_{LC}(\nu + i\eta) = \frac{i}{2\pi C}\frac{\nu + i\eta}{(\nu_0)^2 - (\nu + i\eta)^2}. \tag{3.14}$$

The real (dissipative) part of this expression is

$$Re\left[Z_{LC}(\nu)\right] = \pi^2 Z_0 \nu_0 \left\{\delta(\nu+\nu_0) + \delta(\nu-\nu_0)\right\}. \tag{3.15}$$

Finally, we implement this dissipative component into the Emission/Absorption spectrum of the quantum harmonic oscillator (formula 3.13) and obtain the Quantum Fluctuation-Dissipation Theorem [7]:

$$\boxed{S_\varphi(\nu) = \frac{Re\left[Z_{LC}(\nu)\right]}{2\pi^2 R_Q}\frac{1}{\nu\left[1 - e^{-\beta h\nu}\right]}} \tag{3.16}$$

with $R_Q = h/e^2$ the quantum of resistance.

Caldeira-Leggett transformation - From non dissipatice LC circuit to resistor description

Following the Caldeira-Leggett approach [90], a dissipative element can be modeled as an infinite assembly of harmonic oscillators. The Hamiltonian $H_{Z(\nu)}$ of an assembly of N

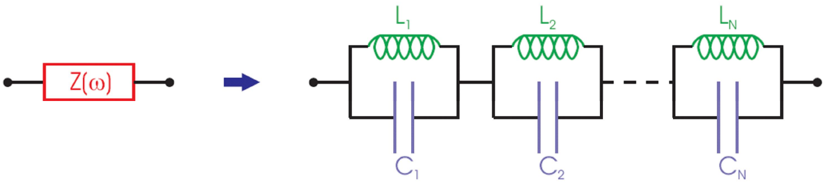

Figure 3.2: Schematic representation of the Caldeira-Leggett model: a linear dissipative element $Z(\nu)$ can be modeled as a set of quantum harmonic oscillators $\{L_K, C_K\}_{k=[1:N]}$.

harmonic oscillators $\{L_K, C_K\}_{k=[1:N]}$ as shown in Fig.3.2 is then:

$$H_{Z(\nu)} = \sum_{k=1}^{N} \{H_Q^k + H_L^k\} = \sum_{k=1}^{N} \left\{ \frac{(q^{C,k})^2}{2C_k} + \frac{(\phi^{L,k})^2}{2L_k} \right\} = \sum_{k=1}^{N} \left\{ h\nu_k \left(a_k^+ a_k + \frac{1}{2} \right) \right\}. \quad (3.17)$$

This hamiltonian can, exactly as in the previous part, be recast in terms of creation and annihilation operators a_k^+ and a_k associated to each element k. With those notations, the phase-phase correlation function becomes:

$$S_\varphi(\nu) = \sum_{k=1}^{N} \left\{ \frac{Re\left[Z_k(\nu)\right]}{2\pi^2 R_Q} \frac{1}{\nu\left[1 - e^{-\beta h\nu}\right]} \right\}, \quad (3.18)$$

and can be simplified, at the thermodynamic limit $N \to \infty$ into

$$S_\varphi(\nu) = \frac{Re\left[Z(\nu)\right]}{2\pi^2 R_Q} \frac{1}{\nu\left[1 - e^{-\beta h\nu}\right]}. \quad (3.19)$$

Finally, according to Eq.3.11 one has $S_V = \hbar^2\nu^2/e^2.S_\varphi$ and the equilibrium voltage noise spectrum of a linear dissipative element $Re[Z(\nu)]$ is:

$$\boxed{S_V(\nu) = \frac{2Re\left[Z(\nu)\right] h\nu}{\left[1 - e^{-\beta h\nu}\right]}.} \quad (3.20)$$

This formula describes the crossover between thermal noise at low frequency and quantum noise related to the zero point fluctuations of the electromagnetic field at finite frequency. We have represented in figure 3.3 the calculated frequency dependence of the voltage noise for a resistor R at three temperatures. These curves highlight the strong asymmetry between emission and absorption noise. Especially, at low temperature, no emission noise (negative frequencies) is observed while the absorption noise (positive frequencies) scales linearly with the frequency. At higher temperatures, emission noise appears and absorption noise increases.

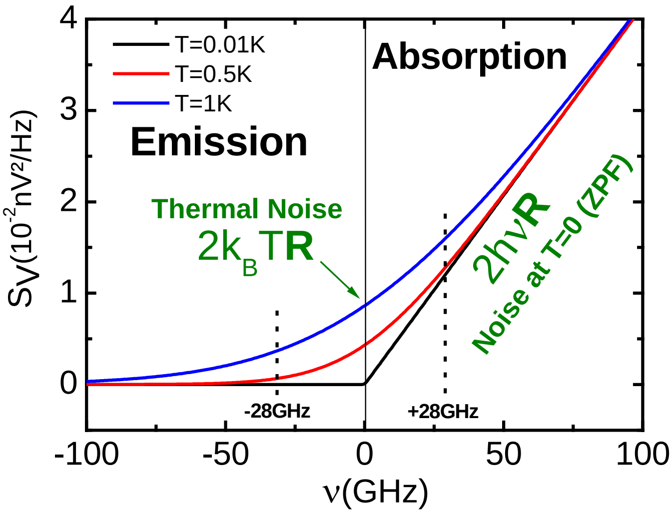

Figure 3.3: Expected frequency dependence of the equilibrium voltage noise of a resistor $R = 300\Omega$ at three different temperatures (formula 3.44) . At $\nu = 0$, the prediction follows the Johnson-Nyquist formula for a non symmetrized thermal noise. At $T = 0$, there is no emission noise whereas the absorption noise increases linearly with frequency. This noise at $T = 0$ is related to the zero point fluctuations of the electromagnetic field accross the resistor at equilibrium

3.2.2 Shot noise in the quantum regime - A scattering approach

The finite frequency limit corresponds to a regime where frequencies are much higher than the temperature i.e. $h\nu >> k_B T$. In this limit the noise acquires a frequency dependence with signatures of the relevant energy scales $k_B T$ and eV (with T the temperature and V the bias voltage on the device) and has been found to increase linearly with frequency above $k_B T/h$ [70, 71]. Similarly the excess noise, *i.e.* the difference between the noise at a given bias and the noise at equilibrium, measured in the limit $eV \gg k_B T$ has been found to decrease linearly with frequency and go to zero at frequency eV/h both in diffusive wires [72] and GaAs ballistic quantum point contacts [73].

We now address the out-of-equilibrium finite frequency noise properties of mesoscopic devices using a Landauer-Büttiker formalism (scattering approach) [6]. General expressions of conductance and noise for a non interacting mesoscopic system with an energy dependent scattering matrix are derived. The energy independent case is developped yielding an intuitive interpretation of the noise in terms of emitted or absorped photons during inelastic processes.

Scattering approach

The scattering approach is a very powerful tool to address the transport properties of a quantum system knowing its scattering properties. The system can be either at equilibrium or out-of-equilibrium and we consider the case of a two terminal scattering problem with one transverse channel [91]. The chemical potential of the reservoirs are characterized by distribution functions $f_\alpha(E)$, with $\alpha = L, R$ designing the left and right contacts in a two terminal experiment, whose chemical potentials are shifted by the voltage bias energy eV. The reservoirs are at temperatures T_α and chemical potentials μ_α. Taking fermionic contacts, the distribution functions of the reservoirs are:

$$f_\alpha(E) = \frac{1}{1 + exp[(E - \mu_\alpha)/k_B T_\alpha]}, \alpha = L, R. \tag{3.21}$$

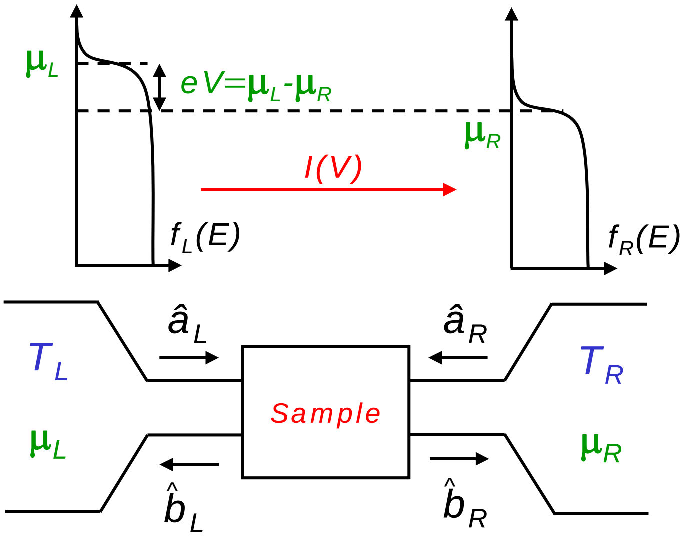

Figure 3.4: Two terminals, one transverse channel, scattering problem

The physics of the system is contained into the scattering matrix s. The scattering matrix relates the incident waves to the scatterer to reflected and transmitted waves. By considering a system with N transverse channels ($N_L = N_R = N$), the creation (annihilation) operator of an electron with total energy E in the transverse mode n in the left lead, incident to the sample is $\hat{a}^{+}_{L,n}(E)$ ($\hat{a}_{R,n}(E)$). The creation (annihilation) operator of an electron with total energy E in the transverse mode n in the left lead, going out the sample is $\hat{b}^{+}_{L,n}(E)$ ($\hat{b}_{R,n}(E)$). Those operators are related by the scattering matrix s according to:

$$\begin{pmatrix} \hat{b}_{L,1} \\ \dots \\ \hat{b}_{L,N} \\ \hat{b}_{R,1} \\ \dots \\ \hat{b}_{R,N} \end{pmatrix} = s \begin{pmatrix} \hat{a}_{L,1} \\ \dots \\ \hat{a}_{L,N} \\ \hat{a}_{R,1} \\ \dots \\ \hat{a}_{R,N} \end{pmatrix}. \tag{3.22}$$

The matrix s has dimensions $(2N)^2$ with a block structure:

$$s = \begin{pmatrix} s_{LL,11} & \cdot & \cdot & \cdot & s_{LL,1N} & s_{RL,11} & \cdot & \cdot & \cdot & s_{RL,1N} \\ \cdot & \cdot & \cdot & \cdot & \cdot & \cdot & \cdot & \cdot & \cdot & \cdot \\ \cdot & \cdot & \cdot & \cdot & \cdot & \cdot & \cdot & \cdot & \cdot & \cdot \\ \cdot & \cdot & \cdot & \cdot & \cdot & \cdot & \cdot & \cdot & \cdot & \cdot \\ s_{LL,N1} & \cdot & \cdot & \cdot & s_{LL,NN} & s_{RL,N1} & \cdot & \cdot & \cdot & s_{RL,NN} \\ s_{LR,11} & \cdot & \cdot & \cdot & s_{LR,1N} & s_{RR,11} & \cdot & \cdot & \cdot & s_{RR,1N} \\ \cdot & \cdot & \cdot & \cdot & \cdot & \cdot & \cdot & \cdot & \cdot & \cdot \\ \cdot & \cdot & \cdot & \cdot & \cdot & \cdot & \cdot & \cdot & \cdot & \cdot \\ \cdot & \cdot & \cdot & \cdot & \cdot & \cdot & \cdot & \cdot & \cdot & \cdot \\ s_{LR,N1} & \cdot & \cdot & \cdot & s_{LR,NN} & s_{RR,N1} & \cdot & \cdot & \cdot & s_{RR,NN} \end{pmatrix} = \begin{pmatrix} s_{LL} & s_{RL} \\ s_{LR} & s_{RR} \end{pmatrix} = \begin{pmatrix} r & t' \\ t & r' \end{pmatrix}. \tag{3.23}$$

The diagonal blocks r and r' ($N \times N$) describe the electrons reflected back to the left and right reservoirs, respectively. The off-diagonal blocks t and t' instead, relates the electron transmission accross the system. To conserve the current, the matrix s is unitary ($ss^+ = 1$).

Conductance

Using this formalism, one writes the time dependent current operator in the left electrode:

$$\hat{I}_L(t) = \frac{e}{h} \sum_n \int dE dE' e^{i(E-E')t/\hbar} \left[\hat{a}^+_{L,n}(E) \hat{a}_{L,n}(E') - \hat{b}^+_{L,n}(E) \hat{b}_{L,n}(E') \right]. \tag{3.24}$$

The time averaged current is:

$$\langle I_L \rangle = \frac{e}{h} \int dE Tr[t^+(E) t(E)][f_L(E) - f_R(E)] \tag{3.25}$$

$$= \frac{e}{h} \int dE Tr[s^+_{LR}(E) s_{LR}(E)][f_L(E) - f_R(E)]. \tag{3.26}$$

In this expression, the matrix t^+t can be diagonalized in the basis of the eigen channels n. It has real eigenvalues that are the transmission probabilities $T_n(E)$ of an electron in channel n to be transmitted through the scatterer. Finally the mean current simplifies:

$$\langle I_L \rangle = \frac{e}{h} \sum_n \int dE T_n(E)[f_L(E) - f_R(E)], \tag{3.27}$$

and the conductance reads:

$$G = \frac{e^2}{h} \sum_n T_n(E). \tag{3.28}$$

When one bias the sample with a voltage $V = V_L - V_R = (\mu_L - \mu_R)/e$, each perfectly transmitted channel induces an electrical current $I = e^2/h.V = G_0.V$. The conductance $G = I/V = G_0$ of a single ballistic channel device is then a constant: the quantum of conductance $G_0 = e^2/h \approx 38.74 \mu S \approx 1/(25.8 k\Omega)$. If transmission is lowered, conductance is also lowered proportionally to the channel transmission.

Noise

In the following, we introduce the general expressions for the current noise of a noninteracting conducting system in a Landauer/Buttiker formalism as done in ref [6,92]. To do so, we introduce the operator $\delta\hat{I}_\alpha(t) = \hat{I}_\alpha(t) - \left\langle \hat{I}_\alpha \right\rangle$. With this operator the non symmetrized noise spectrum is expressed as:

$$\boxed{C_{\alpha,\beta}(\nu) = \frac{1}{2\pi}\int_{-\infty}^{+\infty} d\tau e^{i2\pi\nu\tau}\left\langle \delta\hat{I}_\alpha(t+\tau)\delta\hat{I}_\beta(t)\right\rangle,} \tag{3.29}$$

with α, β representing the two metallic leads L, R. One defines two auto-correlation functions when $\alpha = \beta$: $C_{LL}(\nu)$ and $C_{RR}(\nu)$ and two cross-correlation functions when $\alpha \neq \beta$: $C_{LR}(\nu)$ and $C_{RL}(\nu)$. By taking the net current going through the sample $\hat{I} = (\hat{I}_L - \hat{I}_R)$, one can write the current noise spectral density:

$$S_I(\nu) = \frac{1}{4}\left[C_{LL}(\nu) + C_{RR}(\nu) - C_{LR}(\nu) - C_{RL}(\nu)\right]. \tag{3.30}$$

Hereafter we consider the general expression for the time dependent current operator in lead α:

$$\hat{I}_\alpha(t) = \frac{e}{h}\sum_{\gamma,\gamma'}\int dEdE' e^{i(E-E')t/\hbar} A_{\gamma,\gamma'}(\alpha,E,E')\hat{a}^+_\gamma(E)\hat{a}_{\gamma'}(E'), \tag{3.31}$$

with $\hat{a}^+_\gamma(E)$ ($\hat{a}_\gamma(E)$ respectively), the creation (respectively annihilation) operator of an electron in lead γ at energy E and

$$A_{\gamma,\gamma'}(\alpha,E,E') = \delta_{\gamma,\gamma'}\delta_{\alpha,\gamma} - s^*_{\alpha,\gamma}(E)s_{\alpha,\gamma'}(E'). \tag{3.32}$$

Greek letters denote the leads and $s_{\alpha,\gamma}$ the elements of the scattering matrix characterizing the sample.

With those notations, the noise spectrum reads:

$$C_{\alpha,\beta}(\nu) = \frac{e^2}{h}\int_{-\infty}^{+\infty} dE \sum_{\gamma,\gamma'} F^{\alpha,\beta}_{\gamma,\gamma'}(E,\nu) f_\gamma(E-h\nu)\left[1 - f_{\gamma'}(E)\right], \tag{3.33}$$

where $f_\gamma(E) = 1/(1 + e^{(E-\mu_\gamma)/k_BT})$ is the Fermi distribution in reservoir γ which is held at the chemical potential μ_γ[3] and

$$F^{\alpha,\beta}_{\gamma,\gamma'}(E,\nu) \equiv A_{\gamma,\gamma'}(\alpha,E-h\nu,E)A_{\gamma,\gamma'}(\beta,E,E-h\nu). \tag{3.34}$$

One finally finds the expression for current noise:

$$\boxed{S_I(\nu) = \frac{e^2}{4h}\int_{-\infty}^{+\infty} dE \sum_{\gamma,\gamma'} F^{(-)}_{\gamma,\gamma'}(E,\nu) f_\gamma(E-h\nu)\left[1 - f_{\gamma'}(E)\right],} \tag{3.35}$$

---

[3] Note than within this formalism $V = (\mu_L - \mu_R)/e$ and $\mu_L = -\mu_R = eV/2$.

where

$$F_{LL}^{(-)}(E,\nu) = |1 - s_{LL}^*(E-h\nu)s_{LL}(E) + s_{RL}^*(E-h\nu)s_{RL}(E)|^2, \tag{3.36}$$
$$F_{LR}^{(-)}(E,\nu) = |s_{LL}^*(E-h\nu)s_{LR}(E) - s_{RL}^*(E-h\nu)s_{RR}(E)|^2. \tag{3.37}$$

The other correlation functions $F_{RR}^{(-)}(E,\nu)$, $F_{RL}^{(-)}(E,\nu)$ can be obtained by interchanging L and R in the previous expressions. This general expression of the current noise associated to a non interacting device of scattering matrix $s(E)$ can be simplified in several limits corresponding to zero temperature, zero bias, zero frequency and/or energy independent scattering matrix.

A simple case: the energy independent scattering matrix

In the simple approximation of an energy independent scattering matrix, the finite frequency current noise of a quantum conductor with N channels of transmissions T_n at temperature T (here $\beta = 1/k_B T$) becomes:

$$\begin{aligned} S_I(\nu, eV, T) &= \frac{e^2}{h}\sum_n T_n^2 \frac{2h\nu}{1-e^{-\beta h\nu}} \\ &+ \frac{e^2}{h}\sum_n T_n(1-T_n)\frac{h\nu+eV}{1-e^{-\beta(h\nu+eV)}} \\ &+ \frac{e^2}{h}\sum_n T_n(1-T_n)\frac{h\nu-eV}{1-e^{-\beta(h\nu-eV)}}. \end{aligned} \tag{3.38}$$

Zero frequency limit of noise and Fano factor Taking formula 3.38 for an unbiased system at thermal equilibrium (temperature T), one recovers the the thermal noise or Johnson-Nyquist noise expression:

$$\boxed{S_I(\nu = 0, eV = 0, T) = 2k_B T\frac{e^2}{h}\sum_n T_n = 2k_B T G(0),} \tag{3.39}$$

with G(0) the conductance of the system at zero frequency.

By now taking the system at zero temperature but out-of-equilibrium, one finds the shot noise expression:

$$S_I(\nu = 0, eV, T = 0) = \frac{e^2}{h}\sum_n T_n(1-T_n)eV = e\frac{\sum_n T_n(1-T_n)}{\sum_n T_n}I. \tag{3.40}$$

Not however than the results differ by a factor 2 from the classical expressions given in the introductive part of this chapter. This factor 2 comes from the use of the non symmetrized correlator.

The normal tunnel junction corresponds to a large number of channels with $T_n << 1$. The previous noise expression can be reduced to

$$S_{P,I}(\nu = 0, eV, T = 0) = eI \tag{3.41}$$

which is the expression for the non-symmetrized shot noise. The tunnel junction is commonly used as a reference for noise measurement. It allows to define the Fano factor F as the ratio of the current noise emitted by the system under investigation and the poissonnian limit:

$$F = \frac{S_I(\nu = 0, eV, T = 0)}{S_{P,I}(\nu = 0, eV, T = 0)} = \frac{\sum_n T_n(1 - T_n)}{\sum_n T_n}. \tag{3.42}$$

One can then rewrite the general expression for the shot noise at zero frequency:

$$\boxed{S_I(\nu = 0, eV, T = 0) = eFI.} \tag{3.43}$$

A Fano factor higher than one ($F > 1$) means the system is superpoissonian (exhibits more noise than a poissonian element when the same current flows into it) while a Fano factor smaller than one ($F < 1$) means subpoissonian (exhibits less noise).

Finite frequency equilibrium Noise The finite frequency equilibrium noise ($eV = 0$) of a conductor with energy independent conductance $G = e^2/h \sum_n T_n$ can be deduced from formula 3.38. It leads to the already mentioned expression of the fluctuation dissipation theorem:

$$\boxed{S_I(\nu, eV = 0, T) = \frac{e^2}{h} \sum_n T_n \frac{2h\nu}{1 - e^{-\beta h\nu}} = \frac{2Gh\nu}{1 - e^{-\beta h\nu}}.} \tag{3.44}$$

Finite frequency shot noise The finite frequency shot noise of a system described by a scattering matrix $s(E)$ obeys the general formula 3.35. It simplifies in the case of an energy independent scattering matrix to Eq. 3.38. As an example, we can write this relation for the tunnel case (normal or superconducting tunnel junctions). With $I_{QP}(V)$ the $I(V)$ characteristic of the junction, the noise spectrum is[4] [9, 93] :

$$S_{I_{QP}}(\nu, V_S) = e \left[\frac{I_{QP}(h\nu/e + V_S)}{1 - e^{-\beta(h\nu + eV_S)}} + \frac{I_{QP}(h\nu/e - V_S)}{1 - e^{-\beta(h\nu - eV_S)}} \right] \tag{3.45}$$

We have represented in figure 3.5 the zero temperature noise spectrum of a normal tunnel junction for different bias voltages. One clearly sees the strong assymmetry between emission and absorption. In particular, the absorption spectrum is finite at any frequencies while the emission noise is zero for $h\nu > eV$.

---

[4] This expression is valid even if the I(V) characteristic of the system is non linear. The perfect example is the Superconducting/Insulator/Superconducting junction which has a non linear I(V) due to the superconducting gap in the density of states but a scattering matrix which is energy independent.

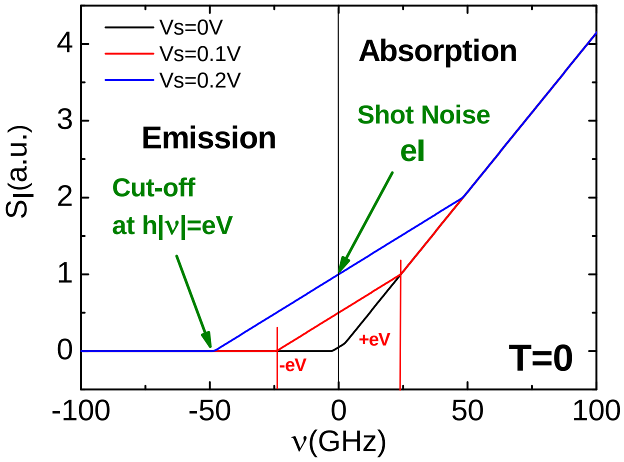

Figure 3.5: Expected frequency dependence of the out-of-equilibrium current noise of a normal tunnel junction at three different bias voltages (formula 3.45) and zero temperature. At $\nu = 0$, the prediction follows the shot noise formula. When $eV = 0$, there is no emission noise whereas the absorption noise increases linearly with the frequency. At $eV \neq 0$, two singularities appears at $\nu = \pm eV/h$ and the emission noise is zero for $h\nu > eV$.

A comment on excess noise measurement - Symmetrized *vs* non-symmetrized In practice, most experiments measure excess noise which is the difference between the noise at bias V and noise at equilibrium $V = 0$. We have represented in Fig.3.6a,b and c the expected result of such excess noise measurement applied to a linear system (the normal tunnel junction) for both conventions of the measured noise: Symmetrized and non-symmetrized. It is interesting to note than the excess noise expectations only differ by a factor 2. Calibration procedure is thus of primary importance to understand which quantity is effectively measured in a excess noise measurement applied to a linear system. It has been shown however, than the use of a non linear system (superconducting tunnel junction for instance) as a noise source allows to determine whether or not the non-symmetrized noise correlator is measured [9, 94].

3.2.3 Finite frequency noise in terms of photon emission and absorption

Hereafter, we intuitively interprete the meaning of the autocorrelation function $S_I(\nu)$, namely the non-symmetrized quantum noise in terms of inelastic tunneling processes. To do so, it is convenient to rewrite the expression 3.35 in the form [88, 95]

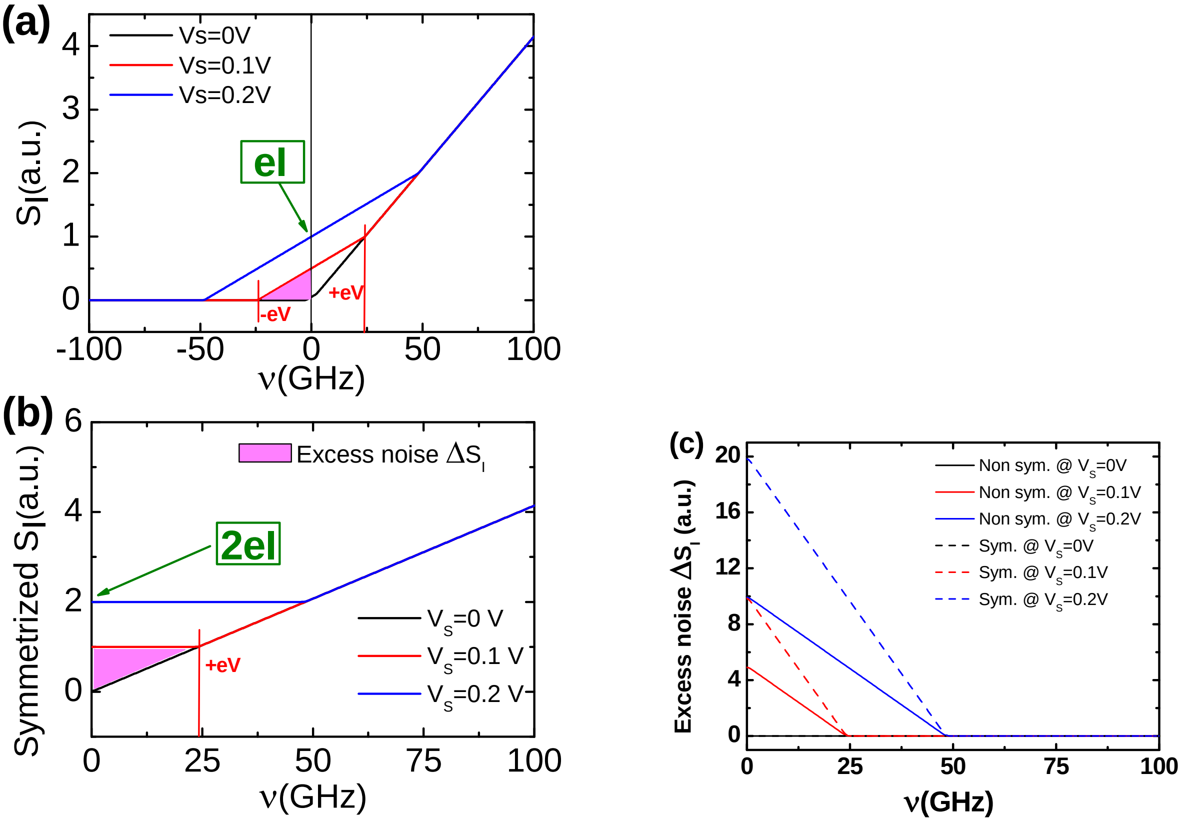

Figure 3.6: Expected frequency dependence of the (a) non-symmetrized and (b) symmetrized out-of-equilibrium current noise of a normal tunnel junction at three different bias voltages (formula 3.45) and zero temperature. At $\nu = 0$, the symmetrized value is twice the non-symmetrized one. (c) Expected excess noise using both conventions. Once again, a factor 2 is present. Calibration is thus of primary importance to understand which quantity is effectively measured in a excess noise measurement applied to a linear system.

$$\begin{aligned} S_I(\nu) &= \int d\tau e^{i2\pi\nu\tau} \left\langle \delta\hat{I}(t+\tau)\delta\hat{I}(t) \right\rangle & (3.46) \\ &= \sum_i P_i \int d\tau e^{i2\pi\nu\tau} \left\langle i|\delta\hat{I}(t+\tau)\delta\hat{I}(t)|i \right\rangle, & (3.47) \end{aligned}$$

where P_i is the probability to be in the state $|i>$. Then, by inserting the identity operator $\sum_f |f><f|$ (closure relation), we obtain relation

$$S_I(\nu) = \sum_i P_i \int d\tau e^{i2\pi\nu\tau} \sum_f \left\langle i|\delta\hat{I}(t+\tau)|f \right\rangle \left\langle f|\delta\hat{I}(t)|i \right\rangle. \tag{3.48}$$

It can be further developped using equality

$$\left\langle f|\delta\hat{I}(t+\tau)|i \right\rangle = \left\langle f|e^{iH\tau/h}\delta\hat{I}(t)e^{-iH\tau/h}|i \right\rangle = e^{i\frac{(E_f-E_i)\tau}{h}} \left\langle f|\delta\hat{I}(t)|i \right\rangle. \tag{3.49}$$

By doing so, we get

$$S_I(\nu) = h\sum_{i,f} P_i| \left\langle i|\delta\hat{I}(t+\tau)|f \right\rangle \left\langle f|\delta\hat{I}(t)|i \right\rangle \int d\tau e^{-i\frac{(E_f-E_i-h\nu)\tau}{h}}. \tag{3.50}$$

Finally, using the identity $\int dte^{i2\pi\nu t} = \delta(\nu)$ one gets a very convenient form for the current noise expression [88, 96]:

$$\boxed{S_I(\nu) = h\sum_{i,f} P_i| \left\langle f|\delta\hat{I}|i \right\rangle |^2\delta(E_i - E_f + h\nu).} \tag{3.51}$$

$|i>$ and $|j>$ stands for the initial and final states of the all system respectively at energies E_i and E_f. With this expression, it is straightforward to see that the autocorrelation function is the rate by which the system absorbs ($\nu > 0$) or emit($\nu < 0$) photons at energy $|h\nu| = |E_f - E_i|$. The noise at negative frequencies is refered as the emission noise while the noise at positive frequencies is the absorption noise. Those two quantities are inequivalent and need to be detected independently. To illustrate this idea, we consider a simple case, the normal tunnel junction as shown in the next two paragraphs.

Inelastic tunneling processes at equilibrium

We have represented a semiconducting picture of a normal tunnel junction in figure 3.7. At equilibrium (zero bias voltage) and zero temperature, the system is in its ground state and thus cannot emit photons. However, it can still absorb some energy. Two sets of processes can be distinguished. The first consists in promoting one electron at the Fermi level in the left lead to an higher energy unoccupied level in the right lead. The second consists in promoting one electron from the left lead below the Fermi level to the Fermi level of the right lead. The higher the energy (frequency) $h\nu$ the higher the number of available states contributing to the inelastic processes.

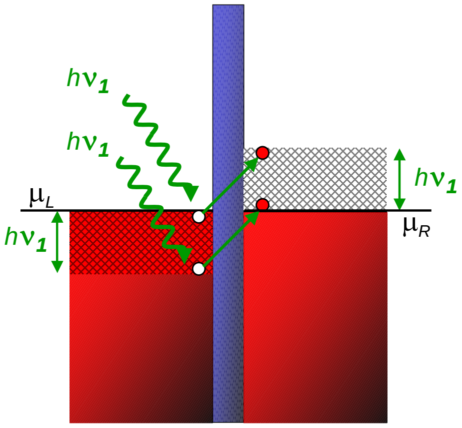

Figure 3.7: Equilibrium inelastic tunneling processes in a normal tunnel junction. At zero temperature and zero bias voltage (equilibrium), the system cannot emit energy but can still absorb some of it. The higher the energy absorbed, the higher the number of available states contributing to the inelastic processes.

Inelastic tunneling processes out-of-equilibrium

In addition to these inelastic processes due to energy quanta absorption, one also can have emission of energy when the system is driven out-of-equilibrium with a bias voltage V. The emission consists in a photon emitted during the inelastic tunneling of an electron taken in the energy interval $[E_{F,L}, E_{F,L} - eV]$ in the left lead going to the Fermi energy of the right lead (see figure 3.8). The maximum energy emitted during this process is eV responsible for the cutoff in the noise spectrum.

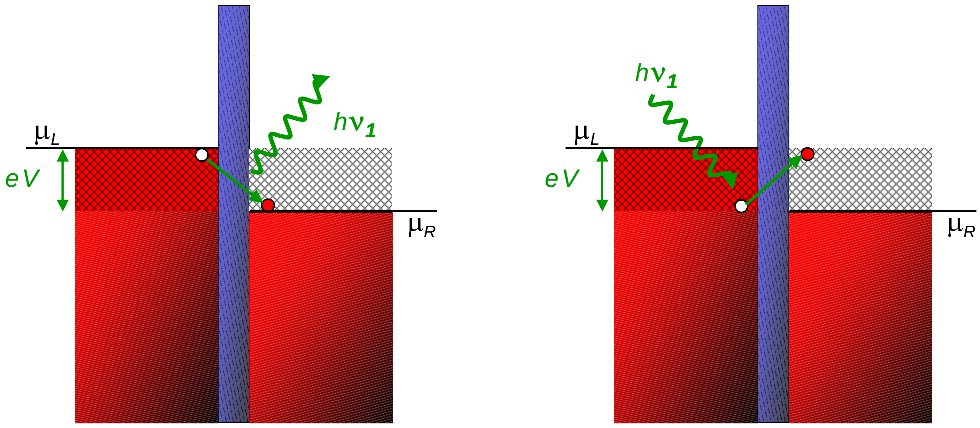

Figure 3.8: Out-of-equilibrium inelastic tunneling processes in a normal tunnel junction. When voltage biased, the tunnel junction can emit photons up to the energy $h\nu = eV$. Absorption processes are still present as mentioned in the equilibrium case.

3.3 Conclusion

In the quantum regime, noise can be interpreted in terms of photons which are either emitted or absorbed by the noise source. These processes are not equivalent and lead to a strong asymmetry in the noise spectrum. In order to measure quantum noise it is then necessary to use a quantum detector able to measure independently the emission and absorption noise.

It is important to notice that most classical amplifiers exchange energy with the system. The resulting measurement is then a combination of emission and absorption noise. In the following chapter we will motivate our choice of the superconducting tunnel junction (Superconductor/Insulator/Superconductor or SIS junction) as a quantum noise detector and introduce the formalism in which detection principle is understood.

Chapter 4

Introduction to quantum noise measurement

In order to measure noise in the quantum regime, one needs a quantum detector able to distinguish between emission and absorption processes as pointed out in chapter 3. There exists a large variety of methods to detect current noise, given the impedance of the device and the range of frequencies which has to be probed. In the following, we present few of them. The choice of the Superconducting/Insulator/Superconducting (SIS) tunnel junction is motivated and one theoretically presents the detection principle. In particular, we will see that a quantitative treatment of the detection can be derived in the framework of the $P(E)$ theory (section 4.2) where the detector together with its noisy environment must be treated on an equal footing.

Contents

4.1 Different noise detection techniques

4.1.1 Low frequency noise measurement ($h\nu << k_B T$)

There exists a broad variety of low frequency noise techniques. The principal one is presented, another is mentioned.

Cross-correlation technique With modern high speed digital sampling techniques, it is perfectly feasible to measure a random classical noise signal as a function of time and directly compute the autocorrelation function

$$C_V(\tau) = < V(t+\tau)V(t) > . \tag{4.1}$$

This is typically done using cross-correlation techniques (see Fig.4.1). The voltage fluctuations accross the source are amplified by two independent amplifiers (*i.e.* their own noise are uncorrelated). Afterwise, an analog-to-digital conversion of the noise signal is done allowing to numerically compute the autocorrelation function. Very importantly, the contribution from the amplifiers averages out after the correlation product. One finally get a much higher signal to noise ratio.

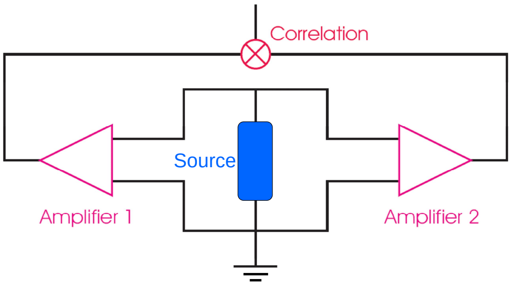

Figure 4.1: Detection scheme relying on a cross-correlation method.

Using equation

$$\mathrm{S}_V(\nu) = \int_{-\infty}^{+\infty} d\tau e^{i2\pi\nu\tau} C_V(\tau) \tag{4.2}$$

one further numerically Fourier transforms the autocorrelation function[1]. Note that practically the ensemble average is not realized. Instead, a sufficiently long time T *i.e.* much longer than the correlation time of noise, is used. This approach is most appropriate for signals at frequencies well below 1 GHz.

Other technique The tank-circuit setup has been used for example to measure the shot noise associated with fractional charge of Laughlin quasiparticles [83] or more recently to measure noise of a Kondo quantum dot [97].

---

[1] Note than the classical noise $\mathrm{S}(\nu)$ is written using small capital letter in opposition to quantum noise $S(\nu)$.

4.1.2 High frequency noise measurement ($h\nu >> k_BT$)

In principle it is possible to measure the non symmetrized noise, but for this a special detector is needed [8, 88, 98]. This *quantum spectrum analyzer* must be able to distinguish between emission and absorption processes. To measure the emission part $S(\nu < 0)$, the detector needs to be passive and return a signal only if energy is transferred from the noise source. Conversely, for the measurement of the absorption spectrum, the noise source absorb energy from an active detector (see Fig.4.2). The detector is thus de-excited and measures the $S(\nu > 0)$ side. In the following we describe two types of noise detection scheme which either relies on high frequency electronics or on-chip detectors.

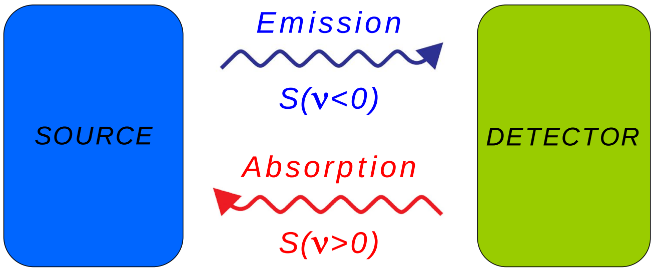

Figure 4.2: Schematic of a noise source coupled to a quantum detector. To measure the emission noise of the source, the detector must be passive. Conversely, to measure the absorption noise it must be active.

High frequency electronics

High frequency electronics has been commonly used to measure high frequency noise of diffusive wires [72], quantum point contact (QPC) [73] and normal tunnel junctions [99]. The measurements setup typically uses low temperature amplifiers followed by different sequence of filters/amplifiers and finally a quadratic detector delivering a voltage proportional to the noise power. This kind of setup typically needs the sample resistance to match the impedance of the transmission line[2] which is often $\approx 50\Omega$. The resulting measurement may be a non trivial combination of emission and absorption noise as pointed out in Ref. [8].

A resonant circuit as spectrum analyzer [8] Lesovik and Loosen have theoretically considered in 1996 the case of a resonant circuit inductively coupled to the noise source as a model for noise detection (see Fig.4.3). They modelled their detector by an LC oscillator and consider the response in the first nonvanishing order in the inductive coupling constant.

The mesoscopic conductor with a fluctuating current $I(t)$ is coupled to the LC oscillator via a mutual inductance α. One can demonstrate that the charge $x(t)$ accumulated accross

---

[2] For the QPC, which is typically a high impedance nanodevice ($R \approx h/e^2 \approx 26k\Omega$), an impedance transformer was used to match the impedance of the transmission line

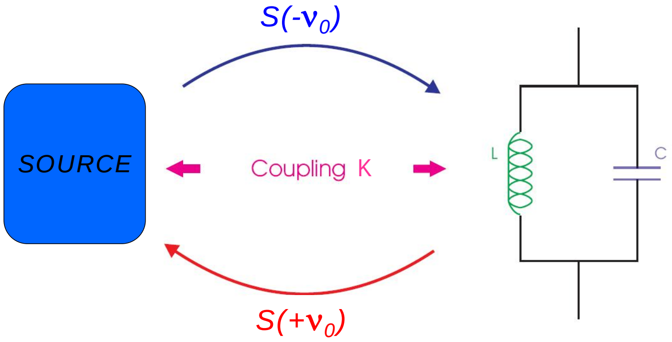

Figure 4.3: Schematic representation of the coupling between a quantum conductor (noise source), and a resonant LC circuit (detector). Parameter K characterizes the inductive coupling strength.

the capacitance of the oscillator can be expressed as:

$$L\ddot{x}(t) = -\frac{x(t)}{C} - \alpha\dot{I}(t) \tag{4.3}$$

where $\alpha\dot{I}(t)$ is the mutual coupling perturbative term. From this, one can calculate the measurable noise spectral density of the LC circuit at the resonant frequency $\nu_0 = 1/2\pi\sqrt{LC}$. They found:

$$\boxed{S_{meas} = KS(-\nu_0) + <n> [S(-\nu_0) - S(+\nu_0)]} \tag{4.4}$$

with

$$\begin{aligned} S(-\nu_0) &= \int dt < I(0)I(t) > e^{i2\pi\nu_0 t}, & (4.5)\\ S(+\nu_0) &= \int dt < I(t)I(0) > e^{i2\pi\nu_0 t}, & (4.6)\\ <n> &= \tfrac{1}{e^{h\nu_0/k_B T_{LC}-1}}, & (4.7)\\ K &= (\tfrac{\alpha}{2L})^2 \tfrac{1}{2\eta}. & (4.8) \end{aligned}$$

η is the finite width of the resonance of the LC oscillator and T_{LC} the temperature of the LC oscillator.

If the detection frequency $h\nu_0 >> k_B T_{LC}$, one has $< n >\approx 0$ and the measured spectral density is

$$S_{meas} = KS(-\nu_0), \tag{4.9}$$

the emission noise of the source. In opposition, if $h\nu_0 << k_B T_{LC}$, one has $< n >\approx k_B T_{LC}/h\nu_0$, $S(-\nu_0) - S(+\nu_0) = -2Gh\nu_0$ and thus

$$S_{meas} = K[S(-\nu_0) - 2k_B T_{LC} G]. \tag{4.10}$$

In the intermediate regime, the measured noise spectral density is a non trivial combination of emission and absorption noise. The interpretation which can be done from such kind of detection scheme is rather general. Indeed, coupling a source noise to a detector implies energy exchange between the two entities. As an example, a noisy amplifier with a noise temperature T_N sends thermal photons to the source which absorb them. As a result the ultimately measured noise is a non trivial combination of emitted and absorbed noise.

On chip detectors

Hereafter, few examples of on-chip quantum detectors are given together with their limitations. The choice of the SIS junction as a quantum noise detector is discussed.

A two level system as spectrum analyzer [98] Let us consider a quantum system (atom or electrical circuit) which has its two lowest energy levels ϵ_0 and ϵ_1 separated by energy $E_{01} = h\nu_{01}$. We suppose for simplicity that all the other levels are far away in energy and can be ignored. The states of any two-level system can be mapped onto the states of a fictitious spin-1/2 particle since such a spin also has only two states in its Hilbert space. With spin up representing the ground state ($|0>$) and spin down representing the excited state ($|1>$), the Hamiltonian is:

$$H_0 = -\frac{h\nu_{01}}{2}\sigma_z \tag{4.11}$$

with σ_z the Pauli matrix[3] in z direction.

Current fluctuations $f(t)$ through a nearby source generate a perturbative potential $V_{perturb}(t) = Af(t)\sigma_x$ at the detector stage, where A is a coupling constant. This potential may induce transitions between the two states of the two level system. Assuming that the coupling A is small enough, the noise can be treated in lowest order perturbation theory. This allows to relate the transition rates to the non-symmetrized noise of the source:

$$\Gamma_\uparrow = \tfrac{A^2}{\hbar^2} S(-\nu_{01}) \tag{4.12}$$

$$\Gamma_\downarrow = \tfrac{A^2}{\hbar^2} S(+\nu_{01}) \tag{4.13}$$

with $\Gamma_\uparrow$ the rate at which the detector is excited from ground $|0>$ to excited state $|1>$ and $\Gamma_\downarrow$ the decay rate from the excited state to the ground state (see Fig.4.4).

We now see that a two-level system (TLS) does indeed act as a quantum spectrum analyzer for the noise. One prepares the system either in its ground state or in its excited state, weakly couple it to the noise source, and after an appropriate interval of time, simply measures whether the system is in its excited state or ground state. Repeating this protocol over and over again, one can measure $\Gamma_\uparrow$ and $\Gamma_\downarrow$, and thereby the noise spectral density at positive and negative frequencies. Negative frequency noise transfers energy from the noise source to the spectrometer. That is, it represents energy emitted by the noise source.

---

[3] $\sigma_x = \begin{pmatrix} 0 & 1 \\ 1 & 0 \end{pmatrix}$, $\sigma_y = \begin{pmatrix} 0 & -i \\ i & 0 \end{pmatrix}$, $\sigma_z = \begin{pmatrix} 1 & 0 \\ 0 & -1 \end{pmatrix}$

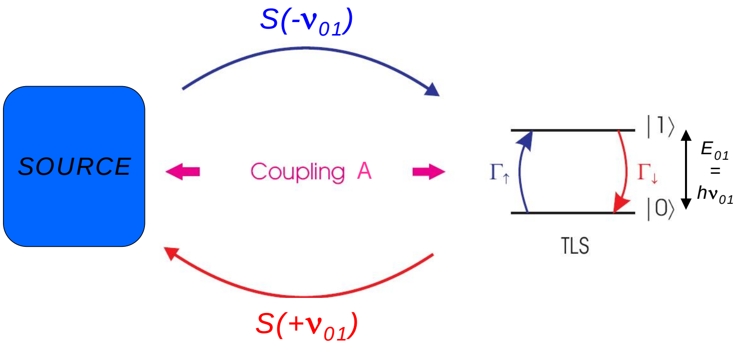

Figure 4.4: Schematic representation of the coupling between a quantum conductor (noise source), and a two level system (detector). Parameter A characterizes their coupling strength.

Positive frequency noise transfers energy from the spectrometer to the noise source. This detection scheme was implemented by Astafiev *et al.* [100], using a Cooper pair box as a TLS. However, it seems that the sensitivity of charge q-bits as spectrometers is limited by the coupling to the external environment which destroys the TLS coherence.

A double quantum dot as a spectrum analyzer [74, 101] A double quantum dot can be used as an on chip spectrum analyzer. In this case, current fluctuations generated by the capacitively coupled device modify the I-V characteristics of the detector. Actually, the source noise induces fluctuations in the energy difference δE between the levels of the two quantum dots as shown in Fig.4.5. This leads to inelastic tunneling events, in which electrons exchange energy with the environment (either absorb or emit).

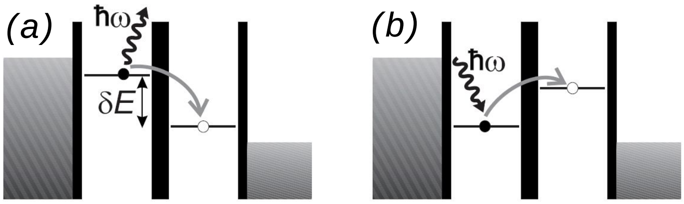

Figure 4.5: Taken from [102]. Schematic representation of a double dot system acting as a spectrum analyzer. At bias V_{bias}, the double dot levels can be tuned such that the inelastic tunneling current carries information over (a) the absorption noise or (b) the emission noise of the environment where is embedded the test sample.

If the central barrier (between the dots) is high, transport is dominated by inter-dot tunneling events and the inelastic current contains information about the noise power spectrum. Interestingly, the double dot can be tuned such that it is either sensitive to the absorption $S_I(\nu)$ or the emission noise $S_I(-\nu)$ of the source. The detection frequency ν is set by the energy difference $\delta E/h$. The lower measurable frequency is attributed to the width of the resonant tunneling peaks which is in the GHz range. The high frequency cut-off is given by the energy level spacing in the dots. It can be as high as several meV corresponding to a detection frequency in the THz range. The main problem of this technique is that a special care should be taken to remove electron pumping effects between one dot and the adjacent lead. The calibration procedure is also difficult since the coupling strength highly depends on the specific sample geometry. However, this technique has been successfully tested experimentally in Ref. [101] using time resolved charge-detection techniques and a QPC as the noise source. The detection scheme is suitable for frequency resolved measurements, in the GHz range. However, only the excess emission noise of the QPC has been measured so far and asymmetry of the equilibrium noise of the environment was not probed yet.

The superconducting tunnel junction (SIS) as a spectrum analyzer [9, 75] We have chosen to use a superconducting tunnel junction as a quantum noise detector. There exists two ways of using it as a noise detector. First one can look at how the switching current is affected by a noise source. This has been done for example in Ref. [103] where they provide detailed informations over the third cumulant of noise in a normal tunnel junction [104, 105].

We chose the second approach which consists in looking at inelastic quasiparticles tunneling mediated by noise. This technique has already been used by Deblock *et al.* [75] to measure the noise of a TLS, Onac *et al.* [106] for the noise of a carbon nanotube quantum dot and Billangeon *et al.* for the noise of a Josephson junction [9] and a superconducting single electron transistor [107]. It is now quite well established than this detector is able to independently measure the emission and absorption excess noise of a nearby device. One of the difficulty of this detection scheme is the quantitative extraction of the noise spectrum from the response of the detector. From now on, we concentrate on the description of the principle of the SIS junction as a quantum detector.

4.2 $P(E)$ theory

In the framework of the quantum description of electronic circuits, one can treat a complete system *mesoscopic device + environment* within the same formalism. In the following, we present those calculations for the specific case of a small normal tunnel junction (normal state resistance R_N and junction capacitance C) embedded into an environment of impedance $Z(\nu)$. We introduce the $P(E)$ theory [11] which address the charge tunneling rates in ultrasmall junctions. In particular, it will be seen that the noisy environment modifies the dc $I(V)$ characteristic of the tunnel junction with an energy scale given by the charging energy. We finally consider the case of the superconducting tunnel junction, our selected quantum noise detector. In this specific case, an interpretation in terms of photo-assisted tunneling current associated to the voltage noise of the environment is given. This is the starting point for the noise detection principle.

4.2.1 Hamiltonian description

In order to determine the effects of the environmental degrees of freedom on the $I(V)$ characteristic of a tunnel junction, one needs to consider the total Hamiltonian of the system $H = H_{qp} + H_T + H_{env}$. This Hamiltonian takes into account the quasiparticles in each lead, the tunneling in between and the environment. Hereafter we develop those three terms.

Quasiparticles Hamiltonian

The quasiparticles in the two metallic electrodes are described by Hamiltonian

$$H_{QP} = \sum_{k,\sigma} \epsilon_k c^{+}_{k,\sigma} c_{k,\sigma} + \sum_{q,\sigma} \epsilon_q c^{+}_{q,\sigma} c_{q,\sigma} \tag{4.14}$$

where the first and second sum correspond respectively to the left and right electrodes. ϵ_k and ϵ_q denotes the energies of the quasiparticles with wave vector k and q while σ is their spin. $c^{+}_{k,\sigma}$ (respectively $c_{k,\sigma}$) is the creation (respectively annihilation) operator of a quasiparticle with wave vector k and spin σ.

Tunneling Hamiltonian

The tunneling from one electrode to the other is introduced by the tunneling Hamiltonian [108, 109]

$$H_T = \sum_{k,q,\sigma} \left\{ T_{k,q} c^{+}_{q,\sigma} c_{k,\sigma} e^{-i\varphi} + T^{*}_{k,q} c^{+}_{k,\sigma} c_{q,\sigma} e^{i\varphi} \right\}. \tag{4.15}$$

The coupling of the electromagnetic modes of the environment to the electronic modes of the junction is described by means of the phase term $e^{-i\varphi}$. This operator acts as a *translation* operator changing the charge on the junction by an elementary charge e:

$$e^{i\varphi} Q e^{-i\varphi} = Q - e. \tag{4.16}$$

Environmental Hamiltonian

Within the Caldeira-Leggett formalism presented in previous chapter (section 3.2.1), one can write the environmental Hamiltonian:

$$H_{env} = \sum_{k=1}^{N} \left\{ \frac{(q^{C,k})^2}{2C_k} + \frac{(\phi^{L,k})^2}{2L_k} \right\} = \sum_{k=1}^{N} \left\{ h\nu_k \left(a^{+}_k a_k + \frac{1}{2} \right) \right\}. \tag{4.17}$$

From the total hamiltonian H, one can extract the tunneling rates of quasiparticles through the tunnel barrier. The environment can be taken into account by a probabilistic term expressing its capability to exchange energy with the junction during a tunnelling event.

4.2.2 Tunneling rate formula and probability to exchange energy with the environment $P(E)$

Tunneling rate

By treating the tunneling hamiltonian in perturbation compared to the *quasiparticle + environment* hamiltonian and using the Fermi Golden rule, one expresses the forward tunneling rate (from left to right) as [11]:

$$\overrightarrow{\Gamma}(V)=\frac{1}{e^2R_N}\int_{-\infty}^{+\infty} dEdE'f(E)\left[1-f(E')\right]\times\left\{\int_{-\infty}^{+\infty}\frac{d\tau}{h}e^{\frac{i}{\hbar}(E-E'+eV)\tau}\left\langle e^{i\tilde{\varphi}(t+\tau)}e^{-i\tilde{\varphi}(t)}\right\rangle\right\}, \tag{4.18}$$

with $\tilde{\varphi}(t)=\varphi(t)-\frac{e}{\hbar}Vt$, the reduced phase. From now on, we simplify this expression.

Probability to exchange energy with the environment $P(E)$

Assuming gaussian fluctuations of the fluctuating phase $\tilde{\varphi}$, the phase-phase correlation term can be simplified according to Wick theorem. The identity $\left\langle e^{i\tilde{\varphi}(t+\tau)}e^{-i\tilde{\varphi}(t)}\right\rangle=e^{\langle[\tilde{\varphi}(t+\tau)-\tilde{\varphi}(t)]\tilde{\varphi}(t)\rangle}$ is used and one conveniently introduces the generalized phase-phase correlation function

$$J(\tau)=\left\langle\left[\tilde{\varphi}(t+\tau)-\tilde{\varphi}(t)\right]\tilde{\varphi}(t)\right\rangle. \tag{4.19}$$

This function is of primary interest to introduce the probability $P(E)$ for the junction to exchange energy E with the environment during a tunneling process [11] and is defined as:

$$\boxed{P(E)=\frac{1}{h}\int_{-\infty}^{+\infty} d\tau exp\left[J(\tau)+\frac{i}{\hbar}E\tau\right].} \tag{4.20}$$

Within this formalism, the forward tunneling rate of Eq.4.18 can be rewritten as a function of $P(E)$ so that

$$\begin{aligned}\overrightarrow{\Gamma}(V)&=\frac{1}{e^2R_N}\int_{-\infty}^{+\infty} dEdE'f(E)\left[1-f(E'+eV)\right]P(E-E')\\&=\frac{1}{e^2R_N}\int_{-\infty}^{+\infty} dE\frac{E}{1-e^{-\beta E}}P(eV-E).\end{aligned} \tag{4.21}$$

This last expression relates the dc I(V) characteristic of the junction to the function $P(E)$ as shown in the following.

4.2.3 $P(E)$ and $I(V)$ characteristic

Taking benefit from the relation $\overleftarrow{\Gamma}(V)=\overrightarrow{\Gamma}(-V)$, the current response $I(V)$ of the normal tunnel junction to a voltage bias V in presence of an environment having a probability $P(E)$

to exchange energy E is:

$$\boxed{\begin{aligned} I_{QP}(V) &= e(\overrightarrow{\Gamma}(V) - \overleftarrow{\Gamma}(V)) \\ &= \frac{1}{eR_N}\int_{-\infty}^{+\infty} dE \frac{1-e^{-\beta eV}}{1-e^{-\beta E}} EP(eV-E). \end{aligned}} \tag{4.22}$$

We hereafter explicit two examples: the ohmic environment and the single environmental mode at energy $h\nu_0$.

Ohmic environment

Making use of the FDT of formula 3.19, one can rewrite expression 4.19 as:

$$J(\tau) = \int_{-\infty}^{+\infty} \frac{d\nu}{\nu} \frac{Re[Z_t(\nu)]}{R_Q} \frac{e^{-i2\pi\nu t}-1}{1-e^{-\beta h\nu}} \tag{4.23}$$

with $Re[Z_t(\nu)]$ the real part of the total impedance seen by the junction. A low impedance environment is realized when condition $Re[Z(\nu)]/R_Q << 1$ is fulfilled[4]. In this case, assuming $Z_t(\nu) = 0$ $J(t)$ vanishes. It follows $P(E) = \delta(E)$ which corresponds to the fact that in the absence of environmental modes, only elastic tunneling is possible. The I(V) characteristic is linear $I_{QP}(V) = V/R_N$ as shown in figure 4.6. Opposingly, in the high impedance limit $Re[Z(\nu)]/R_Q >> 1$, the tunneling electrons may easily excite modes. These modes have a spectral density peaked at $\nu = 0$. Taking $Z(\nu) = R$, the real part of the total impedance is $Re[Z_t(\nu)] = R/(1+(2\pi\nu RC)^2$. For very large resistance R, the probability to exchange energy E with the environment is:

$$P(E) = \frac{1}{\sqrt{4\pi E_C k_B T}} exp\left[-\frac{(E-E_C)^2}{4E_C k_B T}\right] \tag{4.24}$$

with $E_C = e^2/2C$ the charging energy. At zero temperature the expression for the current yields:

$$I(V) = \frac{eV-E_C}{eR_N}\Theta(eV-E_C) \tag{4.25}$$

where $\Theta(E)$ is the unit step function. This expression means that it is necessary to apply at least a voltage $|V| > E_C/e$ to allow charge tunneling. This effect is called *dynamical Coulomb blockade*. In the intermediate regime of resistance, the I(V) characteristic of the junction evolves continuously from one case to the other as illustrated in figure 4.6.

As a conclusion, the I(V) characteristic of a small tunnel junction may be drastically modified in the presence of a resistive environment and a natural energy scale appears in the system: the charging energy.

---

[4] Note than $Z_t(\nu) \equiv Z(\nu)//\ (1/j2\pi\nu C)$ with C the geometrical capacitance of the junction and $Z(\nu)$ the impedance in series with the junction.

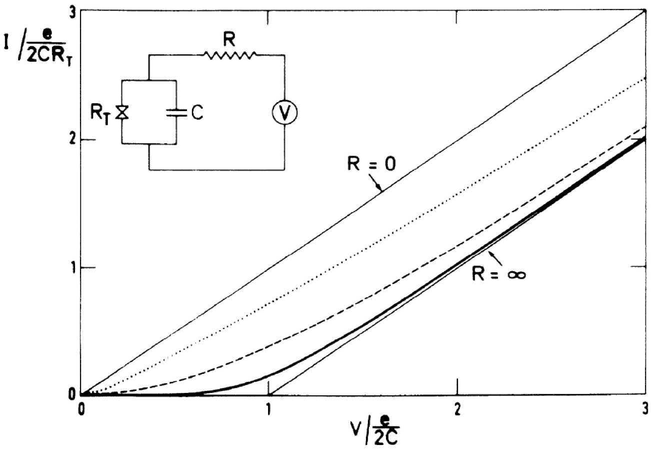

Figure 4.6: Taken from [109]. The zero temperature I(V) characteristic of a tunnel junction coupled to an environment characterized by a resistance R for $R/R_Q = 0, 0.1, 1, 10, \infty$.

Single mode environment

The coupling to a single mode environment can be accomplished using an inductance L into the external circuit. In this case, according to previous expression 3.14 the total impedance Z_t seen by the junction is, with C the geometrical capacitance of the junction:

$$Z_t(\nu) = lim_{\eta \to 0} Z_{LC}(\nu + i\eta) = \frac{i}{2\pi C} \frac{\nu + i\eta}{(\nu_0)^2 - (\nu + i\eta)^2} \tag{4.26}$$

where $\nu_0 = 2\pi/\sqrt{LC}$ is the frequency of the environmental mode. With those notations the dissipative part is given by

$$Re[Z_t(\nu)] = \frac{\pi}{2C} \left\{ \delta(\nu + \nu_0) + \delta(\nu - \nu_0) \right\}. \tag{4.27}$$

By inserting now this expression into Eq.4.20, we obtain a novel expression for $P(E)$:

$$P(E) = \frac{1}{h} \int_{-\infty}^{+\infty} dtexp[\rho(coth(\frac{\beta h \nu_0}{2})(cos(2\pi\nu_0 t) - 1) - isin(2\pi\nu_0 t)) + i\frac{E}{h}t], \tag{4.28}$$

where the parameter $\rho = 2\pi^2/CR_Q\nu_0 = E_C/h\nu_0$ is the ratio between the charging energy $e^2/2C$ and the eigen state excitation energy $h\nu_0$. The integral over time can be done leading to the reduced expression[5]:

$$\boxed{P(E) = exp[-(\rho_a + \rho_e)] \sum_{m,n} \frac{\rho_a^m \rho_e^n}{m!n!} \delta(E - (n-m)h\nu_0).} \tag{4.30}$$

The quantities ρ_e and ρ_a are respectively the probabilities to emit and absorb a quantum of energy $h\nu_0$. They are related to the Bose-Einstein occupation factor $N = 1/[e^{\beta h\nu_0} - 1]$ through relations:

$$\rho_e = \rho(1 + N) \text{ and } \rho_a = \rho N. \tag{4.31}$$

The function $P(E)$ is then a series of delta functions at energies $kh\nu_0$ with $k \in \mathbb{Z}^*$. Finally by inserting this expression into Eq.4.22 we obtain the I(V) associated to a single mode environment at zero temperature:

$$\boxed{I(V) = \frac{1}{eR_N} e^{-\rho} \sum_{k=0}^{n} \frac{\rho^k}{k!} (eV - kh\nu_0)} \tag{4.32}$$

where n is the largest integer smaller or equal to $|eV/h\nu_0|$. Indeed, the sum runs over all possible numbers of excited quanta where the maximum number of modes which can be excited is given by n. The factor $e^{-\rho}$ determines the slope at zero bias. If $\rho = E_C/h\nu_0 >> 1$ the Coulomb blockade is strong and the zero bias conductance is almost zero. On the contrary, if $\rho << 1$ Coulomb blockade is lifted and the zero bias conductance is about $1/R_N$. So again this example shows that Coulomb blockade can only be found if the environmental impedance is large enough. At higher bias, everytime the voltage becomes an integer multiple of the mode energy $h\nu_0$, the slope of the I(V) characteristic changes. This is more apparent in the differential conductance dI/dV (see Fig.4.7) where steps appear at voltages $kh\nu_0/e$.

4.3 SIS junction as a quantum noise detector

The P(E) theory previously described generalizes simply to superconducting tunnel junctions, our selected detector. In this case the normal leads are replaced by superconducting leads described by BCS theory. They consequently exhibit a gap in the density of states around the Fermi energy. Due to this absence of available states[6] the junction does not

---

[5] **N.B.** Assuming a poissonian distribution, the probability for the junction to simultaneously absorb n quanta emitted and emit m quanta absorbed by the environmental mode would be:

$$p(m,n) = \frac{e^{-(\rho_e+\rho_a)} \rho_a^m \rho_e^n}{m!n!}. \tag{4.29}$$

As this probability is exactly contained in formula 4.30, one can conclude that emission and absorption processes are statistically independent.

[6] We choose to not address here the Cooper pairs condensate at the Fermi energy which obviously allows to have a supercurrent at zero bias voltage.

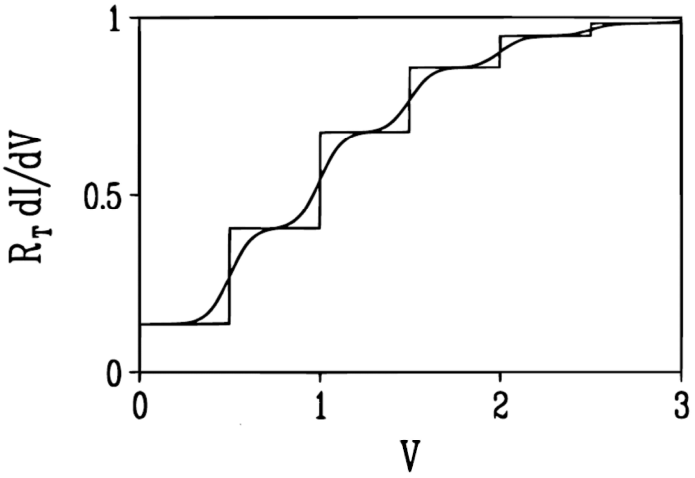

Figure 4.7: Taken from [11]. Normalized derivative of the current-voltage characteristic in a single mode environment $h\nu_0$ for $\rho = 2$. The voltage is given in units of the charging energy E_C. The step like curve correspond to zero temperature while the smooth curve is for $k_B T = 0.04 E_C$. Each jump corresponds to the absorption by the environment of an energy quanta $h\nu_0 = E_C/\rho$.

carry quasiparticles current below a voltage threshold $|V| = 2\Delta/e$. Above this value, quasiparticles current flows as for the normal tunnel junction case. In the following, we write down the expression of this dc I(V) characteristic as a function of the relevant parameters of the system in absence of environment. Changes due to the environment are calculated within the same P(E) formalism and an interpretation is given in terms of photo-assisted tunneling induced by the noisy environment.

4.3.1 DC properties of the SIS junction

Without environment, the I(V) characteristic of a SIS junction is determined by the *BCS* density of states $N_S(E)$[7]

$$I_{QP,0}(V) = \frac{1}{eR_N} \int_{-\infty}^{\infty} \frac{N_S(E) N_S(E+eV)}{N_0^2} [f(E) - f(E+eV)] dE, \qquad (4.33)$$

with N_0 the normal density of states corresponding to a Fermi level in the middle of the superconducting gap 2Δ. After integration, it reads

---

[7] $\frac{N_S(E)}{N_0} = \begin{cases} \frac{|E|}{\sqrt{E^2 - \Delta^2}} \text{ if } |E| > \Delta \\ 0 \text{ if } |E| < \Delta \end{cases}$

$$I_{QP,0}(V) = \begin{cases} \frac{V}{R_N}\left\{E\left(\sqrt{1-|\frac{2\Delta}{eV}|^2}\right) - 2|\frac{\Delta}{eV}|^2 K\left(\sqrt{1-|\frac{2\Delta}{eV}|^2}\right)\right\} \text{ if } |eV| > \Delta \\ 0 \text{ if } |eV| < \Delta \end{cases} \tag{4.34}$$

where Δ stands for the superconducting gap and R_N the normal state resistance of the junction. Functions K and E are complete elliptic integrals of the first and second kind respectively[8].

4.3.2 Photo-assisted tunnelling current as a probe of voltage noise

Exactly as previously, one can express the modified $I(V)$ characteristic of the junction as a function of the probability $P(E)$ for the environment to exchange energy:

$$\boxed{I_{QP}(V_D) = \int_{-\infty}^{+\infty} dE' \, \frac{1-e^{-\beta eV_D}}{1-e^{-\beta E'}} P(eV_D - E') I_{QP,0}(\frac{E'}{e})} \tag{4.35}$$

with $I_{QP,0}(V_D)$ the IV characteristic of the junction without environment and $\beta = 1/k_BT$. At low temperature and making use of the detailed balance relation $P(-E) = e^{-\beta E}P(E)$, this expression simplifies to:

$$I_{QP}(V_D) = P \otimes I_{QP}(V_D) = \int_{0}^{+\infty} dE' \, P(eV_D - E') I_{QP,0}(\frac{E'}{e}). \tag{4.36}$$

From now on, we demonstrate that in some limits, the influence of the environment can be interpreted in terms of photo-assisted tunneling (PAT) current of quasiparticles induced by the noisy environment. In the particular case of low noise amplitude one has $J(\tau) = \langle[\tilde{\varphi}(t+\tau) - \tilde{\varphi}(t)]\,\tilde{\varphi}(t)\rangle << 1$ and the Taylor development

$$exp[J(\tau)] \approx 1 + J(\tau) \tag{4.37}$$

can be done. Once introduced into Eq.4.20, one obtains a simplified version of the probability $P(E)$ than we straightforwardly relate to voltage fluctuations of the environment $S_V(\nu)$ [74]:

$$\begin{aligned} P(E) &= \frac{1}{h}\int_{-\infty}^{+\infty} d\tau (1 + J(\tau)) exp\left[\frac{i}{\hbar}E\tau\right] \\ &= \left[1 - \frac{e^2}{h^2}\int_{-\infty}^{+\infty} d\nu \frac{S_V(\nu)}{\nu^2}\right]\delta(E) + \frac{e^2}{h}\frac{S_V(E/h)}{E^2}. \end{aligned} \tag{4.38}$$

---

[8] $$\begin{cases} K(x) = \int_0^{\pi/2} \sqrt{1-x^2 sin^2\theta} d\theta \\ E(x) = \int_0^{\pi/2} \frac{1}{\sqrt{1-x^2 sin^2\theta}} d\theta \end{cases}$$

One obtains the expression for the total current $I_{QP}(V_D)$ flowing through the junction in the presence of environment from expressions 4.38 and 4.36. By substracting the value of the current without environment $I_{QP,0}(V_D)$ we obtain the photo-assited tunneling (PAT) current through the detector. This expression reads, as a function of bias voltage V_D and the non-symmetrized spectral density of voltage noise $S_V(\nu)$ of the environment [11, 74], in the limit $k_BT \ll eV_D$ and small voltage noise $S_V(\nu)$:

$$\begin{aligned} I_{PAT}(V_D) &= I_{QP}(V_D) - I_{QP,0}(V_D) \\ &= \underbrace{\int_0^{\infty} d\nu \left(\frac{e}{h\nu}\right)^2 S_V(-\nu) I_{QP,0}(V_D + \frac{h\nu}{e})}_{\textit{Emission contribution to the PAT current}} \\ &+ \underbrace{\int_0^{eV_D/h} d\nu \left(\frac{e}{h\nu}\right)^2 S_V(\nu) I_{QP,0}(V_D - \frac{h\nu}{e})}_{\textit{Absorption contribution to the PAT current}} \\ &- \underbrace{\int_{-\infty}^{+\infty} d\nu \left(\frac{e}{h\nu}\right)^2 S_V(\nu) I_{QP,0}(V_D)}_{\textit{Renormalization of the elastic current}} . \end{aligned} \tag{4.39}$$

The first term of eq. 4.39 is related to the emission noise, the second to the absorption noise and the third corresponds to the renormalization of the elastic tunneling current. We show in figure 4.8 typical I(V) characteristics of a SIS junction with (green curve) and without noisy environment (black curve = $I_{QP,0}(V_D)$). It turns out that whether the SIS junction is voltage biased below or above the gap, two different scenarios are possible.

Emission noise sensitive region $|V_D| < 2\Delta/e$ This situation corresponds to the subgap regime (infinite dc resistance in theory). In the so-called semiconductor representation (see left inset of figure 4.8), one can clearly see that no quasiparticles can tunnel from one electrode to the other. However, under high frequency irradiation (emitted noise by the environment), quasiparticles can absorb photons of energy $h\nu = (2\Delta - e|V_D|)$, which gives them enough energy to tunnel through the tunnel barrier. This leads to the appearence of a small step of photo-assisted current, which corresponds to photons emitted by the environment. A source sample can eventually be placed in this environment as we will see later on.

$$I_{PAT}(|V_D| < 2\Delta/e) = \int_0^{\infty} d\nu \left(\frac{e}{h\nu}\right)^2 S_V(-\nu) I_{QP,0}(V_D + \frac{h\nu}{e})$$

Absorption noise sensitive region $|V_D| > 2\Delta/e$ In this case, a finite quasiparticle current flows through the junction and is mostly due to elastic tunneling processes. In addition, quasiparticles can inelastically tunnel and emit photons at energy $h\nu = e|V_D| - 2\Delta$. These inelastic events happen only if these photons are absorbed by the environment (see right inset of figure 4.8). One then probes the capability for the environment, to absorb energy (absorption noise). The quasiparticles current is decreased and a negative step is seen in the I(V).

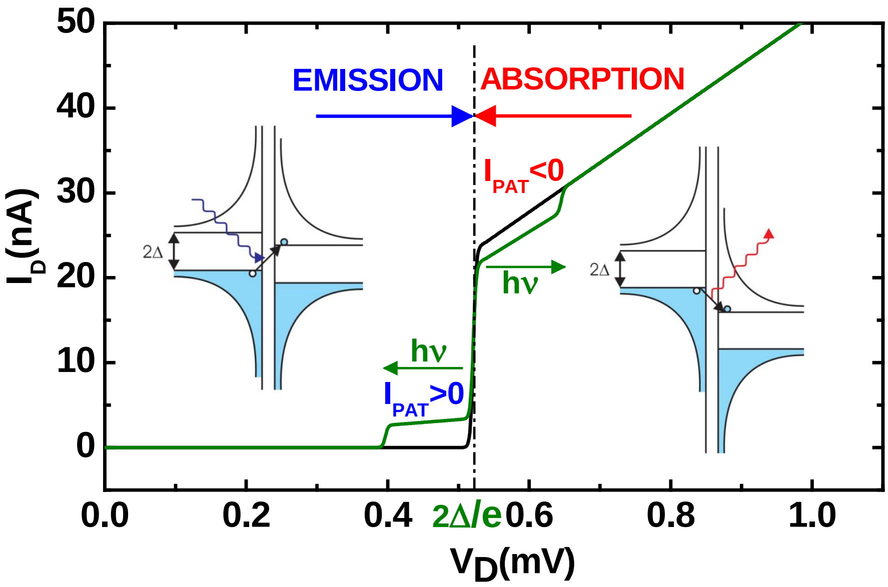

Figure 4.8: Black curve: Current voltage characteristic of a typical SIS junction. Green curve : calculated IV curve of the detector under irradiation giving rise to photoassisted tunneling current I_{PAT}. Below the gap, the detector is *emission* sensitive. Above the gap, the detector is mainly *absorption* sensitive. The amplitude of the PAT current is arbitrarily increased for the purpose of clarity. Schematic drawings correspond to semiconducting representations of the SIS junction when it is voltage biased below or above the gap. Below the gap a photon emitted by the environment allows the tunneling of a quasiparticle from one superconductor to the other (positive PAT current). Above the gap a photon absorbed by the environment decreases the overall tunneling rate of quasiparticles from one superconductor to the other (negative PAT current).

4.4 Conclusion

In this chapter, we have demonstrated that under certain conditions a SIS junction can be used as a good quantum noise detector able to distinguish between emission and absorption processes. The principle is based on inelastic tunneling of quasiparticles which is enhanced in presence of a noisy environment. The theoretical analysis of such detector is based on $P(E)$ theory which quantifies tunneling rates modifications induced by the noisy environment.
In the following, we experimentally incorporate a noise source in the environment of an SIS junction to measure its out-of equilibrium noise properties.

Chapter 5

High Frequency Measurements with an On-chip Resonant Circuit

In this chapter we show that by incorporating the quantum detector and the tested device, a Josephson junction, in an on-chip superconducting resonant circuit it is possible to detect the emission and absorption noise of the resonator at *equilibrium* and the excess noise of the probed device at the resonance frequencies. In particular, at the frequencies probed in the experiment, at low temperature the resonator does not emit noise wheras it shows absorption noise related to its zero point fluctuations. This technique also allows a direct extraction of the excess noise spectral density of quasiparticles tunneling through a Josephson junction at 28.4 and 80.2 GHz, the resonance frequencies of the resonator. We also demonstrate that the complex conductance at finite frequency of the system coupled to the detector via the resonant circuit can be extracted from the measurement of the $I(V)$ characteristic of the detector. The real and imaginary part of the complex conductance are measured at the resonance frequencies of the resonator and exhibits frequency dependent singularity related to the superconducting density of states.

After a short motivation section on the choice of the coupling circuit (section 5.1), the section 5.2 of this chapter is devoted to the description of the experimental setup and its modelling. It allows to determine the parameters affecting the resonance frequencies and quality factors of the resonant circuit. Section 5.3 is devoted to the measurement of the complex quantum conductance of a Josephson junction at finite frequency. We then present in section 5.4 the separate measurement of the emission and absorption noise in the quantum regime of the superconducting resonant circuit at equilibrium and discuss the limitation of the detection scheme. Finally, section 5.5 expose the extraction of the emission noise power of quasiparticles tunneling through the Josephson junction.

Contents

5.1 Choice of the coupling geometry

An important issue of the experiment is the coupling of the detector to the noise source. In the following we remind the previously used capacitive coupling [9, 74, 75, 101] to motivate our choice of the resonant circuit.

Transimpedance We know from chapter 4 that the SIS detector is sensitive to voltage noise of the environment where a noise source may be introduced. In this case, the current fluctuations $S_I(\nu)$ generated by the noise source couples to the detector via an on chip coupling circuit characterized by the *transimpedance* $Z_t(\nu)$. This transimpedance quantifies the link between voltage noise $S_V(\nu)$ appearing accross the detector and current noise generated by the source so that

$$S_V(\nu) = |Z_t(\nu)|^2 S_I(\nu). \tag{5.1}$$

In order to get a reasonable amount of photo-assisted tunneling current through the detector it is then of great interest to use a coupling circuit with a large transimpedance[1].

Capacitive coupling By using a capacitive coupling as shown in Fig.5.1, the source and detector can be DC biased independently while ensuring a reasonable and quasi frequency independent coupling at high frequency [9, 75, 106]. Typical values for the transimpedance that have been reached is $|Z_t| \sim 200\Omega$ [110]. However this value saturates due to the unavoidable coupling to ground and the deconvolution of the frequency dependence of noise is difficult.

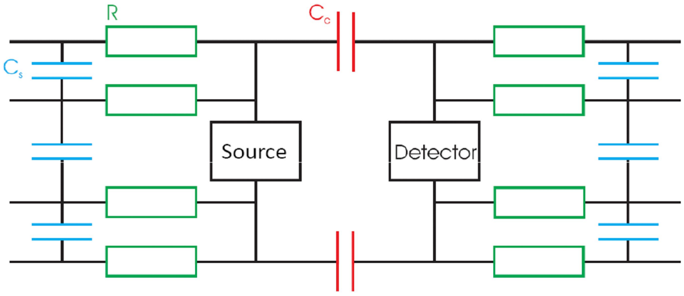

Figure 5.1: Sketch of a typical sample where source and detector are capacitively coupled. Coupling capacitances are denoted by C_C. Resistors R and shunt capacitances C_S isolate the circuit from the external world and play a fundamental role in the coupling efficiency.

Resonant coupling We choose to use an on-chip resonant circuit instead. In this case, the coupling is only efficient at the resonance frequencies of the coupling circuit but the transimpedance value is proportional to the quality factor of the cavity. In our experiment we had typically $|Z_t| > 1000\Omega$ on resonance.

5.2 Sample Fabrication and Modelling

In the following, we present the sample and model it to extract the parameters responsible for coupling strength limitation. Ideas to improve the coupling will be proposed.

---

[1] However the transimpedance mustn't be too high for the noise detection scheme works (see chapter 4).

5.2.1 Sample Fabrication

The device probed in this experiment consists of two coupled coplanar transmission lines. Each transmission line is connected to the ground plane via a small superconducting tunnel junction of size 240×150 nm^2 and consists of two sections of same length l but with different width, thus different characteristic impedance $Z_a \approx 110\Omega$ and $Z_b \approx 25\Omega$ (Fig. 5.2). Due to the impedance mismatch the transmission line acts as a quarter wavelength resonator, with resonances at frequency $\nu_n = nv/4l = n\nu_1$, where v is the propagation velocity and n an odd integer [111]. The two transmission lines are fabricated close to one another to provide a good coupling at the resonance frequencies and are terminated by two on-chip Pt resistors $(150\mu m \times 2\mu m \times 30nm)$ in parallel $2R_{End} = 826\Omega$. The junctions have a SQUID geometry with different areas and small geometrical inductance to tune separately their critical currents with a magnetic flux. The junctions and the resonator are fabricated in aluminum $(Al(30nm)/Al_2O_3/Al(50nm)$, superconducting gap $\Delta = 260\mu$eV) on a high resistivity oxidized silicon wafer. The system is thermally anchored to the cold finger of a dilution refrigerator of base temperature 20 mK and measured through filtered lines with a standard low frequency lock-in amplifier technique. In the following we call one junction the detector junction and the other the source.

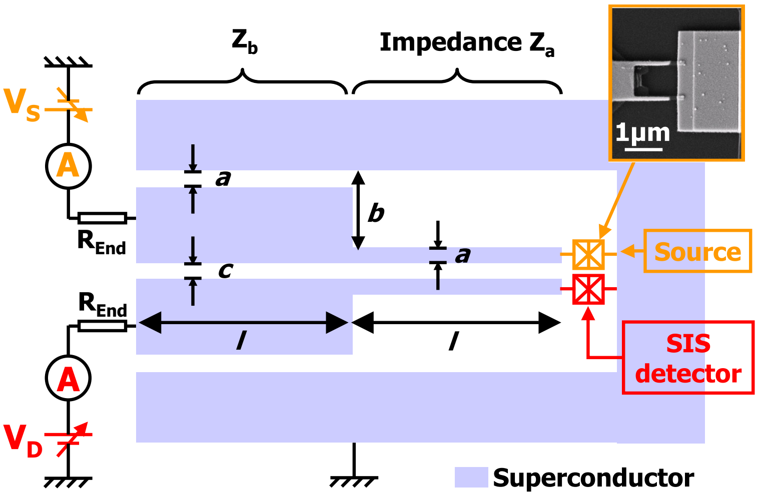

Figure 5.2: Sketch of the sample, with $a = 5\mu m$, $b = 100\mu m$, $c = 5\mu m$ and $l = 1mm$. The two transmission lines are terminated by two on-chip Pt resistors in parallel resulting in $R_{End} = 413\Omega$. The SIS junctions are made by shadow angle evaporation and have a SQUID geometry with different area in order to tune their Josephson currents.

5.2.2 Coupled transmission lines description

In this section we model the two coupled transmission lines and introduce the impedance matrix describing the coupling circuit between the source and the detector.

Model

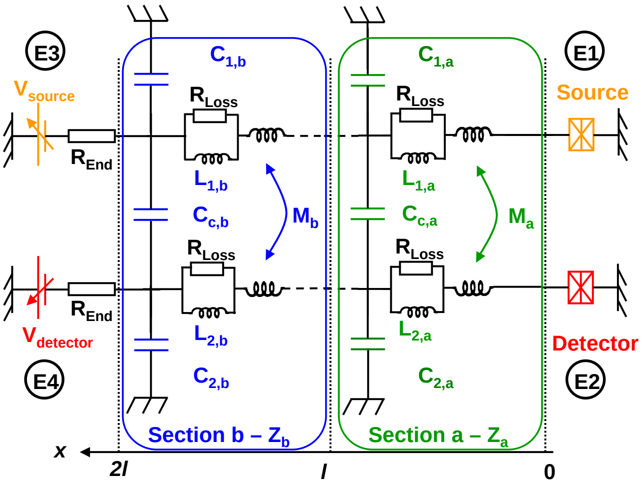

Figure 5.3: Model circuit used to extract the eigen frequencies of the two coupled transmission line resonators and estimate the quality factors. The system is considered as a 4 ports circuits. The ports are denoted E_1,E_2,$E_3$and E_4. The source junction is connected to the port E_1 and the detector to the port E_2. The impedances of ports E_3 and E_4 are resistors R_{End}. Section a and b have different values of distributed inductance and capacitance leading to an impedance mismatch in $x = l$. The values are fixed by the geometry and the choice of materials.

The sample is modelled as two distributed LC transmission lines capacitively and inductively coupled via the distributed coupling capacitance C_C and the distributed mutual inductance M as shown in Fig.5.3. Both transmission lines have an impedance mismatch at $x = l$. We call $V_1(x)$ and $V_2(x)$ the voltages developping along the transmission line 1 (top) and 2 (bottom) and $i_1(x)$ and $i_2(x)$ the currents flowing into these same lines. The equations of propagation along the line 1 read at frequency $\nu = \omega/2\pi$:

$$\begin{cases} \frac{d^2V_1}{dx^2} = \Gamma_+^2 V_1 + \Gamma_-^2 V_2 \\ \frac{dV_1}{dx} = -j\omega L' i_1 - j\omega M i_2 \end{cases} \tag{5.2}$$

with $L' = LR_{Loss}/(R_{Loss}+j\omega L)$, $\Gamma_+^2 = j\omega L'.j\omega(C+C_C)+j\omega M.j\omega C_C$, $\Gamma_-^2 = j\omega M.j\omega(C-C_C)-j\omega L'.j\omega C_C$ and $j^2 = -1$. R_{Loss} is the value of the distributed resistance of the transmission line, L the distributed inductance and C the distributed capacitance. The equation for line 2 can be deduced by exchanging 1 and 2 in the previous expressions.

Eigen modes of the resonator

We now introduce the eigen modes of the resonator which are *even* and *odd* modes defined respectively as $V_E = (V_1 + V_2)/2$, $V_O = (V_1 - V_2)/2$, $i_E = (i_1 + i_2)/2$ and $i_O = (i_1 - i_2)/2$. One can then read $V_1 = V_E + V_O$ and $V_2 = V_E - V_O$. The previous equations simplify to :

$$\begin{cases} \frac{d^2V_E}{dx^2} = \Gamma_E^2 V_E; \frac{d^2V_O}{dx^2} = \Gamma_0^2 V_O \\ \frac{dV_E}{dx} = -j\omega(L' + M))i_E; \frac{dV_O}{dx} = -j\omega(L' - M))i_O \end{cases} \tag{5.3}$$

with $\Gamma_E^2 = j\omega(L' + M).j\omega C$ and $\Gamma_O^2 = j\omega(L' - M).j\omega(C + 2C_C)$. From these relations we deduce that, neglecting the loss in the resonator, for the even mode the effective inductance is $L_{eff,E} = L + M$ and the effective capacitance is $C_{eff,E} = C$. For the odd mode the inductance is $L_{eff,O} = L - M$ and the capacitance is $C_{eff,E} = C + 2C_C$. For each section of the transmission line we have numerically (using Sonnet software) computed the characteristic impedance $Z = \sqrt{L_{eff}/C_{eff}}$ and the velocity $v = 1/\sqrt{L_{eff}C_{eff}}$ of the even and odd mode [2] and extracted from them the value of the parameters of the resonant circuit (table 5.1). With those parameters it is possible to compute the impedance of the resonant circuit.

Parameters	L_a	L_b	M_a	M_b
values	$1.047\mu H/m$	$0.283\mu H/m$	$0.615\mu H/m$	$0.117\mu H/m$
Parameters	C_a	C_b	$C_{C,a}$	$C_{C,b}$
values	$43.7pF/m$	$182.5pF/m$	$61.1pF/m$	$125.8pF/m$

Table 5.1: Values of the distributed inductance and capacitance of the resonator calculated from the geometry of the system (Fig.5.3).

Impedance matrix

In the experiment, the junctions impedance can be changed in-situ by a dc voltage bias. Other parameters of the sample such as end resistances R_{End}, loss R_{Loss} in the transmission line or source/detector coupling are fixed by the geometry and the choice of materials. The circuit can then be modelled by a 2×2 matrix which relates currents i_S and i_D to voltages V_S and V_D appearing at the source and detector port (Figure 5.4). This matrix reads :

$$\begin{pmatrix} V_D \\ V_S \end{pmatrix} = \overbrace{\begin{pmatrix} Z_r & Z_t \\ Z_t & Z_r \end{pmatrix}}^{\text{Impedance matrix}} . \begin{pmatrix} i_D \\ i_S \end{pmatrix} \tag{5.4}$$

where Z_r is the complex impedance of the transmission lines resonator and Z_t is the transimpedance which quantifies the coupling between the junctions. The experiment allows to determine the real part of the impedance seen by the detector $Re[Z(\nu)]$. In the following, we describe how this can be done and highlight the link of this quantity with the elements of the matrix impedance.

---

[2] The values of the velocity for even and odd modes are very close to each other. It results the coupled lines must be seen as a single resonator where the resonance frequencies are only fixed by the impedance mismatch.

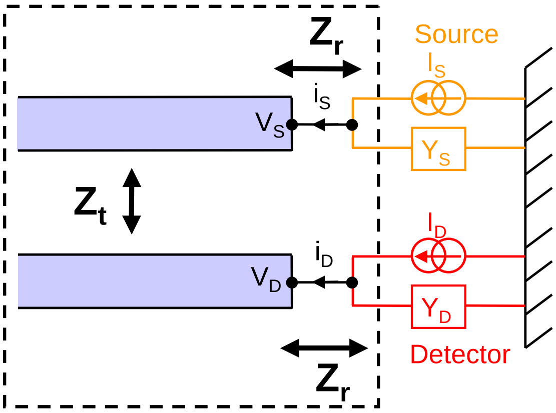

Figure 5.4: Circuit used to model the source and the detector coupled by the resonator. The coupling is modelled by a two channels HF circuit on which are connected the detector and the source junctions. This circuit is characterized by an impedance matrix.

5.2.3 Experimental extraction of $Re[Z(\nu)]$ and relation with the matrix impedance

The $I(V)$ characteristic of a small Josephson junction depends on the impedance of its electromagnetic environment [11]. We use this to calibrate the impedance seen by the detector, which will be used as a ac current source in the following paragraph .

Principle

As measured by Holst *et al.* [111], in the particular case of a Josephson junction coupled to a superconducting transmission line resonator, current peaks in the I(V) of the junction appear in the subgap region $V_D < 2\Delta/e$ due to the excitation of the resonator modes by the ac Josephson effect [112, 113]. These resonances in current are directly related to the resistive part of the impedance $Re[Z(\nu)]$ seen by the detector as:

$$I(V) = \frac{I_C^2}{2}\frac{Re[Z(2eV/h)]}{V} = eI_C^2\frac{Re[Z(\nu)]}{h\nu} \tag{5.5}$$

with $I_C = \pi\Delta/(2eR_N)$ the critical current of the junction, $R_N = 18.7k\Omega$ the normal state resistance of the junction [112, 114] and $\nu = 2eV/h$, the Josephson frequency. This relation is deduced from the effect of the electromagnetic environment on the tunneling of Cooper pairs through the small Josephson junction [11]. Within this interpretation, the $I(V)$ characteristic reads [74]:

$$I(V) = \frac{\pi e E_J^2}{\hbar}\left(P'(+2eV) - P'(-2eV)\right) \tag{5.6}$$

with E_J the Josephson energy and $P'(E)$ the probability to exchange the energy E during the tunneling of a Cooper pair. The probability for the environment to absorb energy is proportional to its dissipative part and follows at high energy the equation :

$$P'(+2eV) = \frac{2}{2eV}\frac{Re[Z(2eV/\hbar)]}{R_Q} \tag{5.7}$$

with $R_Q = h/4e^2$ the quantum resistance associated to the tunneling of Cooper pairs. Finally, the probability to emit energy is linked to the probability to absorb by the detailed balance relation at temperature T:

$$P'(-E) = e^{-\frac{E}{k_B T}} P'(+E). \tag{5.8}$$

At very low temperature $k_BT << E$, the probability to emit energy is very small and can be neglected. Relation 5.7 is valid when $E_J \times P'(E) << 1$. We compute $E_J = \frac{\hbar I_C}{2e} \approx 40\mu eV$. At $2eV = h\nu_1$ with $\nu_1 \approx 28GHz$, one obtain that $Re[Z(2eV/h)] << \frac{h\nu_1 R_Q}{2E_J} \approx 9400\Omega$ is a sufficient condition for expression 5.7 to be valid. All together these conditions lead to equation 5.5. Alternatively it can be derived by writing that the dc power provided by the voltage source to the Josephson junction, $I(V)V$, is equal to the AC power dissipated by the resistive part of the environment $Re[Z(\nu)]$ due to the AC Josephson effect at the Josephson frequency $\nu = 2eV/h$, $Re[Z(\nu)]I_C^2/2$.

Measurement of $Re[Z(\nu)]$

In figure 5.5, the $I(V)$ characteristic of the junction is shown in the subgap region for I_C maximized with magnetic flux. Using Eq.5.5 the subgap resonances allow to extract the real part of the impedance seen by the junction $Re(Z[\nu])$. It exhibits peaks at frequencies $\nu_{1,2,3} = 28.4, 54.9$ and 80.2GHz. With a length $l = 1$mm the first resonance was expected at 30 GHz. We attribute the difference with the measured resonance frequency to the capacitance of the junction which shifts the resonance. The relatively low quality factors Q_n, typically 10, are related to the unavoidable direct connection of the biasing circuit to the transmission line. The fact that we see resonances at frequencies $\nu_n = nv/4l$, with n not only an odd integer but also an even integer is attributed to the rather small ratio $Z_a/Z_b < 10$ of the impedances of the transmission lines. The amplitude of the peak at $28GHz$ is equal to 714Ω in agreement with condition of validity of Eq.5.7 *i.e.* $Re[Z] << 9400\Omega$. Moreover, we have checked that data corresponding to different values of E_J (tuned with a small magnetic flux in the SQUID area) can be rescaled with a factor independent of V (see Fig.5.6). This good scaling is another proof that we do satisfy conditions of validity of the $P(E)$ theory within first order.

Relation between $Re[Z(\nu)]$ and $Z_r(\nu)$ in the matrix impedance

In this part we address the relation between the measurable quantity $Re[Z(\nu)]$ and the impedance $Z_r(\nu)$ of the resonator entering in the matrix impedance (Eq.5.4). Approximating first the Josephson junction as a ac Josephson current source of negligible admittance

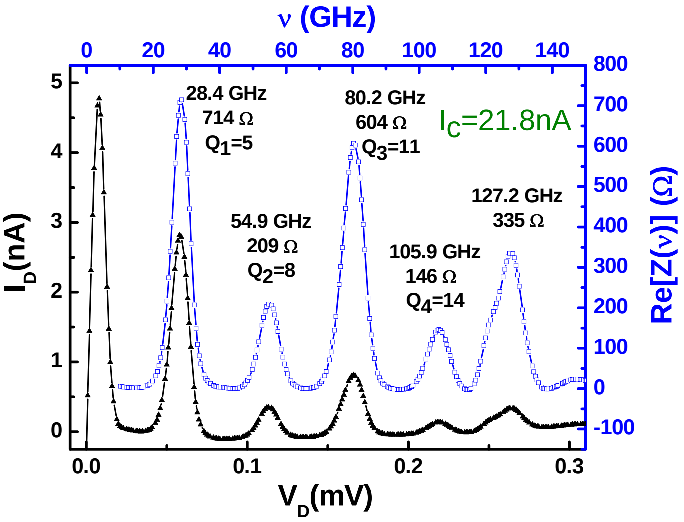

Figure 5.5: Lower curve : $I(V)$ dc characteristic of the detector junction in the subgap region with I_C maximized by adjusting the magnetic flux. Upper curve : the real part of the impedance seen by the detector junction, extracted from the previous curve using Eq. 5.5, exhibits several resonances with quality factor ≈ 10.

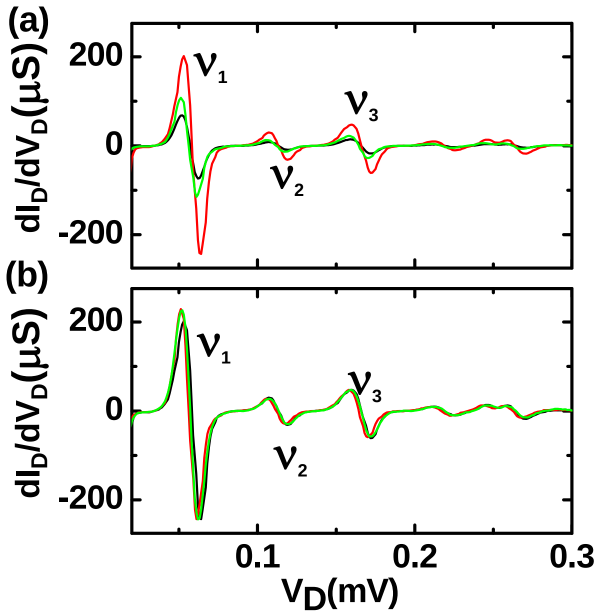

Figure 5.6: (a) dI/dV_D characteristics of the detector in a subgap position for different values of the Josephson current I_C (tuned by a small magnetic flux applied to the SQUID). (b) Same curves rescaled to the first peak amplitude. All the rescaled curves have the same behaviour. This is expected from equation 5.5 and is an evidence of its validity.

we find that the presence of the impedance Y_S at the end of line is responsible for a reduction of the impedance of the resonator:

$$Z_{r,eff}(\nu, Y_S) = Z_r(\nu) - \frac{Y_S(\nu, V_S)Z_t(\nu)^2}{1 + Y_S(\nu, V_S)Z_r(\nu)}. \tag{5.9}$$

However, the detector does not behave as a pure ac Josephson current source and one also has to consider its finite admittance Y_D. This leads to a measured $Z(\nu)$ which reads (see figure 5.7):

$$Z(\nu) = \frac{Z_{r,eff}(\nu, Y_S)}{1 + Y_D(\nu)Z_{r,eff}(\nu, Y_S)} \tag{5.10}$$

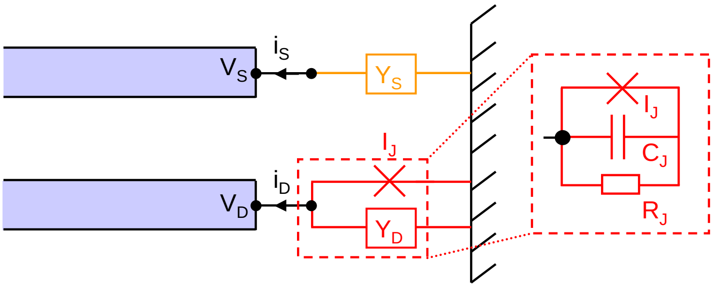

Figure 5.7: Modelling of the ac currents and voltages through and accross the resonator in the $Re[Z(\nu)]$ measurement. The measured impedance seen by the detector depends on two parameters which are the admittance of the detector Y_D (RC parallel circuit) and the effective impedance of the resonator $Z_{r,eff}$. This latter quantity does itself depend on Z_r and the source impedance Y_S via the transimpedance Z_t (see text).

Limit in which $Z(\nu)$ is equivalent to $Z_r(\nu)$

When computing Z for small real admittances $Y_D(\nu)$ and $Y_S(\nu)$ ($Y_{D,S} << 1/Z_r, 1/Z_t$ which is the case in the experiment) one easily finds that $Z \approx Z_r$. On the other hand when $Y_S(\nu)$ and $Y_D(\nu)$ are pure capacitances $Y_S(\nu) = Y_D(\nu) = jC_J 2\pi\nu$, Z exhibits resonances shifted compared to the original Z_r with identical amplitudes and quality factors. In general, a precise analysis of Z yields information on the impedance of the source. This is exploited in section 5.3.

5.2.4 Parameters influencing $Z(\nu)$

In this part we address the influence on the real part of the impedance seen by the detector $Re[Z(\nu)]$ of different parameters : loss in the transmission line R_{Loss}, end resistance R_{End}, impedance of the source Z_S and the detector Z_D.

Influence of linear loss along the transmission line resonator

To understand how R_{Loss} influences the resonator we plot as a function of frequency ν and different loss R_{Loss}, the quantity $Re[Z(\nu)]$ (figure 5.8). These curves are shown in the intermediate regime of loss $R_{Loss} \approx L\omega$. It corresponds to the crossover regime between a non dissipative and a dissipative transmission line. When $R_{Loss} >> L\omega$, the system is non dissipative and exhibits a sharp resonance. When $R_{Loss} << L\omega$, the transmission line is dissipative and does not exhibit any resonant behaviour. In the intermediate regime the increase of R_{Loss} leads to an increase of the peak amplitude. The qualitative behavior of the influence of R_{Loss} is the same for each frequency.

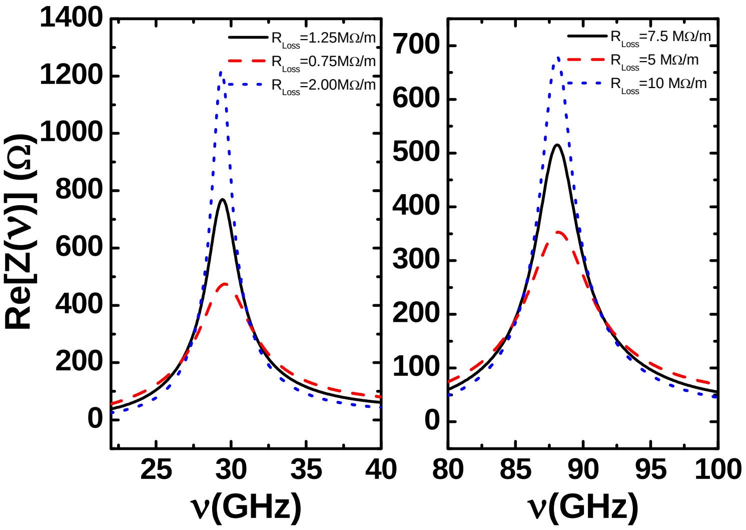

Figure 5.8: Real part of the impedance seen by the detector junction $Re[Z(\nu)]$ as a function of frequency for different loss $R_{Loss}(M\Omega/m)$ along the transmission lines. The impedances of each channels are fixed to $Z_S = Z_D = R_{End} = 10M\Omega$ and the parameters of the transmission line are given in table 5.1

Influence of R_{End}

We study the response of the resonator as a function of R_{End} (fig.5.9). When this resistance is high (typically $1k\Omega$), the resonator exhibits strong resonant peaks at frequencies defined by the geometry (30 and 90 GHz). The amplitudes of the main peaks are almost constant($\approx 800\Omega$) when the resistance R_{End} is higher than 800Ω. The saturation comes from finite loss introduced into the calculations. If R_{End} is lower than 800Ω the amplitude of the peaks goes down and the peaks split when $R_{End} \leq 15\Omega$. This latter case corresponds to the resonant circuit being short-circuited in E_3 and E_4. The resonator is then drastically perturbed and resonates at eigen frequencies determined by the impedance mismatch at $x = 2l$ leading to eigen frequencies two times smaller than the original ones. From these results we conclude that R_{End} has a critical value ($\approx 800\Omega$) above which the amplitude of the resonances saturates to the value determined by the intrinsic losses.

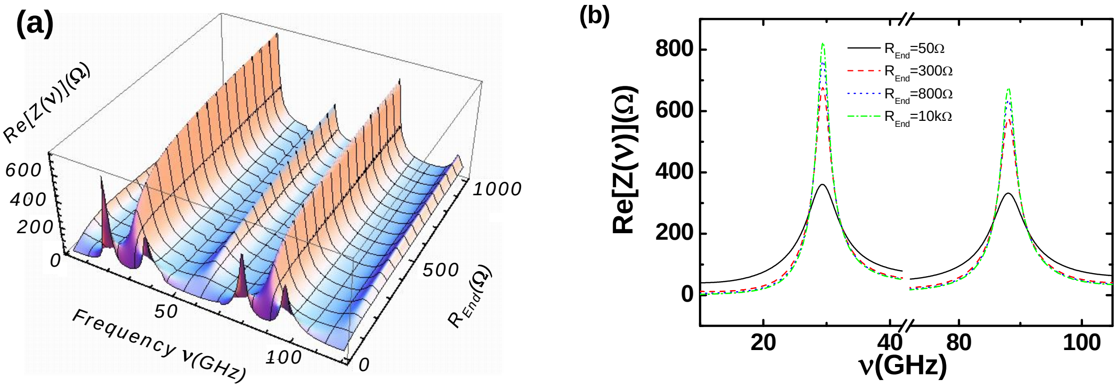

Figure 5.9: (a) 3D graph of $Re[Z(\nu)]$ as a function of frequency and resistance at the end of the transmission lines R_{End}. The other parameters are fixed to $Z_S = Z_D = 10M\Omega$, $R_{Loss} = 1.4M\Omega/m$ around ν_1, $R_{Loss} = 5.5M\Omega/m$ around ν_2, $R_{Loss} = 10M\Omega/m$ around ν_3. (b) $Re[Z(\nu)]$ as a function of frequency for several resistances R_{End} with the same conditions.

Influence of the impedance of the junctions

We now study the influence of Z_S and Z_D on the resonator. In the first case we consider $R_{End} = 10M\Omega$, $R_{Loss} = 1.4M\Omega/m$ around ν_1, $5.5M\Omega/m$ around ν_2 and $10M\Omega/m$ around ν_3 and study the influence of Z_S considered as a pure resistor $Z_S = R_J$. We have represented in a three dimensional graph, $Re[Z(\nu)]$ as a function of frequency and R_J (fig.5.10). We find that when $R_J \approx 0$, no resonant peaks are observed. When R_J increases, broad peaks appear and get sharper. Both amplitude ($Re[Z]_{max} \approx 800\Omega$ at ν_1) and quality factors ($Q_{Max} \approx 10$) saturates at high impedance($Z_J > 6k\Omega$) corresponding to the intrinsic losses of the lines. The eigen frequencies are unaffected by R_J.

When Z_S is a capacitance C_J in parallel with $R_J = 10M\Omega$, we have $Z_S = Re[Z_S] + iIm[Z_S]$ with $Re[Z_S] = R_J/(1+(R_JC_J\omega)^2)$ and $Im[Z_S] = -R_J^2C_J\omega/(1+(R_JC_J\omega)^2)$ with $\omega = 2\pi\nu$. We plot in fig.5.11a a three dimensional graph of $Re[Z(\nu)]$ as a function of frequency and C_J. The position in frequency of the resonant peaks shifts to lower frequency when the value of C_J is increased and their amplitudes slightly decrease. This corresponds to well known effects in resonant circuit *i.e.* a real admittance ($Re[1/Z_S]$) at the end of a resonator affects quality factors while imaginary part ($Im[1/Z_S]$)shifts resonances.

5.2.5 Comparison with the experiment

We now propose to fit the experimental curve of $Re[Z(\nu)]$ with the model previously described (Fig.5.12). This can be done in two ways.

1. First we can consider the experimental parameters $R_{End} = 413\Omega$, $R_J = 10M\Omega$ and $C_J = 7fF$. With these parameters, it is necessary to introduce losses along the transmission line $R_{Loss}(\nu_1) \approx 1.36M\Omega/m$, and $R_{Loss}(\nu_3) \approx 10,15M\Omega/m$ to reproduce the

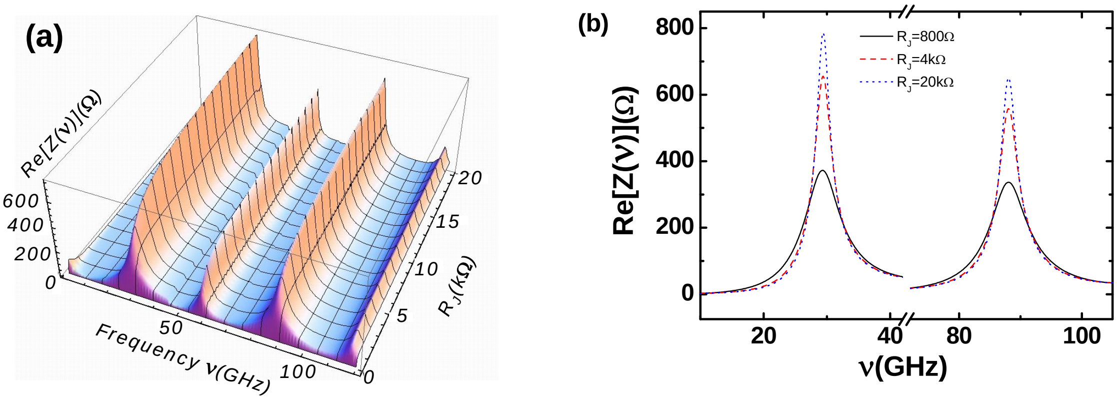

Figure 5.10: (a) 3D graph of $Re[Z(\nu)]$ as a function of frequency and dissipative impedance R_J in position E_1 and E_2. The other parameters are $R_{End} = 10M\Omega$, $R_{Loss} = 1.4M\Omega/m$ around ν_1, $R_{Loss} = 5.5M\Omega/m$ around ν_2, $R_{Loss} = 10M\Omega/m$ around ν_3.(b) $Re[Z(\nu)]$ as a function of frequency for several junction resistances R_J with identical conditions.

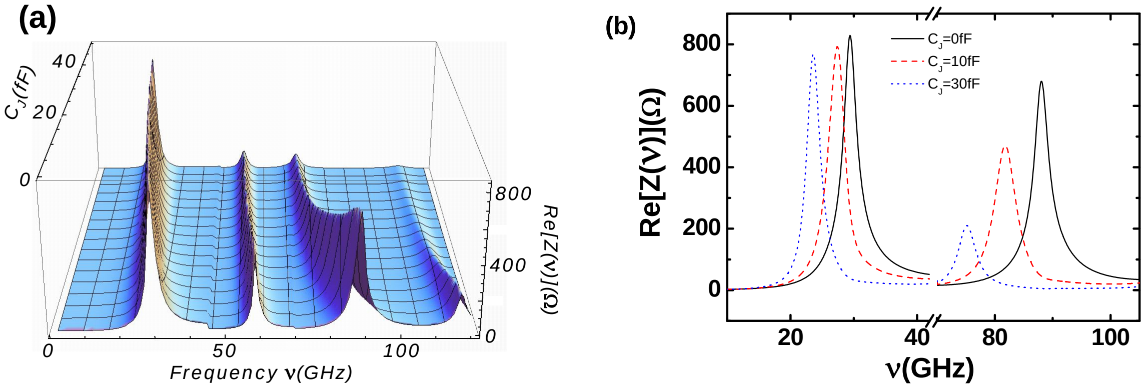

Figure 5.11: (a) 3D graph of $Re[Z(\nu)]$ as a function of frequency and the junctions capacitance C_J (in parallel with resistor $R_J = 10M\Omega$). The other parameters are fixed to $R_{End} = 10M\Omega$, $R_{Loss} = 1.4M\Omega/m$ around ν_1, $R_{Loss} = 5.5M\Omega/m$ around ν_2, $R_{Loss} = 10M\Omega/m$ around ν_3.(b) $Re[Z(\nu)]$ as a function of frequency for several junction capacitances C_J in the same conditions.

amplitude of the peaks. At the same time the quality factors are approximately 2 times higher than in the experiment. These losses are unphysical because aluminum and the low doping substrate used in the experiment are not known for exhibiting such amount of losses.

2. We can fit the experimental data by taking an effective R^*_{End} without intrinsic losses. The fit reproduces the peak amplitude with $R^*_{End} = 59\Omega$ near ν_1 and $R^*_{End} = 50.5\Omega$ near ν_3. The quality factor discrepancy is still of a factor ≈ 2. This points out the difficulty to take into account all the dissipation source in our model.

The effective value of the end resistor is smaller than expected ($R^*_{End} << R_{End}$) due to unwanted capacitive coupling to the ground.

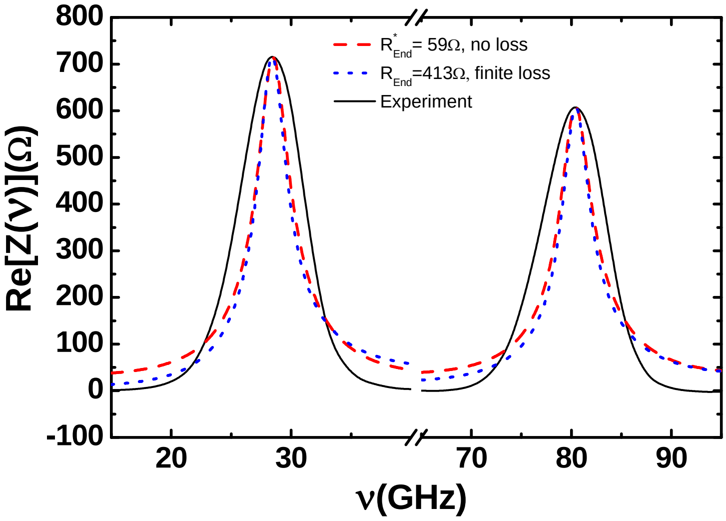

Figure 5.12: Black full lines : experimental $Re[Z(\nu)]$ seen by the detector. Red dashed curves : fit obtained by considering $R_{Loss} = \infty$ and an effective R^*_{End} ($R^*_{End} = 59\Omega$ near ν_1 and $R^*_{End} = 50.5\Omega$ near ν_3) without dissipation. Blue dotted curves : fit obtained by considering $R_{End} = 413\Omega$ with finite dissipation ($R_{Loss} = 1.36M\Omega/m$ near ν_1 and $R_{Loss} = 10.15M\Omega/m$ near ν_3).

5.2.6 Dependence of the source/detector coupling Z_t with inter transmission lines distance

The source/detector coupling is given by the transimpedance Z_t which relates the voltage accross the detector to the current flowing through the source. The transimpedance presents peaks at the same frequencies as $Re[Z]$ and amplitudes depend strongly on the distance c between the transmission lines (see figure 5.13). For ν_1 (respectively ν_3) the transimpedance decreases monotonously from 580Ω (500Ω) to 350Ω (300Ω) while the distance c varies from 1 to $7\mu m$. For the same interval of c the amplitude of the peaks of

$Re[Z]$ are unaffected while the quality factor is slightly lowered. This may be explained by a smaller confinement of electric field lines between the lines.

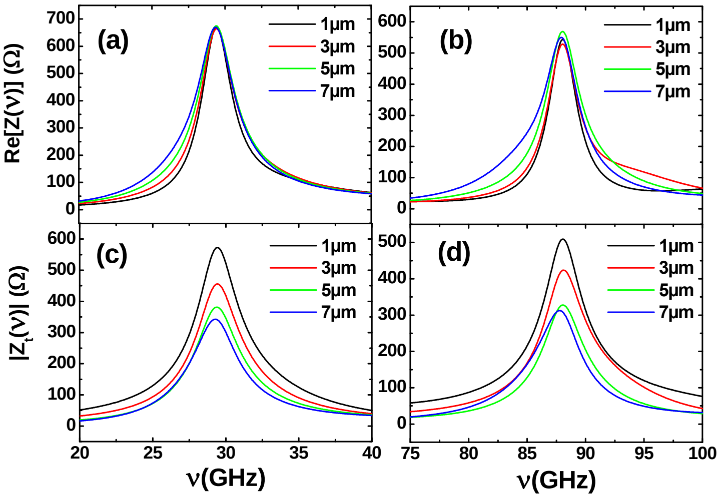

Figure 5.13: (a) and (b) $Re[Z(\nu)]$ as a function of frequency for different inter-transmission lines distance c respectively around ν_1 and ν_3. (c) and (d) Modulus of the transimpedance $|Z_t|$ source/detector as a function of frequency for different inter-transmission lines distance respectively around ν_1 and ν_3.

5.2.7 Proposals to improve the coupling circuit

Here are several ideas to improve the resonant cavity quality factor:

1. **Inductance at the end of line L_{End}:** By using an inductance at the end of line instead of the resistor R_{End} we should improve the coupling. Indeed whereas R_{End} is frequency independent, the impedance of an inductance increases with frequency $Z_L = j2\pi L\nu$ and thus isolates more the sample from the high frequency components of the external environment. Of particular interest is a kinetic inductance L_K made out of a very thin layer of Aluminum. For a $150nm$ wide, $2\mu m$ long and $80nm$ thick, one would have $L_K = 14nH$ and thus an impedance $|Z| = 420\Omega$ at 30GHz [115].

2. **Interdigit of the two large sections:** By interdigiting the large section of the resonator together with the ground plane, one should be able to increase the impedance mismatch at $x = l$ and accordingly improve the coupling.

3. **Resonator made out of Niobium:** Niobium has a larger gap than Aluminum and should, as a result, exhibit less loss than Aluminum and allows to probe higher frequencies.

4. **Sapphire substrate:** It is known from the high frequency community than saphire substrate exhibit much less high frequency loss than typical Si substrates. Interestingly sapphire has a low electrical conductivity and a good thermal conductivity.

5. ...

Some of these ideas have been tested during this thesis. Further studies are still necessary.

5.2.8 Conclusion

We have modelled the resonant coupling circuit and compared our results to experimental data. It allowed us to qualitatively understand the role of several sample parameters on the efficiency of the coupling circuit. The impedance at the end of the resonator is found to be a critical parameter.

5.3 High Frequency Admittance Measurement with an On-chip Resonant Circuit

In this part, we show how, using the setup described previously, one can measure the bias dependence of the complex admittance of the source $Y_S = Re[Y_S] + iIm[Y_S]$ at the resonance frequencies of the resonator. In the following, $Re[Y_S]$ is called the quantum conductance and $Im[Y_S]$ the quantum susceptance of the source [116–118].

5.3.1 Principle of the experiment

We have derived in section 5.2.3 the relation 5.10 between the impedance seen by the detector and the admittance of the source junction Y_S. By measuring the dependence of $Re[Z(\nu)]$ *vs* the bias voltage V_S of the source junction we can determine $Y_S(V_S)$. Hereafter we will assume the measured impedance $Z(\nu)$ can be approximated as $Z_r(\nu)$ shifted by a quantity proportional to the geometrical capacitances of the junctions (source and detector). The sensitivity of the experiment is calculated by using equation 5.10 and by assuming the resonant peaks of $Z(\nu)$ and $Z_t(\nu)$ extracted from the experiment can be approximated by a sum of Lorentzian functions centered around resonant frequencies of the resonator so that:

$$Z(\nu) = \sum_{i=0}^{n} \frac{Z_i}{1 + j\alpha_i(\nu - \nu_i)} \tag{5.11}$$

$$Z_t(\nu) = \sum_{i=0}^{n} \frac{Z_{t,i}}{1 + j\beta_i(\nu - \nu_i)} \tag{5.12}$$

with ν_i the i^{th} eigen frequency, Z_i and $Z_{t,i}$ the amplitude of the resonance and α_i and β_i fitting parameters corresponding respectively to the width of the resonances of $Z(\nu)$ and $Z_t(\nu)$ at frequency ν_i.

We present in the top panel of figure 5.14 calculated curves of $Re[Z(\nu)]$ for different values of the real part of the admittance Y_S ($Im(Y_S)$ is fixed to its geometrical value $jC_J 2\pi\nu$) around ν_1 (Fig.5.14). As expected, increasing $Re[Y_S]$ reduces the amplitude and the quality factor of the resonance. This behaviour is roughly linear with respect to a moderate increase of $Re[Y_S]$. The inflection point of the Lorentzian peak, denoted by the horizontal dashed arrow, is not affected by $Re[Y_S]$ changes. Bottom pannel of figure 5.14 describes the impedance seen by the detector junction for different imaginary part of the admittance of Y_S ($Re[Y_S]$ is fixed to 0). The main effect is a shift of the resonance frequency with a displacement proportional to $Im[Y_S]$. On the other side, both amplitudes and quality factors are nearly unchanged.

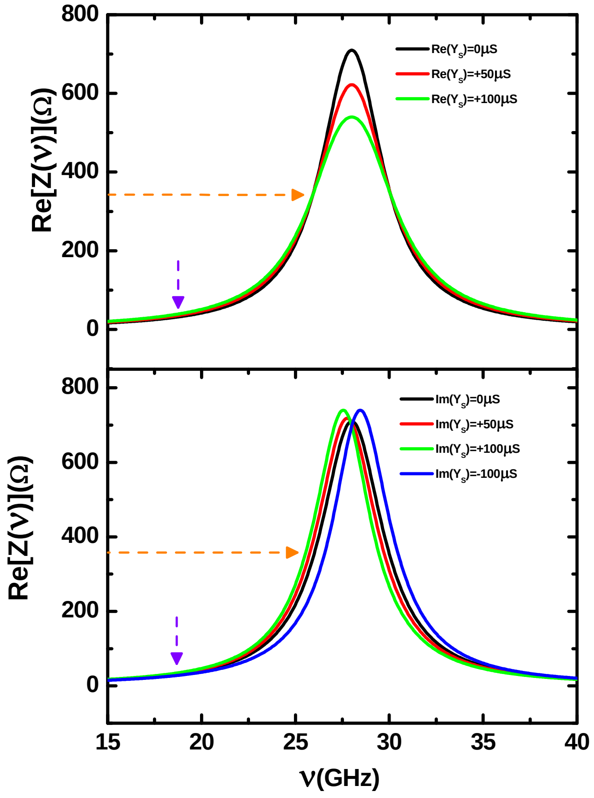

Figure 5.14: Calculated evolution of $Re[Z(\nu)]$ as a function of the real $Re[Y_S]$ (top panel) and imaginary $Im[Y_S]$ (bottom panel) components of the source junction impedance near ν_1. The calculations are done by using the best Lorentzian fits of the experimental curves of $Re[Z]$ and $|Z_t|$. The specific point denoted by the horizontal dashed arrows is not affected by $Re[Y_S]$ changes while it is very sensitive to changes of $Im[Y_S]$. Even far from resonance, influence of $Re[Y_S]$ on quality factors is visible as shown by the dashed vertical arrows.

5.3.2 Sensitivity of the detector to the high frequency admittance of the source

From the previous subsection, we conclude that by measuring the shape and position of the resonances we can access the bias dependence of the real and imaginary part of Y_S. This is exploited in the following using the detector in the ac Josephson regime as a generator like in section 5.2.3. In the experiment the quality factors are low, the amplitude of the peaks are weak and the voltage biasing is not perfect. To increase sensitivity we ac bias the source and measure the resulting signal on the detector with a lock-in amplifier technique. In the following we compare two different techniques we used to determine Re and $Im[Y_S]$ as a function of V_S by using the detector either in a voltage or a current bias mode. In both cases we modulate the source voltage V_S and measure by lockin detection either the induced current modulation $\partial I_D/\partial V_S$ or voltage modulation $\partial V_D/\partial V_S$ on the detector.

Voltage biased detector

We describe the sensitivity of the detector to a variation of Re or ImY_S by 2 coefficients: S^i_{Re} and S^i_{Im} respectively equal to $\partial Re(Z)/\partial ReY_S$ and $\partial Re(Z)/\partial ImY_S$. The current response of the detector to a low frequency modulation of V_S is then:

$$\frac{\partial I_D}{\partial V_S} = \frac{\partial I_D}{\partial Re(Z)}\left[S^i_{Re}\frac{\partial ReY_S}{\partial V_S} + S^i_{Im}\frac{\partial ImY_S}{\partial V_S}\right] \tag{5.13}$$

$\partial I_D/\partial Re(Z)$ can be calculated using Eq.5.5 and is equal to $eI_C^2/h\nu$ (see part 5.2.3) with ν the Josephson frequency $2eV_D/h$ associated with the bias of the detector. The quantities S^i_{Im}, S^i_{Re} can be calculated and are plotted in fig.5.15 as a function of the frequency in the vicinity of the fundamental mode of the resonator. As expected S^i_{Re} is maximum at resonance whereas S^i_{Im} is equal to zero. On the other hand S^i_{Im} is maximum at the inflexion point of the resonance. Unfortunately the stability of the detector is not excellent and it was not possible to adjust precisely the detection frequency at these optimum points. A better accuracy was obtained on the detection of $\partial ReY_S/\partial V_S$ when the detector was polarized below the inflexion point of the resonance denoted by vertical dashed arrows (bottom of the peaks) in figure 5.15 a. For this bias value of the detector, the contribution of $Im[Y_S]$ is lower than the contribution of $Re[Y_S]$ by a factor 0.56.

Current biased detector

A better sensitivity for the determination of $\partial Im[Y_S]/\partial V_S$ is obtained by *current* instead of voltage biasing the detector and measuring voltage. The current value is adjusted on the side of the investigated resonance peak (taking advantage of the hysteresis behavior of $V_D(I_D)$). The quantity measured is then the derivative of the dc voltage across the detector versus the bias voltage of the source $\partial V_D/\partial V_S$ with a lock-in detector. It is related to the admittance of the source as follows :

$$\frac{\partial V_D}{\partial V_S} = \frac{2e}{h}\left[S^v_{Re}\frac{\partial ReY_S}{\partial V_S} + S^v_{Im}\frac{\partial ImY_S}{\partial V_S}\right] \tag{5.14}$$

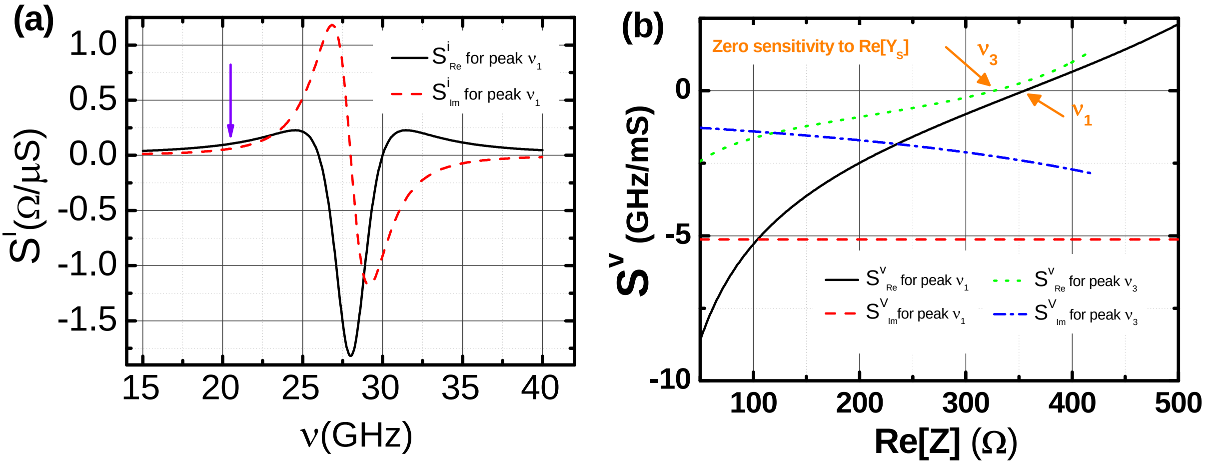

Figure 5.15: (a) Voltage biased detector: calculated sensitivity of $Re[Z]$ to the real and imaginary part of the admittance of the source Y_S as a function of the detector bias near ν_1. (Fixing the voltage bias of the detector V_D is equivalent to fix the measurement frequency ν). The sensitivity to the imaginary part in the voltage biased configuration (see text). S^i_{Im} is either positive or negative depending on which side of the resonance the measurement is done. It is zero at the resonance frequency. The sensitivity to the real part S^i_{Re} is maximum at the resonant frequency. Far from resonance, the vertical dashed arrows denotes the chosen detector position where S^i_{Re} is greater than S^i_{Im}. (b) Current biased detector: The voltage measured on the detector is proportional to the frequency. Its sensitivity to Im and ReY_S as a function of the current bias of the Josephson junction is shown around the first resonance ν_1. The sensitivity to the imaginary part in the current biased configuration S^v_{Im} is almost constant along the resonance peak. The sensitivity to the real part S^v_{Re} is zero at points denoted by vertical dashed arrows. At these points the detector is thus only sensitive to $Im[Y_S]$.

Where the quantities $S^v_{Re} = \partial\nu/\partial ReY_S$, and $S^v_{Im} = \partial\nu/\partial ImY_S$ describe the voltage sensitivity of the detector (in frequency units) to a variation of Re and ImY_S. They are depicted in Fig.5.15b as a function of the current bias on the detector.

From the analysis of these curves, we conclude that by current biasing the detector at the inflection point of the resonant peaks we measure a signal only proportional to $Im(Y_S)$, the imaginary part of the source junction. This position is denoted by the arrows in figure 5.15b.

5.3.3 High frequency admittance of the Josephson junction

In the following we show how one can deduce the full bias dependence of the complex admitance of a Josephson junction [118] at the eigen frequencies of the resonator. There are two contributions to the measured signals ($\partial I_D/\partial V_S$ or $\partial V_D/\partial V_S$). Beside the contribution of the bias dependent admittance of the source we have to consider the finite frequency shot noise contribution which can be measured independently (see section 5.5) and thus removed from the data [3]. We finally integrate the signal function with respect to V_S and deduce Re and ImY_S using the coefficients S^i and S^v calculated previously. The bias dependent quantum conductance $G_Q(V_S)$ and susceptance $B_Q(V_S)$ of the Josephson junction are thus measured at the two frequencies ν_1 and ν_3 depending on which peak the detector is biased (see figure 5.16 b). It can be compared to the theoretical expressions derived in [117]:

$$\begin{aligned} G_Q(V_S) &= \tfrac{e}{2h\nu}\left[I_{QP}(V_S + nh\nu/e) - I_{QP}(V_S - nh\nu/e)\right] \\ B_Q(V_S) &= \tfrac{e}{2h\nu}\left[I_{KK}(V_S + nh\nu/e) + I_{KK}(V_S - nh\nu/e) - 2I_{KK}(V_S)\right] \end{aligned} \tag{5.15}$$

where $I_{QP}(V_S)$ is the I(V) characteristic of the junction close to the gap and $I_{KK}(V_S)$ the Kramers-Kronig transform of $I_{QP}(V_S)$, defined as :

$$I_{KK}(V_S) = P\int_{-\infty}^{\infty} \frac{dV_0'}{\pi} \frac{I_{QP}(V_S') - V_S'/R_n}{V_S' - V_S}. \tag{5.16}$$

R_n is the normal state resistance of the junction and P represents the Cauchy principal value.

We plot in figure 5.16b, the theoretical and experimental curves obtained for the measured Josephson junction.

Concerning the quantum conductance $Re[Y_S]$, the result of the experiment is accurate concerning the positions of the observed steps at frequencies ν_1 and ν_3. On the other hand the experimental data exhibit a large dip in the interval $I_1 = [2\Delta/e - h\nu_1/e, 2\Delta/e + h\nu_1/e]$. We attribute the difference between the measurement and the theoretical prediction to a direct cross talk between the source junction and the detector in $V_S = 2\Delta/e$ and to a non-zero sensitivity to the imaginary part of the junction admittance. For frequency ν_3,

---

[3] To remove the noise contribution we assume that for $V_S >> 2\Delta/e$, the quantum admittance is constant and thus its derivative is zero. The noise, however leads to a constant value in the measured signal. We can thus subtract the contribution of the emission noise.

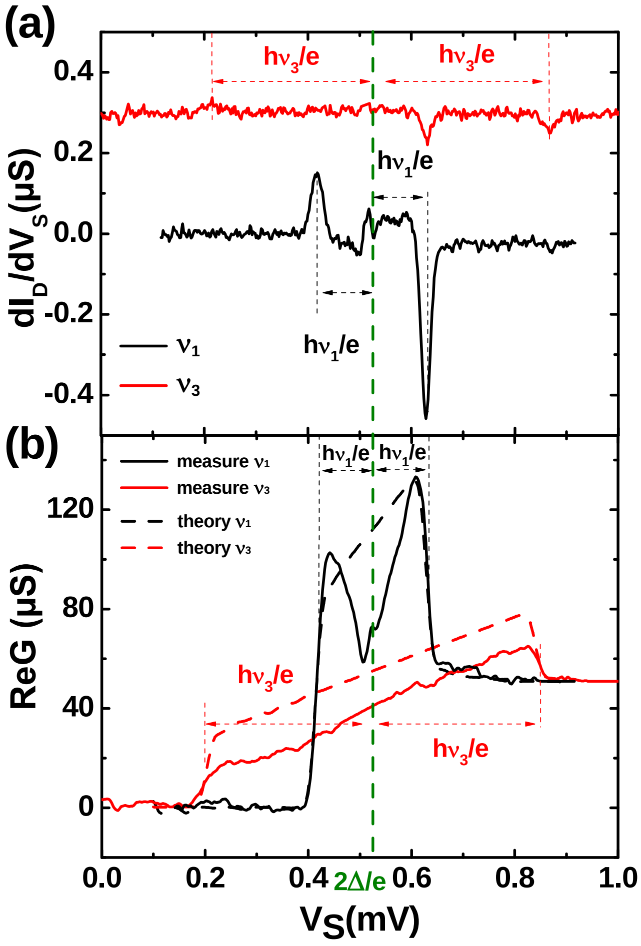

Figure 5.16: (a) Experimental dI_D/dV_S curves obtained by voltage biasing the detector at the bottom of the resonant peaks ν_1 and ν_3 and measuring the detector current modulation versus the voltage bias V_S of the source (see text). (b) Experimental quantum conductance, near the quasiparticles branch, extracted from curve (a). It is obtained after removing the emission noise contribution and numerical integration in V_S. The dashed lines correspond to the quantum conductance predicted by theory.

the detection is less sensitive and the cross talk in $V_S = 2\Delta/e$ is not visible anymore. The quantum conductance extracted is thus more reliable in the interval $I_3 = [2\Delta/e - h\nu_3/e, 2\Delta/e + h\nu_3/e]$ than for ν_1 but the experimental value is approximately 2 times smaller than the expected one. We attribute this difference to a lack of sensitivity of the detector at this frequency. On the other hand we also obtain a good agreement between theory and experiment for the order of magnitude of the susceptance and the positions in V_S of the singularities. However, the exact theoretical shapes are not recovered.

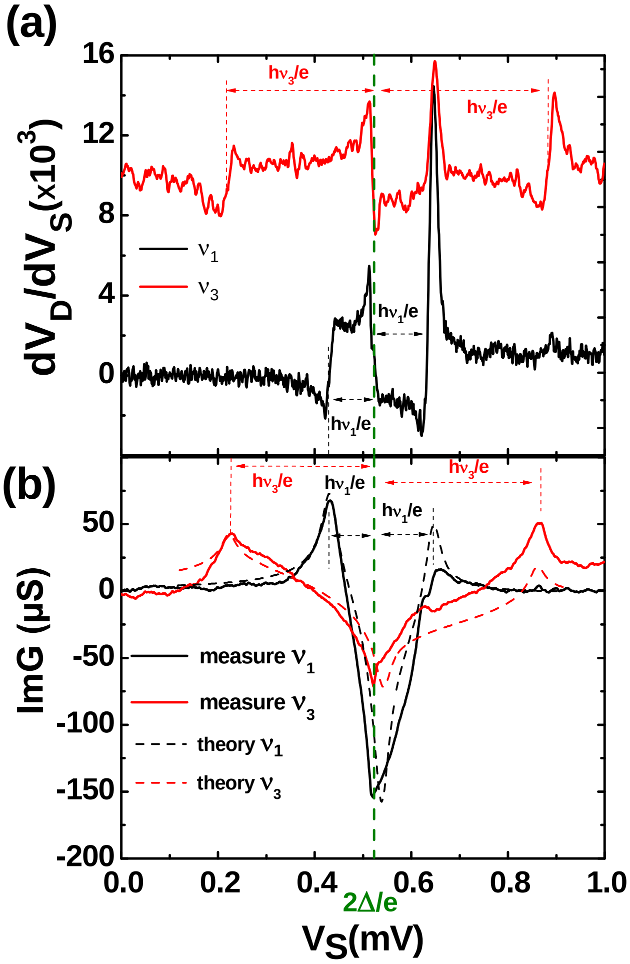

Figure 5.17: (a) Experimental dV_D/dV_S curves obtained by current biasing the detector at the middle edge of the resonant peaks ν_1 and ν_3 and measuring the detector voltage modulation versus the voltage bias of the source. (b) Experimental and theoretical quantum susceptance, near the quasiparticles branch, obtained after removing the emission noise contribution and numerical integration in V_S.

5.3.4 Conclusion

We have presented a semi-quantitative way to measure the high frequency admittance of a high impedance nanodevice, the Josephson junction. The technique described above can be used to probe other relatively resistive mesoscopic devices at high frequency.

5.4 Equilibrium Noise Measurement with an On-chip Resonant Circuit

In this section we show how using the same setup described above, one can measure the high frequency quantum noise of the resonator at equilibrium. The noise detector is one of the two superconducting SIS junctions and the principle of detection is based on photo-assisted tunneling as presented in the theoretical part of this thesis (see section 4.3). The $I(V)$ characteristic of the detector is modified by the resonator. This allows to extract the noise properties of the resonant circuit at *equilibrium* as we will see in this section.

5.4.1 Theoretical expectation for the noise of the resonator

According to the Quantum Fluctuation-Dissipation Theorem (QFDT), the voltage fluctuations of a resistive circuit at equilibrium of impedance $Z(\nu)$ reads [7,119]:

$$\begin{aligned} S_V(\nu,T) &= 2Re[Z(\nu)]h|\nu| \\ &\times \{n_B(h|\nu|)\Theta(-\nu) + [n_B(h|\nu|)+1]\Theta(\nu)\} \\ &= \frac{2Re[Z(\nu)]h\nu}{1-\exp\left(-h\nu/k_BT\right)} \end{aligned} \tag{5.17}$$

with $n_B(h|\nu|)$ the Bose-Einstein occupation factor at energy $h|\nu|$ and $\Theta(\nu)$ the Heaviside step function. This formula describes the crossover between thermal noise at low frequency and quantum noise related to the zero point fluctuations of the electromagnetic field at frequency higher than k_BT as already mentioned in the theoretical section 3.2.1. In the specific case of the resonator, the resonances seen in $Re[Z(\nu)]$ at ν_n give rise to noise peaks at frequencies $+\nu_n$ (absorption, with $\nu_n > 0$) and $-\nu_n$ (emission). At low temperature only peaks in absorption are predicted whereas when the temperature increases peaks in emission should appear.

5.4.2 Measurement of dI_D/dV_D as a probe of voltage noise S_V

We have seen in a previous section that the subgap $I(V)$ characteristic of the detector (low bias in the ac Josephson effect range) is modified by the resonant environment. Hereafter we also demonstrate that the resonant circuit coupled to the junction has also an effect on the quasiparticles branch of the detector. To probe more conveniently this effect the magnetic flux is adjusted in order to minimize the critical current of the detector. We measure the dI/dV rather than $I(V)$ characteristic of the detector junction (Fig. 5.18a) to increase the sensitivity of the experiment. At low temperature, on top of the expected dI/dV curve of the detector, we see peaks (denoted by arrows on figure 5.18) at bias voltages $eV_D = 2\Delta + h\nu_n$ with ν_n the resonance frequency of the circuit coupled to the detector. These peaks are not detected for bias voltage below 2Δ. This is not true at higher temperature where a peak at $eV_D = 2\Delta - h\nu_1$ appears and grows with temperature between 20mK and 1K. The position in V_D of the peaks changes due to the temperature dependence of the superconducting gap. Higher temperature were not considered due to the strong temperature dependence of the SIS detector for $T > 1$K. These peaks in the dI/dV characteristics of the detector are attributed to its sensitivity to the voltage fluctuations of the resonant circuit. Hereafter, we treat the data to extract emission and absorption noise power at the resonance frequencies of the on-chip circuit.

5.4.3 Extraction of the equilibrium noise of the resonator

The noise extraction is based on eq.4.39 demonstrated in the theoretical part of this thesis (see section 4.3). This formula relates the photoassisted tunneling current I_{PAT} appearing through the device to the noise spectrum $S_V(\nu)$ accross the detector. We remind here this expression:

$$\begin{aligned} I_{PAT}(V_D) &= I_{QP}(V_D) - I_{QP,0}(V_D) \\ &= \int_0^{\infty} d\nu \left(\frac{e}{h\nu}\right)^2 S_V(-\nu) I_{QP,0}(V_D + \frac{h\nu}{e}) \\ &+ \int_0^{eV_D/h} d\nu \left(\frac{e}{h\nu}\right)^2 S_V(\nu) I_{QP,0}(V_D - \frac{h\nu}{e}) \\ &- \int_{-\infty}^{+\infty} d\nu \left(\frac{e}{h\nu}\right)^2 S_V(\nu) I_{QP,0}(V_D). \end{aligned}$$

For $V_D < 2\Delta/e$ only the first term in eq. 4.39 is non-zero. For an emission noise peaked at frequencies $-\nu_n$ approximating the integral by a sum yields :

$$I_{PAT}(V_D) = \sum_n \left(\frac{e}{h\nu_n}\right)^2 S_V(-\nu_n)\delta\nu_n I_{QP,0}(V_D + \frac{h\nu_n}{e}) \qquad (5.18)$$

with $\delta\nu_n = 1.06\nu_n/Q_n$ related to the width of the resonance at frequency ν_n, which can be extracted from Fig. 5.5 ($\delta\nu_n$ multiplied by the amplitude of the resonance peak is equal to the area of the peak). On the other hand for $V_D > 2\Delta/e$, only the absorption term in eq. 4.39 leads to peaks in dI/dV at $V_D = (2\Delta + h\nu_n)/e$:

$$I_{PAT}(V_D) = \sum_n \left(\frac{e}{h\nu_n}\right)^2 S_V(\nu_n)\delta\nu_n I_{QP,0}(V_D - \frac{h\nu_n}{e}) \qquad (5.19)$$

From these relations we extract the emission and absorption voltage fluctuations of the resonant circuit at $\nu_1 = 28.4$ GHz for T between 20mK and 1K (Fig.5.18b). To do so

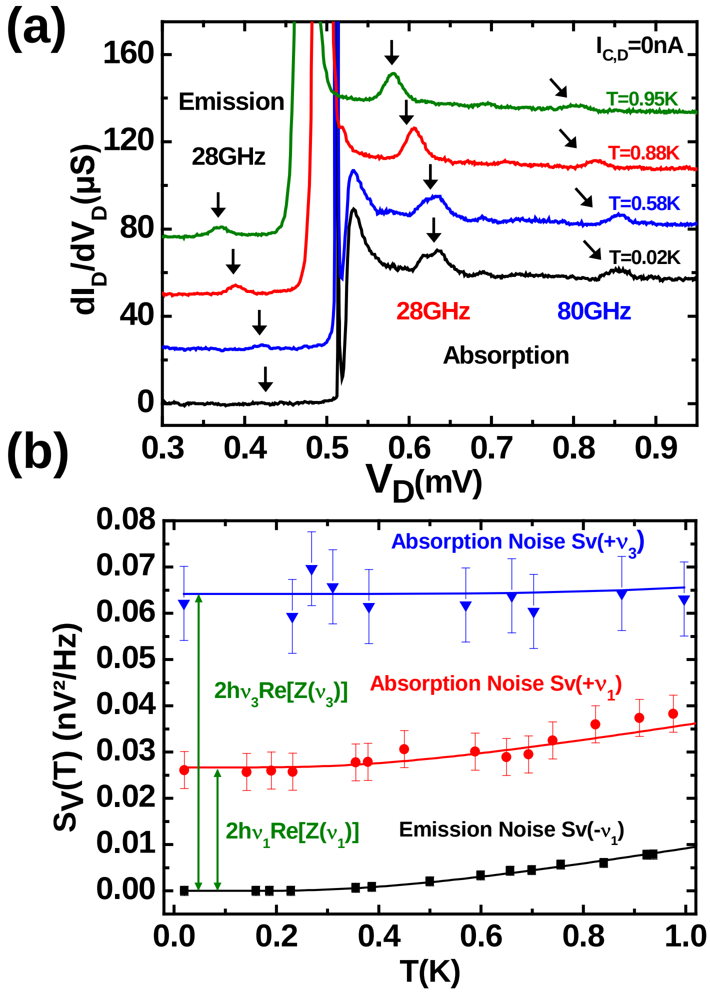

Figure 5.18: (a) Differential conductance dI/dV_D of the detector junction at different temperatures with I_C minimized by adjusting the magnetic flux. The curves are shifted vertically for clarity. The peaks corresponding to the detection of emission or absorption noise are denoted by arrows. (b) Dependence versus temperature of the power of voltage noise at $\nu_1 = 28.4GHz$ and $\nu_3 = 80GHz$ in emission and in absorption. The solid lines correspond to the theoretical predictions (Eq.5.17) with $Re[Z(\nu_1)] = 714\Omega$ and $Re[Z(\nu_3)] = 604\Omega$. Only absorption noise, consistent with zero point fluctuations, is detected below 0.4 K.

we integrate the corresponding peak in dI/dV_D, at $V_D = (2\Delta - h\nu_1)/e$ for emission and $V_D = (2\Delta + h\nu_1)/e$ for absorption, to obtain the value of I_{PAT}. One important point for the absorption part is to substract carefully the baseline due to quasiparticles elastic tunneling in the dI/dV_D curves. This is the main reason why error bars are larger for absorption than for emission. $\delta\nu_1 = 6.66$ GHz is extracted from fig.5.5 and the current $I_{QP,0}(V)$ is measured from the $I(V)$ characteristic of the detector at temperature T. The same treatment can be done for the absorption noise at $\nu_3 = 80.2$Ghz and leads to $S_V(\nu_3) = 0.062 \pm 0.005 \text{nV}^2/\text{Hz}$ between 20 and 700 mK, consistent with the expected value of $0.064 \text{nV}^2/\text{Hz}$. The emission noise has not been measured at ν_3 because the expected signal is too small at these temperatures to overcome the noise of the experimental setup. In addition, in order to look at the expected peaks it is necessary to bias the detector to smaller voltages where the ac Josephson peaks are difficult to be completely turned off with the magnetic flux in the loop area. The temperature dependence of voltage fluctuations agrees quantitatively with theoretical predictions (Eq.5.17) using the calibration of $Re[Z(\nu)]$ described in the previous section. Indeed, deep in the quantum regime, when $h\nu_1 \gg k_B T$, the voltage fluctuations at *equilibrium* of the circuit do not exhibit any emission noise whereas as a result of the zero point fluctuations of the electromagnetic field the circuit still shows absorption noise. In the intermediate regime, when $h\nu_1 \geq k_B T$ we see the crossover to thermal noise.

5.4.4 Conclusion

In conclusion we have shown that by coupling a quantum detector, a SIS junction, to a resonant circuit it is possible to calibrate and measure the emission and absorption noise of the resonant circuit at *equilibrium*. At low temperature the circuit exhibits only absorption noise related to the zero point fluctuations of the electromagnetic field. At higher temperature emission noise is also present.

5.5 Out-of-Equilibrium Noise Measurement with an On-chip Resonant Circuit

The design of the experiment allows to couple a noise source to the detector via the resonant circuit. In the following we measure the noise power of quasiparticles tunneling of the Josephson junction in the quantum regime ($h\nu >> k_B T$). We first calibrate the source/detector coupling thanks to the ac Josephson effect and finally measure the quasiparticles emission shot noise of the Josephson junction.

5.5.1 Calibration of the source/detector coupling $|Z_t|^2$ *i.e.* the transimpedance

When the source junction is biased it emits noise, which couples to the detector *via* the resonant circuit. Consequently the coupling is efficient only close to the resonance frequencies of the resonator. In this part, we extract the coupling between source and detector *i.e.* the transimpedance $Z_t(\nu)$. If the detector is voltage biased below the gap, it is essentially sensitive to voltage emission noise $S_V(-\nu)$. In this case, part of the current fluctuations of the source junction go through the coupling circuit. This leads to voltage fluctuations accross the detector proportional to the transimpedance $Z_t(\nu)$. This quantity is the ratio between voltage fluctuations accross the detector and current fluctuations emitted by the source $S_V(\nu) = |Z_t(\nu)|^2 S_I(\nu)$. To probe $|Z_t(\nu)|^2$ the magnetic flux is adjusted in order to minimize the critical current of the detector, then the detector is biased in the subgap region to be sensitive only to emission and we use the ac Josephson effect of the source junction for calibration. On figure 5.19 the PAT current through the detector versus the source bias voltage V_S is shown at two detector voltages $V_{D1} = 450\mu\text{V}$ and $V_{D2} = 300\mu\text{V}$. In this regime where the detector is irradiated by the Josephson current at frequency $\nu = 2eV_S/h$ the PAT current reads [120] :

$$I_{PAT}(V_D) = \frac{1}{4}\frac{e^2|Z_t(\nu)|^2 I_C^2}{(h\nu)^2} I_{QP}(V_D + h\nu/e) \tag{5.20}$$

with I_C the critical current of the source junction and $I_{QP}(V_D)$ the IV characteristic of the detector. Using this formula we can extract from the PAT current measured at V_{D1} the value of the coupling $|Z_t(\nu)|^2$ (inset of fig. 5.19). It exhibits resonances at the same frequencies as the resonator. This detection scheme is characterized by a strong coupling proportional to the quality factor of the resonances of $|Z_t(\nu)|^2$, for a finite value of frequencies. This contrasts with previous experiments using a capacitive coupling between source and detector [9, 75] which leads to a relatively small coupling over a wide range of frequencies.

Relation between the measured transimpedance $Z_{t,m}$ and Z_t in the matrix impedance

In previous section 5.2 we have emphasized the difference between Z and Z_r in the matrix impedance. We now compare $Z_{t,m}$ experimentally measured and Z_t in the matrix impedance. It leads to:

$$Z_{t,m} = \frac{Z_t(\nu)}{1 + Z_r(\nu)[Y_S(\nu, V_S) + Y_D(\nu, V_D)] + Y_S(\nu, V_S)Y_D(\nu, V_D)[Z_r(\nu)^2 - Z_t(\nu)^2]}. \tag{5.21}$$

Limit in which $Z_{t,m}$ is identical to Z_t

Equation 5.21 describes the evolution of the transimpedance as a function of Y_S, Y_D and Z_r. In the case where admittances Y_S and Y_D are zero ($Y_S, Y_D << 1/Z_r, 1/Z_t$), we find that the measured transimpedance is exactly the transimpedance of the impedance matrix. Indeed, in this case the resonator is only slightly perturbated so that no difference can be seen between these two quantities. In the other limit where Y_S and Y_D are large compared to $1/Z$ and $1/Z_t$, the effective transimpedance vanishes. This is due to the fact that the

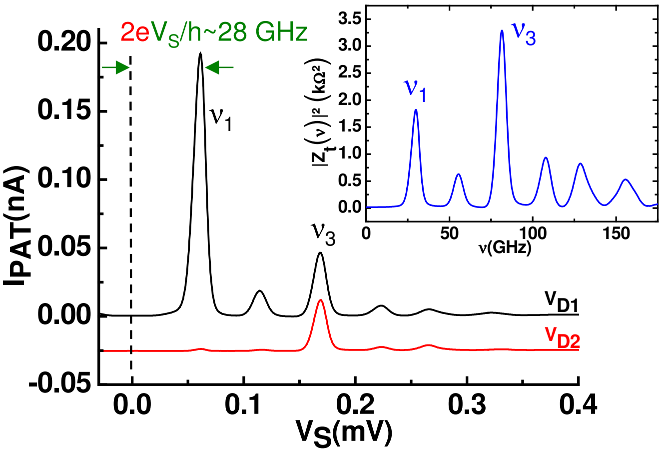

Figure 5.19: For calibration, we measure the PAT current through the detector versus the source junction bias V_S, when the source is in the regime of ac Josephson effect. The curves are shifted vertically for clarity. V_D selects the noise frequencies ν of interest : the upper curve is taken at $V_{D1} = 450\mu$V, corresponding to $\nu \geq (2\Delta - eV_{D1})/h = 17GHz$ whereas the lower curve, at $V_{D2} = 300\mu$V, corresponds to $\nu \geq$ 53GHz. Inset : Frequency dependence of the coupling $|Z_t(\nu)|^2$ deduced from the curve taken at V_{D1}.

resonator is short circuited by the impedance of the source or the detector. We finally conclude that differences between the amplitude of the effective transimpedance measured and the transimpedance of the resonator alone are small in the case of relatively high impedance nanodevices. However, as already mentioned, junctions also have capacitances which shift resonances to lowest frequencies. This resonance shift constitutes the main difference between $Z_{t,m}$ and Z_t.

Comparison between $Re[Z(\nu)]$ and $|Z_t(\nu)|$

In this part we want to adress the relation between $Re[Z(\nu)]$ and $|Z_t(\nu)|$. First the resonant frequencies are identical for both quantities (fig.5.20). Second, there is an important difference of magnitudes between these two quantities. The scaling factors $|Z_t|/Re[Z]$ depend on the frequency and are 1.65 at ν_1, 3.08 at ν_2, 2.71 at ν_3 and 5.28 at ν_4. The determination of these factors is essential for the calibration of noise measurements applied to another noise source (assuming than nothing else than the source change from one sample to the other).

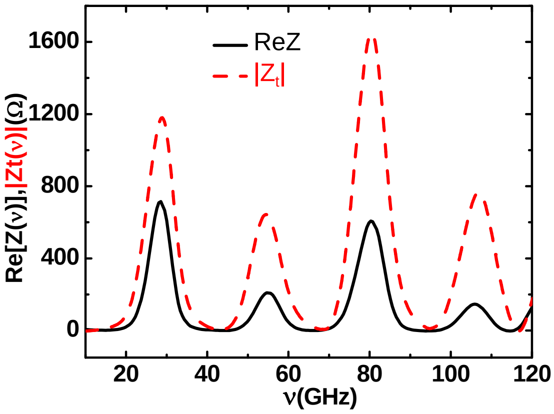

Figure 5.20: Comparison of $Re[Z(\nu)]$ and $|Z_t(\nu)|$. Eigen frequencies are almost identical and the scaling factors $|Z_t|/Re[Z]$ depend on the frequency

5.5.2 Out of equilibrium emission shot noise measurement

We have seen in section 5.5.1 that we are able to calibrate the coupling between the source and the detector. In this section we measure quantitatively the emission noise associated with the tunneling of quasiparticles when the source junction is biased on the quasiparticle branch ($eV_S \geq 2\Delta$). To do so, we apply a dc voltage bias to the detector in the emission noise sensitive region ($eV_D \leq 2\Delta$) while sweeping the dc voltage source close to its quasiparticle branch. In addition of this dc voltage is applied a small ac one ($\approx 3\mu V$ at 13.33 Hz) and the modulated current through the detector is measured by a lock-in amplifier technique. The measured quantity is $\partial I_{PAT}/\partial V_S$ the derivative of the photoassisted current with respect to the source bias. Such a detection scheme is not sensitive to other noise contributions beside the source and increase the sensitivity of the measurement. The PAT current is obtained by a numerical integration of the signal. It is shown on figure 5.21 for two values of detector bias V_{D1} and V_{D2}. We use eq. 5.18, with $S_V(\nu) = |Z_t(\nu)|^2 S_{I_{QP}}(\nu, V_S)$ and $\delta\nu_n$ the width of the resonances of $|Z_t(\nu)|^2$ in order to extract quantitatively the noise spectrum from data in fig.5.21. When the detector is biased at V_D with $V_D < 2\Delta/e$, only the frequencies higher than $(2\Delta - eV_D)/h$ have to be considered in the sum. Consequently for $V_D = V_{D1}$ the detector is mainly sensitive to the noise at frequencies ν_1 and ν_3, whereas for $V_D = V_{D2}$ only the noise at frequency ν_3 is detected. The noise at ν_1 is extracted from the curve $I_{PAT}(V_{D1}) - \alpha I_{PAT}(V_{D2})$ with α (> 1) a constant taking into account differences in sensitivity at frequency ν_3 for the two detector positions. This constant is obtained by extracting the renormalization factor of the third peaks for the two detector positions in the calibration measurements (see fig.5.19). One finally obtain the spectral density of quasiparticle noise in emission at $\nu_1 = 28.4$GHz and $\nu_3 = 80.2$GHz (Fig. 5.21). We compare these results to the theoretical prediction (Eq.3.45) and to the noise integrated over the detection bandwidth $\delta\nu_n$. The agreement is within 5% in amplitude with this last quantity and the frequency dependence is well reproduced. To our knowledge this is the first direct quantitative measurement in the quantum regime

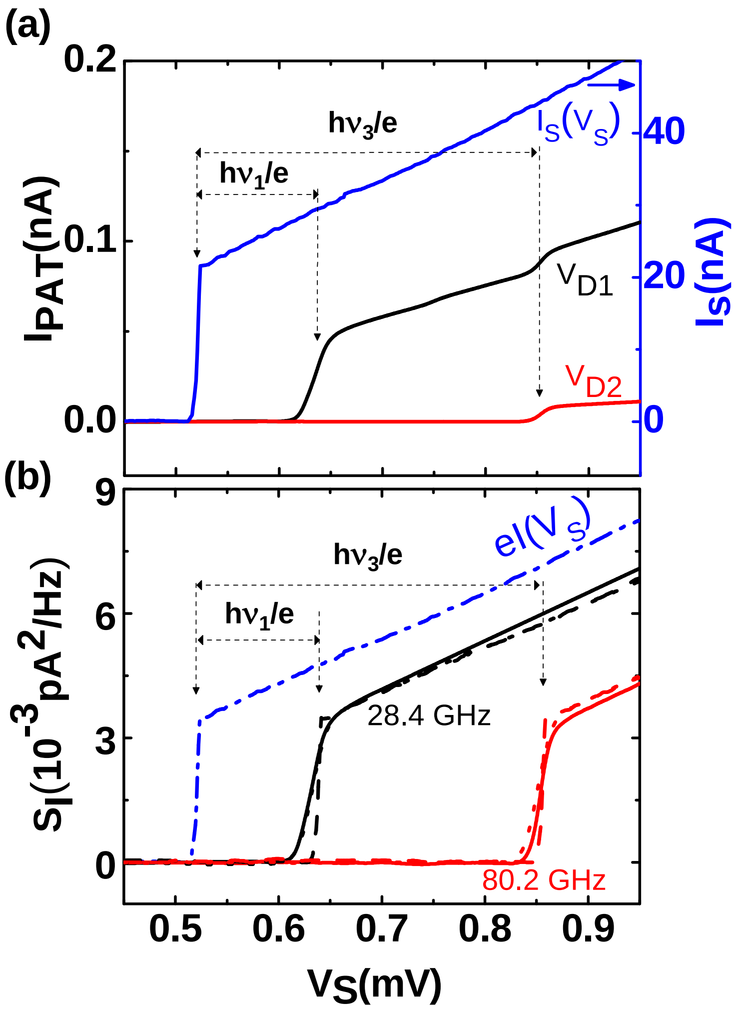

Figure 5.21: (a) PAT current through the detector versus the source junction bias V_S, when the source is biased on the quasiparticle branch. The two curves are taken at V_{D1} and V_{D2}. The $I(V)$ characteristic of the source junction is superimposed on the graph. (b) Extracted noise power in emission at $\nu_1 = 28.4$GHz and at $\nu_3 = 80.2$GHz. For comparison the expected noise power is plotted (dashed curve) together with the noise average over the bandwidth $\delta\nu_n$ of detection (dotted line). The agreement of this latter quantity is within 5% with the extracted noise power. The expected zero frequency emission noise power is plotted in dashed-dotted line.

$h\nu >> k_B T$ of the noise associated with the quasiparticles tunneling.

Sensitivity of the noise measurement

The sensitivity of this detection scheme is essentially limited by noise of the room temperature amplifiers which leads to a lowest measurable current of $20fA/\sqrt{Hz}$. This gives a minimum measurable current noise with this setup of $2fA^2/Hz$ at $28GHz$ and $8fA^2/Hz$ at $80GHz$. If we convert this result in terms of noise temperature T_N accross a $20k\Omega$ resistor, we get respectively $T_N(28GHz) = 1.5mK$ and $T_N(80GHz) = 5.8mK$. We stress here that this detection scheme only works for high impedance nanodevices.

5.5.3 Detector in the absorption sensitive part

The detection principle of the absorption noise is the same as in the previous section with the detector junction biased on the quasiparticles branch. However, in this configuration, the direct extraction of the noise spectra is very delicate. This is due to the contribution of the simultaneous absorption of the noise source and the resonator which is itself influenced by the impedance of the source [9]. The expected signal finally results on a non trivial combination of the absorption noise of the resonator and the source.

5.5.4 Conclusion

In conclusion we have shown that by coupling a quantum detector, the SIS junction, to another device through the resonant circuit it is possible to measure quantitatively its out-of-equilibrium emission noise at the resonance frequencies of the resonant circuit with an accuracy proportional to their quality factors. In the case of a Josephson junction biased above the superconducting gap it was possible to probe quantitatively the spectral density of quasiparticles current noise at 28.4GHz and 80.2GHz and in particular its strong frequency dependence.

5.6 Conclusion

In this chapter we have shown that by coupling a quantum detector, a SIS junction, to a resonant circuit it is possible to calibrate and measure the emission and absorption noise of the resonant circuit at *equilibrium*. At low temperature the circuit exhibits only absorption noise related to the zero point fluctuations of the electromagnetic field. At higher temperature emission noise is also present. The design of the resonant circuit allows to couple another device to the detector and to measure quantitatively its noise and admittance components at the resonance frequencies of the resonant circuit. The coupling strength is then proportional to their quality factors. In the case of a Josephson junction biased above the superconducting gap it was possible to probe quantitatively the spectral

Extracted quantity	**Critical current of the detector** $I_{C,D}$	**Critical current of the source** $I_{C,S}$	**Detector polarisation**	**Source polarisation**	**Measured quantities**
$Re[Z(\nu)]$	Maximum	Minimum	sweep $V_D \in [-2\Delta/e, 2\Delta/e]$	fix $V_S = 0$	dI_D/dV_D, $I_D(V_D)$
$Z_t(\nu)$	Minimum	Maximum	fix $V_D \in \pm[(2\Delta - h\nu)/e, 2\Delta/e]$	sweep $V_S \in [-2\Delta/e, 2\Delta/e]$	dI_D/dV_S, $I_D(V_S)$
S_V **resonator**	Minimum	Minimum	sweep $V_D \in \pm[(2\Delta - h\nu)/e, (2\Delta + h\nu)/e]$	fix $V_S = 0$	dI_D/dV_D, $I_D(V_D)$
S_I **source**	Minimum	Minimum	fix $V_D \in \pm[(2\Delta - h\nu)/e, 2\Delta/e]$	sweep $V_S \in \pm[(2\Delta - h\nu)/e, (2\Delta + h\nu)/e]$	dI_D/dV_S, $I_D(V_S)$
Quantum Conductance $G_Q(\nu)$	Maximum	Minimum	fix V_D bottom resonant peak	sweep $V_S \in \pm[(2\Delta - h\nu)/e, (2\Delta + h\nu)/e]$	dI_D/dV_S, $I_D(V_S)$
Quantum Susceptance $B_Q(\nu)$	Maximum	Minimum	fix I_D inflection point of resonant peak	sweep $V_S \in \pm[(2\Delta - h\nu)/e, (2\Delta + h\nu)/e]$	dV_D/dV_S, $V_D(V_S)$

Table 5.2: Summary of the different experimental conditions used to measure interesting quantities.

density of quasiparticles current noise at 28.4GHz and 80.2GHz and in particular its strong frequency dependence. Singularities in the finite frequency admittance components measurements have also been measured. The technique described above can be used to probe other relatively resistive mesoscopic devices at high frequency. The next chapter reports measurements realized with a carbon nanotube quantum dot in the Kondo regime.

Chapter 6

Emission Noise of a Carbon Nanotube Quantum Dot in the Kondo regime

In a bulk conductor the Kondo effect corresponds to the screening of local magnetic moments embedded in the conductor by the spin of the conduction electrons for temperature below the Kondo temperature T_K [58] as shown in the introduction chapter 2. The recent possibility to fabricate at the nanoscale systems where the electronic spin can be localized has lead to the discovery of this many-body phenomenon in quantum dots and carbon nanotube [26, 64, 121]. The Kondo effect can then be probed at a single spin level and in an out-of-equilibrium situation. It leads to a strong increase of the conductance of the quantum dot at zero bias due to the opening of a spin degenerate conducting channel, the transmission of which can reach unity. This system has been extensively studied in transport and more recently by current fluctuations measurements in the low frequency limit, which can provide detailed information on electronic transport [97, 122–128]. However the noise in the high frequency limit has not been explored experimentally despite the fact that it allows to probe the system at time scales of the order or smaller than h/k_BT_K at which the Kondo effect takes place [129].

In this chapter we present the first measurements of the current fluctuations of a carbon nanotube quantum dot in the Kondo regime at high frequency. We find a high frequency noise presenting a singularity at $h\nu \approx eV$, which is associated with the Kondo resonance, for frequency ν of the order of k_BT_K/h, and a strong reduction of this singularity in the noise for $h\nu \approx 3k_BT_K$.

In order to measure the current fluctuations of the CNT at high frequency we coupled it to the quantum noise detector previously described, the Superconductor-Insulator-Superconductor (SIS) junction, *via* a superconducting resonant circuit as shown in figure 6.1. This allows to probe at the resonance frequencies of the coupling circuit (29.5 GHz and 78 GHz) the emission part of the quantum noise of the CNT by measuring the photo-assisted tunneling current through the detector [130].

Contents

6.1 Sample fabrication

The probed sample consists of two coupled coplanar transmission lines. One line is connected to the ground plane via a carbon nanotube and the other by a superconducting tunnel junction of size 240×150 nm^2 (Fig. 6.1). the design of the resonant circuit is similar to the one described in chapter 5. Each transmission line consists of two sections of same length l but different widths, thus different characteristic impedance $Z_1 \approx 110\Omega$ and $Z_2 \approx 25\Omega$. Due to the impedance mismatch the transmission line acts as a quarter wavelength resonator, with resonances at frequency $\nu_n = nv/4l = n\nu_1$, with v the propagation velocity and n an odd integer [130]. The two transmission lines are close to one another to provide a good coupling at resonance and are terminated by on-chip Pd resistors. The junction has a SQUID geometry to tune its critical current with a magnetic flux.

The carbon nanotube (CNT) is first grown by chemical vapor deposition on an oxidized undoped silicon wafer [131] (see *Experimental techniques* part of this thesis). Individual CNT is located relative to predefined markers and contacted to palladium contacts using electron-beam lithography. The junction and the resonator are then fabricated in aluminum (superconducting gap $\Delta = 182\mu$eV). A nearby side-gate allows to change the electrostatic state of the nanotube. The system is thermally anchored to the cold finger of a dilution refrigerator of base temperature 20 mK and measured through low-pass filtered lines with a standard low frequency lock-in amplifier technique.

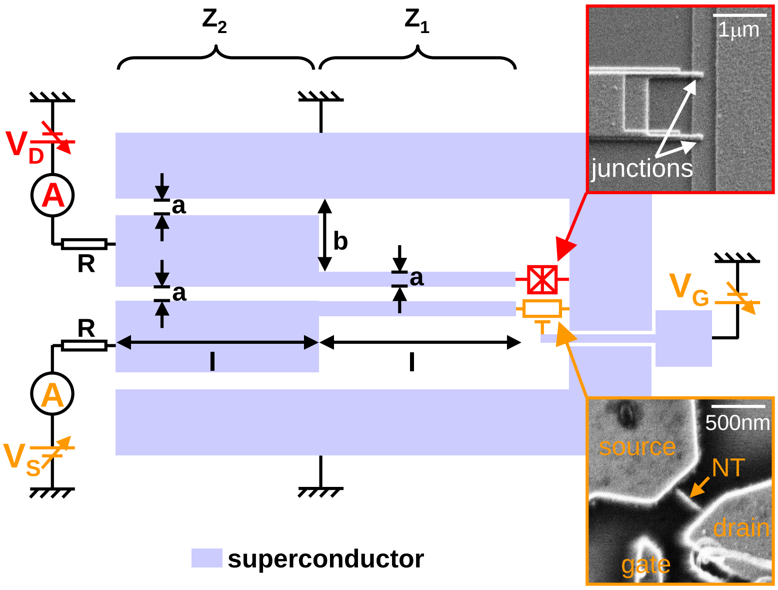

Figure 6.1: Sketch of the sample : a carbon nanotube (bottom electron microscope picture) is coupled to a superconductor-insulator-superconductor (SIS) junction (top electron microscope picture), used as a quantum detector, by a superconducting resonant circuit. This circuit is constituted by two transmission lines, placed close to one another, made of aluminum and terminated by on-chip Pd resistors. The SIS junction is made by shadow angle evaporation and has a SQUID geometry in order to tune its Josephson current. The carbon nanotube is CVD grown, connected with Palladium contacts and side-gated.

6.2 Transport measurements

The Kondo effect is usually regarded as a spin-related phenomenon. In principle, however, the role of the spin could be replaced by other degrees of freedom, such as an orbital quantum number [132, 133]. It has been shown that the unique electronic structure of carbon nanotubes enables the observation of orbital Kondo effect [27]. When orbital and spin degeneracies are present simultaneously it was observed a strongly enhanced Kondo effect, with a multiple splitting of the Kondo resonance at finite magnetic field. This obeys a so-called SU(4) symmetry [134, 135]. Due to the band structure of the CNT, a double orbital degeneracy plays the role of a pseudospin, which is entangled with the spin. Quantum fluctuations between these 4 degrees of freedom result in a SU(4) Kondo effect at low temperatures. This exotic Kondo effect manifests as a four-peak splitting in the nonlinear conductance when an axial magnetic field is applied. In the following, we show that our nanotube does not present SU(4) symmetry and that presumably, only the electronic spin 1/2 of the confined electron in the dot expresses in the observed Kondo effect. This is done by studying the conductance *vs* magnetic field, temperature and voltage in a Kondo region of the stability diagram of the dot.

6.2.1 Stability diagram and Kondo temperature

We first characterize the CNT-quantum dot. To do so we measure the differential conductance dI/dV as a function of dc bias voltage V_S and gate voltage V_G (Fig. 6.2a). For particular values of the gate voltage the CNT shows a strong increase of the conductance at zero bias, a signature of the Kondo effect. From the half width at half maximum of the Kondo peak we extract the Kondo temperature $T_K = 1.4\text{K}$ in the center of the ridge [26] (Fig. 6.2b). This value is consistent with the temperature dependence of the conductance at zero bias (Fig. 6.4a). The Kondo temperature is related to the charging energy U of the CNT quantum dot, the coupling $\Gamma = \Gamma_L + \Gamma_R$ to the electrodes and the position ϵ of the energy level measured from the center of the Kondo ridge, according to the Bethe-Ansatz [67, 68]:

$$T_K = \sqrt{U\Gamma/2}\,\exp\left[-\frac{\pi}{8U\Gamma}|4\epsilon^2 - U^2|\right] \tag{6.1}$$

Assuming $U = 2.5\text{meV}$, deduced from the size of the Coulomb diamond, and $T_K = 1.4\text{K}$ in the center of the Kondo ridge we deduce $\Gamma = 0.51\text{meV}$. The asymmetry $a = (\Gamma_L - \Gamma_R)/(\Gamma_L + \Gamma_R)$ of the contact can be deduced from the value of the conductance at zero bias and is equal to 0.67.

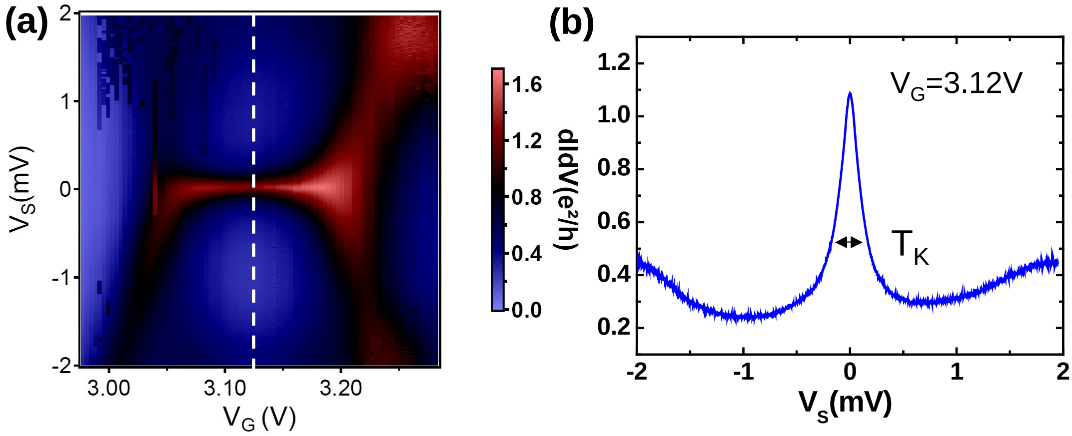

Figure 6.2: (a) Differential conductance dI/dV of the carbon nanotube as a function of voltage bias V_S and gate voltage V_G. It exhibits a Kondo ridge for gate voltage between 3.05 and 3.20 V with an increase of conductance at zero bias. (b) Trace of the differential conductance dI/dV as a function of bias voltage at $V_G = 3.12V$, the center of the Kondo ridge. From the half width at half maximum of the Kondo peak we extract the Kondo temperature $T_K = 1.4\text{K}$.

6.2.2 Magnetic field dependence

We study the zero bias conductance peak as a function of magnetic field. The Anderson impurity model [67, 68, 136], used to explain the zero bias peak along the kondo ridge requires a degeneracy. For a slightly lifted degeneracy, which can be achieved using a magnetic field for instance, the Kondo resonance is expected to split. Here we present conductance measurements in magnetic fields showing split Kondo resonances which occurs as a function of magnetic field (Fig.6.3). This hints a real spin degeneracy since the splitting of the Kondo resonances reflects a Zeeman splitting $\Delta E = 2g\mu_B B$ with the Landé g-factor equals 2.

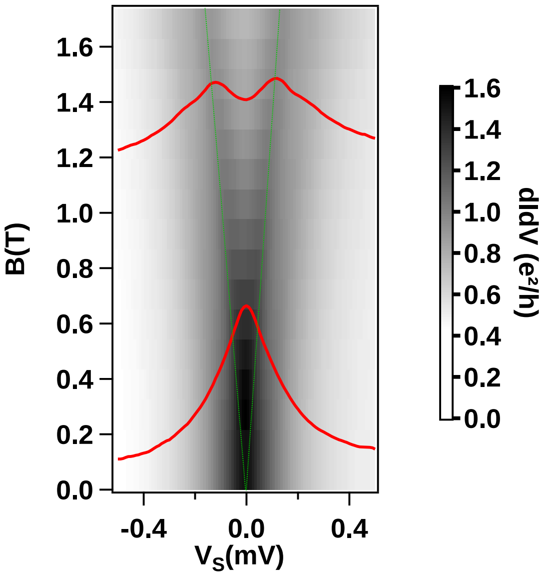

Figure 6.3: Perpendicular to the plane magnetic field splitting of the zero bias peak at the center of the Kondo ridge. The exchange energy is $E = 2g\mu_B B$. Red curves are traces taken for $B = 0.108T$ and $B = 1.302T$. Green dashed curves are the expected lines of the position of the splitted peaks maximum for a $g = 2$ Landé factor.

6.2.3 Universal scaling

An important property of the Kondo effect is its universal behaviour [26, 64, 69, 137]. In particular, it has been demonstrated that the normalized conductance of different Kondo dots from different samples with different Kondo temperatures T_K collapse in a single curve when represented as a function of reduced parameters T/T_K or $eV_{SD}/k_B T_K$ [137]. This implies the only relevant energy scale in the system is the Kondo temperature.

Universal temperature dependence

We have represented the reduced zero bias peak amplitude $(G - G_C)/G_0$ *vs* the reduced temperature T/T_K as shown in figure 6.4a. G_C is the Coulomb background conductance at zero bias. $G_0 = G_{Max} - G_C$ with G_{Max} the saturated amplitude of the peak at low temperature. We have then fitted this curve with the empirical formula given in reference [69] :

$$G = G_C + G_0/(1 + (2^{1/s-1}(T/T_K)^2))^s \tag{6.2}$$

with s a constant which depends on Kondo type correlations. This empirical formula derives from a fit to NRG calculations and is known to reasonably reproduce the temperature dependence of the zero bias peak. By using $T_K = 1.4K$ and $s = 0.22$ into the fit, we confirm the hypothesis of a spin 1/2 Kondo effect [69].

Universal voltage dependence

Universal scaling in nonequilibrium transport was verified for three Kondo peaks taken on the same Kondo ridge but with different T_K. To do so we have considered the raw data of the conductance as a function of the applied bias voltage $G = f(V_S)$. From these curves we substract the background conductance G_C due to Coulomb effect. Note that this procedure is approximate since we should substract the real background curve and not a constant. We then renormalize it to G_0 and finally plot $(G(V_S) - G_C)/G_0$ *vs* the reduced voltage eV_S/k_BT_K as shown in figure 6.4b. T_K was extracted from the half wifth at half maximum (HWHM) of the different peaks. The three curves taken for different Kondo temperature approximately collapse in this representation. This supports the universal scaling of the out-of-equilibrium Kondo effect. For relatively small bias voltages, an empirical formula does exist [137]. It reads :

$$G(T, V_S) = G_C + G_{EK}(T, 0)(1 - \frac{c_T\alpha}{1 + c_T(\frac{\gamma}{\alpha} - 1)(\frac{T}{T_K})^2}(\frac{eV}{k_BT_K})^2) \tag{6.3}$$

with $G_{EK}(T, 0) = G_0/(1 + (T/T'_K)^2)^s$ and $T'_K = T_K/\sqrt{2^{1/s} - 1}$. In the specific case of the spin 1/2 Kondo effect, the different constants are $c_T = 5.49$, $\gamma = 0.5$, $\alpha = 0.11$ and $s = 0.22$. At $T = 20mK$, the temperature of the fridge, $G_{EK}(T, 0) \approx G_0$. The inset of figure 6.4b is a zoom in of the reduced curves together with the theoretical predictions. The agreement is reasonably good. Discrepancies are likely due to the data processing which does not consider the real background conductance.

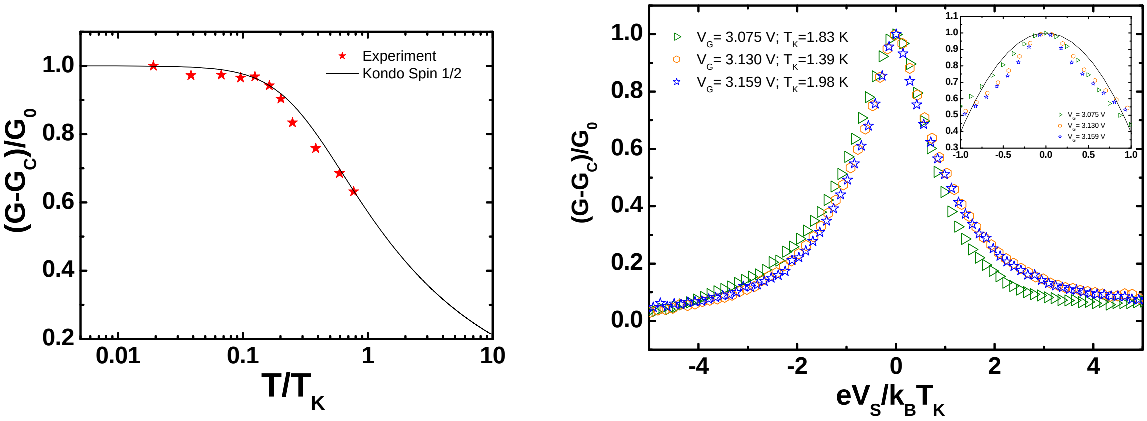

Figure 6.4: (a) Reduced zero bias peak amplitude $(G-G_C)/G_0$ *vs* the reduced temperature T/T_K. G_C is the Coulomb background conductance at zero bias. $G_0 = G_{Max} - G_C$ with G_{Max} the saturated amplitude of the peak at low temperature. Full line is the empirical formula $G = G_C + G_0/(1+(2^{1/s-1}(T/T_K)^2))^s$ drawn for $T_K = 1.4K$ and $s = 0.22$ according to a spin 1/2 Kondo effect. (b) Reduced zero bias peaks $(G-G_C)/G_0$ *vs* the reduced voltage bias eV_S/k_BT_K. The three curves taken for different Kondo temperature approximately collapse once reduced supporting the universal scaling of the out-of-equilibrium Kondo effect. Inset: Comparison with theoretical expectations 6.3 of the low bias behaviour of the reduced Kondo peaks.

6.2.4 Conclusion

In this section, we have studied the stability diagram of the carbon nanotube quantum dot in the Kondo regime. An analysis of the magnetic field, temperature and voltage dependence of the Kondo effect was performed. Altogether, these data are consistent with a spin 1/2 Kondo effect. At half filling (center of the Kondo ridge), the Kondo temperature is $T_K = 1.4K$, $\Gamma = 0.51$meV and the barrier asymmetry is $a = 0.67$.

6.3 Source/detector coupling

A very important aspect of the present detection scheme is the source/detector coupling calibration. In previous samples, where the source was a Josephson junction, the ac Josephson effect was used to calibrate the coupling. Hereafter it is no more possible. One therefore needs to make several assumptions to infer the coupling factor from the quality factor of the cavity. In particular, we assume that the coupling circuit is the same from one sample to the other provided that they are fabricated in the same way. This section explains how one can extract the source/detector coupling.

6.3.1 Quality factor of the resonator

To characterize the superconducting resonant circuit which couples the detector junction to the CNT we measure the subgap $I(V)$ characteristic of the junction which depends on the impedance of its electromagnetic environment [11] (see section 5.2.3). It exhibits resonances that are related to the real part of the impedance $Z(\nu)$ seen by the junction :

$$I(V) = Re[Z(2eV/h)]\, I_C^2/2V \tag{6.4}$$

with $I_C = \pi\Delta/(2eR_N)$ the critical current [113] and $R_N = 28.6k\Omega$ the normal state resistance of the junction. Figure 6.5 shows the $I(V)$ characteristic of the junction in the subgap region for I_C maximized with magnetic flux. Using Eq. 6.4 the subgap resonances allow to extract the real part of the impedance seen by the junction (Fig. 6.5). It exhibits large peaks at frequencies $\nu_1 = 29.5$ and $\nu_3 = 78$GHz.

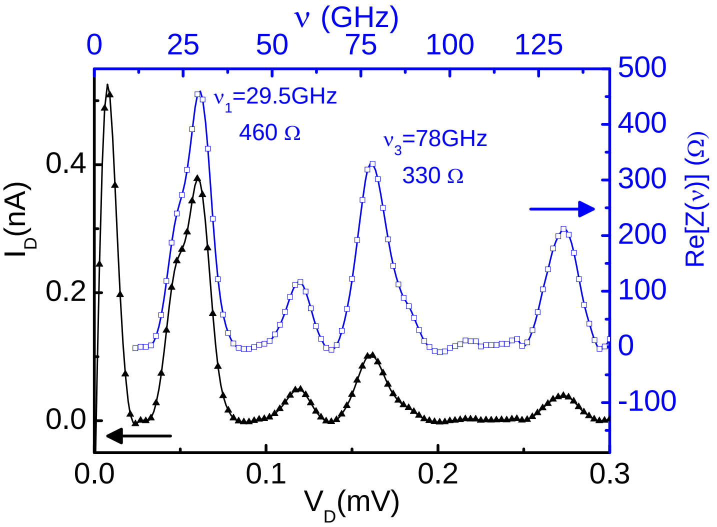

Figure 6.5: Bottom curve: $I(V)$ of the detector in the subgap region. Upper curve: The real part of the impedance seen by the detector extracted from I(V) curve. It exhibits several resonances.

6.3.2 Determination of the coupling and self consistency

Using the values of the height and the width of the resonance peaks of $Re[Z(\nu)]$ one can infer the value of the coupling between the junction and the CNT [130,138]. Knowing this coupling we translate a photo-assisted tunneling (PAT) quasiparticle current measurement, below the superconducting gap of the junction, into a current emission noise measurement for the resonance frequencies of the coupling circuit. The relation between the PAT current and the current noise at a resonance frequency ν_n is given by

$$I_{PAT}(V_D) = \sum_n K_n S_I(-\nu_n) \tag{6.5}$$

with

$$K_n = (\frac{e}{h\nu_n})^2 |Z_t(\nu_n)|^2 \delta\nu_n I_{QP}(V_D + h\nu_n/e). \tag{6.6}$$

In this formula ν_n is the resonance frequency, $Z_t(\nu_n)$ the transimpedance, $\delta\nu_n = 1.06\nu_n/Q_n$ with Q_n the quality factor of the resonant peak of $|Z_t(\nu_n)|^2$ as introduced in previous section 5.4. Finally $I_{QP}(V_D + h\nu_n/e)$ is the I(V) characteristic of the detector. It is proportional to the superconducting gap Δ and invertedly proportional to the normal state resistance R_N.

Determination of the coupling factor K

From now on we infer the coupling values K'_n of the nanotube sample from K_n the coupling values of the reference sample. The sample parameters of the reference sample presented in previous chapter are shown in table 6.1. From them, we extract reference values $K_1 = 6969Hz/pA$ and $K_3 = 1759Hz/pA$.

Going from one sample to the other, the real I(V) characteristic of the detector is measured. From it one extracts the new values, designed by a coma, of the superconducting gap $2\Delta'$ and the normal state resistance R'_N (related to I'_{QP}). According to $Re[Z]'$ determination (section 6.3.1), one also has resonant frequencies ν'_1 and ν'_3. Unfortunately, it is not possible to directly measure the new value of the product $A'_n = |Z'_t(\nu_n)|^2\delta\nu'_n$ corresponding to the area below the curve of $|Z'_t(\nu_n)|^2$. Hereafter we assume than this product can be infered from the $Re[Z]'$ measurement. To do so, we calculate the area α'_n which is below the curve of $Re[Z]'$ for each resonant peak and assume that one can express A'_n as $A'_n = (\frac{\alpha'_n}{\alpha_n})^2.A_n$. The different sample parameters are shown in table 6.1.

Reference	$R_N(k\Omega)$	$2\Delta(\mu eV)$	ν_1(GHz)	ν_3(GHz)	α_1 (Ω.GHz)	α_3 (Ω.GHz)
	18.7	520	28.4	80.2	4882	4941
Nanotube	$R'_N(k\Omega)$	$2\Delta'(\mu eV)$	ν'_1(GHz)	ν'_3(GHz)	α'_1 (Ω.GHz)	α'_3 (Ω.GHz)
	19.3	365	29.3	78	4240	3360

Table 6.1: Experimental parameters extracted for the reference (presented in previous chapter) and the nanotube sample.

Considering all the presented elements, K'_n compares to K_n as:

$$K'_n = K_n \; . \left(\frac{\alpha'_n}{\alpha_n}\right)^2 . \left(\frac{R_N}{R'_N}\right) . \left(\frac{2\Delta'_n}{2\Delta_n}\right) . \left(\frac{\nu_n}{\nu'_n}\right)^2 . \tag{6.7}$$

The numerical application gives $K'_1 = 3359Hz/pA$ and $K'_3 = 585Hz/pA$.

Self consistency

In order to verify the self consistency of the coupling extraction, we polarize the source junction at high bias in a region where a theoretical expression for noise is known. From the adjustment between the raw data $I_{PAT} = f(V_S)$ and the theoretical expression of noise

$S_I = f(V_S)$, we obtain K''_n factors ($I_{PAT} = K''.S_I$) $K''_1 = 3040 Hz/pA$ and $K''_3 = 650 Hz/pA$. By comparing to K'_1 and K'_3, we see a difference of the order of only 10%.

Comparison with fully calibrated sample

Comparison between K factors is done in table 6.2. It highlights a strong difference of coupling between the two samples. At ν_1 and ν_3 the coupling is twice, respectively three times smaller for the nanotube sample than for the calibrated circuit shown in previous chapter. This is partially explained by the presence of the additional gate, the higher resistance of the detector and the smaller value of the Pd resistance at the end of line. Further studies are necessary to improve the nanotube/detector coupling.

Reference coupling	K_1 (Hz/pA)	K_3 (Hz/pA)
	6969	1759
Infered nanotube coupling	K'_1 (Hz/pA)	K'_3 (Hz/pA)
	3359	585
Nanotube coupling from theoretical adjustment	K''_1 (Hz/pA)	K''_3 (Hz/pA)
	3040	650

Table 6.2: Green (top): measured value of K factors for fully calibrated sample (previous chapter). Red (center): infered value of K factors for the nanotube sample as explained in section 6.3.2. Blue (bottom): deduced value of K factors for the nanotube sample from an adjustment to theoretical predictions in specific conditions as explained in section 6.3.2

6.4 Quantum noise measurement

To measure the quantum noise of the CNT we modulate the bias voltage V_S and monitor the modulated part of the PAT current through the detector for a given bias voltage V_D of the detector. V_D selects the frequency range of the measurement. We have thus access to the derivative of the PAT current versus CNT bias voltage dI_{PAT}/dV_S at a given frequency. Using the previously estimated coupling coefficients K'_n we translate this quantity into the derivative of the current noise S_I at one of the resonance frequency versus V_S, dS_I/dV_S. This quantity is plotted in the center of the Kondo ridge, *i.e.* $\epsilon = 0$ at two frequencies (Figure 6.6a and b)[1]. For each frequency the data exhibits a region where $dS_I/dV_S = 0$ close to $V_S = 0$. This corresponds to $|eV_S| < h\nu$, where the system does not have enough energy to emit noise at frequency $h\nu$. This zero noise region is a strong evidence that we are indeed only sensitive to the emission noise of the tube. For $|eV_S| > h\nu$ the system emits noise which may have signature of the Kondo physics. For the first resonance frequency $\nu_1 = 29.5$GHz, with $h\nu_1 \approx k_B T_K$, the measured derivative of the noise shows a singularity

---

[1] In this analysis, we will not consider gate voltages away from half filling. The reason is that the theory used to fit the experimental data only holds at half filling. For a map of noise the reader should refer in section 6.6.

for bias voltage close to the measured frequency. At higher bias voltage dS_I/dV_S is much smoother. At higher frequency $h\nu_3 \approx 2.7 k_B T_K$ the previous singularity is absent and we measure only a practically flat behavior of dS_I/dV_S versus V_S.

6.5 Theoretical interpretation

The high frequency noise of quantum dots in the Kondo regime has been studied theoretically at equilibrium using the numerical renormalization group technique [139]. Non-equilibrium results for the the finite-frequency noise is theoretically much more demanding. They were obtained only for peculiar values of parameters (strongly anisotropic exchange couplings) of the Kondo problem using bosonization methods [140], and by using non-equilibrium real time renormalization group approaches [4, 141]. The latter approaches assume $h\nu, eV_S \gg k_B T_K^{\mathrm{RG}}$, with T_K^{RG} the Kondo temperature defined from the renormalization group. In particular, for frequencies that are large compared to the RG Kondo temperature (i.e., $h\nu >> k_B T_K^{RG}$), a strong amount of emission noise is found in the noise spectral density at $eV = h\nu$ as shown in figure 6.7.

We have collaborate with the authors of paper [4] to reproduce our data using their theoretical findings. In the following, we present an interpretation using RG calculations and highlight the importance of decoherence.

6.5.1 A real-time functional renormalization group approach

Very importantly, T_K^{RG} differs from T_K (defined experimentally as the half width at half maximum of the differential conductance) by a numerical factor between 1 and 10 which has to be determined (see below). The real time functional renormalization group (FRG) approach developed in Ref. [4] is used to compute the non-equilibrium frequency-dependent noise and compare it to the experimental results. The Kondo Hamiltonian is given by :

$$H_K = \frac{1}{2} \sum_{\alpha,\beta=L,R} \sum_{\sigma,\sigma'} j_{\alpha\beta}\, \psi^{\dagger}_{\alpha\sigma}\, \mathbf{S} \cdot \boldsymbol{\sigma}_{\sigma\sigma'}\, \psi_{\beta\sigma'}\ . \tag{6.8}$$

Here the $j_{\alpha\beta}$ denote the Kondo couplings, α, β are indices for the left (L) and right (R) leads, $\boldsymbol{\sigma}$ stands for the three Pauli matrices, and the operator $\psi_{\alpha\sigma}$ destroys an electron of spin σ in lead $\alpha \in \{L, R\}$. The dimensionless exchange couplings $j_{\alpha\beta}$ are parametrized as $j_{\alpha\beta} = j\ v_\alpha v_\beta$, with the factors $\{v_L, v_R\} = \{\cos(\phi/2), \sin(\phi/2)\}$ accounting for the asymmetry of the quantum dot, $\cos(\phi) = a$, and related to the $T = 0$ conductance as $G(T = 0) = (2e^2/h)\ \sin^2(\phi)$.

The Kondo Hamiltonian assumes that charge fluctuations in the CNT quantum dot are frozen. Therefore, the theoretical results based on hamiltonian 6.8 can and shall be compared with experimental ones only for bias voltages $V_S \ll U/e$ and $\epsilon \approx 0$ (middle of the Kondo ridge). As a first step, to determine the ratio T_K^{RG}/T_K, the equilibrium conductance

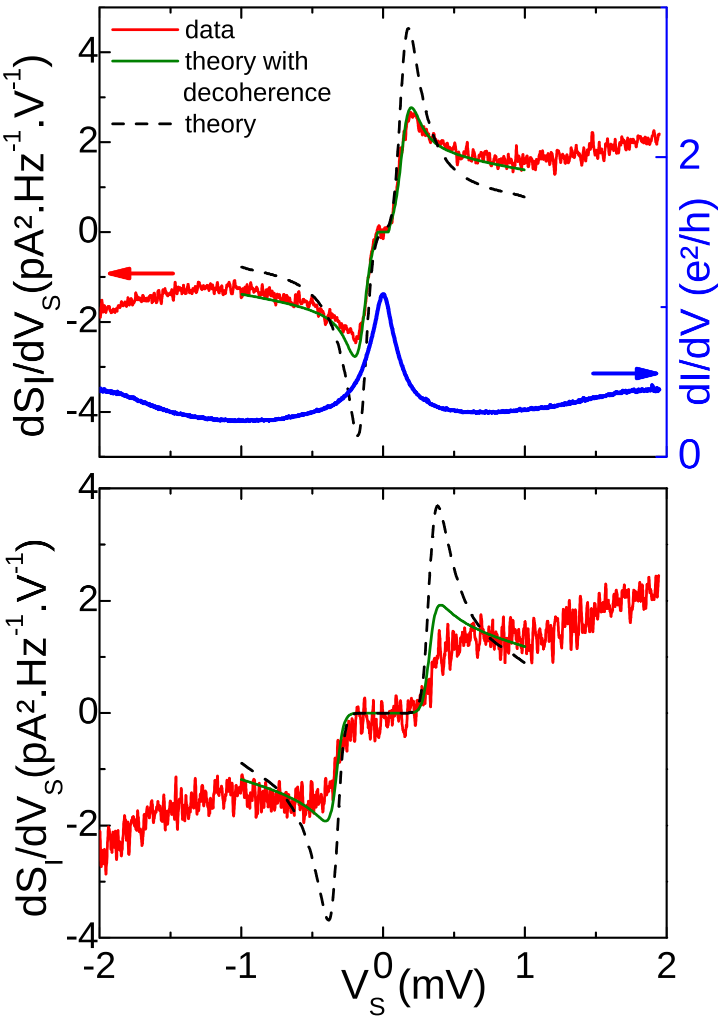

Figure 6.6: (a) Derivative of the current noise and differential conductance of the CNT versus V_S in the center of the Kondo ridge. Left axis : dS_I/dV_S at 29.5GHz as a function of bias voltage V_S. The green line correspond to the calculated dS_I/dV_S based on FRG calculations with additional voltage dependent decoherence (see text). It fits reasonably well the experimental data. Right axis : Differential conductance dI/dV of the CNT in unit of e^2/h. (b) Same data at 78GHz. The green line corresponds to the calculated dS_I/dV_S based on FRG calculations with the same voltage dependent decoherence rate.

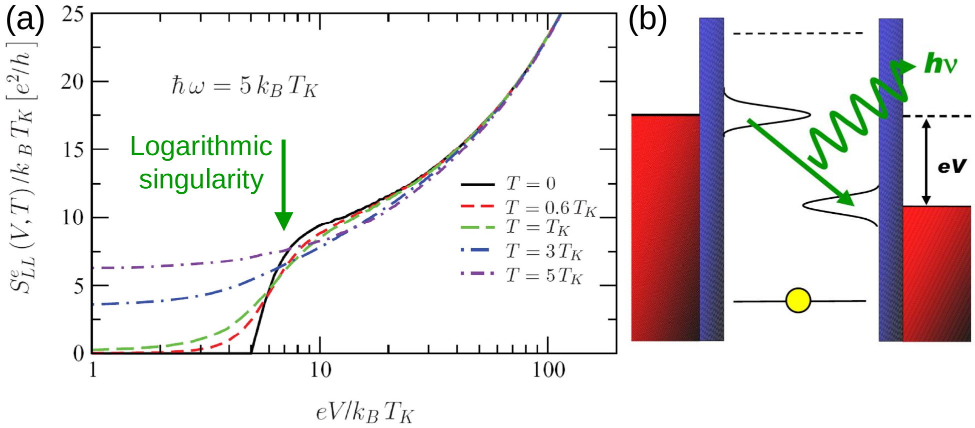

Figure 6.7: (a) Taken from [4]. Voltage and temperature dependence of the emission noise as computed through FRG at $h\nu = 5k_BT_K$. (b) The logarithmic singularity in the noise spectral density at $eV = h\nu = 5k_BT_K$ is due to the resonances in the density of state of the dot at Fermi energies of the leads.

is computed using numerical renormalization group methods [2] than we have compared to experimental data. This enabled us to establish that $T_K \sim 3.7\ T_K^{\mathrm{RG}}$. Therefore, the condition $h\nu \gg k_BT_K^{\mathrm{RG}}$ for the FRG approach to apply is certainly met for the frequency ν_3, and still reasonably satisfied for ν_1.

Within the Kondo model, one can express the Fourier transform of the emission noise S_I as:

$$S_I(V_S,\nu) = \frac{e^2}{h}\,T_K^{\mathrm{RG}}\ s\left(\frac{eV_S}{k_BT_K^{\mathrm{RG}}},\frac{h\nu}{k_BT_K^{\mathrm{RG}}},\frac{T}{T_K^{\mathrm{RG}}},A\right), \tag{6.9}$$

where s is a complicated dimensionless function, which is calculated by solving numerically the functional renormalization group equation. Since the measurement temperature satisfies $T \ll T_K$, T is assumed to be zero in the calculations (it was checked that inclusion of a finite but small temperature does not affect the results). Note that no fitting parameter has been included at this level, since the asymmetry parameter a and $T_K^{\mathrm{RG}} \approx 0.38$ K were directly extracted from the experimental data. The dashed lines in Fig. 6.6a and Fig. 6.6b show the calculated dS_I/dV_S curves for frequencies $\nu_1 = 29.5$GHz and $\nu_3 = 78$GHz, respectively. The computed curves are only shown in the bias range $|V_S| < 1$ mV, where the Kondo Hamiltonian in Eq. 6.8 is appropriate to describe the physics of the CNT quantum dot. For both frequencies, the theoretical curves exhibit sharp singularities at $eV_S = h\nu$, much more pronounced than the experimental ones. This especially holds for the resonance frequency, $\nu_3 = 78$GHz, where the resonance is almost completely absent experimentally. The singularity at the threshold, $eV_S \approx h\nu$ is related to the existence of two Kondo resonances associated with the Fermi levels of the two contacts. Inelastic transitions between them lead to an increase of the slope dS_I/dV_S of the noise for frequencies corresponding

---

[2] For these calculations, they have used the open access Budapest DM-NRG code, http://neumann.phy.bme.hu/ dmnrg/.

to the energy separation between them, $h\nu \approx eV_S$ (Fig. 6.8).

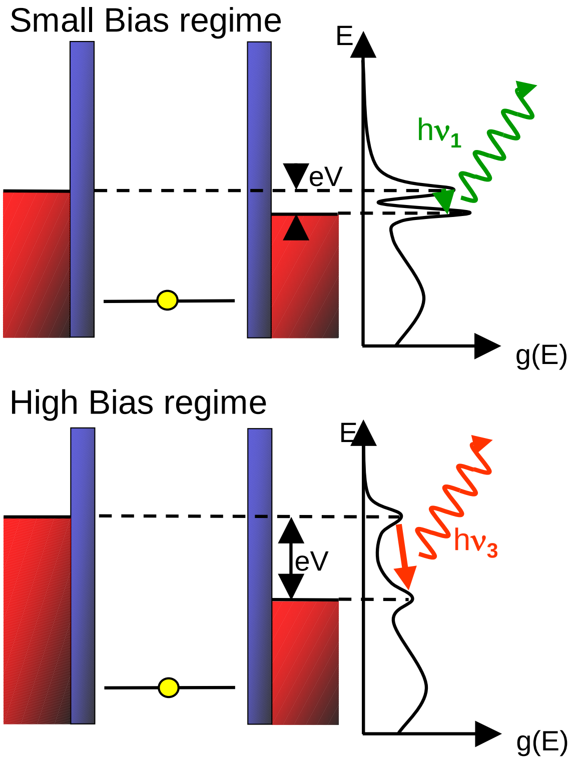

Figure 6.8: Schematic drawing of a quantum dot in the out-of-equilibrium Kondo regime together with the density of states for two distinct bias voltages. When the quantum dot is voltage biased, the Kondo resonance splits into two distinct resonances separated by the applied bias voltage. This leads to an increase of the emission noise at frequency $eV_S = h\nu$. The amplitude of the resonance peaks, and thus the emission noise at $eV_S = h\nu$, can be reduced due to decoherence effects induced by the applied bias voltage.

To compute the dashed curves in Fig. 6.6, an intrinsic spin decoherence time, τ_S, induced by the large bias was included and calculated self-consistently in the FRG approach [14]. The decoherence of the Kondo effect induced by a large d.c. voltage bias is a well-known feature which has indeed been measured [12, 13], and has been predicted to lead to a strong reduction of the Kondo resonance due to inelastic processes [14–16]. Since the singularity in the noise is associated with the transition between the two Kondo resonances pinned at the Fermi levels of the contacts, this singularity is also strongly suppressed by inelastic processes. However, as shown in Fig. 6.6, the computed intrinsic decoherence time is insufficient to explain the experimentally observed suppression of the peak in dS_I/dV_S.

6.5.2 Additional decoherence

In order to improve the model we decided to incorporate a voltage-dependent external decoherence rate in the calculations, $\tau_S^{-1}(V_S)$. The consistency of this approach can be checked against the experiments: a single choice of $\tau_S^{-1}(V_S)$ must simultaneously reproduce the voltage dependence of the differential conductance through the dot $dI/dV_S(V_S)$, and those of the $\nu_1 = 29.5$ GHz and $\nu_1 = 78$ GHz noise spectra, $dS_I/dV_S(V_S)$. Furthermore, τ_S^{-1} should be suppressed for $V_S < T_K^{\mathrm{RG}}$. Finally, it was found that a bias-dependent decoherence rate of the form

$$h/\tau_S \approx \alpha\, k_B T_K^{\mathrm{RG}} \mathrm{atan}(\frac{\beta e V_S}{k_B T_K^{\mathrm{RG}}}), \tag{6.10}$$

with $\alpha = 14$ and $\beta = 0.15$ satisfied all criteria above (see Fig.6.9). The continuous lines in Fig. 6.6 show the $dS_I/dV_S(V_S, \nu)$ curves computed with this form of h/τ_S, and fit fairly well the experimental data for both resonator frequencies.

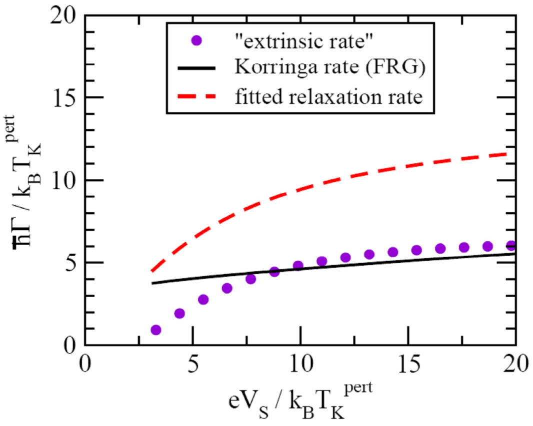

Figure 6.9: Voltage dependence of the fitted and intrinsic relaxation rates (T_K^{pert} is T_K^{RG}), and their difference, termed as extrinsic spin relaxation rate in the voltage range, $V_S \geq 0.1$ mV. The intrinsic rate was calculated by FRG, while the form and overall magnitude of the extrinsic rate was inferred from the differential conductance data. The reason why the intrinsic rate increases at low bias is due to the fact that theoretical predictions do not apply in this range.

6.5.3 Consistency with conductance

As a final consistency check, we also computed the differential conductance through the dot (taking into account the above form of τ_S^{-1}) and compared it to the measured dI/dV_S curves. A very good agreement is found without any other adjustable parameter in the voltage-range $V_S > 0.1mV$, where the FRG approach is appropriate (Fig. 6.10).

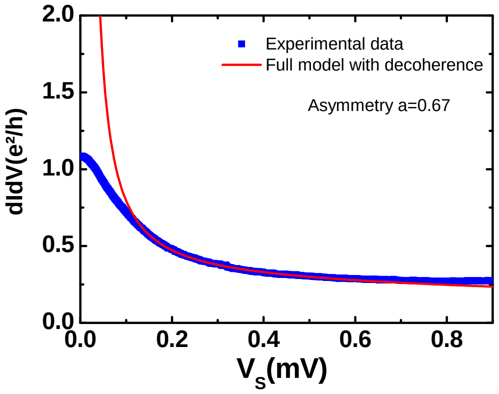

Figure 6.10: Experimental and theoretical differential conductance of the CNT versus V_S in the center of the Kondo ridge. The model fits reasonably well the high bias behaviour of the conductance. At low bias the model does not hold.

6.5.4 Conclusion

From the theoretical fits we infer that the experimentally observed noise spectra and differential conductance can be understood in terms of a decoherence rate, which is about a factor of ~ 2 larger than the theoretically computed intrinsic rate. One possibility for this discrepancy is that the experimentally observed decoherence is intrinsic, and FRG - which is a perturbative approach - underestimates the spin relaxation rate in this regime (which is indeed almost out of the range of perturbation theory). Another possibility is that the experimental set-up leads to additional decoherence. In fact, the emission current noise is measured by coupling the CNT quantum dot to a quantum resonator, which transfers photons to the superconducting detector. Since the coupling between the nanotube and the resonator is rather strong, one may speculate that the feedback of the detector and the resonator on the quantum dot may be responsible for the observed large decoherence.

6.6 Finite frequency Fano like factor

The experiment also allows to draw a complete map of the noise in the region of the Kondo ridge. To compare the derivative of the noise to the expected theoretical value we have defined the quantity

$$F(V) = \frac{dS_I/dV_S}{e\, dI/dV_S(V_S - h\nu/e)}, \tag{6.11}$$

i.e. the ratio of the derivative of the noise with the differential conductance shifted in voltage by an amount corresponding to the measured frequency. For a linear system or for a non linear system with energy independent transmission at low temperature this quantity is equal to the Fano factor. We have plotted $F(V)$ for $\nu_1 = 29.5$GHz (Fig. 6.11a) and $\nu_3 = 78$GHz (Fig. 6.11b). For $|eV_S| < h\nu$, where the emission noise is zero, $F(V)$ is arbitrarily fixed to zero. For both frequencies the noise is found to be sub-poissonian, with $F(V)$ close to one in the poorly conducting regions and a strong decrease of $F(V)$ along the conducting regions. This is consistent qualitatively with the reduction of the Fano factor for a conducting channels of transmission close to one.

However, this contrasts with low frequency noise where it has been predicted [125] and demonstrated experimentally [97, 127, 128] than in certain limits Fano factors could be higher than 1. However, these results were obtained in the quasi-unitary limit and at small bias where no decoherence is expected.

6.7 Conclusion

In conclusion we have measured for the first time the high frequency current fluctuations of a carbon nanotube quantum dot in the Kondo regime by coupling it to a quantum detector *via* a superconducting resonant circuit. We find a high frequency emission noise which is strongly frequency dependent and exhibits a strong resonance when the voltage bias is of the order of the frequency at which it is measured. FRG calculations including a strong decoherence rate allowed to quantitatively reproduce the experimental findings. The noise is found to be subpoissonian close to the Kondo ridge.

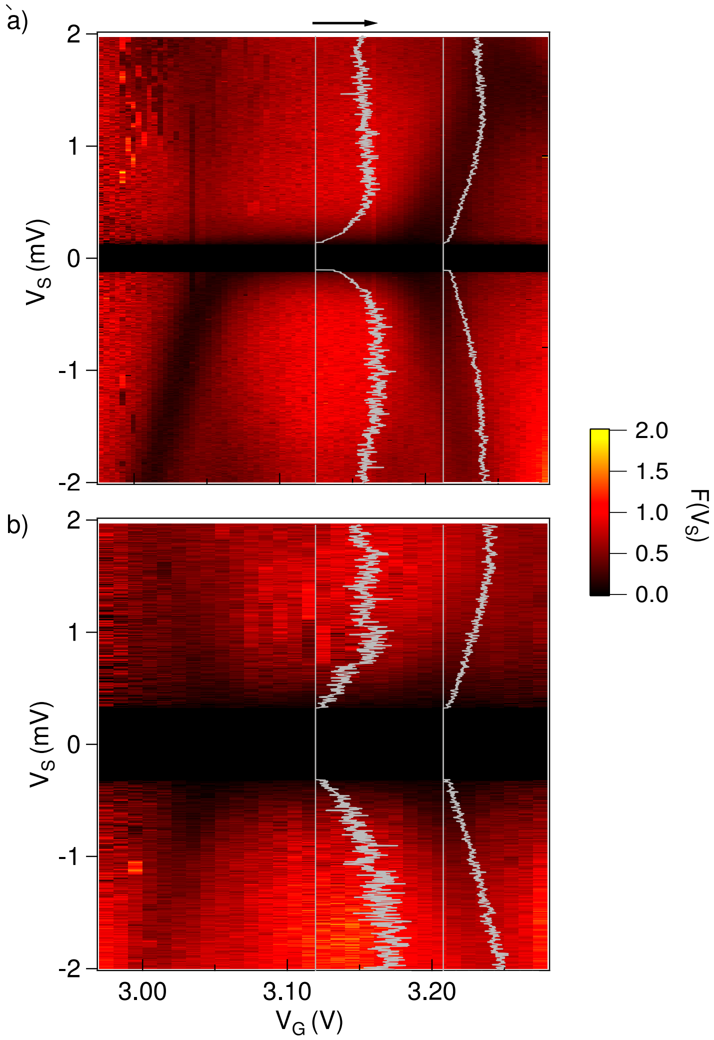

Figure 6.11: Fano like factor $F(V)$ as a function of the bias voltage V_S and the gate voltage V_G at $\nu_1 = 29.5$GHz (a) and $\nu_3 = 78$GHz (b). F is arbitrarily fixed to zero in the interval $e|V_S| < h\nu$. The gray curves on top of the colorplot corresponds to the bias voltage dependence of the Fano like factor at $V_G = 3.12$V and $V_G = 3.21$V. The black arrow indicates a value of the Fano factor equal to 1. When the conductance is low, the Fano factor is close to one while it is reduced in the highly conducting region.

Conclusions and perspectives

Conclusions

In this part we have seen that in the quantum regime, noise can be interpreted in terms of photons that are either emitted or absorbed by the noise source. These processes are not equivalent and lead to a strong asymmetry in the noise spectrum. In order to measure quantum noise it is necessary to use a quantum detector able to measure independently the emission and absorption noise.

To do so, we chose to use a superconducting tunnel junction as a quantum noise detector and introduced the formalism in which detection principle is understood. It is based on inelastic tunneling of quasiparticles which is enhanced in presence of a noisy environment. The theoretical analysis of such detector is based on $P(E)$ theory which quantifies tunneling rates modifications induced by the noisy environment.

Then came the experiments which allowed us to obtain three important results:

- **Result 1:** We demonstrate that by coupling the SIS junction to a resonant circuit it is possible to quantitatively measure the emission and absorption noise of the resonant circuit at *equilibrium*. At low temperature the circuit exhibits only absorption noise related to the zero point fluctuations of the electromagnetic field. At higher temperature emission noise is also present.

- **Result 2:** The design of the resonant circuit allowed us to couple another device to the detector and measure quantitatively its *out-of-equilibrium* emission noise and admittance components at the resonance frequencies of the resonant circuit. In the case of a Josephson junction biased above the superconducting gap it was possible to probe quantitatively the spectral density of quasiparticles current noise at 28.4GHz and 80.2GHz. Singularities in the finite frequency admittance components measurements have also been measured.

- **Result 3:** We have measured for the first time the high frequency current fluctuations of a carbon nanotube quantum dot in the Kondo regime. We find a high frequency emission noise which is strongly frequency dependent and exhibits a strong resonance when the voltage bias is of the order of the frequency at which it is measured. This singularity is related to the existence of two Kondo resonances pinned at the Fermi levels of the two contacts. Inelastic transitions between them lead to an increase of the slope of the noise for frequencies corresponding to the energy separation between them, $h\nu \approx eV_S$. FRG calculations including a strong decoherence rate allowed to quantitatively reproduce the experimental findings. The results indicate a large decoherence of the out of equilibrium Kondo effect. The noise is found to be subpoissonian close to the Kondo ridge.

Perspectives

The technique presented in this part is *a priori* applicable to any high impedance mesoscopic devices. In particular, it is possible for a carbon nanotube quantum dot to exhibit different conduction regimes such as strong Coulomb blockade or Fabry-Perot[3]. In the strong Coulomb blockade regime signature on noise of the charging energy should be visible [92]. In the Fabry-Pérot regime, signature of nanotube length and Luttinger liquid properties are expected by theory [142–144]. Note than this regime has already been studied in the low frequency regime [145].

Even more interesting is the case where superconducting contacts would replace the normal leads [4]. In this case, general questions arise such as: Can we see a signature on noise of the superconducting phase dynamics? How does this dynamic compete with the Kondo physics characterized by energy scale $k_B T_K$? Can we see modifications of the ac Josephson effect when the frequency $\nu = 2eV/h$ reach the frequency associated to the Kondo temperature $k_B T_K/h$? Is Andreev reflection a noisy process? ...

Replacing carbon nanotube by strong spin/orbit interactions materials such as InAs or InSb nanowires can also be interesting. In this case, noise may bear signatures of the spin/orbit coupling strength [146].

This emission noise measurement procedure using a SIS junction [9, 75] may also be a good candidate to observe signature of the existence of Majorana fermions [147, 148]. Indeed, the emission noise of such peculiar state of matter is predicted to emit noise in the superconducting state at $h\nu = eV$ instead of $h\nu = 2eV$ for classical Josephson junctions.

Finally, our technique is potentially able to experimentally prove the generalized out-of-equilibrium quantum fluctuation dissipation theorem proposed by Ref. [144]. A deeper analysis is however required to be able to measure the out-of-equilibrium absorption noise.

---

[3] Actually, further experiments not detailed in this thesis allowed us to measure the noise of the same carbon nanotube in a Coulomb blockade area exhibiting inelastic co-tunneling. The data analysis is still in progress.

[4] Note than we ran preliminary experiments going this way (not detailed in this thesis) using a superconducting single electron transistor ($s - SET$). The data analysis is still in progress.

Part II

Current-phase Relation of Hybrid Junctions

Introduction

When a normal conductor is connected to a superconductor it gets influenced by correlations induced by the superconductor, this is the proximity effect [17]. The mechanism responsible for this effect is the Andreev reflection [18] at the normal/superconductor interface (see chapter 7). In this process an electron from the normal metal is reflected backward into a hole creating a Cooper pair in the superconductor. This phenomena is the topic of a long standing research activity, particularly in mesoscopic physics. Indeed nowadays it is perfectly feasible to manipulate normal metals with submicron dimensions. In this case, it has been proven than zero resitance transport between two superconductors separated by a normal metal could occur provided than phase coherence is preserved along the normal metal. The supercurrent is therefore carried by phase dependent entangled electron/hole states (Andreev states) in the normal metal area. As a result, the proximity effect probe the quantum properties of the normal metal part. Measuring the current-phase relation (CPR) of such system is thus of primary interest to probe the normal metal properties (see [149] for example).

In the following we consider the case of hybrid junctions in which the normal metal is replaced by a quantum dot. In this case, the proximity effect is greatly modified by electronic interactions induced by the dot. In particular, it was demonstrated that if the transparency of the contacts is intermediate, the supercurrent depends on the number of electrons into the dot [12]. If the number of electrons is odd, and thus the dot carry a spin, the current phase relation is π shifted. Having a slightly higher transmission can also be interesting. In this case Kondo correlations with characteristic energy $k_B T_K$ may appear. The spin of the dot together with the spin of the conduction electrons form a spin singlet ground state that compete with the BCS singlet state of binding energy Δ of the superconductor in contact. The study of this competing regime is thus of great interest. Peculiar current/phase relations have been predicted and phase induced transitions between $'0'$ and $'\pi'$ states are expected. The strong anharmonicity of the CPR results from a transition between a spin singlet state (non-magnetic) and a doublet state (magnetic) which reveals the instability of the Kondo correlations. Measuring the current-phase relation would allow us to probe the stability of the Kondo correlations in the presence of superconducting reservoirs.

The work reported in this part of the thesis is divided in three chapters. First, we will provide an introduction to current-phase relation measurements (chapter 7). In this context, one explicitely presents the concept of Andreev bound states, comment on quantum dot specificities, highlights the experimental difficulties and propose a technique to measure it conveniently. Second, we show results of a test experiment of the proposed technique than we applied to a small Josephson junction (chapter 8). Third, we present the results obtained for a carbon nanotube quantum dot in the strong coupling regime (chapter 9).

Chapter 7

Introduction to current-phase relation measurement

In a BCS type superconductor cooled below its critical temperature, electrons with opposite spins form coherent pairs called Cooper pairs. It results in a macroscopic quantum state described by a wave function $|\Psi|e^{i\theta}$ with superconducting correlations extending over a length ξ named *superconducting coherence length*. Here $|\Psi|$ is the amplitude of the wave function and θ the superconducting phase. The condensate is characterised by a zero electrical resistance. The prediction that a dissipationless current, the supercurrent, should flow between two superconductors separated by a thin insulator barrier was made since 1962 by Josephson [150]. In this case, the superconducting wave functions of the two contacts overlap allowing a tunneling of Cooper pairs from one contact to the other when a finite superconducting phase difference exists between the two superconductors. Since then many works have extended the validity of this prediction to other kinds of weak links such as narrow constrictions of the superconductor thin film (ScS) or Superconducting/Normal metal/Superconducting junctions (SNS) [20,112,113]. The supercurrent varies periodically with the macroscopic phase difference $\Delta\theta$ of the wavefunctions of the two electrodes. The maximum of this supercurrent is called the critical current of the junction. The existence of this supercurrent relies on the formation of Andreev bound states in the normal part. It consists in discrete entangled electron/hole states in the weak link area [151]. This aspect is essential since it explains the observation of supercurrent flowing over lengths longer than the superconducting coherence length ξ. This will be developped in this chapter. In particular, we will address the case of the quantum dot as a weak link and motivate our interest in measuring the primary manifestation of the Andreev Bound States in such a device: the current phase relation.

Contents

7.1 Andreev Bound states

The formation of Andreev Bound States (ABS) relies on the Andreev reflection process at a Normal metal/Superconductor interface [18, 152–159].

7.1.1 Andreev Reflection

Let us consider a quasiparticle in a normal metal of energy $E_e = E_F + \epsilon$ with $\epsilon < \Delta$, wavevector $k_e = k_F + q$ and phase ϕ_e reaching a perfect NS interface (see figure 7.1). Due to the superconducting gap in the density of states of the superconductor [17, 18], the probability for this particle to be reflected is one since no available states are present in the superconductor at energies below the gap ($t_{ee} = t_{eh} = 0$). In addition to this, conditions over the continuity of the wave function and its derivative at the N/S interface give that the incoming electron being reflected as an electron is not allowed ($r_{ee} = 0$). Finally it only leaves the possibility for the incoming particle to be reflected as a hole ($r_{eh} = 1$), this is the *Andreev reflection*. The reflected hole is characterized by energy $E_h = E_F - \epsilon$, wavevector $k_h = -k_F + q$ and phase $\phi_h = \phi_e + \theta - arccos(\epsilon/\Delta)$ with θ the phase of the superconductor. Conversely, the conjugate process reflects a hole as an electron. Note that the particular relation between k_h and k_e depends of the nature of the weak link. Nevertheless, the overall charge transfered into the superconductor during this process is twice the electronic charge *i.e.* the Cooper pair charge $2e$. The two electrons enter as evanescent waves in the superconductor and condense within the superconducting coherence length ξ.

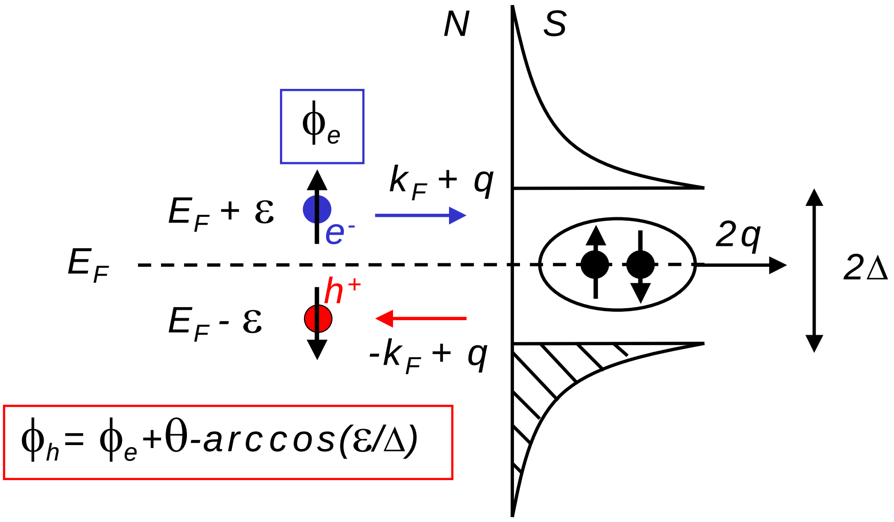

Figure 7.1: Andreev reflection process at a N/S interface. An incoming electron e with energy $E_e = E_F + \epsilon$, wavevector $k_F + q$ and phase ϕ_e is reflected backward into a hole with energy $E_h = E_F - \epsilon$, wavevector $-k_F + q$ and phase $\phi_h = \phi_e + \theta - arccos(\epsilon/\Delta)$ with θ the superconducting phase in the superconductor and Δ the superconducting energy gap.

7.1.2 Bound states

By adding a second SN interface, we form a SNS junction. The hole produced by the reflection at the first NS interface is reflected backward in an electron at the second interface, closing the cycle (see figure 7.2a). If the length of the normal part is small enough to insure coherence along the whole path, a Cooper pair is transferred coherently from one superconducting contact to the other, and a non-dissipative current flows through the junction. The combination of these processes gives rise to an infinite series of Andreev reflections. The resonance condition can be established by taking into account the amplitude of the individual Andreev reflection and the phase accumulated by electrons and holes propagating through the normal region and reads, in the ballistic case, with n the number of cycles:

$$\boxed{2n\pi = \theta_2 - \theta_1 + (k_e - k_h)L - 2arccos(\epsilon/\Delta)}. \tag{7.1}$$

The energy spectrum can then be deduced from equation [20]:

$$\boxed{\epsilon(\varphi) = \Delta cos\left[\frac{\varphi}{2} - \frac{k_F L}{2}\left(\frac{\epsilon(\varphi)}{E_F}\right) - n\pi\right]} \tag{7.2}$$

with $\varphi = \theta_2 - \theta_1$ the phase difference between the two superconductors.

This equation admits multiple solutions which correspond to bound states inside the superconducting gap (see figure 7.2b), called *Andreev Bound states* (ABS) or *Andreev - Kulik states* [18, 152]. To each conduction channel corresponds a set of two energy symmetric ABS. Their positions depend periodically of the phase difference $\varphi = \theta_2 - \theta_1$ between the superconducting leads. The experimental visualisation of individually resolved Andreev Bound state has been recently achieved in a single wall carbon nanotube [151]. In the specific case of long diffusive SNS junctions, the Andreev bound states spectrum describe a quasi-continuum of phase dependent levels with a small energy gap at zero phase difference, called the minigap [149, 160–162]. In the following, we will consider the short junction limit $L << \xi$ with $\xi = \frac{\pi v_F}{\Delta}$ in the ballistic case.

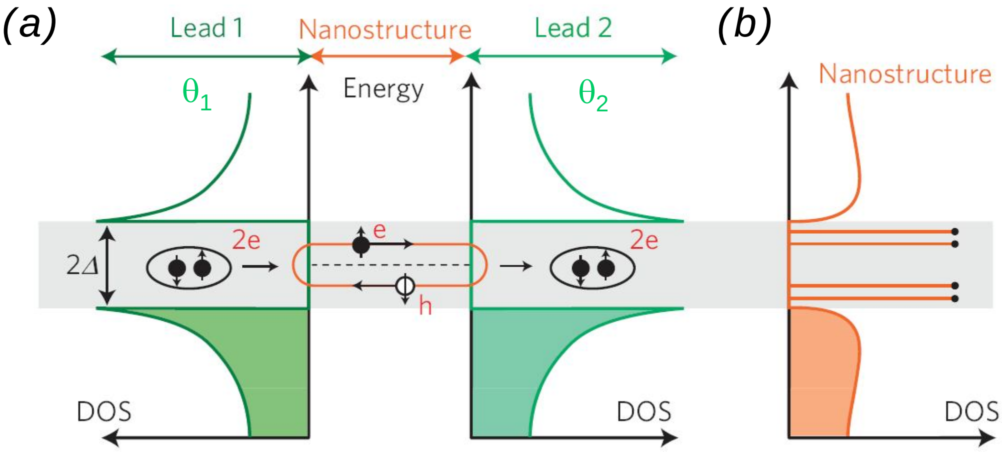

Figure 7.2: Taken from [151]. Principle of Andreev Bound States (ABS). (a) Schematic of an ABS in a coherent weak link placed between two superconducting leads. The density of states (DOS) in the superconductor is gapped around Fermi energy. Inside the superconducting gap (grey band) the Andreev reflection process (reflection of an electron (e) as a hole (h) - its time-reversed particle - and vice versa) leads to the formation of discrete resonant states of entangled eh pairs confined between the superconductors. (b) The local DOS in the nanostructure exhibits a set of resonances in the gap at the energies of the ABS. The energies of the ABS depend periodically on the superconducting phase difference $\varphi = \theta_2 - \theta_1$.

7.2 Current-phase relation

The primary manifestation of Andreev Bound states is the current phase relation $I(\varphi)$. Each one of the two Andreev bound states of a channel carries a supercurrent proportional to the derivative of the Andreev Bound states energy with respect to the phase φ:

$$\boxed{I(\varphi) = 2e/\hbar(d\epsilon/d\varphi).} \tag{7.3}$$

At low temperature, only the lower energy states are occupied and the current is easily computed. The current phase relation is easier to measure [19, 20, 163] than the Andreev spectrum. Hereafter we derive several simple limits addressing current-phase relation.

Single, short and perfectly transmitted channel Considering one channel with perfect N/S interfaces in the short junction limit ($L << \xi$) one has $\epsilon_{\pm} = \pm\Delta cos(\varphi/2)$. At zero temperature, the corresponding 2π periodic current phase relation reads in the phase interval $[-\pi, \pi]$ [155]:

$$I(\varphi) = \frac{e\Delta}{\hbar} sin(\varphi/2). \tag{7.4}$$

We have represented in figure 7.3a and b the corresponding energy spectrum and the associated current phase relation at zero temperature in the interval $[0, 2\pi]$. The crossing of the energy levels at $\varphi = \pi$ leads to a discontinuity in the current phase relation at $T = 0$.

N, short and perfectly transmitted channels One can sum the contributions of N independently transmitted channels yielding, at finite temperature, with $\epsilon(\varphi)$ the phase dependent energy of the ABS [156]:

$$I(\varphi) = \frac{Ne\Delta}{\hbar} sin\left(\varphi/2\right) tanh\left(\frac{\epsilon(\varphi)}{2k_BT}\right). \tag{7.5}$$

Single, short and transmission τ channel The case of an arbitrary normal transmission can also be analyzed [158, 159, 164]. For a single conduction channel of transmission τ, one obtains two bound states at energies

$$\epsilon_{\pm}(\varphi) = \pm\Delta\sqrt{1 - \tau sin^2(\varphi/2)}. \tag{7.6}$$

The current phase relation yields

$$I(\varphi) = \frac{e\tau\Delta}{2\hbar}\frac{sin\varphi}{\sqrt{1 - \tau sin^2(\varphi/2)}} tanh\left(\frac{\epsilon(\varphi)}{2k_BT}\right), \tag{7.7}$$

simplifying at very low temperature to:

$$\boxed{I(\varphi) = \frac{e\tau\Delta}{2\hbar}\frac{sin\varphi}{\sqrt{1 - \tau sin^2(\varphi/2)}}}. \tag{7.8}$$

One has represented in figure 7.3 the Andreev spectrum and the associated current phase relation at zero temperature for different values of the transmission τ. When τ is small, the current-phase relation is nearly harmonic while it becomes very anharmonic when τ increases.

N, short and normal transmission probability τ_i channels Considering N channels with a transmission probability τ_i at zero temperature, one obtains the generalized expression for the current phase relation :

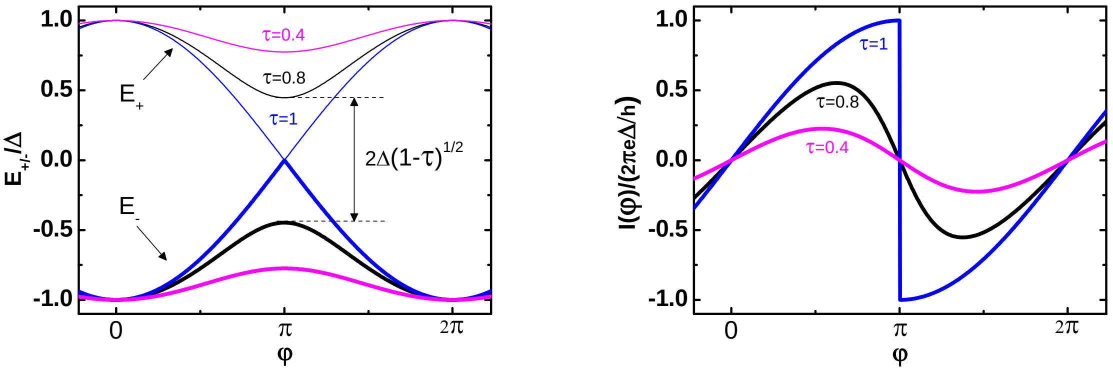

Figure 7.3: (a) Andreev bound states energy spectrum for a single channel with three different transmissions $\tau = 0.4, 0.8, 1$. (b) Current phase relations associated to the previous spectrum at zero temperature.

$$\boxed{I(\varphi) = \sum_{i=1}^{N} \frac{e\tau_i\Delta}{2\hbar} \frac{sin\varphi}{\sqrt{1-\tau_i sin^2(\varphi/2)}}.} \tag{7.9}$$

This relation has been confirmed by the quantronics group in Saclay (2007) on tunable atomic point contacts [19]. In particular they were able to quantatively relate the measured relation to the transmission probabilities τ_i determined by another type of measurement.

Case of the tunnel junction In the case of a tunnel junctio, the channels are very weakly transmitted and one has the relation

$$I(\varphi) = \sum_{i=1}^{N} \frac{e\tau_i\Delta}{2\hbar} sin\varphi = \frac{R_K}{R_N}\frac{e\Delta}{4\hbar} sin\varphi = I_0 sin\varphi, \tag{7.10}$$

with $R_K = h/e^2$ the quantum of resistance, R_N the normal state resistance of the junction and $I_0 = \frac{\pi}{2}\frac{\Delta}{eR_N}$ the Ambegaokar-Baratoff formula for the critical current of the junction [114].

7.3 Multiple Andreev Reflection (MAR)

When applying a finite voltage accross a SNS junction, the phase difference evolves continuously with time according to the Josephson relation, i.e. $\varphi(t) = \omega_0 t$, where $\omega_0 = 2eV/\hbar$ is the Josephson frequency. The response of the system cannot anymore be described by Eq. 7.7 in an adiabatic approximation. This is due to the fact that excitations of quasiparticles come into play and can give the main contribution. It turns out the total current through the junction contains all the harmonics of the Josephson frequency and can be written as [165, 166]

$$I(V,t) = \sum_n I_n(V)e^{in\omega_0 t} = I_0 + 2\sum_{m>0} Re[I_m(V)]cos(m\omega_0 t) - 2\sum_{m>0} Im[I_m(V)]sin(m\omega_0 t), \tag{7.11}$$

with $I_m(V)$ the ac current at frequency $m\omega_0/2\pi$ and applied voltage V.

The quantity which is more directly accessible in the experiment is the dc component I_0. This dc current highlights subgap structures (SGS) consisting in a series of more or less pronounced current bumps, located at $eV = 2\Delta/n$ with n an integer number, in the $I_0(V)$ characteristic. These SGS can be understood in terms of multiple Andreev reflections (MAR), as proposed by ref. [167]. The qualitative picture of these processes is shown in figure 7.4. In particular, figure 7.4 a highlights the single quasiparticle process only possible when $eV > 2\Delta$. In this case the transferred quasiparticles reach the available states on the right superconductor with a probability p_1 proportional to the contact transmission τ. It gives a contribution to the current-voltage relation as indicated schematically in Fig. 7.4 d. At lower bias voltages current is possible due to Andreev processes. The simplest Andreev process is depicted in Fig. 7.4 b, where two quasiparticles are transmitted with a probability p_2 proportional to the square of the normal transmission τ^2, creating a Cooper pair on the right side. These processes give a contribution to the IV with a threshold at $eV = \Delta$. At even lower biases higher order Andreev processes can give a contribution. In general, a n^{th} order process in which n quasiparticles are transmitted gives a contribution proportional to the n^{th} power of the transmission τ and with a threshold at $eV = 2\Delta/n$. For illustration we have shown in figure 7.5, some calculated [20, 166] IV characteristics of a single mode superconducting contact with different transparencies τ. The SGS are very pronounced at low transmission whereas they become smoother when the transmission is close to 1. At perfect transmission the structures completely disappear and the zero bias current reaches the value $e\Delta/\hbar$.

7.4 Hybrid Superconductor/Quantum dot Physics

In the following, we propose to detail the specific case of an hybrid superconductor/quantum dot device. This choice is motivated by experiments we aim to realize.

An hybrid superconductor/quantum dot device [31] is a structure comporting superconducting leads addressing a peculiar non superconducting area : the quantum dot. The quantum dot can be seen as an artificial atom with confined electronic states in which the number of electrons can be changed down to unity. The three characteristics energy scales which governs the physics of the system are the width of the levels Γ (related to the barriers transparency), the pairing energy of Cooper pairs in the superconducting contacts Δ and the charging energy U to pay for adding an electron or a Cooper pair on the dot. In the limit of a spacing between successive energy levels in the quantum dot $\Delta\epsilon >> \Gamma, U, Delta$, only one level of the dot at energy ϵ_0 plays an important role (Anderson model approximation [136]). One can therefore distinguish three different regimes (see figure 7.6), depending on the relative values of the three energy scales [168–172]. When $\Gamma > \Delta, U$, the system is in

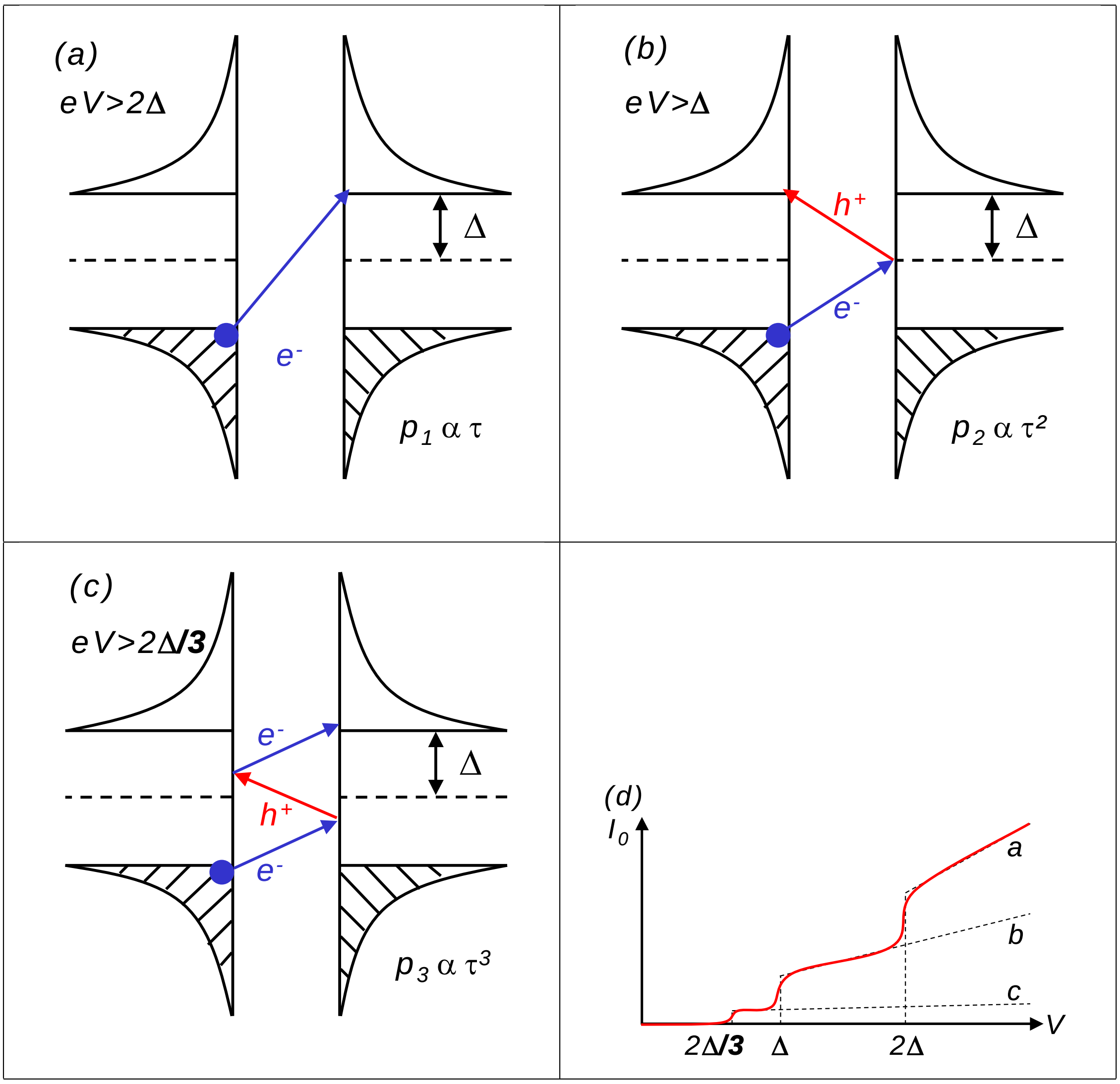

Figure 7.4: Schematic explanation of the subgap structure in a single mode superconducting atomic point contact. Figures (a), (b) and (c) respectively represents the multiple Andreev reflection processes responsible for current steps in the $I_0(V)$ characteristic at voltages $2\Delta/e$, Δ/e and $2\Delta/3e$ as represented in figure (d). (d) Handmade zero temperature $I_0(V)$ characteristic of a typical superconducting atomic point contact exhibiting three steps related to processes shown in figures (a), (b) and (c). The probability for the n^{th} order process to occur is proportional to τ^n with τ the transmission of the atomic point contact. The higher order is the process, the lower probability to occur, the lower the current step is.

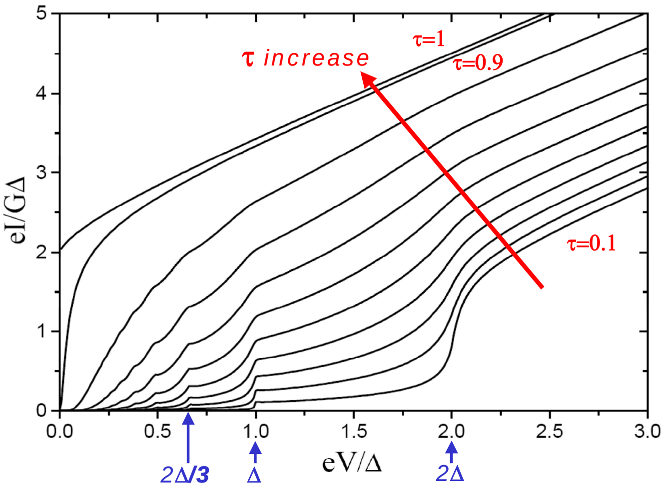

Figure 7.5: Taken from [20, 166]. Zero-temperature dc component of the current in a single mode superconducting contact. The values of the normal transmission increase from $\tau = 0.1$ in the lower curve by increments of 0.1. The upper two curves correspond to $\tau = 0.99$ and 1.

the *Strong coupling regime*. If $\Gamma << (\Delta, U)$, the system is in the *Weak coupling regime* and finally, if $\Gamma \approx \Delta \approx U$, the system is in the *Intermediate coupling regime*. The intermediate coupling limit reveals very complex phenomena which obviously are the more interesting to study as we will see in the following. Let us detail the first two limits.

7.4.1 Strong coupling regime

The strong coupling limit corresponds to a charging energy and a superconducting gap being negligible compared to the width of the energy levels. The quantum dot levels are strongly hybridised with the electronic wave functions of the electrodes and the dot behaves as a constriction. In this case, by aligning the Fermi energy of the leads with the energy level in the dot, one reaches resonant conditions [29]. Andreev Bound states forms and resonant Cooper pair tunneling occurs leading a high supercurrent. The supercurrent flowing through the dot is maximum when the dot level is aligned with the Fermi energy of the leads (ON state in figure 7.7) and zero when driven out-of-resonance (OFF state in figure 7.7). According to what has been shown previously concerning ABS, the sign and amplitude of this supercurrent can be tuned, varying the phase difference between left and right electrodes. The position and spectral width of the Andreev Bound states depend of the energy level position and width of the dot.

N.B. Note that if the condition $\Delta\epsilon >> \Gamma$ is not fulfilled, the ON/OFF states are no more visible. The quantum confinement is lifted and the system either acts as a quantum point contact (QPC) or a Fabry-perot interferometer if the system is one dimensional.

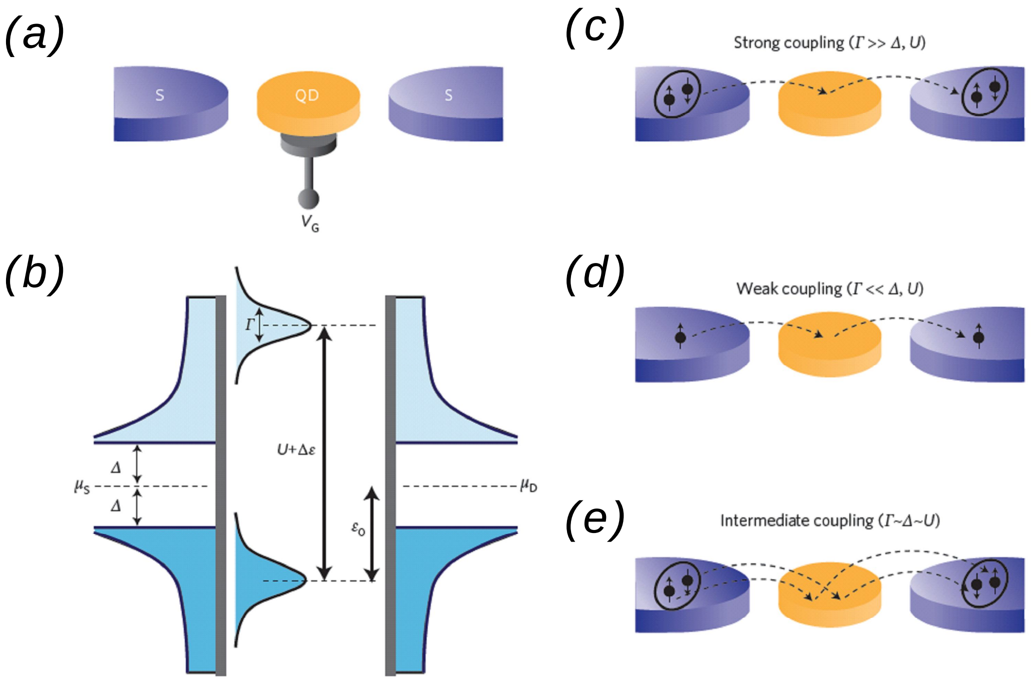

Figure 7.6: Taken from [31]. Characteristic energy scales and transport regimes. (a) Schematic device geometry with superconducting (S) source and drain electrodes attached to a quantum dot (QD) capacitively coupled to a gate electrode (V_G). (b) Energy diagram for the device shown in (a). Δ is the superconducting gap μ_S and μ_D are the Fermi energies of the source and drain electrodes; Γ is the width of the quantum dot energy levels; U is the charging energy associated to a single electron; $\Delta\epsilon$ is the spacing between successive energy levels in the quantum dot; and ϵ_0 is the difference between the energy of the highest occupied level (HOMO level) and the Fermi energy of the leads at zero bias ($\epsilon_F = \mu_S = \mu_D$). (c) Strong-coupling regime: Cooper pairs can tunnel from the source to the drain through a single orbital level on the quantum dot when it is aligned with the Fermi energies of the leads ($\epsilon_0 = 0$). The supercurrent is important. (d) Weak-coupling regime : single electrons can tunnel from filled quasiparticle states in the source to empty quasiparticle states in the drain. This requires a minimum applied bias voltage of $2\Delta/e$. (e) Intermediate-coupling regime: Cooper pairs can be transported from the source to the drain under certain conditions, with a phase shift (0 or π) depending on the occupation number of the quantum dot.

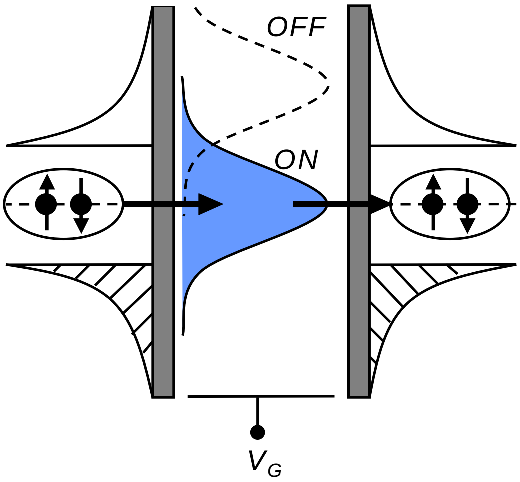

Figure 7.7: Adapted from [31]. Energy level diagram of the quantum dot in the strong coupling regime. Depending on gate voltage, the dot can be in a *ON* state (Fermi energy of the leads aligned with a quantum dot level) where supercurrent is maximal : resonant Cooper pair tunneling. When energy level of the dot is put away from Fermi energy, the system is in a *OFF* state and supercurrent is suppressed.

7.4.2 Weak coupling regime

In the weak coupling regime ($\Gamma << \Delta, U$) the barrier transparency is low and charging effects are strong. The Cooper pair tunneling is suppressed. Single electron transport is however possible. It happens under two conditions. 1- The applied bias voltage V is sufficient to overcome the superconducting gap ($eV > 2\Delta$). 2- A level of the dot is aligned with the occupied quasiparticle state in the left electrode and empty state in the right lead (achieved with a gate voltage compensating charging energy U and level spacing $\Delta\epsilon$) as shown in figure 7.8.

7.4.3 Intermediate coupling regime

In the intermediate coupling regime ($\Gamma \approx \Delta \approx U$), it is favorable for a Cooper pair to split while crossing the dot. The electrons will eventually recombine after if the time for a single electron to tunnel h/Γ is shorter than the coherence time associated to Cooper pairing h/Δ ($\Delta < \Gamma$). The way in which the charge transfer is performed is described by Andreev bound states in the dot area. These states are intimately related to the discrete electronic levels of the dot and its occupation number [66,151,171]. In particular, it was found that depending of the HOMO (Higher Occupied Molecular Orbital) level filling factor, a reversal of the current phase relation $I(\varphi)$ could occur [173–176]. This is explained in figure 7.9 where is presented the fourth order co-tunneling process responsible for Cooper pair transport through the dot. It illustrates that for a HOMO level fully occupied (N even, $S = 0$), the transfer of a Cooper pair is achieved without changing

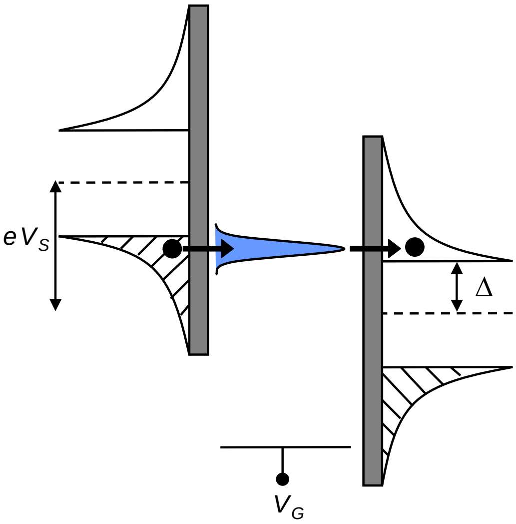

Figure 7.8: Adapted from [31]. Energy level diagram of a quantum dot in the weak coupling regime. Notice the width of the energy level in the dot which is much thinner than previously (strong coupling). The tunneling of Cooper pairs is suppressed. One needs to provide at least energy $eV = 2\Delta$ for the quasiparticles tunneling to take place.

the relative orientation of the Cooper pair spins. For a half occupied HOMO level (N odd, $S = 1/2$) instead, the spin ordering is reversed giving place to a π phase shift in the current phase relation. This kind of junction is called *$'\pi'$ junction* in opposition to the *$'0'$ junction* previously described (see figure 7.10). Let us notice than a $'\pi'$ junction supports a smaller supercurrent than a $'0'$ junction. Thanks to the high degree of tunability of the quantum dot one can induce transitions ($0/\pi$ transition) simply by changing the gate voltage. This has already lead to many experimental works [173,177–180]. The concept of π junction is quite general and was first proposed (and measured) for ferromagnetic weak links [175,181–183]. In addition to this interesting phenomena adds the competition with the Kondo effect previously described in this thesis.

7.4.4 Kondo screening and Cooper pairing competition

A very interesting topic is the competition/interplay between the Kondo effect and the Cooper pairing. The Kondo screening leads to the formation of a many-body spin singlet state accounting for the conduction electrons in the leads and the single spin 1/2 in the dot. On average, the quantum dot spin is like bound to one electron of the leads with a binding energy $k_B T_K$. In the presence of superconducting leads, the Kondo singlet state competes with the pairing energy Δ of the Cooper pairs. The resulting physics of the system is in first approximation given by the ratio T_K/Δ. (see figure 7.11 and reference [5]). Note that the contact asymmetry also plays a role as we will see later in this chapter.

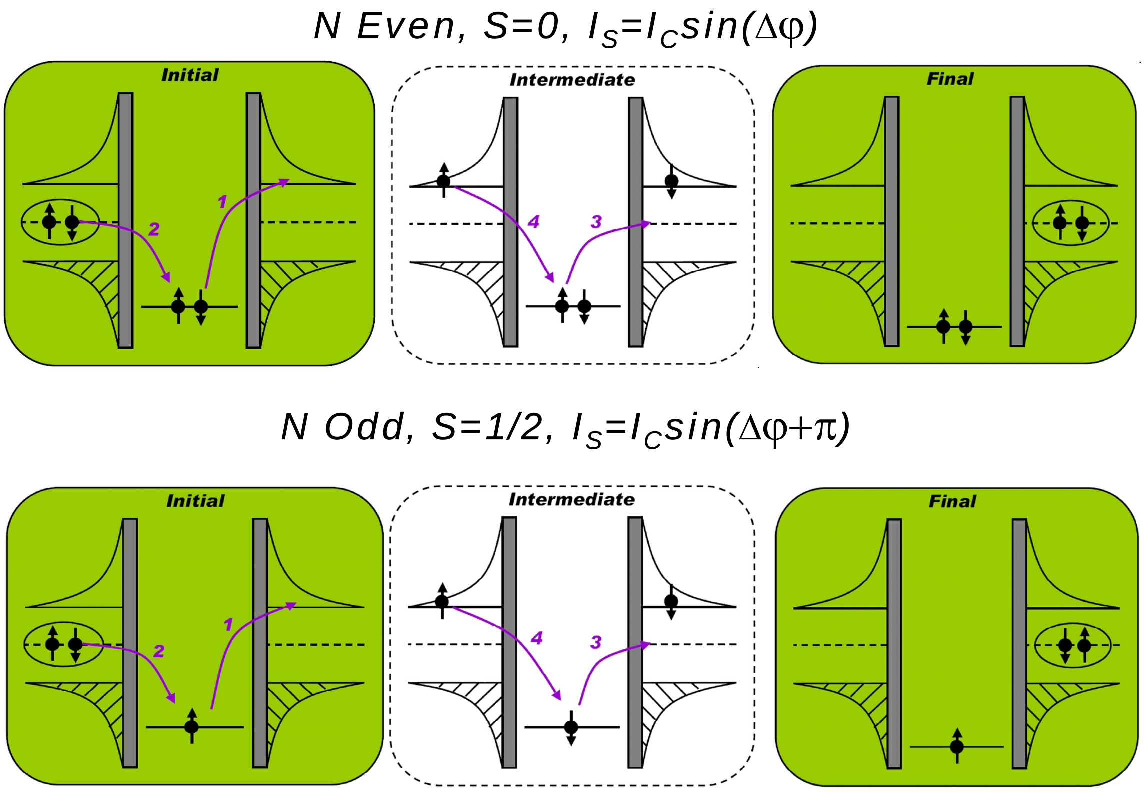

Figure 7.9: Adapted from [31]. Fourth order co-tunneling processes (arrows labelled 1,2,3 and 4) responsible for Cooper pair transport accross the dot in the intermediate coupling regime. When the number of electrons into the dot is even (fully occupied level, total spin $S = 0$), the order in which the spins of the Cooper pair are in the left lead is the same as in the right lead. The current phase relation is usual (increasing function near $\Delta\varphi = 0$): $I_S = I_C f(\Delta\varphi)$. Here, I_C is the amplitude of the current phase relation and $f(x)$ the periodic function adressing the shape of the current phase relation ($|f(x)| \leq 1$). When the number of electrons into the dot is odd (half occupied level, total spin $S = 1/2$), the order in which the spins are in the left lead is reversed compared to the order in the right lead. The current phase relation is π shifted: $I_S = I_C f(\Delta\varphi + \pi)$.

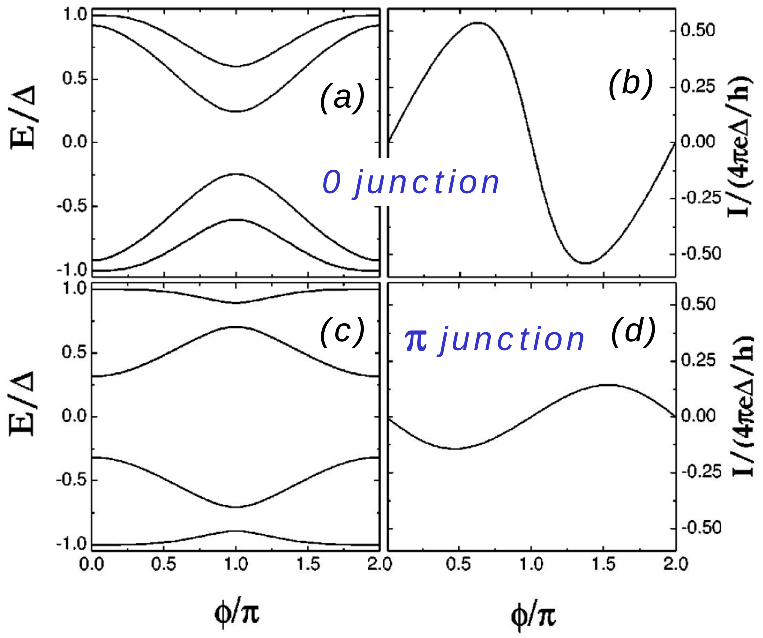

Figure 7.10: Taken from [171]. Andreev bound states spectrum and current phase relation for a $'0'$ junction (a) and (b). *idem* for a $'\pi'$ junction (c) and (d). Note the reversal of the current phase relation from one to the other and the relative amplitude of the supercurrent.

- $T_K/\Delta << 1$ **:** Here, the binding energy of the spin in the dot and an electron in the leads is small compared to the Cooper pairing energy. The Kondo effect is absent and one recovers a π junction behaviour (spin doublet state) with a π shifted current phase relation and a small supercurrent [5].

- $T_K/\Delta > 1$ **:** In this case, the resonance at the Fermi energy of the electrodes, due to the Kondo effect, survives and resonant Cooper pair tunneling occurs. Kondo effect and superconductivity are not antagonist anymore. A strong supercurrent can be observed (see figure 7.11) and a $'0'$ junction is recovered. In the unitary limit of the Kondo effect, the critical current should be $I_C = \frac{e\Delta}{\hbar}$.

Up to now, only the amplitude of the supercurrent was measured in the competing regime $T_K/\Delta \approx 1$ [177, 179, 180, 184]. It seems to follow theoretical predictions (fig.7.11 and 7.12) but it is necessary to measure the entire current/phase relation to check the consistency of the measurement. In particular, the crossover between these two regimes underlies a transition and peculiar current/phase relations are expected depending on the ratio T_K/Δ as shown by figures 7.13 and 7.14. Figure 7.13 shows two current phase relations taken in the extreme limits $\Delta/T_K >> 1$ and $\Delta/T_K << 1$. If $\Delta/T_K >> 1$ the doublet state is favored, an harmonic π shifted current phase relation is observed. If $\Delta/T_K << 1$ the singlet state (non magnetic) is favored, a strongly anharmonic $'0'$ junction current phase relation is observed. Figure 7.14 represents the crossover regime $\Delta \approx T_K$ between the singlet and doublet state. In this case the magnetic state of the dot depends on the phase

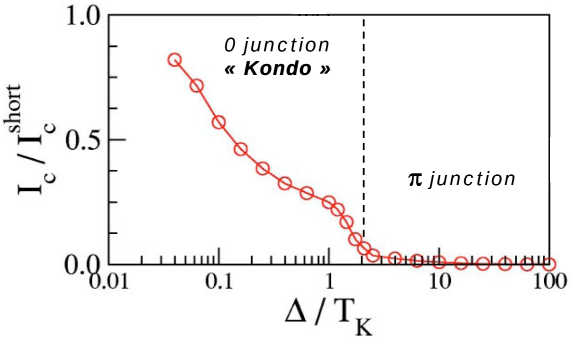

Figure 7.11: Taken from [5]. Predicted normalized critical current of the dot as a function of Δ/T_K. At high pairing energy $\Delta/T_K >> 1$, one has a $'\pi'$ junction and the critical current is small. When $\Delta/T_K < 1$, one has a $'0'$ junction due to Kondo effect and critical current increases.

difference. Whereas near $\Phi \approx \pm\pi$ the current phase is nearly harmonic and minimum ($'\pi'$ junction behaviour), discontinuities appear around $\Phi \approx 0$. These discontinuities are the hallmark of the singlet/doublet competition leading to a $0/\pi$ transition induced by changing the macroscopic phase difference between the two superconducting leads. They move away from 0 as the ratio Δ/T_K is lowered. In between the two symmetric jumps, the current phase relation is quasi-linear. Note than in this crossover regime, a $0/\pi$ transition can be induced by tuning T_K at fixed phase difference. T_K being tunable with a nearby gate voltage.

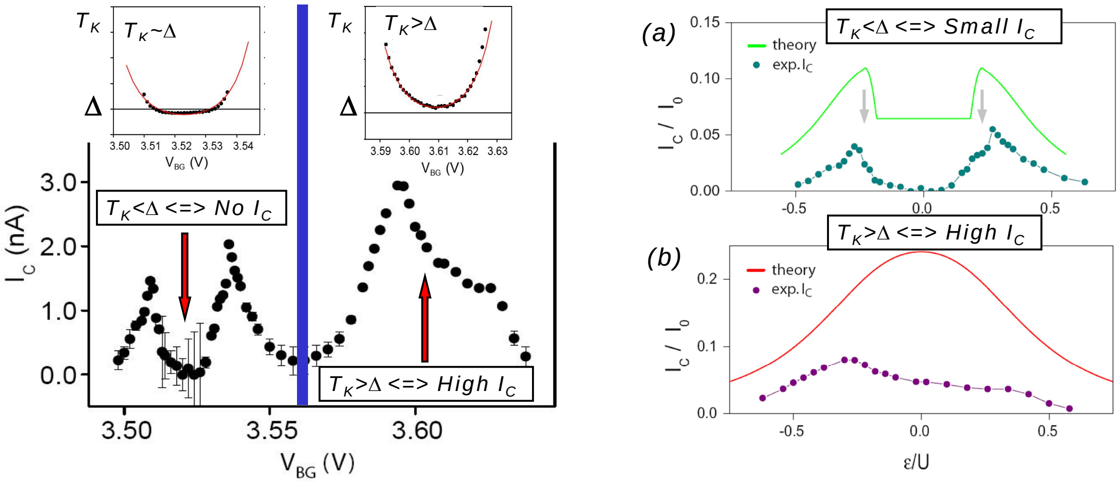

Figure 7.12: Adapted from [179]. (a) Experimental data showing the evolution of the supercurrent as a function of the gate voltage. The gate voltage tuning the Kondo temperature, one sees a clear difference depending on the ratio Δ/T_K. (b) Fit to theoretical predictions. The qualitative behaviour is recovered.

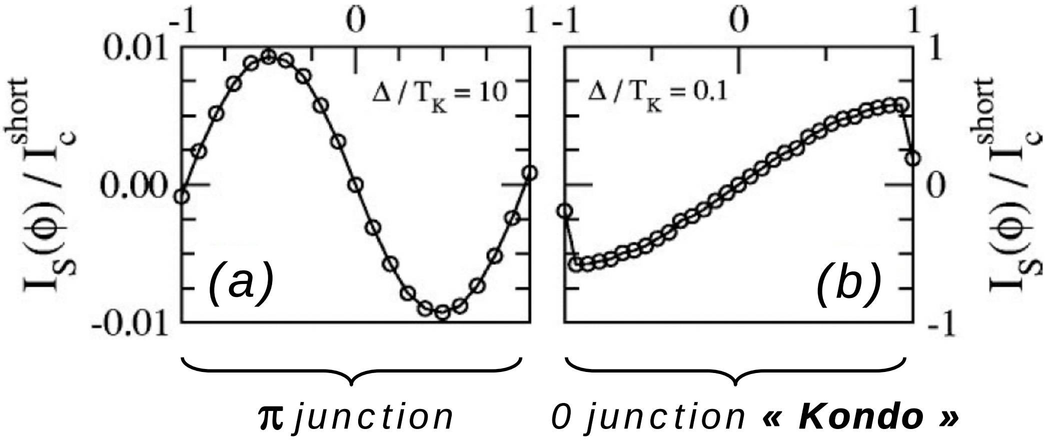

Figure 7.13: Taken from [5]. Predicted current phase relation of a quantum dot at (a) $\Delta/T_K = 10$: The negative slope of the curve at $\phi = 0$ means the dot is in a $'\pi'$ state. Note the small amplitude of the supercurrent; (b) $\Delta/T_K = 0.1$: The positive slope at $\phi = 0$ means the dot is in a $'0'$ state. The supercurrent amplitude is high and discontinuities are visible.

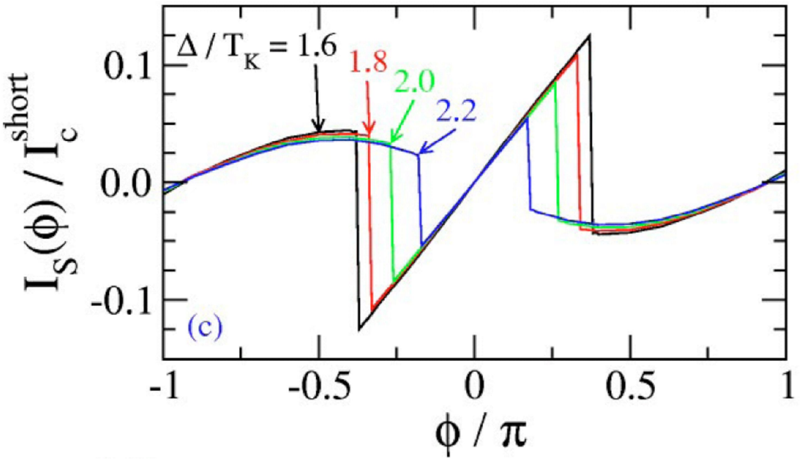

Figure 7.14: Taken from [5]. Calculated current phase relation of a quantum dot for different values of Δ/T_K chosen near the critical point. The higher the ratio Δ/T_K, the closer from $\phi = 0$ appear the discontinuities and conversely.

Role of the contact assymetry All what has been told so far was implicitely considering a dot with symmetric barriers. In the experiment, it is in general not the case and we have to take into account the contact asymmetry $a = \Gamma_L/\Gamma_R$. What has been demonstrated [5, 171, 185] is that it does not significantly affect the qualitative behaviour presented above. However, the asymmetry tends to slightly stabilize the Kondo singlet compared to the doublet phase. Even if those modifications are small in a stability diagram, the Andreev levels and thus the current phase relation can be strongly affected. In particular the contact asymmetry renormalizes the amplitude of the current phase relation and the position of the singularity in the intermediate regime $\Delta \approx k_B T_K$.

7.5 Current phase relation measurement

We aim to measure the current-phase relation of an hybrid superconductor/quantum dot structure with the dot made out of a carbon nanotube. Ideally, competition between superconductivity and Kondo correlations will be studied. In the following, we present our strategy to measure this current-phase relation.

7.5.1 State of the art

Measuring the current phase relation connected through a weak link has been the topic of a long standing research activity [163, 182]. The first measurement was made for a tunnel junction in 1963 [186] and extends now to ferromagnetic weak links [183] (π junction behaviour), semiconducting nanowires [173], carbon nanotubes [177, 180] ($0/\pi$ transition), atomic point contacts [19, 187, 188]... However, only the last of these works (atomic point contacts) has reported a quantitative test of the proposed theory. We here adapt their original technique to measure, in the same run of experiment, the current phase relation and the dc conductance of the investigated weak link as needed for a full comparison with theory.

7.5.2 The idea: asymmetric SQUID with central contact

In order to phase bias a weak link, one includes it into a loop through which a magnetic flux is applied. In such a configuration, the weak link is short circuited and one cannot directly measure its conductance in the superconducting state. To overcome this difficulty, we have considered a strongly asymmetric micron scale ($\approx 80 \mu m^2$) *dc* superconducting quantum interferometer device (SQUID) [19] as shown in figure 7.15. In this figure, contacts A and C respectively represent the source and drain of the SQUID. One arm contains the weak link (small Josephson junction, carbon nanotube quantum dots,...). The other supports two almost identical large Josephson junctions in series with a central contact (depicted by the letter B). The interest of this device is threefold. First, the asymmetry between the branches of the SQUID allows to measure simply the current phase relation of the weak link (see reference [19] and next section). Second, the third contact between the two large junctions allows to measure the normal state resistance of the weak link at room temperature. Third, one can use the same third contact to measure the conductance of the weak link in the superconducting state without using the hysteresis loop[1].

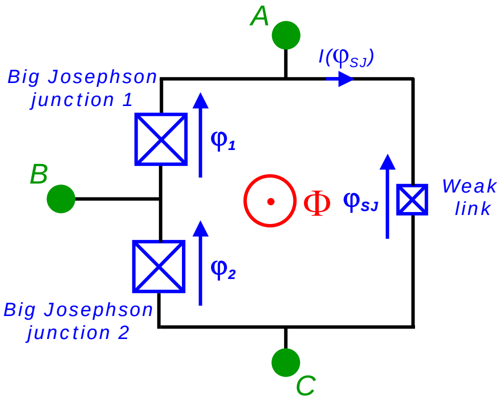

Figure 7.15: Equivalent circuit of the SQUID. The phase φ_1, φ_2 and φ_{SJ} are linked to one another by the magnetic flux through the loop ϕ by relation $\varphi_{SJ} - (\varphi_1 + \varphi_2) = -2\pi\phi/\phi_0 + 2n\pi$ with $\phi_0 = h/2e$. Contacts A and C are respectively the SQUID source and drain. Contact B is the additional central contact between the two almost identical big junctions and allows to determine the normal state resistance of each junctions.

7.5.3 Principle of the experiment

In this system the phase accross the junctions are related to one another. We denote φ_1, φ_2 the phase difference accross the two big junctions and φ_{SJ} the phase accross the weak link. Due to fluxoïd quantization, one has $\varphi_{SJ}-(\varphi_1+\varphi_2) = -2\pi\phi/\phi_0+2n\pi$ with $\phi_0 = h/2e$ being the flux quantum, ϕ the applied magnetic flux and n an integer number. The maximum supercurrent flowing into the big junctions is noted I_0 (fixed by the more resistive of the big junctions) and through the weak link $I_{SJ,0}$. Due to the strong asymmetry of the loop, one has $I_0 >> I_{SJ,0}$. In this limit [19] the critical current of the SQUID I_C (determined principally by the large Josephson junctions) is obtained when $\varphi_1 \cong \varphi_2 \cong \pi/2$ yielding $\varphi_{SJ} \cong -2\pi\phi/\phi_0 + \pi + 2n\pi$. It follows :

$$I_C(2\pi\phi/\phi_0) \cong I_0 + I_{SJ,0} f(\pi - 2\pi\phi/\phi_0), \tag{7.12}$$

with $I_{SJ,0} f(x)$ being the current phase relation of the weak link. The critical current measurement of the SQUID with respect to the applied magnetic field B ($\propto \phi$) will then consist in a periodic signal with mean value I_0 and amplitude $I_{SJ,0}$. These modulations directly probe the current phase relation of the weak link.

---

[1] Indeed, the use of the hysteresis loop of SQUIDs is common to voltage bias them. However the lower energy part cannot be measured due to a finite rettraping current.

7.5.4 Josephson junction dynamics - Resistively Capacitively Shunted Junction (RCSJ) model

In practice, the current at which a Josephson junction switches from the zero resistance state to the resistive state (switching current I_S) is always smaller than the critical current I_C predicted by theory. This problem is related to the dynamics of the superconducting phase accross the junction and has been widely studied in the last decades [112,189–191]. In particular it was shown that the switching current depends on the electromagnetic environment in which is embedded the junction and that it can be taken into account within the $RCSJ$ model. Let us notice that the intrinsic junction has its own geometrical capacitance C and shunt resistance R corresponding to residual quasiparticles states into the superconducting gap of the junction. One then considers the real junction as a perfect Josephson element in parallel with a RC circuit. The equivalent circuit is shown in figure 7.16 with γ the phase difference between the two superconductors.

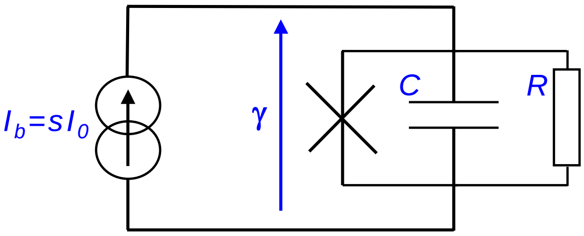

Figure 7.16: Resistively Capacitively Shunted Junction (RCSJ) model for the Josephson junction alone.

We then consider such a junction biased with a current $I_b = sI_0$ where I_0 is the critical current of the junction (determined by theory [114]) and $s \in [-1, 1]$ a real number. Within this formalism the current is

$$i_b = I_0 sin(\gamma) + \frac{V}{R} + C\frac{dV}{dt}. \qquad (7.13)$$

This expression can be recasted using the Josephson relation $V = \frac{\hbar}{2e}\frac{d\gamma}{dt}$ leading to a second order differential equation [112]

$$d^2\gamma d\tau^2 + Q^{-1}\frac{d\gamma}{d\tau} + sin(\gamma) = s \qquad (7.14)$$

in which is introduced a dimensionless parameter $\tau = \omega_P t$, with $\omega_P = \sqrt{2eI_0/\hbar C}$ the plasma frequency of the junction and $Q = \omega_P RC$ the quality factor of the junction. The differential equation 7.14 is analog to the equation of motion of a particle of mass $m = (\hbar/2e)^2 C$ moving along the γ axis in the effective potential $U(\gamma)$ of the system made of the Josephson junction and the current source. It is a *tilted-washboard potential* which reads (see figure 7.17):

$$U(\gamma) = -\varphi_0 I_0 cos(\gamma) - \varphi_0 I_0 s\gamma, \tag{7.15}$$

with $\varphi_0 = \hbar/2e$ and γ the superconducting phase difference accross the junction.

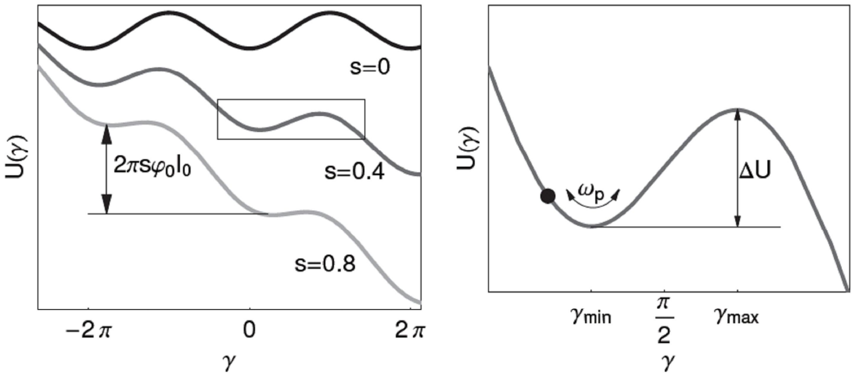

Figure 7.17: Taken from [163]. Left panel: Washboard potentials $U(\gamma)$ associated to the Josephson junction for three values of the bias current $I_b = sI_0$. Right panel: enlargement of the area enclosed by the box on the left plot. The phase oscillates around γ_{min} at the plasma frequency ω_P which depends on the barrier height ΔU.

Thermal escape The phase can be mapped onto the position of a massive particle evolving in a $1D$ potential $U(\gamma)$ as represented in figure 7.17. When the particle is trapped into a local minimum, it oscillates at the plasma frequency ω_P. These oscillations are damped with a time scale $Q/\omega_P = RC$ depending on the friction of the particle (Q being the quality factor of the junction). In addition, thermal energy $k_B T$ activates the particle. If $k_B T$ is comparable with the height barrier ΔU, the phase has a finite probability $P_t(s)$ to escape the well in a time t [192]. This probability is described by an Arrhenius-like activation rate $\Gamma(s)$ at which the particle escapes the well. One then has

$$P_t(s) = 1 - e^{-\Gamma(s)t} \tag{7.16}$$

with

$$\Gamma(s) = a(Q)\frac{\omega_P(s)}{2\pi}e^{-\Delta U(s)/k_B T_{esc}}. \tag{7.17}$$

The function $a(Q)$ takes into account the friction and T_{esc} is the escape temperature (temperature of the electromagnetic environment). The plasma frequency is given by

$$\omega_P(s) = \sqrt{\frac{I_0}{\varphi_0 C}}(1-s^2)^{1/4} = \omega_0(1-s^2)^{1/4}, \tag{7.18}$$

with C the parallel capacitance. The barrier height ΔU can be approximated by

$$\Delta U(s) = \frac{4\sqrt{2}}{3}\varphi_0 I_0 (1-s)^{3/2} + O[(1-s)^{5/2}]. \tag{7.19}$$

Note than when $s = 1$, the barrier height vanishes and the particle escapes. A finite voltage appears accross the junction according to the second Josephson relation $d\gamma/dt = 2eV/\hbar$.

Coming back to the finite barrier height, one sees that depending on the friction, the particle which escaped the well can have different behavior. Neglecting friction, the particle can gain enough kinetic energy to overcome the second barrier height and go over the next barrier. The particle runs away indefinitely and a finite voltage appears. Reducing the current bias changes the slope of the potential and the kinetic energy of the particle is reduced. It can be retrapped at a finite value of bias current called rettrapping current. The rettrapping current is smaller than the critical current. The V(I) cycle is hysteretic. This regime is called the *underdamped regime*. In the opposite limit, the *overdamped regime*, the strong friction reduces the kinetic energy of the particle escaping the well. It will get trapped in the subsequent well and no hysteresis is observed. One can parametrize these two limits using the quality factor $Q = \omega_P RC$ of the junction . When $Q >> 1$, the junction is underdamped while for $Q \leq 1$ it is overdamped. The function $a(Q)$ presented previously depends strongly on this parameter and can be summarized in table 7.1 [193, 194].

Damping	Validity range	a(Q)
Underdamped, low	$Q > 1,\ \ 2\pi\frac{\Delta U}{k_B T}\frac{\omega_0}{Q\omega_P} < 1$	$2\pi\frac{\Delta U}{k_B T}\frac{\omega_0}{Q\omega_P} < 1$
Underdamped, moderate	$Q > 1,\ \ 2\pi\frac{\Delta U}{k_B T}\frac{\omega_0}{Q\omega_P} > 1$	1
Overdamped	$Q < 1$	$\frac{Q\omega_P}{\omega_0}$

Table 7.1: Criterion for crossover between different damping regimes and the prefactor $a(Q)$ of the tunneling rate formula 7.17

As a conclusion of this thermally activated process, the junction switches at currents which are smaller than the expected critical current. The particular value of this switching current is stochastic but depends of the time left to the particle to escape the well, the height of the barrier and the temperature of the environment.

Quantum escape In addition to thermal escape one has to consider quantum escape. Indeed since the phase is a quantum variable it may tunnel through the barrier. This tunneling rate is well approximated in the underdamped regime by [189, 191, 195]

$$\Gamma_{Tunnel}(s) = 6^{3/2}\sqrt{\pi}\omega_P(s)\sqrt{\frac{\Delta U(s)}{\hbar\omega_P(s)}}e^{\frac{-36\Delta U(s)}{5\hbar\omega_P(s)}}. \tag{7.20}$$

The crossover temperature between thermal and quantum escape is given by $T_{Cross} = \hbar\omega_0/2\pi k_B$.

7.5.5 Theoretical phase dynamics of the asymmetric SQUID

In the following, we will consider the three junctions as resistively and capacitively shunted junctions as shown in figure 7.18 and previously introduced. It allows to verify the principle of the experiment within this new geometry.

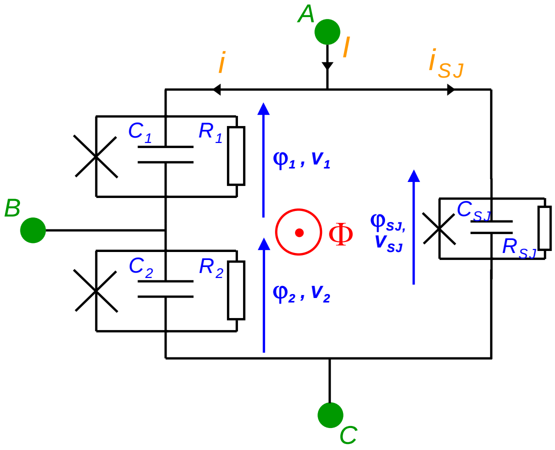

Figure 7.18: RCSJ model for the asymmetric SQUID considered in the experiment.

To do so let us first write the second Josephson equation together with the current conservation formula and fluxoïd quantization:

$$\left\{\begin{aligned} V_{SJ} &= V_1 + V_2 \\ V_1 &= \frac{\hbar}{2e}\frac{d\varphi_1}{dt} \\ V_2 &= \frac{\hbar}{2e}\frac{d\varphi_2}{dt} \\ I &= i + i_{SJ} \\ \varphi_{SJ} &= \varphi_1 + \varphi_2 - 2\pi\phi/\phi_0 \end{aligned}\right. \tag{7.21}$$

Using the $RCSJ$ model, one obtains three differential equations for the currents flowing through each junctions:

$$\left\{\begin{aligned} i_{SJ} &= I_{SJ,0} f(\varphi_{SJ}) + \frac{V_{SJ}}{R_{SJ}} + C_{SJ}\frac{dV_{SJ}}{dt} \\ i_1 = i &= I_{C1} sin(\varphi_1) + \frac{V_1}{R_1} + C_1\frac{dV_1}{dt} \\ i_2 = i &= I_{C2} sin(\varphi_2) + \frac{V_2}{R_2} + C_2\frac{dV_2}{dt} \end{aligned}\right. \tag{7.22}$$

By replacing the voltages by the Josephson equations and introducing $\varphi = \varphi_1 + \varphi_2$ and $\delta = \varphi_1 - \varphi_2$, the total current expression becomes :

$$\left\{\begin{array}{ll} I = & I_{SJ,0}f(\varphi - 2\pi\phi/\phi_0) + \frac{1}{2}I_{C1}sin(\frac{\varphi+\delta}{2}) + \frac{1}{2}I_{C1}sin(\frac{\varphi-\delta}{2}) \\ + & \frac{\hbar}{2eR_{Tot}}\frac{d\varphi}{dt} + \frac{\hbar C_{Tot}}{2e}\frac{d^2\varphi}{dt^2} \\ + & \frac{\hbar}{2e}(\frac{1}{2R_1} - \frac{1}{2R_2})\frac{d\delta}{dt} + \frac{\hbar}{2e}(\frac{C_1}{2} - \frac{C_2}{2})\frac{d^2\delta}{dt^2} \end{array}\right. \tag{7.23}$$

with $\frac{1}{R_{Tot}} = \frac{1}{R_{SJ}} + \frac{1}{2R_1} + \frac{1}{2R_2}$ and $C_{Tot} = C_{SJ} + \frac{C_1}{2} + \frac{C_2}{2}$. This expression is very general and takes into account the eventual asymmetry between the two junctions in series. However, assuming the two big junctions 1 and 2 being equivalent, one has $R_1 = R_2$, $C_1 = C_2$, $I_{C1} = I_{C2} = I_0$ and then $\varphi_1 = \varphi_2$ at any time. The previous equation simplifies into :

$$\boxed{I = I_{SJ,0}f(\varphi - 2\pi\phi/\phi_0) + I_0 sin(\frac{\varphi}{2}) + \frac{\hbar}{2eR_{Tot}}\frac{d\varphi}{dt} + \frac{\hbar C_{Tot}}{2e}\frac{d^2\varphi}{dt^2}.} \tag{7.24}$$

From this equation we recover that for the case of a static phase with $I_0 >> I_{SJ,0}$, the critical current of the SQUID is obtained when $\varphi/2 = \pi/2$. The critical current of the SQUID depends on the applied flux according to $I_C \approx I_0 + I_{SJ,0}f(\pi - 2\pi\phi/\phi_0)$. The washboard potential extracted from this equation reads :

$$U(\varphi) = \varphi_0\left[\int\left(I_{SJ,0}f(\varphi - 2\pi\phi/\phi_0) + I_0 sin(\frac{\varphi}{2})\right)d\varphi - I\varphi\right]. \tag{7.25}$$

Assuming the current phase relation of the small junction being $f(x) = sinx$ (case of a Josephson junction for instance), one can plot such potential for different parameters as shown in figure 7.19. It reads:

$$U(\varphi) = \varphi_0\left[-I_{SJ,0}cos(\varphi - 2\pi\phi/\phi_0) - 2I_0 cos(\frac{\varphi}{2}) - I\varphi\right]. \tag{7.26}$$

This potential depends on parameters $s = I/(I_0 + I_{SJ,0})$, $I_{SJ,0}/I_0$ and magnetic flux ϕ. In particular one sees that a change in the applied flux strongly affects a rather symetric SQUID while it does not change the landscape for a strongly asymmetric one. In the last case, the potential is sinusoidal with an amplitude ΔU essentially related to the Josephson energy of the large junctions. The dynamic of the asymmetric SQUID is dominated by the large junctions.

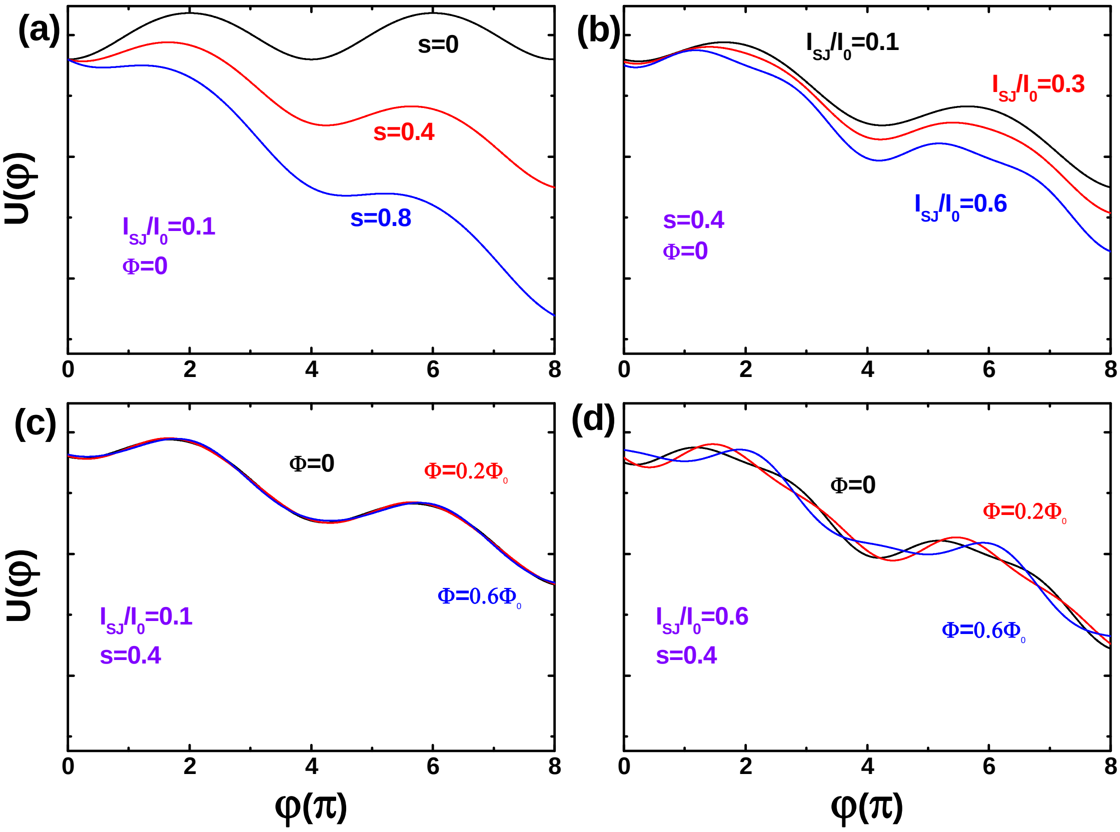

Figure 7.19: Potential $U(\varphi)$ for the asymmetric SQUID with the weak link being a small Josephson junction. (a) Small asymmetry $I_{SJ}/I_0 = 0.1$ and $\phi = 0$ for $s = I/(I_0 + I_{SJ,0}) = 0, 0.4, 0.8$. The potential is nearly sinusoidal meaning the small junction does not affect too much the switching process. Note the 4π periodicity of the potential energy. (b) $s = 0.4$ and $\phi = 0$ for supercurrent asymmetry $I_{SJ}/I_0 = 0.1, 0.3, 0.6$. Restablishing the symmetry completely changes the washboard potential, the switching process is strongly affected. (c) $s = 0.4$ and $I_{SJ}/I_0 = 0.1$ for $\phi = 0, 0.2\phi_0, 0.6\phi_0$. When using a strong asymmetry, changing the magnetic flux does not affect the landscape potential. (d) $s = 0.4$ and $I_{SJ}/I_0 = 0.6$ for $\phi = 0, 0.2\phi_0, 0.6\phi_0$. With a moderate asymmetry, changing the magnetic flux strongly affects the landscape potential.

7.6 Conclusion

Through this chapter, we have seen that a weak link connected to superconducting electrodes can support a supercurrent. This current is carried by Andreev Bound states into the weak link area. The energy spectrum of these subgap states depends on the phase difference between the two superconductors leading to a current which is also phase dependent. This is the current/phase relation. The shape and position of the ABS also depends of the nature of the weak link. We saw that in the specific case of the quantum dot, the ABS are intimately related to the electronic state of the dot and that the associated current phase can exhibit a wide variety of behavior. In order to measure these current phase relations we have proposed an original experiment allowing to measure in the same run of experiment, the superconducting $I(V)$ characteristics and the current phase relation.

Chapter 8

Experimental validation of the technique : current-phase relation of a small Josephson junction

In the following we propose to test the proposal made in the previous chapter. To do so we use a small Josephson junction as the weak link of the assymetric SQUID.

Contents

8.1 Experimental techniques

For further details concerning the sample fabrication, the reader should refer to the *Nanofabrication* appendice.

The junctions have been designed by electron beam lithography on the surface of both oxidized and highly doped silicon wafers. One uses an angular Joule evaporation technique to deposit the sequence of materials $Pd(4nm)/Al(70nm)/Al_2O_3/Al(120nm)$ (see Fig.8.1). Note that this complicated sequence has been chosen in order to be compatible with carbon nanotube connection as we will see in next chapter. The oxidation step is carried out for

10 minutes under an oxygen pressure of 3.10^{-1} mbar. The three terminals A, B and C allow the determination of the room temperature resistances of the junctions : $R_1 = 1.53k\Omega$, $R_2 = 1.52k\Omega$ and $R_{SJ} = 17.3k\Omega$.

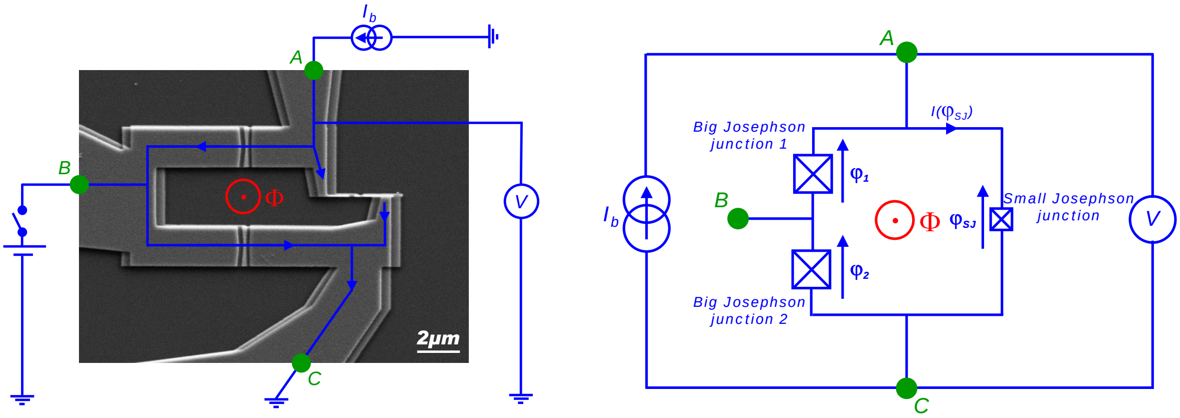

Figure 8.1: (a) Scanning electron microscope picture of the assymetric superconducting SQUID loop. (b) Equivalent circuit of the SQUID. The phase φ_1, φ_2 and φ_{SJ} are linked to one another by the magnetic flux through the loop ϕ by relation $\varphi_{SJ} - (\varphi_1 + \varphi_2) = -2\pi\phi/\phi_0 + 2n\pi$ with $\phi_0 = h/2e$. Contacts A and C are respectively the SQUID source and drain. Contact B is the additional central contact between the two big junctions. It allows to determine the normal state resistance of each junctions.

8.2 Experimental results

8.2.1 $V(I)$ characteristics of the assymetric SQUID

The V(I) characteristic of the assymetric SQUID is mainly determined by the two big junctions in series. It exhibits an hysteretic behavior in agreement with quality factors $Q \geq \omega_P R_{Tot} C_{Tot} = 7$ ($R_{Tot} = 1.4k\Omega$, $C_{Tot} = 45fF$ and $\omega_P/2\pi = 18.6GHz$). We show in figure 8.2, a typical V(I) curve. The hysteresis presented in this figure is modulated by a perpendicular to plane magnetic field. In particular, the field dependence of the critical current of the big junctions I_m exhibits a Fraunhoffer pattern (see figure 8.2 b): $I_m = I_0|sin(\pi\phi/\phi_0)/(\pi\phi/\phi_0)|$ with $\phi = 2BLW = 2BS_{BJ}$ the flux applied through the surface S_{BJ} of the junctions. Note than here, B is the applied field, W the width of the junctions and L the length. By taking $B_0 = 14.4G$, we obtain $S_{BJ} = 0.713h/2eB_0 = 1.03\mu m^2$. This value is in the same order of magnitude with the sample design of surface $S = 0.43\mu m^2$.

The possibility to suppress the supercurrent through the big junctions helps to measure the voltage bias dependence of the small junction in the superconducting state. We will discuss this point later.

N.B. Let us notice here that if the applied magnetic field is bigger than the critical field of the superconductor, superconductivity is suppressed and every junctions become normal. The measured conductance of the loop is the sum of the conductance of the small junction and the conductance of the big junctions placed in parallel. The dc $I(V)$ curve of the ring is linear corresponding to a conductance which is constant. However, if instead of the small Josephson junction were placed a highly non-linear system (quantum dot,...), the $I(V)$ would become non linear with a non linearity entirely due to the non linear system. This will be exploited in the next chapter.

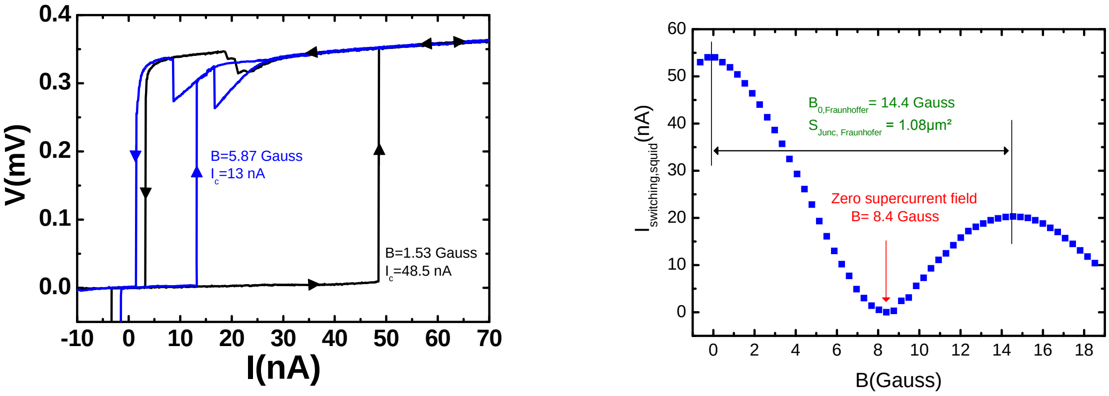

Figure 8.2: (a) V(I) hysteresis loop of the current biased SQUID for two values of the magnetic field $B_1 = 1.53$ Gauss and $B_2 = 5.87$ Gauss. The quality factor of the SQUID is $Q = \omega_P R_{Tot} C_{Tot} = 7 >> 1$ (underdamped) responsible for the hysteretic behavior. The evolution of the switching current as a function of the magnetic field evolves as a Fraunhoffer pattern. Anomalies in the rettraping current are due to the asymmetry between the big junctions. (b) Switching current of the SQUID loop as a function of magnetic field. The evolution is consistent with a Fraunhoffer like pattern $I_m = I_0 |sin(\pi\phi/\phi_0)/(\pi\phi/\phi_0)|$ with $\phi = 2BLW = 2BS_{BJ}$.

8.2.2 Current Phase relation measurement

To measure the current phase relation of the small junction we measure the switching current by triggering the source signal on the voltage measurement as shown in figure 8.3a. This switching current exhibits fluctuations coming from finite temperature, electromagnetic environment and quantum tunneling. To reduce this uncertainty, we average over more than 2000 values of the switching current. The phase bias is insured by a superconducting coil producing a perpendicular to the plane magnetic field. The mean switching current is measured as a function of the magnetic field. We have represented in figure 8.3b the current phase relation associated to this measurement. To do so, we remove the vertical offset corresponding to the switching current I_0 of the large junctions[1]. From the analysis of the Fraunhoffer pattern one can determine the *zero* of the phase. Considering the sign of the flux with respect to the sign of the applied magnetic field, we set the $+2\pi$ phase

---

[1] Note than this switching current $I_0 \approx 54nA$ is approximately three times smaller than the expected critical current ($180nA$). This is certainly due to an uncontrolled environment which increases the escape temperature.

one period after the *zero* phase point. One finally compares with theoretical predictions. The results fully agrees with a sinusoïdal evolution of the critical current with respect to the phase as expected in Josephson junctions. The fit gives us that $I_{S,SJ} = I_{S0,SJ} sin\Phi$ with $I_{S0,SJ} = 1.753nA$. Assuming the value of the superconducting gap of the PdAl bilayer is $\Delta_{PdAl} = 160\mu eV$ and that the normal state resistance of the small junction is $R_{N,SJ} = 27k\Omega$, one should have a critical current $I_C = 8.765nA$. The measured quantity is thus a factor of 5 below the expected value.

The phase φ_{SJ} is related to the magnetic field through the relation $\varphi_{SJ} = 2\pi B/B_0$ with B_0 corresponding to the field B to apply in order to reach one flux quantum through the loop. We obtain $B_0 = 0.31Gauss$. This corresponds to an effective area of the SQUID loop $S_0 = h/2eB_0 = 66.7\mu m^2$. This area is consistent with the size of the loop ($\approx 70\mu m^2$) and approximately corresponds to 3/4 of the area corresponding to the external side of the metal[2].

8.2.3 Extraction of the differential conductance dI/dV of the small junction in the superconducting state

In the described SQUID geometry it is difficult to unambiguously measure the conductance of one arm independently of the other arm. One technique would consist in measuring the conductance of the SQUID, then opening one side of the SQUID, measuring the conductance of the remaining side and by substraction, extract the conductance of the opened arm. This technique is commonly used for break junctions [19]. It can be adapted to a gate tunable system exhibiting strong reduction of the conductance but it is hopeless for a simple Josephson junction for instance. A second technique is to use the rettraping branch of a single big junction to obtain information on the small weak link. This however does not allow to extract the low voltage bias behaviour due to the finite voltage at which the phase is rettraped. In the following, we present a way to solve this problem. The idea is to dc voltage bias the SQUID (between A and C) and monitor the current flowing out in point C. In this configuration the dI/dV characteristic of the whole loop is measured with a lock-in amplifier technique (ac voltage $V_{ac} = 2\mu V$ at frequency $\nu = 81.45Hz$). The curves exhibit complicated features due to the sum of the currents flowing through the two arms of the SQUID. In the following, we measure the conductance of the small Josephson junction alone. To do so we use the third channel B to fix the dc voltage bias between B and C : V_{BC} to be smaller than the superconducting gap of the junction, where no dc current should flow (out of the Josephson branch). In those conditions, the results were not satisfying enough due to the supercurrent through the big junctions. To overcome this difficulty, we apply a magnetic field $B = 8.5Gauss$ to cancel the supercurrent through the big junctions thanks to the Fraunhoffer pattern shown in figure 8.2 b. One then success-

---

[2] Note than the maximum width of the squid is $W = 2\mu m$ whereas the penetration length of the magnetic field for a thin layer of Aluminum is $\lambda_L \sim 160nm$ [196]. This consequently does not explain the estimated surface. However, in this limit if the loop area is comparable to the size of the loop one can have a focus of the magnetic field lines [149].

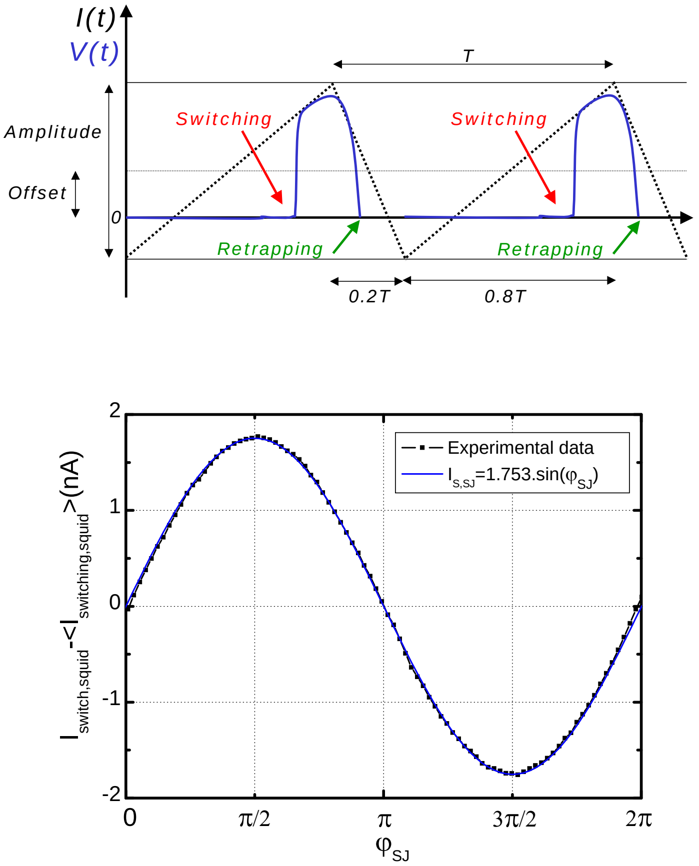

Figure 8.3: (a) Schematic of the sequence of the applied current and measured voltage accross the SQUID to measure the current phase relation of the small junction. The SQUID is current biased with a low frequency generator which produces a $80Hz$ periodic signal of voltage bias sent to the sample through a $1M\Omega$ resistor. Each period consists in a ramp (linear increase of the voltage bias) from $-10mV$ up to $+70mV$ followed by a way down from $+70mV$ to $-10mV$ (linear decrease). The time attributed to the way up corresponds to 80% of the cycle. At the same time, the voltage drop V_{AC} accross the loop is measured. At small bias, the SQUID is on its supercurrent branch and there is no voltage accross the SQUID. Above the switching current, a sharp jump appears in the voltage measurement. As this voltage is triggered to the source, we obtain the corresponding value of the bias current at which this jump appears. The phase bias is insured by a superconducting coil producing a perpendicular to the plane magnetic field. The mean switching current is finally measured as a function of the magnetic field. (b) Current phase relation of the small Josephson junction extracted from the experiment. The sinusoïdal fit is perfectly accurate proving the validity of the technique.

fully measures the voltage bias dependence of the conductance of the small junction as shown in figure 8.4.

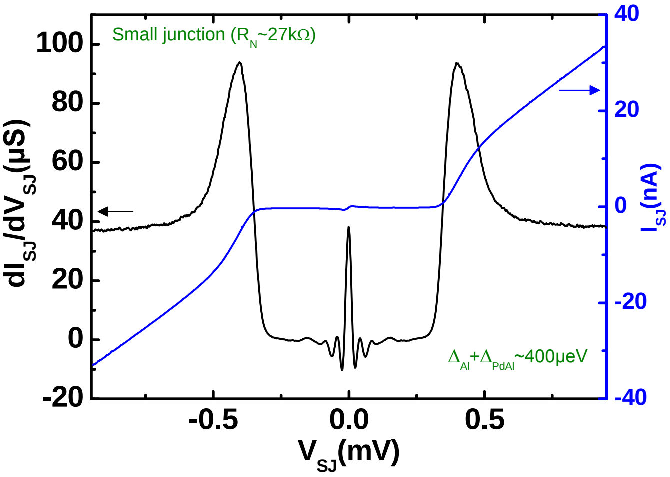

Figure 8.4: Differential conductance dI_{SJ}/dV_{SJ} and dc $I_{SJ}(V_{SJ})$ characteristics of the small junction. The traces are obtained by fixing V_{BC} to be below the superconducting gap of the corresponding large junction (acting as a switch off for the large arm of the SQUID) and under a magnetic field $B = 8.5$ Gauss to eliminate traces of the supercurrent in the big junctions. Superconducting gap is found to be $\Delta_{PdAl} + \Delta_{Al} = 400 \mu eV$ and the normal state resistance $R_{N,SJ} = 27k\Omega$

8.2.4 Adaptability to other types of weak link

A priori, the described technique is adapted to any kind of weak link provided that $I_0 >> I_{SJ,0}$. In particular we want to use a carbon nanotube quantum dot deposited on an oxidized and doped Si substrate which can be used as a backgate. We then have checked that the use of this gate does not modify the measurement principle. To do so, we have compared the switching currents of identical SQUID (weak link = Josephson junction) on doped and undoped Si substrates and also studied the influence of the applied voltage on the dopes Si backgate. No effects were visible.

8.3 Conclusion

In this chapter, we have evaluated an extension of the technique introduced by the Quantronics group [19] to measure the current phase relation of a small weak link and its dc conductance. It was found that the technique is accurate with respect to the harmonicity of the current phase relation tested. This point is necessary to consider more elaborate (anharmonic) systems using the same device geometry. The evolution, with respect to [19], is the unambiguous possibility to measure in the same experiment, the dc conductance and the current phase relation of the weak link in the superconducting state. We think this scheme opens a new route towards a better understanding of the relations between phase and voltage biased superconducting weak link. Hereafter we use the same detection scheme to measure the current phase relation of a carbon nanotube quantum dot.

Chapter 9

Current Phase relation of a carbon nanotube quantum dot

This chapter is devoted to the presentation of our recent results concerning the current phase relation of a carbon nanotube quantum dot. The experimental results are still under analysis.

Contents

9.1 Sample Fabrication

For further details concerning the sample fabrication, the reader should refer to the *Nanofabrication* annex.

We use the same parameters size of the loop, size of the leads, size of the junctions,... than in the previous chapter. The carbon nanotube is grown by chemical vapor deposition [131] and is connected with $PdAl/Al_20_3/Al$ contacts in the same run of deposition than the big junctions in parallel. The three points measurements made at room temperature allows to determine the resistance of each junctions : $R_1 = 771\Omega, R_2 = 769\Omega$ and $R_{Tube} = 9.1k\Omega$.

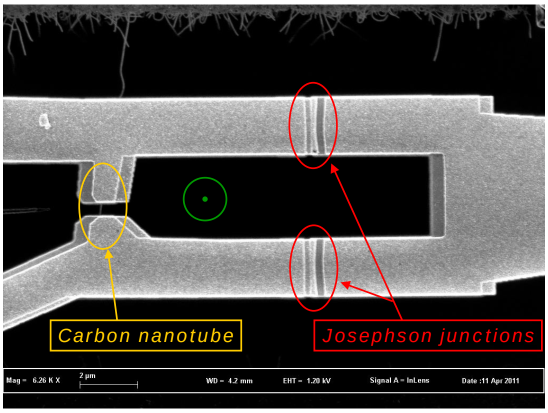

Figure 9.1: Scanning electron microscope picture of the assymetric SQUID used in the experiment. Junctions and carbon nanotube contacts are made of $PdAl/Al_20_3/Al$ and are fabricated in the same step of metal deposition. Nanotube contacts are separated by $\approx 450nm$.

9.2 Normal state characterization of the carbon nanotube quantum dot

The normal state characterization of the carbon nanotube is achieved by first applying a magnetic field $B \approx 0.18T$ which suppresses superconductivity. The SQUID current response to a voltage bias is then measured with a lock-in amplifier technique. The measured current exhibit variations related to the conductance of the nanotube. One has represented in figure 9.2a the stability diagram *i.e.* differential conductance $dIdV$ *vs* bias voltage V_{SD} and gate voltage V_{BG}, of the carbon nanotube quantum dot. One observes the nanotube is globally highly conducting with a maximum conductance approaching $4e^2/h$. Its conductance can be lowered by a factor of 4 with the simple use of the back-gate voltage and there is no strong evidences for Coulomb blockade or Kondo effect. Not even clear Fabry-Pérot oscillations are visible. The nanotube is strongly coupled to the leads. Several traces of the conductance *vs* source-drain voltage are shown in fig.9.4a for different back-gate voltages. It illustrates the multiple behaviors exhibited by the nanotube.

9.3 Superconducting state characterization of the carbon nanotube(s) quantum dot

To measure the superconducting behavior of the carbon nanotube, one reduces the magnetic field to zero and uses the technique described in the previous chapter. We show in

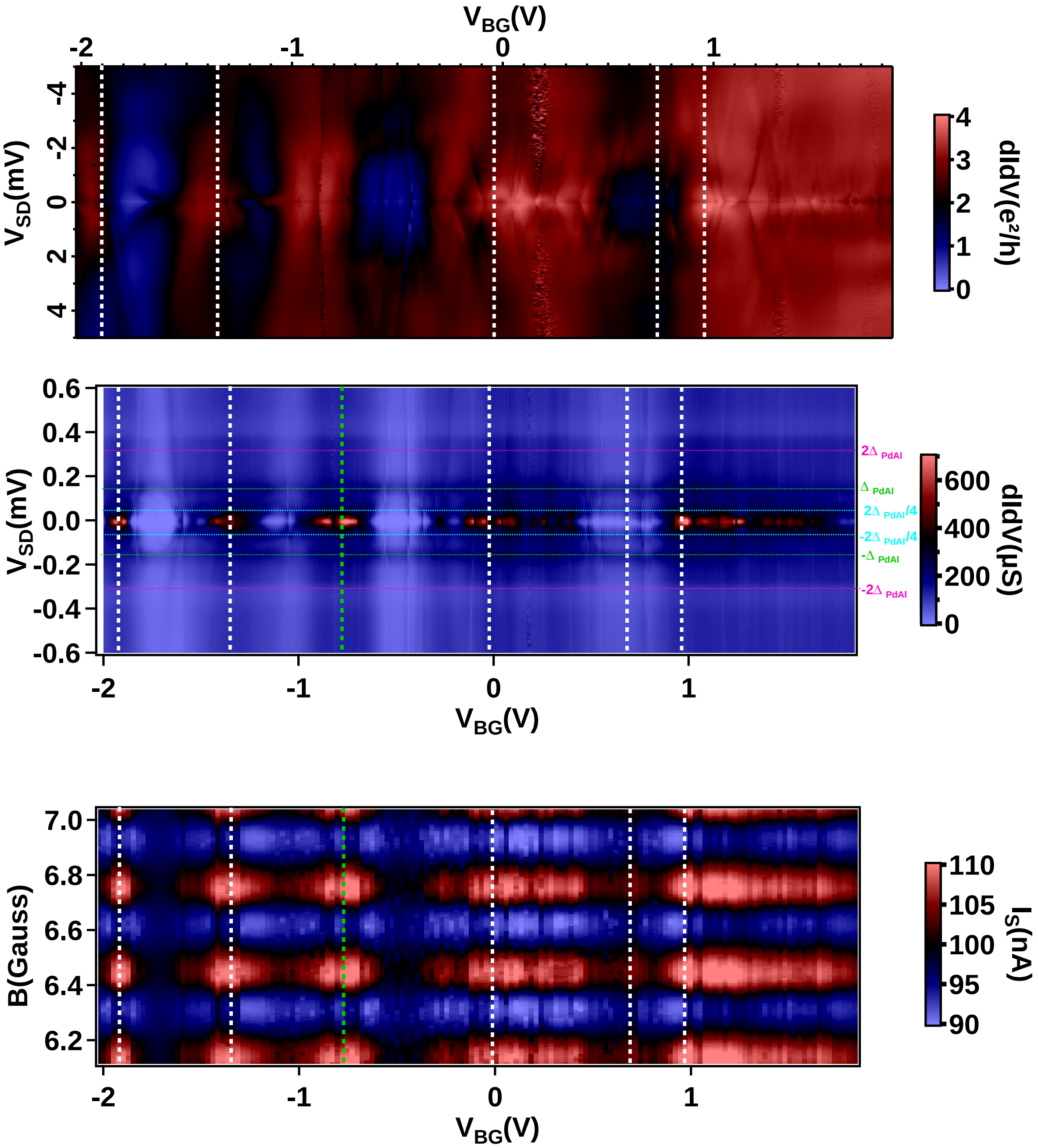

Figure 9.2: (a) Normal state stability diagram of the carbon nanotube quantum dot *i.e.* differential conductance $dIdV$ *vs* bias voltage V_{SD} and gate voltage V_{BG}. The nanotube is globally highly conducting and do not exhibit strong evidence for Coulomb blockade or Kondo effect as we are looking for. (b) Superconducting state stability diagram of the carbon nanotube quantum dot. One can observe zero bias anomalies in regions of high normal state conductances. Out of the zero bias, one also see traces (conductance bumps) of the multiple andreev reflections at fixed voltages. (c) Modulation of the SQUID supercurrent *vs* the applied magnetic field$B$ and the backgate voltage. Strong modulations are experienced in the highly conducting regions. No modulation is observed in the poorly conducting areas.

figure 9.2b the stability diagram of the tube in the superconducting state. Several traces are also shown in fig 9.4b. We observe zero bias peaks in the regions of high normal state conductances and dips in the low conductance region. In addition to this, traces of multiple andreev reflections are also visible at fixed voltages $2\Delta/n$ with n an integer number ($n = \pm 1, \pm 2$ here). Finally, far away from the superconducting gap ($|V_{SD}| >> 2\Delta$), the conductance remains constant.

9.4 Current phase relation measurement

In the following, we describe the experiment and present the raw data. We then focus on two different values of gate voltage corresponding to poorly and highly conducting regions of the stability diagram.

9.4.1 Experimental details

As mentioned in the previous chapter, one needs to average over a large number of switching events to define precisely the switching current. In this part, we have improved the detection setup by using a time counter as presented in figure 9.3. The switching current I_S is related to the introduced parameters (see legend of figure 9.3) by relation:

$$I_S(A) = \frac{V_{Offset}(V)}{R_{Polar}(\Omega)} + \frac{V_{PeaktoPeak}(V).\nu(Hz)}{duty(0 \longleftrightarrow 1).R_{Polar}(\Omega)}.t(s) \tag{9.1}$$

The counter accumulates and averages directly the switching times during a fixed counting time T_{Count}. As an example, for $T_{Count} = 5s$ and frequency $\nu = 414Hz$, the number of averaged switching events is $N = T_{Count}.\nu = 5 * 414 = 2070$. The phase bias is again insured by a superconducting coil producing a perpendicular to the plane magnetic field. This new technique allows to quickly realize maps of the *switching current/magnetic field* relation as a function of the gate voltage.

9.4.2 Raw data

One shows in figure 9.2c such a map in the same range of back-gate voltages than in previous sections. Some extracted traces are also shown in figure 9.4c. What is striking is first the correspondence between the highly (respectively poorly) conducting regions determined in the normal state and the regions of strong (respectively small) supercurrent in the nanotube. The value of the supercurrent can range from 0 to $10nA$ depending on gate voltage. We have represented in figure 9.5 the comparison between the zero bias normal state conductance and the maximum supercurrent flowing into the tube as a function of backgate voltage. It allows to determine the product eR_NI_S shown in the same figure. It is in average two times smaller than the superconducting gap of $PdAl$ contacts. This discrepancy is not understood yet. It is however interesting to note that we observe larger supercurrents than previous experiments performed on similar samples [29, 177]. Whereas

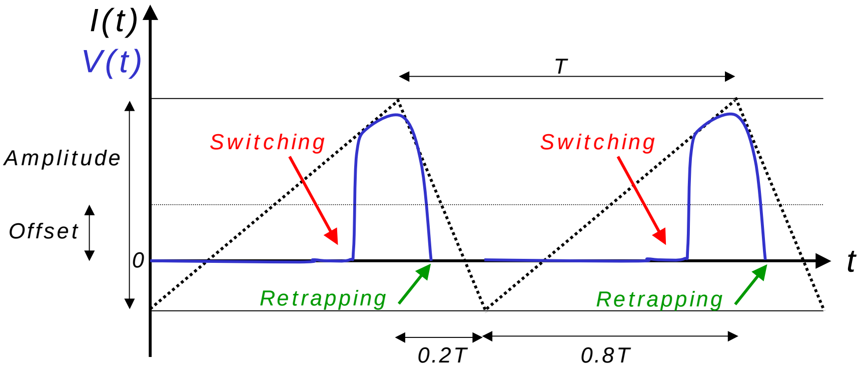

Figure 9.3: Schematic of the sequence of the applied current and measured voltage accross the SQUID to measure the current phase relation of the nanotube. The periodic voltage signal is produced at frequency $\nu = 414Hz$ through Cu filters in series with a resistor $R_{Polar} = 1M\Omega$. This is the current source. Each period consists of a ramp from $-50nA$ to $+150nA$ followed by a way back down to $-50nA$ ($V_{PeaktoPeak} = 200mV$, $V_{Offset} = 50mV$). The time attributed to the way up corresponds to 80% of the cycle (duty cycle = 0.8). The counter measures the time $t_B - t_A$ flowing between a synchronization time t_A and the time t_B where the voltage V accross the SQUID becomes higher than a fixed voltage threshold : the switching time. The phase bias is insured by a superconducting coil producing a perpendicular to the plane magnetic field. The mean switching time is finally measured as a function of the magnetic field.

in the small supercurrent region, the $I_S = f(B)$ curves are harmonics (fitted by a sinusoïdal formula), when supercurrent gets higher some anharmonicity appears.

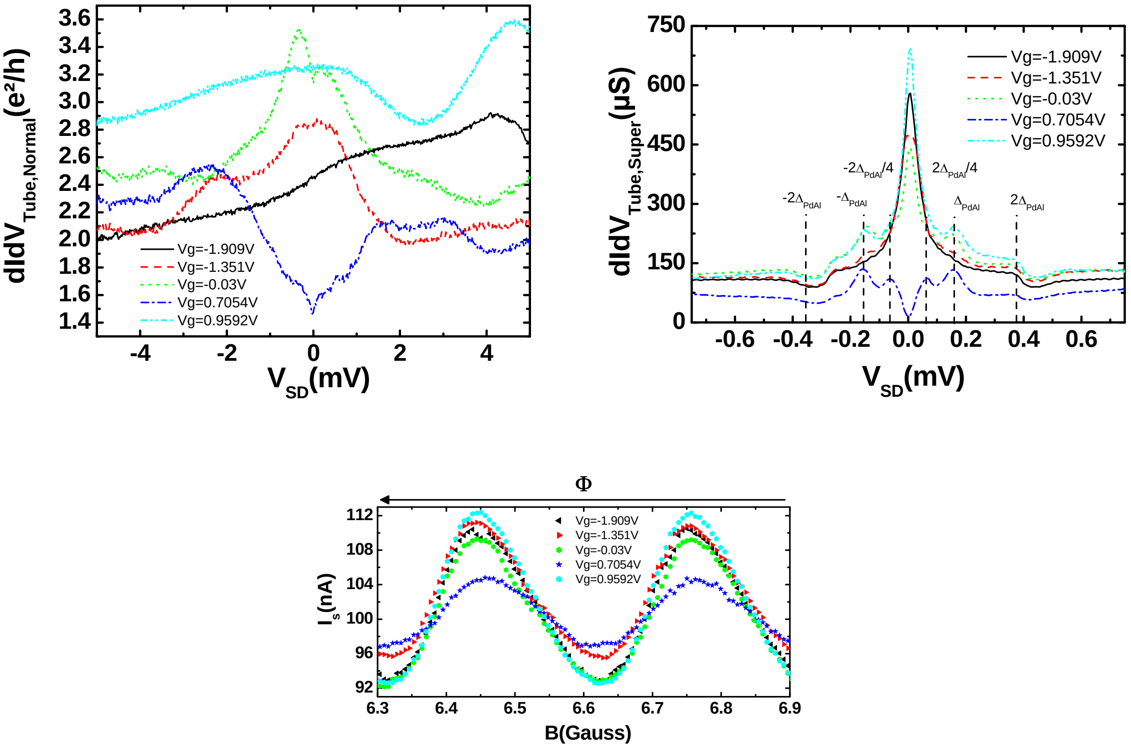

Figure 9.4: (a) Normal state differential conductance of the carbon nanotube quantum dot $dIdV$ *vs* bias voltage V_{SD} at different gate voltages $V_{BG} = -1.909,\ -1.35,\ -0.03,\ 0.705$ and $0.959V$. One can isolate gate voltages where conductance is arbitrarily high or low at zero bias. (b) Superconducting Normal state differential conductance of the carbon nanotube quantum dot for the same back-gate voltages. One can observe zero bias anomalies and traces of the multiple andreev reflections. (c) Modulation of the SQUID supercurrent *vs* the applied magnetic field$B$ for the same back-gate voltages. Strong anharmonic and small harmonic modulations are respectively experienced in the highly ($V_{BG} = -1.909,\ -1.35,\ -0.03$ and $0.959V$) and poorly ($V_{BG} = 0.7054V$) conducting regions.

In the following sections we will discuss in more details these two different behaviours. First, we have to convert the $I_S = f(B)$ measurement in a current phase relation measurement. To do so, we remove the vertical offset corresponding to the switching current of the large junctions and find the magnetic field offset taking advantage of the symmetry of the Fraunhoffer pattern. The sign of the flux with respect to the sign of the applied magnetic field is also considered to set the $+2\pi$ phase point.

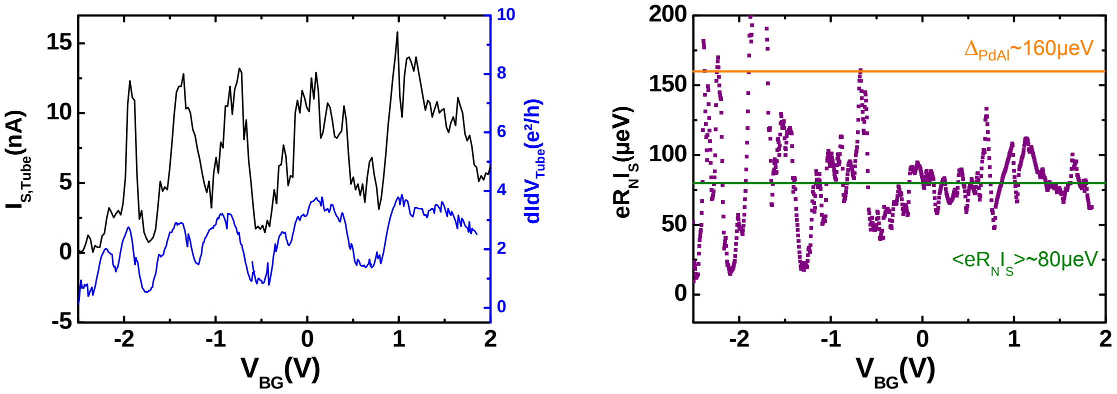

Figure 9.5: (a) Amplitude of the supercurrent and normal state conductance (zero bias) as a function of back-gate voltage. One sees the total correspondence between highly conducting region in the normal state and strong supercurrent in the superconducting state. (b) Experimental product eR_NI_S as a function of backgate voltage. It is in average two times smaller than the superconducting gap of $PdAl$ contacts.

9.4.3 Poorly conducting region: Harmonic current phase relation

We show in figure 9.6 the measured current phase relation for gate voltage $V_{BG} = -1.7V$. In this area, the nanotube has a zero bias normal state conductance $G_N \approx e^2/h$. The amplitude of the current phase modulation is 1.85nA. It is fully harmonic as verified by a sinusoïdal fit. Indeed, when the resistance is high, the tube behaves like a tunnel junction which is known for having an harmonic current phase relation [150]. One can compare the amplitude of the switching current to the predicted critical current $I_C = 6.8$ nA using Ambegaokar formula [114] with $\Delta_{PdAl} = 160\mu eV$. The measured switching current is ≈ 3.7 times smaller than the expected one.

9.4.4 Highly conducting region: Anharmonic current phase relation

Figure 9.7 represents the current phase relation extracted for a zero bias normal state conductance $G_N \approx 3.5e^2/h$. It exhibits a strong amplitude of modulation : 9.0 nA and it is anharmonic. More precisely, the maximum (respectively minimum) of the supercurrent is positively (respectively negatively) phase shifted compared to $\pi/2$ (respectively $3\pi/2$). This effect has already been observed and widely studied in atomic contacts [19]. It is related, in the short junction limit, to a finite number of conduction channels with at least one channel of high transparency. The anharmonicity of this curve is fitted by taking two channels at zero temperature with transparencies $\tau_1 = \tau_2 = 0.82$ corresponding to an estimated normal state conductance $G_{Fit} = 3.28e^2/h$. However the resulting amplitude is too high (see green curve in Fig.9.7). An amplitude renormalization factor 0.8 is needed to accurately reproduce the data (see red curve in Fig.9.7). This factor may be explained

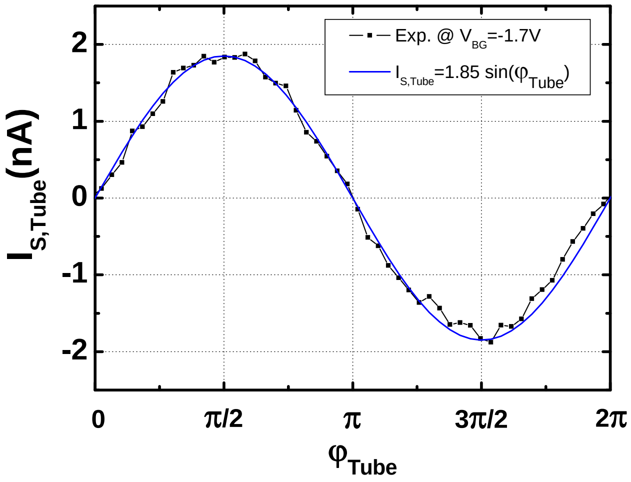

Figure 9.6: Current phase relation of the carbon nanotube quantum dot at $V_{BG} = -1.7V$ (dotted black curve). In this region of moderate normal state conductance, the current phase modulation is 1.85nA's high and fully harmonic as suggested by the sinusoïdal fit (full blue line).

by uncertainties over the superconducting gap of the contacts, the normal state resistance of the tube and also the finite temperature.

Even if this fit gives a reasonable agreement, it is not the only possible physical description of the system. In particular, the role of the barrier assymetry is not taken into account in this description. This is obviously of primary importance for a carbon nanotube quantum dot and further studies are needed. Note that the product $R_N I_S = 66.6\mu eV$ is approximately 2.4 times smaller than the superconducting gap $\Delta_{PdAl} = 160\mu eV$.

9.4.5 Temperature dependence of the current phase relation

We have represented the SQUID switching current *vs* magnetic flux for different temperatures and different gate voltages in fig. 9.8. It shows three key elements. First, the overall switching current of the SQUID is reduced by temperature. Second, the amplitude modulation of the switching current due to the nanotube quickly vanishes with temperature. Third the anharmonic behaviour of the current phase relation seen for several gate voltages is even more sensitive to temperature. The following subsections address these three points.

Temperature dependence of the SQUID switching current

The SQUID switching current is dominated by the large junctions. It depends on temperature as predicted by the *RCSJ* model. To quantify this effect, we have plotted the mean value, with respect to the applied field, of the switching current as a function of

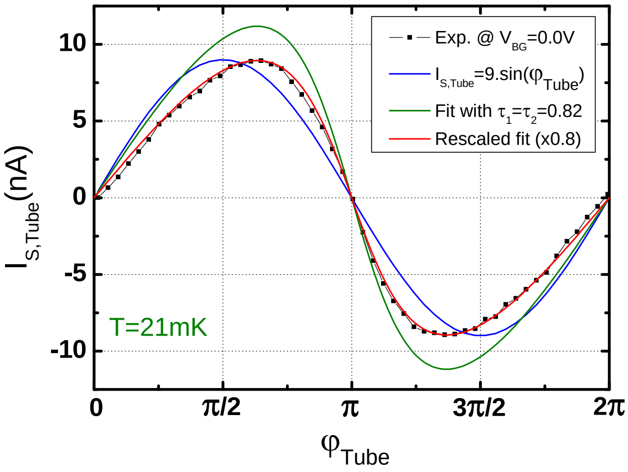

Figure 9.7: Current phase relation of the carbon nanotube quantum dot at $V_{BG} = 0.00V$ (dotted black curve). In this region of high normal state conductance, the current phase modulation is 9.0nA's high and anharmonic. We can fit the anharmonic behaviour of this curve by taking the short junction limit at zero temperature with two channels of transparencies $\tau_1 = \tau_2 = 0.82$ (full green line). In such condition the amplitude is too high. We renormalize it by the factor 0.8 (full red line) which may be explained by uncertainties over the superconducting gap of the contacts, the normal state resistance of the tube and also the finite temperature.

temperature. It is shown in figure 9.9a. We observe that the switching current is reduced with an increase of temperature until it vanishes completely at high temperature.

Temperature dependence of the nanotube switching current

To extract the temperature dependence of the nanotube switching current, we measure the amplitude of the SQUID modulation with respect to the magnetic field at different temperatures. The results are shown in figure 9.9b and show how fast the switching current is reduced by temperature.

A comparative analysis between the SQUID switching current and the nanotube switching current is shown in figure 9.9c. It reveals that the nanotube switching current exhibits a faster decay with respect to temperature than the SQUID. This can be explained by the difference of Josephson energies between the tube and the big junctions.

We have also studied the anharmonicity of the current phase relations with respect to temperature. To do so, we have Fourier transformed the current phase relations and independently analysed the temperature dependence of the first and second harmonics. The spectrum are shown in figure 9.10. We observe essentially one or two peaks at $\varphi^{-1}/(2\pi) = 1, 2$. The higher harmonics are not visible and the low frequency behaviour accounts for the unavoidable switching noise and thermal drift in the measurement setup. The second peak

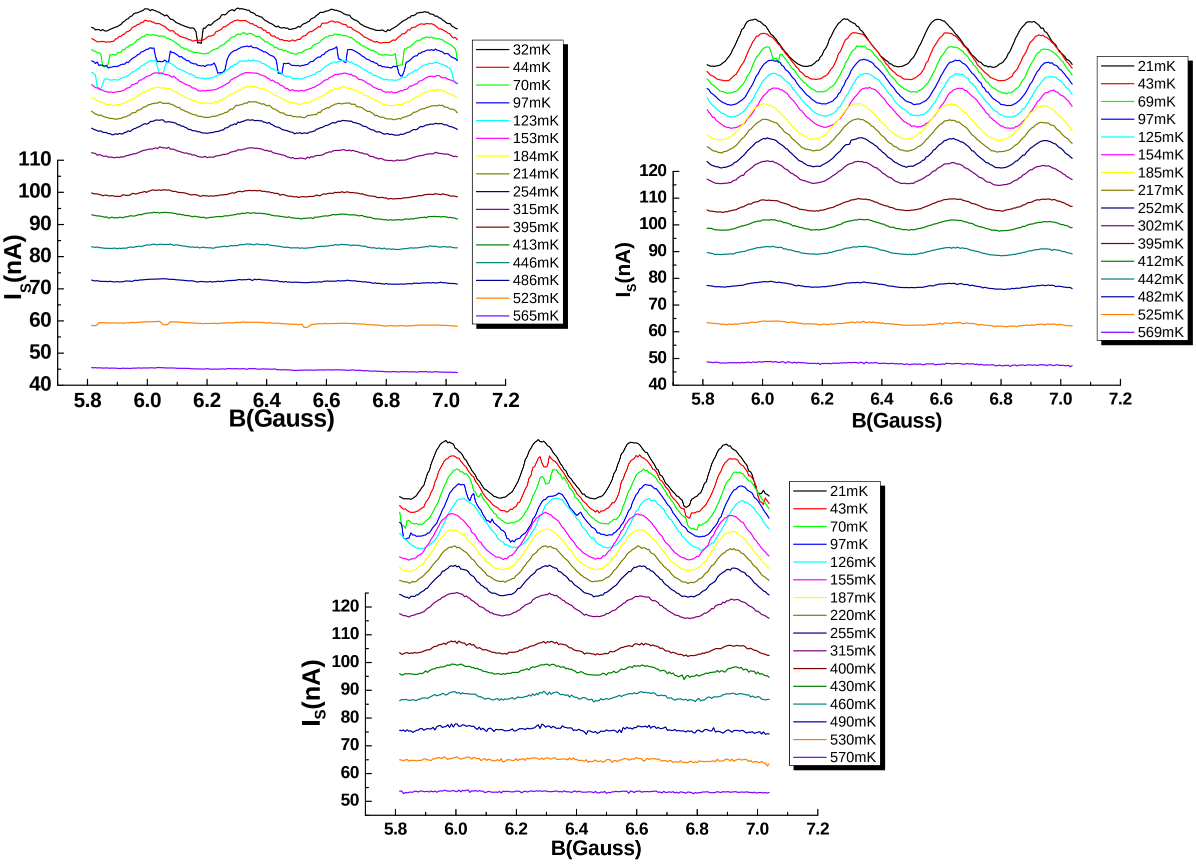

Figure 9.8: Temperature dependence of the SQUID switching current versus magnetic field for (a) $V_{BG} = -0.4V$, (b)$V_{BG} = 0V$, (c)$V_{BG} = +0.96V$. From these curves we can extract 1- The temperature dependence of the SQUID switching current, 2- The temperature dependence of the nanotube switching current and 3- The temperature dependence of the anharmonic current phase relations. In particular, we see the anharmonicities which are present at low temperature for $V_{BG} = 0V$ and $V_{BG} = 0.96V$ are quickly lifted by increasing the temperature.

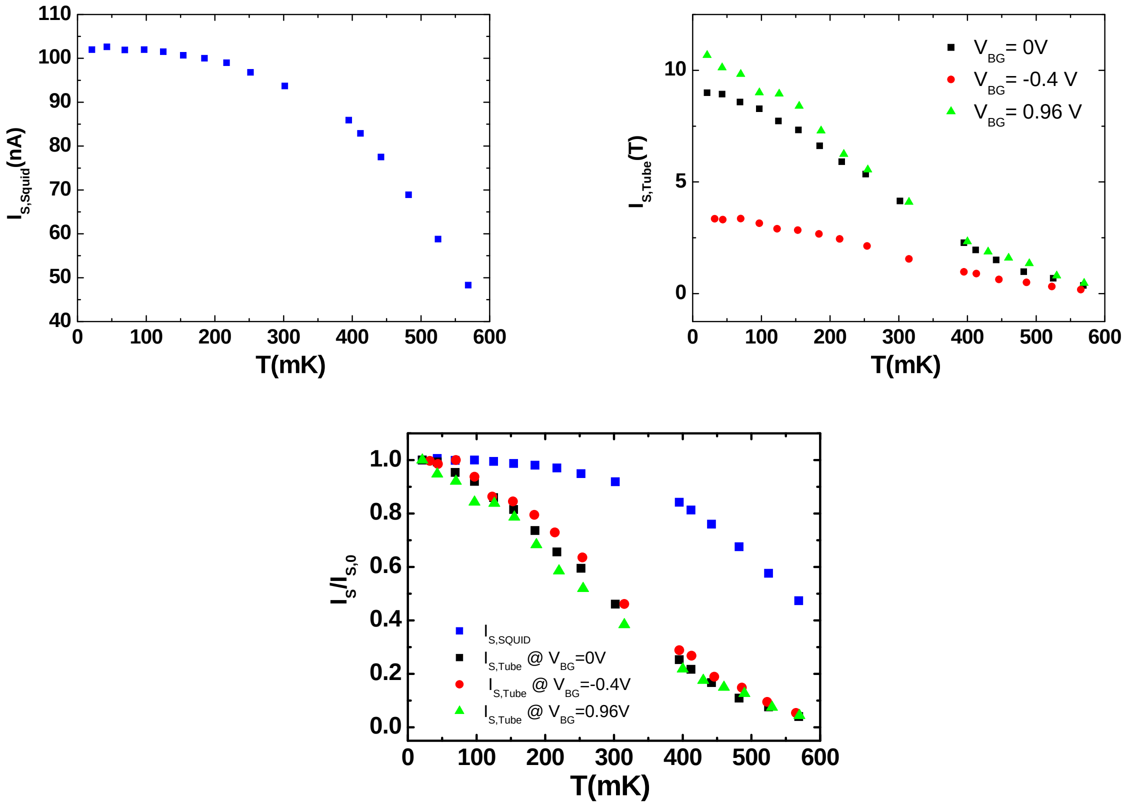

Figure 9.9: Temperature dependence of the (a) SQUID and (b) contribution due to the nanotube at different gate voltages. (c) Normalized temperature dependence of SQUID and nanotube supercurrent. The nanotube supercurrent vanishes faster than the entire SQUID supercurrent.

is visible when the current phase relation seems anharmonic and absent when harmonic. In order to be more quantitative, we have plotted the temperature dependence of the Fourier transform amplitude for the first ($\varphi^{-1}/(2\pi) = 1$) and second harmonics ($\varphi^{-1}/(2\pi) = 2$) at different gate voltages. This is shown in figure 9.11a. Whatever the gate position, the second harmonic amplitude is smaller than the first harmonic and the amplitude of the peaks is lowered by temperature. In order to compare the first and second harmonics behaviour, *i.e.* the harmonic and anharmonic behaviour, we renormalize to the maximum amplitude the first and second harmonics curve as shown in figure 9.11b. Interestingly the rate at which the second harmonic vanishes from a finite value to zero is always faster than for the first harmonic.

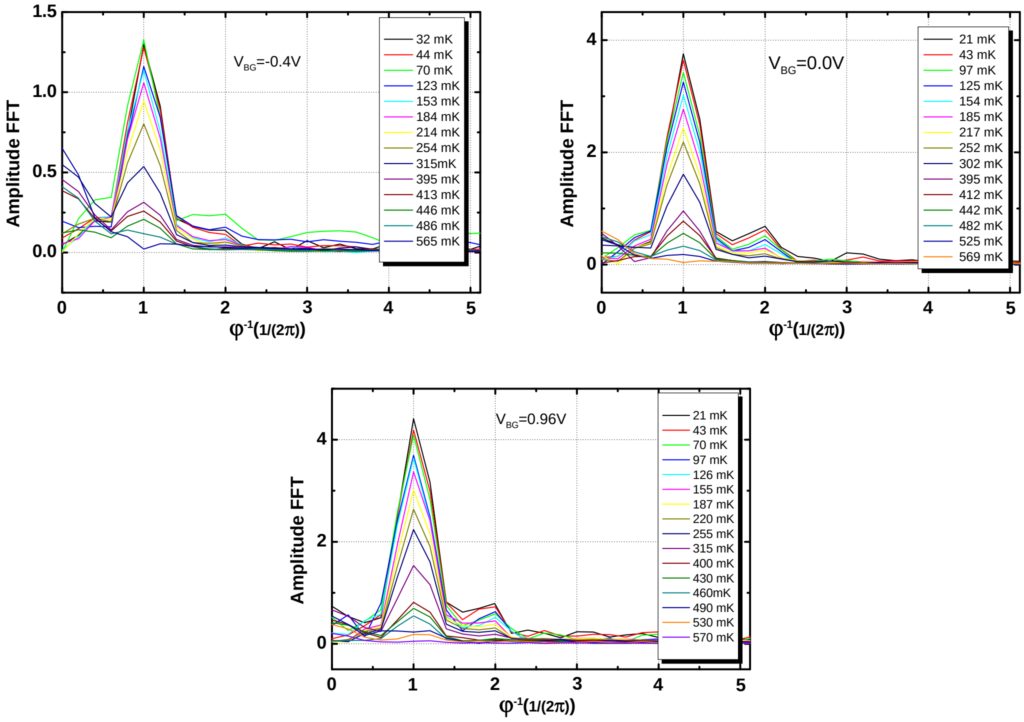

Figure 9.10: Temperature dependence of the current phase relation Fourier spectrum for (a) $V_{BG} = -0.4V$, (b)$V_{BG} = 0V$, (c)$V_{BG} = +0.96V$.

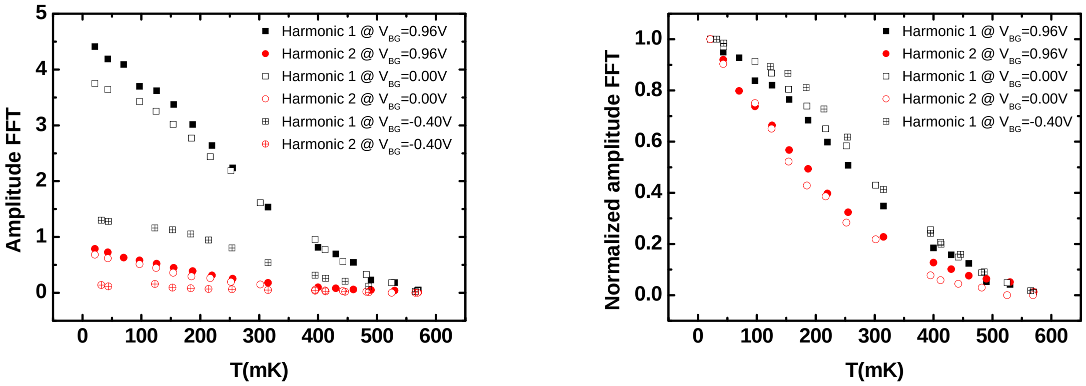

Figure 9.11: (a) Temperature dependence of the first and second harmonic of the current phase relation Fourier transform for $V_{BG} = -0.4,\ 0$ and $+0.96V$. (b)Temperature dependence of the renormalized amplitude of the first and second harmonic of the current phase relation Fourier transform. The second harmonic vanishes faster than the first harmonic.

9.5 Conclusion

In this chapter, we have measured the current-phase relation of a carbon nanotube quantum dot over a large range of gate voltage. At certain gate voltages supercurrents as high as 12 nA were induced through the tube. Jointly, the current-phase relation exhibits an anharmonic behaviour. We studied the temperature dependence of the amplitude and anharmonicity of the current phase relation and highlight that anharmonic components of the CPR vanishes faster than the harmonic component. Data processing and theoretical analysis is still under investigation at this point.

Our detection setup allows to relate the current phase relation measurements to the normal and superconducting states conductance. High supercurrent shows up each time the normal state conductance is high and conversely.

Conclusions and perspectives

Conclusions

Along this part we saw that a weak link connected to superconducting electrodes can support a supercurrent. This current is carried by Andreev Bound states into the weak link area. The energy spectrum of these subgap states depends on the phase difference between the two superconductors leading to a current which is also phase dependent. This is called the current-phase relation. As the shape and position of the ABS also depends on the exact nature of the weak link, one objectives of this thesis was to measure the current-phase relation of a carbon nanotube quantum dot in the regime $\Delta \sim T_K$ where there is a competition between Kondo effect and proximity effect. In this regime, very peculiar CPR are expected. This objective was not fulfilled but *"on the way"* results were obtained.

- **Result 1:** We evaluate an extension of the technique introduced by the Quantronics group [19] to measure in the same experiment the current phase relation of a small weak link together with its superconducting dc conductance. To do so a strongly asymmetric SQUID was considered. On one arm was incorporated a small Josephson junction (the tested weak link), on the other two large junctions in series with a central contact. The technique is accurate with respect to the harmonicity of the current phase relation tested. The adaptability of the proposed setup is *a priori* very large.

- **Result 2:** We measured the current-phase relation of a carbon nanotube quantum dot in the strong coupling regime. Supercurrents as high as 12 nA were induced through the tube. For high supercurrent the current-phase relation is anharmonic whereas for small supercurrent it is harmonic. The temperature dependence of the amplitude and anharmonicity of the current phase relation highlights that anharmonic components of the CPR vanishes faster than the harmonic component. Our detection setup allows to relate the current phase relation measurements to the normal and superconducting states conductance.

Perspectives

We aim to measure the current-phase relation of a carbon nanotube quantum dot in the Kondo regime. Being able to induce transitions between $'0'$ and $'\pi'$ states either making use of the gate voltage or the phase bias is of primary interest. Theoretical predictions in this domain are very numerous whereas the number of related experiments is very small [180].

Whereas carbon nanotubes are good systems to study the superconductivity/Kondo competition, any kind of weak link acting as a quantum dot can be used in this setup. In particular nanowires with strong spin/orbit coupling could be used. In this hypothesis, the spin/orbit interactions would lead to peculiar current phase relation exhibiting traces of the spin/orbit exchange amplitude that are tunable with an in-plane magnetic field for instance [197, 198]. This has never been observed experimentally.

Going a step even further, our technique could be used to detect unambiguously Majorana fermions. Indeed, recently theorists have proposed that Majorana fermions could appear as the fundamental quasiparticles in systems in which superconductors are in contact with materials that have a strong spin/orbit interaction [147, 148, 199, 200]. The Majorana fermions can be detected with a SQUID-like geometry because they would cause the SQUID to oscillate with a period of 4π rather than the usual 2π periodicity [31, 148, 199]. However it is of primary importance to first detect signatures of the effect in a conductance experiment and then measuring this strong evidence of the existence of Majorana fermions. Our detection scheme is at this point a very good candidate because it allows to measure in the same experiment the superconducting state conductance of the system and the current-phase relation.

The dynamics of the Kondo effect could also be studied. Indeed the Kondo effect takes place at a time scale given by the inverse of the Kondo temperature. If the phase difference evolves faster than this establishing time, one should expect a very different behaviour than in the static regime. Kondo correlation does not have time to establish. This could be probed using techniques presented in Ref. [149, 201].

General conclusion

General Conclusion

This thesis has studied two aspects of mesoscopic physics that are the high frequency quantum noise and the superconducting proximity effect. We nevertheless focused on a single model system: the carbon nanotube quantum dot.

The first part of this manuscript was dedicated to high frequency quantum noise measurements. In order to measure those fluctuations we have designed an original on-chip detection scheme in which the noise source and the detector, a Superconductor/ Insulator/ Superconductor junction, were resonantly coupled. This allowed us to measure the equilibrium noise of the resonant coupling circuit, the out-of-equilibrium noise of a Josephson junction and finally the out-of-equilibrium noise of a carbon nanotube quantum dot in the Kondo regime. The equilibrium noise of the resonator exhibits a strong asymmetry between emission and absorption. At low temperature only absorption noise related to zero point fluctuations is present. The out-of-equilibrium emission noise of quasiparticles tunneling of a Josephson junction exhibit a strong frequency dependence. For emission noise to occur at frequency ν, the applied bias voltage to the junction V of superconducting gap Δ must fulfill condition $e|V| \geq 2\Delta + h\nu$. The out-of equilibrium emission noise associated to the Kondo effect (characteristic energy k_BT_K with T_K the Kondo temperature) exhibits a strong singularity at $eV = h\nu$ as long as $k_BT_K \approx h\nu$. This singularity is related to peaks in the density of states of the dot pinned at the Fermi energy of the leads. At higher frequency $h\nu \approx 3k_BT_K$ the singularity vanishes highlighting strong decoherence effects induced by the bias voltage.

In the second part, we developped a technique allowing to measure in the same experiment the current/phase and the current/voltage relations of a weak link separating two superconductors. We have first tested this detection scheme on a small Josephson junction and then applied it to a carbon nanotube quantum dot. In this last case a supercurrent as high as 12 nA were observed jointly with an anharmonic current/phase relation.

Bibliography

[1] M.A. Nielsen and I.L. Chuang. *Quantum computation and Quantum information.* Cambridge, 2000.

[2] L.P. Kouwenhoven, C.M. Marcus, P.L. Mc Euen, S.Tarucha, R.M. Westervelt, and N.S. WingreenG.Schön. *Mesoscopic electron transport.* Kluwer, 1997.

[3] L. P. Kouwenhoven and L. I. Glazman. Revival of the kondo effect. *Phys. World*, 14:33, 2001.

[4] C. P. Moca, P. Simon, C. H. Chung, and G. Zaránd. Nonequilibrium frequency-dependent noise through a quantum dot: A real-time functional renormalization group approach. *Phys. Rev. B*, 83(20):201303, May 2011.

[5] Mahn-Soo Choi, Minchul Lee, Kicheon Kang, and W. Belzig. Kondo effect and josephson current through a quantum dot between two superconductors. *Phys. Rev. B*, 70(2):020502, Jul 2004.

[6] Y. M. Blanter and M. Büttiker. Shot noise in mesoscopic conductors. *Phys. Rep.*, 336:1, 2000.

[7] A. A. Clerk, M. H. Devoret, S. M. Girvin, Florian Marquardt, and R. J. Schoelkopf. Introduction to quantum noise, measurement, and amplification. *Rev. Mod. Phys.*, 82(2):1155–1208, Apr 2010.

[8] G. Lesovik and R. Loosen. On the detection of finite-frequency current fluctuations. *JETP Letters*, 65:295–299, 1997.

[9] P.-M. Billangeon, F. Pierre, H. Bouchiat, and R. Deblock. Emission and absorption asymmetry in the quantum noise of a josephson junction. *Phys. Rev. Lett.*, 96(13):136804, Apr 2006.

[10] M. H. Devoret. *Quantum Fluctuations in electrical circuits.* 1997.

[11] G.L. Ingold and Yu.V. Nazarov. Charge tunneling rates in ultrasmall junctions. In H. Grabert and M.H. Devoret, editors, *Single-Charge Tunneling*, New-York, 1992. Plenum.

[12] S. De Franceschi, R. Hanson, W. G. van der Wiel, J. M. Elzerman, J. J. Wijpkema, T. Fujisawa, S. Tarucha, and L. P. Kouwenhoven. Out-of-equilibrium kondo effect in a mesoscopic device. *Phys. Rev. Lett.*, 89(15):156801, Sep 2002.

[13] R. Leturcq, L. Schmid, K. Ensslin, Y. Meir, D. C. Driscoll, and A. C. Gossard. Probing the kondo density of states in a three-terminal quantum ring. *Phys. Rev. Lett.*, 95(12):126603, Sep 2005.

[14] J. Paaske, A. Rosch, J. Kroha, and P. Wölfle. Nonequilibrium transport through a kondo dot: Decoherence effects. *Phys. Rev. B*, 70(15):155301, Oct 2004.

[15] R. C. Monreal and F. Flores. Kondo resonance decoherence caused by an external potential. *Phys. Rev. B*, 72(19):195105, Nov 2005.

[16] Raphaël Van Roermund, Shiue-Yuan Shiau, and Mireille Lavagna. Anderson model out of equilibrium: Decoherence effects in transport through a quantum dot. *Phys. Rev. B*, 81(16):165115, Apr 2010.

[17] P.G. de Gennes. *Superconductivity of metals and alloys.* W. A. Benjamin, Inc.,New York, 1966.

[18] A. F. Andreev. Thermal conductivity of the intermediate state of superconductors. *Zh. Eksp. Teor. Fiz [Sov. Phys. JETP **19**,1228 (1964)]*, 46:1823, 1964.

[19] M. L. Della Rocca, M. Chauvin, B. Huard, H. Pothier, D. Esteve, and C. Urbina. Measurement of the current-phase relation of superconducting atomic contacts. *Phys. Rev. Lett.*, 99(12):127005, Sep 2007.

[20] van Ruitenbeek J. Agrait N., Levi Yeyati A. Quantum properties of atomic-sized conductors. *Physics Reports*, 377:81–279, 2003.

[21] Hongkun Park, Jiwoong Park, Andrew K. L. Lim, Erik H. Anderson, A. Paul Alivisatos, and Paul L. McEuen. Nanomechanical oscillations in a single-c60 transistor. *Nature*, 407:57–60, 2000.

[22] Jiwoong Park, Abhay N. Pasupathy, Jonas I. Goldsmith, Connie Chang, Yuval Yaish, Jason R. Petta, Marie Rinkoski, James P. Sethna, Héctor D. Abruña, Paul L. McEuen, and Daniel C. Ralph. Coulomb blockade and the kondo effect in single-atom transistors. *Nature*, 417:722–725, 2002.

[23] A. Yu. Kasumov, M. Kociak, S. Guéron, B. Reulet, V. T. Volkov, D. V. Klinov, and H. Bouchiat. Proximity-induced superconductivity in dna. *Science*, 291:280–282, 2000.

[24] S.J. Tans, M.H. Devoret, H. Dai, A. Thess, R.E. Smalley, L.J. Geerligs, and C. Dekker. Individual single-wall carbon nanotubes as quantum wires. *Nature*, 386:474, 1997.

[25] D.V. Averin and K.K Likharev. *Mesoscopic Phenomena in Solids*. Elsevier, Amsterdam, 1991.

[26] D. Goldhaber-Gordon, Hadas Shtrikman, D. Mahalu, David Abusch-Magder, U. Meirav, and M. A. Kastner. Kondo effect in a single-electron transistor. *Nature*, 391:156–159, 1998.

[27] Pablo Jarillo-Herrero, Jing Kong, Herre S.J. van der Zant, Cees Dekker, Leo P. Kouwenhoven, and Silvano De Franceschi. Orbital kondo effect in carbon nanotubes. *Nature*, 488:434, 484, 2005.

[28] A. Yu. Kasumov, R. Deblock, M. Kociak, B. Reulet, H. Bouchiat, I. I. Khodos, Yu. B. Gorbatov, V. T. Volkov, C. Journet, and M. Burghard. Supercurrents through single-walled carbon nanotubes. *Science*, 284(5419):1508–1511, 1999.

[29] P. Jarillo-Herrero, J. A. van Dam, and L. P. Kouwenhoven. Quantum supercurrent transistors in carbon nanotubes. *Nature*, 439:953, 2006.

[30] C. B. Winkelmann, N. Roch, W. Wernsdorfer, V. Bouchiat, and F. Balestro. Superconductivity in a single-c60 transistor. *Nature Phys.*, 5:87–879, 2009.

[31] Silvano De Franceschi, Leo Kouwenhoven, Christian Schönenberger, and Wolfgang Wernsdorfer. Hybrid superconductor-quantum dot devices. *Nature Nanotechnology*, 5:703–711, 2010.

[32] S. Iijima. Helical microtubules of graphitic carbon. *Nature*, 354:56, 1991.

[33] M. M. J. Treacy, T. W. Ebbesen, and J. M. Gibson. Exceptionally high young's modulus observed for individual carbon nanotubes. *Nature*, 381:678, 1996.

[34] H. Dai, A. Javey, E. Pop, D. Mann, and Y. Lu. *NANO: Brief Reports and Reviews*, 1:1–4, 2006.

[35] Seunghun Hong and Sung Myung. Nanotube electronics: A flexible approach to mobility. *Nature Nanotechnology*, 2:207–208, 2007.

[36] B. Q. Wei, R. Vajtai, and P. M. Ajayan. Reliability and current carrying capacity of carbon nanotubes. *Appl. Phys. Lett.*, 79:1172, 2001.

[37] Wikipedia. Carbon nanotube.

[38] C. Schönenberger. *Semiconductor Science and technology*, 21:1, 2006.

[39] M. Bockrath, D.H. Cobden, J. Liu, A.G. Rinzler, R.E. Smalleyand L. Balents, and P.L. McEuen. Luttinger-liquid behaviour in carbon nanotubes. *Nature*, 397:598, 1999.

[40] J. W. G. Wildöer, L. C. Venema, A. G. Rinzler, R. E. Smalley, and C. Dekker. Electronic structure of atomically resolved carbon nanotubes. *Nature*, 391:59, 1998.

[41] T. W. Odom, J.-L. Huang, P. Kim, and C.M. Lieber. Atomic structure and electronic properties of single-walled carbon nanotubes. *Nature*, 391:62–64, 1998.

[42] A. Yu. Kasumov, K. Tsukagoshi, M. Kawamura, T. Kobayashi, Y. Aoyagi, K. Senba, T. Kodama, H. Nishikawa, I. Ikemoto, K. Kikuchi, V. T. Volkov, Yu. A. Kasumov, R. Deblock, S. Guéron, and H. Bouchiat. Proximity effect in a superconductor-metallofullerene-superconductor molecular junction. *Phys. Rev. B*, 72(3):033414, Jul 2005.

[43] L P Kouwenhoven, D G Austing, and S Tarucha. Few-electron quantum dots. *Reports on Progress in Physics*, 64(6):701, 2001.

[44] Marc Bockrath, David H. Cobden, Paul L. McEuen, Nasreen G. Chopra, A. Zettl, Andreas Thess, and R. E. Smalley. Single-electron transport in ropes of carbon nanotubes. *Science*, 275(5308):1922–1925, 1997.

[45] I. L. Kurland, I. L. Aleiner, and B. L. Altshuler. Mesoscopic magnetization fluctuations for metallic grains close to the stoner instability. *Phys. Rev. B*, 62(22):14886–14897, Dec 2000.

[46] I.L. Aleiner, P.W. Brouwer, and L.I. Glazman. *Phys. Rep.*, 358:309, 2002.

[47] Michael Pustilnik and Leonid Glazman. Kondo effect in quantum dots. *Journal of Physics: Condensed Matter*, 16(16):R513, 2004.

[48] M. R. Buitelaar, A. Bachtold, T. Nussbaumer, M. Iqbal, and C. Schönenberger. Multiwall carbon nanotubes as quantum dots. *Phys. Rev. Lett.*, 88(15):156801, Mar 2002.

[49] Stefan Frank, Philippe Poncharal, Z. L. Wang, and Walt A. de Heer. Carbon nanotube quantum resistors. *Science*, 280(5370):1744–1746, 1998.

[50] C.T. White and T.N. Todorov. Carbon nanotubes as long ballistic conductors. *Nature*, 393:240–242, 1998.

[51] C. Dekker. Carbon nanotubes as molecular quantum wires. *Phys. Today*, 52(5):22–28, 1999.

[52] W. Liang, M. Bockrath, D. Bozovic, J. H. Hafner, M. Tinkham, and H. Park. Fabry - perot interference in a nanotube electron waveguide. *Nature*, 411:665, 2001.

[53] B. J. van Wees, L. P. Kouwenhoven, C. J. P. M. Harmans, J. G. Williamson, C. E. Timmering, M. E. I. Broekaart, C. T. Foxon, and J. J. Harris. Observation of zero-dimensional states in a one-dimensional electron interferometer. *Phys. Rev. Lett.*, 62(21):2523–2526, May 1989.

[54] H. R. Zeller and I. Giaever. Tunneling, zero-bias anomalies, and small superconductors. *Phys. Rev.*, 181(2):789–799, May 1969.

[55] D. V. Averin and Yu. V. Nazarov. Virtual electron diffusion during quantum tunneling of the electric charge. *Phys. Rev. Lett.*, 65(19):2446–2449, Nov 1990.

[56] S. De Franceschi, S. Sasaki, J. M. Elzerman, W. G. van der Wiel, S. Tarucha, and L. P. Kouwenhoven. Electron cotunneling in a semiconductor quantum dot. *Phys. Rev. Lett.*, 86(5):878–881, Jan 2001.

[57] P. W. Anderson. Localized magnetic states and fermi-surface anomalies in tunneling. *Phys. Rev. Lett.*, 17(2):95–97, Jul 1966.

[58] Jun Kondo. Resistance minimum in dilute magnetic alloys. *Prog. Theor. Phys.*, 32:37–49, 1964.

[59] P.W. Anderson. A poor man's derivation of scaling laws for the kondo problem. *J. Phys. C: Solid State Phys*, 3:2436, 1970.

[60] Tai Kai Ng and Patrick A. Lee. On-site coulomb repulsion and resonant tunneling. *Phys. Rev. Lett.*, 61(15):1768–1771, Oct 1988.

[61] L. I. Glazman and M. E. Raikh. Resonant kondo transparency of a barrier with quasilocal impurity states. *JETP Letters*, 47:452–455, 1988.

[62] Yigal Meir, Ned S. Wingreen, and Patrick A. Lee. Low-temperature transport through a quantum dot: The anderson model out of equilibrium. *Phys. Rev. Lett.*, 70(17):2601–2604, Apr 1993.

[63] Ned S. Wingreen and Yigal Meir. Anderson model out of equilibrium: Noncrossing-approximation approach to transport through a quantum dot. *Phys. Rev. B*, 49(16):11040–11052, Apr 1994.

[64] Sara M. Cronenwett, Tjerk H. Oosterkamp, and Leo P. Kouwenhoven. A tunable kondo effect in quantum dots. *Science*, 281(5376):540–544, 1998.

[65] W.G. van der Wiel, S. De Franceschi, T. Fujisawa, J.M. Elzerman, S. Tarucha, , and L.P. Kouwenhoven. The kondo effect in the unitary limit. *Science*, 289:2105, 2000.

[66] L.I. Glazman and K. A. Matveev. Resonant josephson current via kondo-impurities in a tunnel junction. *JETP Lett.*, 49:659, 1989.

[67] A. M. Tsvelick and P. B. Wiegmann. Exact results in the theory of magnetic alloys. *Advances in Physics*, 32:453, 1983.

[68] N. E. Bickers. Review of techniques in the large-n expansion for dilute magnetic alloys. *Rev. Mod. Phys.*, 59(4):845–939, Oct 1987.

[69] D. Goldhaber-Gordon, J. Göres, M. A. Kastner, Hadas Shtrikman, D. Mahalu, and U. Meirav. From the kondo regime to the mixed-valence regime in a single-electron transistor. *Phys. Rev. Lett.*, 81(23):5225–5228, Dec 1998.

[70] Roger H. Koch, D. J. Van Harlingen, and John Clarke. Observation of zero-point fluctuations in a resistively shunted josephson tunnel junction. *Phys. Rev. Lett.*, 47(17):1216–1219, Oct 1981.

[71] B. Yurke, P. G. Kaminsky, R. E. Miller, E. A. Whittaker, A. D. Smith, A. H. Silver, and R. W. Simon. Observation of 4.2-k equilibrium-noise squeezing via a josephson-parametric amplifier. *Phys. Rev. Lett.*, 60(9):764–767, Feb 1988.

[72] R. J. Schoelkopf, P. J. Burke, A. A. Kozhevnikov, D. E. Prober, and M. J. Rooks. Frequency dependence of shot noise in a diffusive mesoscopic conductor. *Phys. Rev. Lett.*, 78(17):3370–3373, Apr 1997.

[73] E. Zakka-Bajjani, J. Ségala, F. Portier, P. Roche, D. C. Glattli, A. Cavanna, and Y. Jin. Experimental test of the high-frequency quantum shot noise theory in a quantum point contact. *Phys. Rev. Lett.*, 99(23):236803, Dec 2007.

[74] Ramón Aguado and Leo P. Kouwenhoven. Double quantum dots as detectors of high-frequency quantum noise in mesoscopic conductors. *Phys. Rev. Lett.*, 84(9):1986–1989, Feb 2000.

[75] Richard Deblock, Eugen Onac, Leonid Gurevich, and Leo P. Kouwenhoven. Detection of quantum noise from an electrically driven two-level system. *Science*, 301(5630):203–206, 2003.

[76] M. B. Weissman. $1f$ noise and other slow, nonexponential kinetics in condensed matter. *Rev. Mod. Phys.*, 60(2):537–571, Apr 1988.

[77] Norman O. Birge, Brage Golding, and W. H. Haemmerle. Electron quantum interference and $1f$ noise in bismuth. *Phys. Rev. Lett.*, 62(2):195–198, Jan 1989.

[78] Sh. Kogan. *Electronic noise and fluctuations in solids.* Cambridge University Press, 1996.

[79] J.B. Johnson. Thermal agitation of electricity in conductors. *Phys. Rev.*, 32:97, 1928.

[80] H. Nyquist. Thermal agitation of electric charge in conductors. *Phys. Rev.*, 32:110, 1928.

[81] Andrew H. Steinbach, John M. Martinis, and Michel H. Devoret. Observation of hot-electron shot noise in a metallic resistor. *Phys. Rev. Lett.*, 76(20):3806–3809, May 1996.

[82] A. W. Hull and N. H. Williams. Determination of elementary charge e from measurements of shot-effect. *Phys. Rev.*, 25(2):147–173, Feb 1925.

[83] R. de Picciotto, M. Reznikov, M. Heiblum, V. Umansky, and D. Bunin, G. andMahalu. Direct observation of a fractional charge. *Nature*, 389:162–164, 1997.

[84] L. Saminadayar, D. C. Glattli, Y. Jin, and B. Etienne. Observation of the $e/3$ fractionally charged laughlin quasiparticle. *Phys. Rev. Lett.*, 79(13):2526–2529, Sep 1997.

[85] X. Jehl, P. Payet-Burin, C. Baraduc, R. Calemczuk, and M. Sanquer. Andreev reflection enhanced shot noise in mesoscopic sns junctions. *Phys. Rev. Lett.*, 83(8):1660–1663, Aug 1999.

[86] X. Jehl, M. Sanquer, R. Calemczuk, and D. Mailly. Detection of doubled shot noise in short normal-metal/ superconductor junctions. *Nature*, 405:50, 2000.

[87] R. Landauer and M. Büttiker. Resistance of small metallic loops. *Phys. Rev. Lett.*, 54(18):2049–2052, May 1985.

[88] U. Gavish, Y. Levinson, and Y. Imry. Detection of quantum noise. *Phys. Rev. B*, 62(16):R10637–R10640, Oct 2000.

[89] Y. Imry. *Introduction to mesoscopic physics.* Oxford University Press, 1997.

[90] A.O. Caldeira and A.J. Leggett. *Annals of Physics*, 149:374, 1983.

[91] M. Büttiker. Scattering theory of current and intensity noise correlations in conductors and wave guides. *Phys. Rev. B*, 46(19):12485–12507, Nov 1992.

[92] E. A. Rothstein, O. Entin-Wohlman, and A. Aharony. Noise spectra of a biased quantum dot. *Phys. Rev. B*, 79(7):075307, Feb 2009.

[93] D. Rogovin and D.J. Scalapino. *Annals of Physics*, 86:1, 1974.

[94] Ines Safi. Time-dependent theory of non-linear response and current fluctuations. arXiv:0908.4382, 2009.

[95] U. Gavish. *Quantum current noise in mesoscopic systems.* PhD thesis, Weizmann institute of Science, Israel, 2003.

[96] Landau and Lifchitz. *Electrodynamic of continuous media.* MIR edition, Moscou, 1969.

[97] Yoshiaki Yamauchi, Koji Sekiguchi, Kensaku Chida, Tomonori Arakawa, Shuji Nakamura, Kensuke Kobayashi, Teruo Ono, Tatsuya Fujii, and Rui Sakano. Evolution of the kondo effect in a quantum dot probed by shot noise. *Phys. Rev. Lett.*, 106(17):176601, Apr 2011.

[98] R. J. Schoelkopf, A. A. Clerk, S. M. Girvin, K. W. Lehnert, and M. H. Devoret. Qubits as spectrometers of quantum noise. In Y.V. Nazarov, editor, *Quantum Noise in Mesoscopic Physics*, Dordrecht, 2003. NATO Science Series, Kluwer.

[99] J. Gabelli and B. Reulet. Dynamics of quantum noise in a tunnel junction under ac excitation. *Phys. Rev. Lett.*, 100(2):026601, Jan 2008.

[100] O. Astafiev, Yu. A. Pashkin, Y. Nakamura, T. Yamamoto, and J. S. Tsai. Quantum noise in the josephson charge qubit. *Phys. Rev. Lett.*, 93(26):267007, Dec 2004.

[101] S. Gustavsson, M. Studer, R. Leturcq, T. Ihn, K. Ensslin, D. C. Driscoll, and A. C. Gossard. Frequency-selective single-photon detection using a double quantum dot. *Phys. Rev. Lett.*, 99(20):206804, Nov 2007.

[102] E. Onac. *High frequency noise detection in mesoscopic devices.* PhD thesis, Delft University of Technology, The Netherlands, 2005.

[103] Q. Le Masne, H. Pothier, Norman O. Birge, C. Urbina, and D. Esteve. Asymmetric noise probed with a josephson junction. *Phys. Rev. Lett.*, 102(6):067002, Feb 2009.

[104] L. S. Levitov and G. B. Lesovik. *JETP Lett.*, 55:555, 1992.

[105] B. Reulet, J. Senzier, and D. E. Prober. Environmental effects in the third moment of voltage fluctuations in a tunnel junction. *Phys. Rev. Lett.*, 91(19):196601, Nov 2003.

[106] E. Onac, F. Balestro, L. H. Willems van Beveren, U. Hartmann, Y. V. Nazarov, and L. P. Kouwenhoven. Using a quantum dot as a high-frequency shot noise detector. *Phys. Rev. Lett.*, 96(17):176601, May 2006.

[107] P.-M. Billangeon, F. Pierre, H. Bouchiat, and R. Deblock. ac josephson effect and resonant cooper pair tunneling emission of a single cooper pair transistor. *Phys. Rev. Lett.*, 98(21):216802, May 2007.

[108] D. V. Averin and A. A. Odintsov. Macroscopic quantum tunneling of the electric charge in small tunnel junctions. *Physics Letters A*, 140:251–257, 1989.

[109] M. H. Devoret, D. Esteve, H. Grabert, G.-L. Ingold, H. Pothier, and C. Urbina. Effect of the electromagnetic environment on the coulomb blockade in ultrasmall tunnel junctions. *Phys. Rev. Lett.*, 64(15):1824–1827, Apr 1990.

[110] Pierre-Marie Billangeon. *Détection de bruit quantique mésoscopique à très haute fréquence*. PhD thesis, Université Paris-Sud, Orsay, France, 2008.

[111] T. Holst, D. Esteve, C. Urbina, and M. H. Devoret. Effect of a transmission line resonator on a small capacitance tunnel junction. *Phys. Rev. Lett.*, 73(25):3455–3458, Dec 1994.

[112] M. Tinkham. *Introduction to superconductivity*. McGraw-Hill, Singapore, 2nd edition, 1996.

[113] A. Barone and G. Paterno. *Physics and Applications of the Josephson effect*. Wiley-Interscience, New-York, 1982.

[114] Vinay Ambegaokar and Alexis Baratoff. Tunneling between superconductors. *Phys. Rev. Lett.*, 10(11):486–489, Jun 1963.

[115] Julien Claudon. *Oscillation coherentes dans un circuit quantique supraconducteur*. PhD thesis, Université Joseph Fourier, 2005.

[116] Qing Hu, C. A. Mears, P. L. Richards, and F. L. Lloyd. Observation of nondissipative quasiparticle tunnel currents in superconducting tunnel junctions. *Phys. Rev. Lett.*, 64(24):2945–2948, Jun 1990.

[117] John R. Tucker and Marc J. Feldman. Quantum detection at millimeter wavelengths. *Rev. Mod. Phys.*, 57(4):1055–1113, Oct 1985.

[118] A. H. Worsham, N. G. Ugras, D. Winkler, D. E. Prober, N. R. Erickson, and P. F. Goldsmith. Quantum tunneling currents in a superconducting junction. *Phys. Rev. Lett.*, 67(21):3034–3037, Nov 1991.

[119] R. Kubo. The fluctuation-dissipation theorem. *Reports on Progress in Physics*, 29(1):255, 1966.

[120] P. K. Tien and J. P. Gordon. Multiphoton process observed in the interaction of microwave fields with the tunneling between superconductor films. *Phys. Rev.*, 129(2):647–651, Jan 1963.

[121] J. Nygard, D. H. Cobden, and P. E. Lindelof. Kondo physics in carbon nanotubes. *Nature*, 408:342–346, 2000.

[122] Yigal Meir and Anatoly Golub. Shot noise through a quantum dot in the kondo regime. *Phys. Rev. Lett.*, 88(11):116802, Mar 2002.

[123] Eran Sela, Yuval Oreg, Felix von Oppen, and Jens Koch. Fractional shot noise in the kondo regime. *Phys. Rev. Lett.*, 97(8):086601, Aug 2006.

[124] A. Golub. Shot noise near the unitary limit of a kondo quantum dot. *Phys. Rev. B*, 73(23):233310, Jun 2006.

[125] A. O. Gogolin and A. Komnik. Full counting statistics for the kondo dot in the unitary limit. *Phys. Rev. Lett.*, 97(1):016602, Jul 2006.

[126] Christophe Mora, Xavier Leyronas, and Nicolas Regnault. Current noise through a kondo quantum dot in a su(n) fermi liquid state. *Phys. Rev. Lett.*, 100(3):036604, Jan 2008.

[127] T. Delattre, C. Feuillet-Palma, L. G. Herrmann, P. Morfin, J.-M. Berroir, G. Fève, B. Plaçais, D. C. Glattli, M.-S. Choi, C. Mora, , and T. Kontos. Noisy kondo impurities. *Nature Physics*, 5:208, 2009.

[128] O. Zarchin, M. Zaffalon, M. Heiblum, D. Mahalu, and V. Umansky. Two-electron bunching in transport through a quantum dot induced by kondo correlations. *Phys. Rev. B*, 77(24):241303, Jun 2008.

[129] Peter Nordlander, Michael Pustilnik, Yigal Meir, Ned S. Wingreen, and David C. Langreth. How long does it take for the kondo effect to develop? *Phys. Rev. Lett.*, 83(4):808–811, Jul 1999.

[130] J. Basset, H. Bouchiat, and R. Deblock. Emission and absorption quantum noise measurement with an on-chip resonant circuit. *Phys. Rev. Lett.*, 105(16):166801, Oct 2010.

[131] Y.A. Kasumov, A. Shailos, I.I. Khodos, V.T. Volkov, V.I. Levashov, V.N. Matveev, S. Guéron, M. Kobylko, M. Kociak, H. Bouchiat, V. Agache, A.S. Rollier, L. Buchaillot, A.M. Bonnot, and A.Y. Kasumov. Cvd growth of carbon nanotubes at very low pressure of acetylene. *Applied Physics A: Materials Science and Processing*, 88:687–691, 2007.

[132] A. Cox, D. L. & Zawadowski. Exotic kondo effects in metals: magnetic ions in a crystalline electric field and tunnelling centers. *Adv. Phys.*, 47:599–942, 1998.

[133] O. Yu. Kolesnychenko, R. de Kort, M. I. Katsnelson, A. I. Lichtenstein, and H. van Kempen. Real-space imaging of an orbital kondo resonance on the cr(001) surface. *Nature*, 415:507–509, 2002.

[134] Manh-Soo Choi, Rosa López, and Ramón Aguado. Su(4) kondo effect in carbon nanotubes. *Phys. Rev. Lett.*, 95(6):067204, Aug 2005.

[135] A. Makarovski, A. Zhukov, J. Liu, and G. Finkelstein. Su(2) and su(4) kondo effects in carbon nanotube quantum dots. *Phys. Rev. B*, 75(24):241407, Jun 2007.

[136] P. W. Anderson. Localized magnetic states in metals. *Phys. Rev.*, 124(1):41–53, Oct 1961.

[137] M. Grobis, I. G. Rau, R. M. Potok, H. Shtrikman, and D. Goldhaber-Gordon. Universal scaling in nonequilibrium transport through a single channel kondo dot. *Phys. Rev. Lett.*, 100(24):246601, Jun 2008.

[138] J. Basset, H. Bouchiat, and R. Deblock. High frequency quantum noise and admittance measurement with an on-chip resonant circuit. 2011.

[139] M. Sindel, W. Hofstetter, J. von Delft, and M. Kindermann. Frequency-dependent transport through a quantum dot in the kondo regime. *Phys. Rev. Lett.*, 94(19):196602, May 2005.

[140] Avraham Schiller and Selman Hershfield. Toulouse limit for the nonequilibrium kondo impurity: Currents, noise spectra, and magnetic properties. *Phys. Rev. B*, 58(22):14978–15010, Dec 1998.

[141] Thomas Korb, Frank Reininghaus, Herbert Schoeller, and Jürgen König. Real-time renormalization group and cutoff scales in nonequilibrium applied to an arbitrary quantum dot in the coulomb blockade regime. *Phys. Rev. B*, 76(16):165316, Oct 2007.

[142] Fabrizio Dolcini, Björn Trauzettel, Inès Safi, and Hermann Grabert. Transport properties of single-channel quantum wires with an impurity: Influence of finite length and temperature on average current and noise. *Phys. Rev. B*, 71(16):165309, Apr 2005.

[143] Björn Trauzettel, Inès Safi, Fabrizio Dolcini, and Hermann Grabert. Appearance of fractional charge in the noise of nonchiral luttinger liquids. *Phys. Rev. Lett.*, 92(22):226405, Jun 2004.

[144] Inès Safi, Cristina Bena, and Adeline Crépieux. ac conductance and nonsymmetrized noise at finite frequency in quantum wires and carbon nanotubes. *Phys. Rev. B*, 78(20):205422, Nov 2008.

[145] L. G. Herrmann, T. Delattre, P. Morfin, J.-M. Berroir, B. Plaçais, D. C. Glattli, and T. Kontos. Shot noise in fabry-perot interferometers based on carbon nanotubes. *Phys. Rev. Lett.*, 99(15):156804, Oct 2007.

[146] J. Carlos Egues, Guido Burkard, D. S. Saraga, John Schliemann, and Daniel Loss. Shot noise and spin-orbit coherent control of entangled and spin-polarized electrons. *Phys. Rev. B*, 72(23):235326, Dec 2005.

[147] Jay D. Sau, Roman M. Lutchyn, Sumanta Tewari, and S. Das Sarma. Generic new platform for topological quantum computation using semiconductor heterostructures. *Phys. Rev. Lett.*, 104(4):040502, Jan 2010.

[148] Roman M. Lutchyn, Jay D. Sau, and S. Das Sarma. Majorana fermions and a topological phase transition in semiconductor-superconductor heterostructures. *Phys. Rev. Lett.*, 105(7):077001, Aug 2010.

[149] F. Chiodi. *Dynamical effects in Superconductor/Normal metal/Superconductor long Josephson Junctions.* PhD thesis, Université Paris Sud, 2010.

[150] B. D. Josephson. Possible new effects in superconductive tunnelling. *Physics Letters*, 1(7):251 – 253, 1962.

[151] J-D. Pillet, C. H. L. Quay, P. Morfin, C. Bena, A. Levy Yeyati, and P. Joyez. Andreev bound states in supercurrent-carrying carbon nanotubes revealed. *Nature Physics*, 6:965–969, 2010.

[152] I.O. Kulik. Macroscopic quantization and the proximity e?ect in s-n-s junctions. *Zh. Eksp. Teor. Fiz. [Sov. Phys. JETP* ***30****(5), 944 (1970)]*, 57(5):1745–1759, 1969.

[153] G. E. Blonder, M. Tinkham, and T. M. Klapwijk. Transition from metallic to tunneling regimes in superconducting microconstrictions: Excess current, charge imbalance, and supercurrent conversion. *Phys. Rev. B*, 25(7):4515–4532, Apr 1982.

[154] Akira Furusaki, Hideaki Takayanagi, and Masaru Tsukada. Theory of quantum conduction of supercurrent through a constriction. *Phys. Rev. Lett.*, 67(1):132–135, Jul 1991.

[155] I.O. Kulik and A.N. Omel'yanchuk. Properties of superconducting microbridges in the pure limit. *Fiz. Nizk. Temp. [Sov. J. Low. Temp. Phys.* ***3****, 459 (1977)]*, 3(7):945, 1977.

[156] C. W. J. Beenakker and H. van Houten. Josephson current through a superconducting quantum point contact shorter than the coherence length. *Phys. Rev. Lett.*, 66(23):3056–3059, Jun 1991.

[157] J. Richter W. Haberkorn, H. Knauer. A theoretical study of the current-phase relation in josephson contacts. *Phys. Stat. Sol.*, 47:K161–K164, 1978.

[158] G.B. Arnold. Superconducting tunneling without the tunneling hamiltonian. *Journal of Low Temperature Physics*, 59:143–183, 1985.

[159] A. Martín-Rodero, F. J. García-Vidal, and A. Levy Yeyati. Microscopic theory of josephson mesoscopic constrictions. *Phys. Rev. Lett.*, 72(4):554–557, Jan 1994.

[160] J. M. Rowell. Tunneling observation of bound states in a normal metal—superconductor sandwich. *Phys. Rev. Lett.*, 30(5):167–170, Jan 1973.

[161] H. le Sueur, P. Joyez, H. Pothier, C. Urbina, and D. Esteve. Phase controlled superconducting proximity effect probed by tunneling spectroscopy. *Phys. Rev. Lett.*, 100(19):197002, May 2008.

[162] F. Chiodi, M. Ferrier, K.Tikhonov, P. Virtanen, T.T. Heikkilä, M. Feigelman, S. Guéron, and H.Bouchiat. Microwave response of an ns ring coupled to a superconducting resonator. arXiv:1005.0406, 2010.

[163] Benjamin Huard. *Interactions between electrons, mesoscopic Josephson effect and asymmetric current fluctuations.* PhD thesis, Université Paris 6, France, 2006.

[164] C.W.J. Beenakker. Three ŚuniversalŠ mesoscopic josephson effects. In *H. Fukuyama, T. Ando (Eds.), Proceedings of the 14th Taniguchi International Symposium on Transport Phenomena in Mesoscopic Systems, Springer, Berlin, pp. 235Ű253.*, 1992.

[165] D. Averin and A. Bardas. ac josephson effect in a single quantum channel. *Phys. Rev. Lett.*, 75(9):1831–1834, Aug 1995.

[166] J. C. Cuevas, A. Martín-Rodero, and A. Levy Yeyati. Hamiltonian approach to the transport properties of superconducting quantum point contacts. *Phys. Rev. B*, 54(10):7366–7379, Sep 1996.

[167] T.M. Klapwijk, G.E. Blonder, and M. Tinkham. Explanation of subharmonic energy gap structure in superconducting contacts. *Physica B*, 109 & 110:1657–1664, 1982.

[168] A. V. Rozhkov and Daniel P. Arovas. Josephson coupling through a magnetic impurity. *Phys. Rev. Lett.*, 82(13):2788–2791, Mar 1999.

[169] Jong Soo Lim, Mahn-Soo Choi, M. Y. Choi, Rosa López, and Ramón Aguado. Kondo effects in carbon nanotubes: From su(4) to su(2) symmetry. *Phys. Rev. B*, 74(20):205119, Nov 2006.

[170] Jong Soo Lim and Mahn-Soo Choi. Andreev bound states in the kondo quantum dots coupled to superconducting leads. *Journal of Physics: Condensed Matter*, 20:415225, 2008.

[171] E. Vecino, A. Martín-Rodero, and A. Levy Yeyati. Josephson current through a correlated quantum level: Andreev states and π junction behavior. *Phys. Rev. B*, 68(3):035105, Jul 2003.

[172] Tobias Meng, Serge Florens, and Pascal Simon. Self-consistent description of andreev bound states in josephson quantum dot devices. *Phys. Rev. B*, 79(22):224521, Jun 2009.

[173] Jorden A. van Dam, Yuli V. Nazarov, Erik P. A. M. Bakkers, Silvano De Franceschi, and Leo P. Kouwenhoven. Supercurrent reversal in quantum dots. *Nature*, 442:667–670, 2006.

[174] A. V. Rozhkov, Daniel P. Arovas, and F. Guinea. Josephson coupling through a quantum dot. *Phys. Rev. B*, 64(23):233301, Nov 2001.

[175] V. V. Ryazanov, V. A. Oboznov, A. Yu. Rusanov, A. V. Veretennikov, A. A. Golubov, and J. Aarts. Coupling of two superconductors through a ferromagnet: Evidence for a π junction. *Phys. Rev. Lett.*, 86(11):2427–2430, Mar 2001.

[176] Baselmans J. J. A. Morpurgo A. F. van Wees B. J. Klapwijk T. M. Reversing the direction of the supercurrent in a controllable josephson junction. *Nature*, 397:43–45, 1999.

[177] J.-P. Cleuziou, W. Wernsdorfer, V. Bouchiat, T. Ondarçuhu, and M. Monthioux. Carbon nanotube superconducting quantum interference device. *Nature Nanotechnology*, 1:53, 2006.

[178] H.I. Jorgensen, T. Novotny, K. Grove-Rasmussen, K. Flensberg, and P.E. Lindelof. Critical current 0-pi transition in designed josephson quantum dot junctions. *NanoLetters*, 7:2441, 2007.

[179] A. Eichler, R. Deblock, M. Weiss, C. Karrasch, V. Meden, C. Schönenberger, and H. Bouchiat. Tuning the josephson current in carbon nanotubes with the kondo effect. *Phys. Rev. B*, 79(16):161407, Apr 2009.

[180] Romain Maurand. *SQUID à nanotube de carbone : jonction Josephson à boite quantique, jonction π, effet Kondo et détection magnétique d'aimants moléculaires.* PhD thesis, Université de Grenoble, France, 2011.

[181] T. Kontos, M. Aprili, J. Lesueur, F. Genêt, B. Stephanidis, and R. Boursier. Josephson junction through a thin ferromagnetic layer: Negative coupling. *Phys. Rev. Lett.*, 89(13):137007, Sep 2002.

[182] A. A. Golubov, M. Yu. Kupriyanov, and E. Il'ichev. The current-phase relation in josephson junctions. *Rev. Mod. Phys.*, 76(2):411–469, Apr 2004.

[183] A. Bauer, J. Bentner, M. Aprili, M. L. Della Rocca, M. Reinwald, W. Wegscheider, and C. Strunk. Spontaneous supercurrent induced by ferromagnetic π junctions. *Phys. Rev. Lett.*, 92(21):217001, May 2004.

[184] Jean-Pierre Cleuziou. *Propriétés de transport électronique de nanotubes de carbone: des nanotubes hybrides au nano-SQUID.* PhD thesis, Université de Toulouse, France, 2007.

[185] Akira Oguri Yoshihide Tanaka and A C Hewson. Kondo effect in asymmetric josephson couplings through a quantum dot. *New J. Phys.*, 10:029801, 2008.

[186] P. W. Anderson and J. M. Rowell. Probable observation of the josephson superconducting tunneling effect. *Phys. Rev. Lett.*, 10(6):230–232, Mar 1963.

[187] M. C. Koops, G. V. van Duyneveldt, and R. de Bruyn Ouboter. Direct observation of the current-phase relation of an adjustable superconducting point contact. *Phys. Rev. Lett.*, 77(12):2542–2545, Sep 1996.

[188] E. Scheer, P. Joyez, D. Esteve, C. Urbina, and M. H. Devoret. Conduction channel transmissions of atomic-size aluminum contacts. *Phys. Rev. Lett.*, 78(18):3535–3538, May 1997.

[189] Michel H. Devoret, John M. Martinis, and John Clarke. Measurements of macroscopic quantum tunneling out of the zero-voltage state of a current-biased josephson junction. *Phys. Rev. Lett.*, 55(18):1908–1911, Oct 1985.

[190] Daniel Esteve, Michel H. Devoret, and John M. Martinis. Effect of an arbitrary dissipative circuit on the quantum energy levels and tunneling of a josephson junction. *Phys. Rev. B*, 34(1):158–163, Jul 1986.

[191] Hermann Grabert. Escape from a metastable well: The kramers turnover problem. *Phys. Rev. Lett.*, 61(15):1683–1686, Oct 1988.

[192] H. A. Kramers. *Physica*, 7:284, 1940.

[193] I. Petkovic. *Dynamique de la phase dans des jonctions Josephson ferromagnétiques.* PhD thesis, Université Paris Sud, 2009.

[194] B. Ruggiero, C. Granata, V. G. Palmieri, A. Esposito, M. Russo, and P. Silvestrini. Supercurrent decay in extremely underdamped josephson junctions. *Phys. Rev. B*, 57(1):134–137, Jan 1998.

[195] John M. Martinis, Michel H. Devoret, and John Clarke. Experimental tests for the quantum behavior of a macroscopic degree of freedom: The phase difference across a josephson junction. *Phys. Rev. B*, 35(10):4682–4698, Apr 1987.

[196] T. Van Duzer and C.W. Turner. *Principle of superconductive devices and circuits.* Edward Arnold Publishers, 1981.

[197] L. Dell'Anna, A. Zazunov, R. Egger, and T. Martin. Josephson current through a quantum dot with spin-orbit coupling. *Phys. Rev. B*, 75(8):085305, Feb 2007.

[198] A. Zazunov, R. Egger, T. Jonckheere, and T. Martin. Anomalous josephson current through a spin-orbit coupled quantum dot. *Phys. Rev. Lett.*, 103(14):147004, Oct 2009.

[199] Yuval Oreg, Gil Refael, and Felix von Oppen. Helical liquids and majorana bound states in quantum wires. *Phys. Rev. Lett.*, 105(17):177002, Oct 2010.

[200] Jason Alicea. Majorana fermions in a tunable semiconductor device. *Phys. Rev. B*, 81(12):125318, Mar 2010.

[201] F. Chiodi, M. Ferrier, K.Tikhonov, P. Virtanen, T.T. Heikkilä, M. Feigelman, S. Guéron, and H.Bouchiat. Microwave response of an ns ring coupled to a superconducting resonator. arXiv:1005.0406v1.

[202] Sidney Shapiro. Josephson currents in superconducting tunneling: The effect of microwaves and other observations. *Phys. Rev. Lett.*, 11(2):80–82, Jul 1963.

Appendix A

Nanofabrication

Before performing transport or noise experiments at very low temperature, one first needs to get *good* samples. To do so, several steps are necessary going from carbon nanotube growth to metallic leads deposition. In the following we present each steps of the home-made process.

A.1 Chemical Vapor Deposition Growth of Carbon Nanotubes

A.1.1 The process

The process used to grow carbon nanotubes has been developped by Alik Kasumov [131] and improved/adapted during this thesis. The first step consists in sputtering a very thin layer of Fe catalyst (≈ 1 nm) on top of a silicon substrate (doped for current phase relation measurement and undoped for high frequency measurements). The substrates are placed in a quartz tube (cut in small pieces of 5×5 mm) and placed into the home-made oven presented in figure A.1. The system is pumped to low pressure $\approx 1.10^{-4} mbar$ in the presence of a cold trap (liquid Nitrogen). We then heat the samples up to stabilized temperatures between $800^o C$ and $1000^o C$. When the samples reach the reaction temperature, acetylene C_2H_2 is admitted into the quartz tube up to pressures of 1 mbar for 9 s and then pumped out and extracted from the furnace. One can summarize the process by the list (very specific to our setup):

- Pumping of the quartz down to $P < 0.1 mbar$,
- Heating of the coil for $10'$ at $50V$,
- Heating of the coil for $50'$ at $84V$ ($T \in [800, 1000]^0 C$),
- Injection of C_2H_2 (200 mbar in the regulating pressure area) for 9 seconds,

- Pumping out of the cracked acetylene,
- Reduction of the oven temperature down to room temperature.

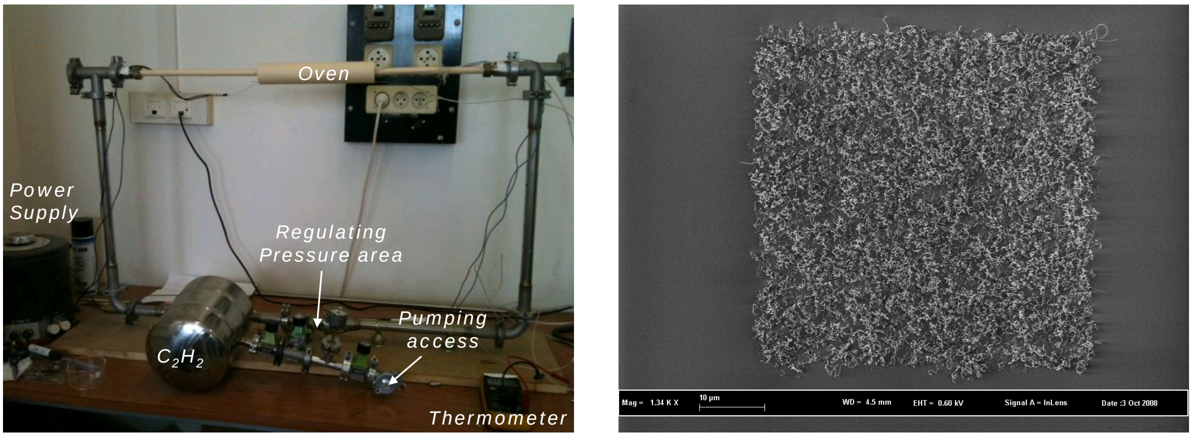

Figure A.1: (a) Picture of the CVD oven used to grow carbon nanotubes of this thesis. (b) SEM picture of carbon nanotubes obtained with a wide surface deposition of Fe catalyst.

We then need to check whether or not we did fabricate carbon nanotubes. This is done by observing them with a scanning electron microscope (SEM).

A.1.2 Optimization and adaptation

A typical picture of carbon nanotubes grown with the described technique is shown in figure A.1 b. It shows that a wide deposition of Fe catalyst leads to a spaghetti-like growth of carbon nanotubes. To isolate single carbon nanotubes, it is necessary to change the size, the density and/or the shape of the catalyst. This is achieved by patterning small areas of catalyst with electron beam lithography (see later). A test sample is shown in figure A.2a, showing the influence of the catalyst islands density (same thickness) on the carbon nanotube growth. After several tests addressing the shape, the size and the density we choose to design $0.75\mu m \times 40\mu m$ lines separated of $20\mu m$ as shown in figure A.2b. With those parameters, rather long and independent nanotubes are formed.

A.2 Connecting the Carbon Nanotubes

A.2.1 Lift-Off technique

The *lift-off* is a well known technique in micro-electronics. It permits in particular to design very thin metallic leads that are necessary to connect carbon nanotubes. It consists in first spinning a photo- or electro-sensitive resist on top of a substrate. One then shines defined regions of this resist with light (photo-lithography) or electrons (e-beam lithography). The shined parts are chemically modified and then react differently with a *developper*. This

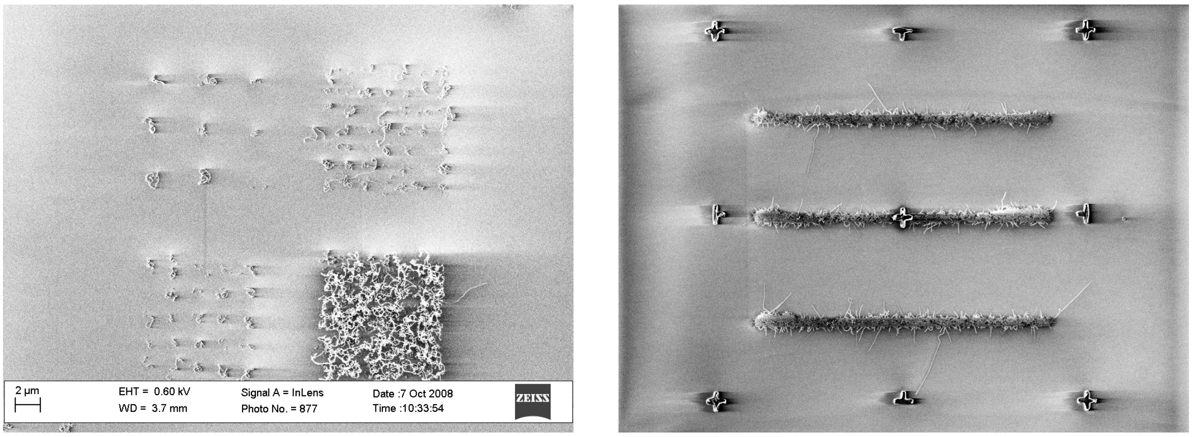

Figure A.2: (a) Tests of the catalyst island density. Lowering the density allows to avoid the spaghetti-like growth. (b) Choosen shape, sizes and density for catalyst island. The growth gives us thin, long and independent nanotube easy to adress for metallic connections.

product disssolves the shined parts and leaves the unshined parts unmodified. At this stage, a negative layout of the defined shapes *i.e.* appearing substrate where metal is wanted and resist everywhere else, is formed. Metallic or oxide deposition fills the holes. The rest of the resist is dissolved and one obtains the wanted positive layout *i.e.* metallic leads where electrons or photons were shined. This process is summarized in figure A.3a and the exact experimental conditions are developped in a next section.

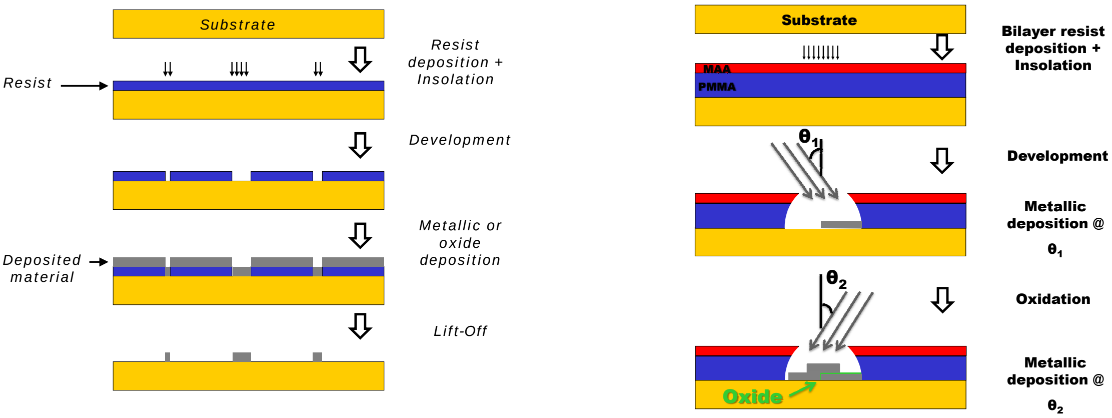

Figure A.3: (a) Left: Classical lift-Off process. (b) Right: Angular evaporation process.

A.2.2 Electron beam lithography

The electron beam lithographies of this thesis have been realized with a scanning electron microscope ZEISS equipped for electron beam lithography. We use *Nanometer Pattern Generation System (NPGS)* to control the electronic beam during lithography and *Design-Cad* to draw the nanoscale designs.

A.2.3 Materials deposition

In order to realize transport experiments with carbon nanotubes, it is necessary to connect them. Many techniques exist to deposit metallic materials. During this thesis, we have used sputtering for Nb, Pt and Fe and evaporation (Joule or e-gun) techniques for Pd, PdNi, Al, Nb, Cu and Au.

The fabrication processes for making samples used in this thesis depend on the experiment. Hereafter we recapitulate the exact experimental conditions used to fabricate the *Noise measurements* (see part II of this thesis) and *Current phase relation measurement* (part II) samples.

Noise measurement samples

The normal metal carbon nanotube connection and the fabrication of the SIS detector cannot be done in a single step. We have chosen to first connect the carbon nanotube and then fabricate the detector together with the coupling resonant cavity.

Normal metal connection of carbon nanotubes The normal metal used to connect carbon nanotube is Palladium Pd. It is known for making relatively transparent contacts with carbon nanotubes due to the small difference of working functions. It was evaporated in the following conditions:

- E-Gun evaporator :
  - Pd : $45nm$ at a rate of $0.17nm/s$, (e-gun current $I = 200mA$), pressure $P = 9.10^{-8}mbar$, angle of evaporation $\theta = 0^0$.
- Joule evaporator :
  - Pd : $45nm$ @ $0.5nm/s$, (load current $I = 267A$), $P = 7.10^{-6}mbar$, $\theta = 0^0$.

SIS noise detector fabrication The SIS noise detector is fabricated together with the resonant cavity. One uses the angular evaporation technique (see Fig.A.3b) which consists in first depositing Aluminum at a certain angle θ, then oxidizing the alumninum surface and finally covering the oxidized surface by another layer of Aluminum at the angle $-\theta$. The exact optimized conditions are:

- E-Gun evaporator :
  - Al : $30nm$ @ $0.5nm/s$, $(I = 500mA)$, $P = 2.10^{-7}mbar$, $\theta = +16^0$.
  - Oxidation : Oxygen O_2 at $P = 3mbar$ for 10 minutes.
  - Al : $50nm$ @ $0.5nm/s$, $(I = 500mA)$, $P = 2.10^{-7}mbar$, $\theta = -16^0$.
- Joule evaporator :

  - Al : $30nm$ @ $2.5nm/s$, $(I = 240A)$, $P = 3.10^{-6}mbar$, $\theta = +12.5^0$.
  - Oxidation : Oxygen O_2 at $P = 3.10^{-1}mbar$ for 10 minutes.
  - Al : $50nm$ @ $2.5nm/s$, $(I = 240A)$, $P = 3.10^{-6}mbar$, $\theta = -12.5^0$.

During this thesis, we have also investigated Al/Nb junctions using the e-gun evaporator. The Niobium film quality is critical and necessits special care. In particular, extremely low vacuum conditions are needed during deposition ($< 1.10^{-7}mbar$). To attain this criteria, we use a dedicated evaporator system pumped with a ionic pump nd a cold finger. The Niobium film deposition is made in two-steps to avoid contamination induced by extreme heating during deposition. The optimized deposition conditions are:

- E-Gun evaporator :
  - Al : $25nm$ @ $0.6nm/s$, $(I = 500mA)$, $P = 5.10^{-8}mbar$, $\theta = +16^0$.
  - Oxidation : Oxygen O_2 at $P = 10mbar$ for 10 minutes.
  - Nb : $20nm$ @ $0.12nm/s$, $(I = 550mA)$, $P = 5.10^{-8}mbar$, $\theta = -16^0$.
  - Nb : $20nm$ @ $0.26nm/s$, $(I = 550mA)$, $P = 5.10^{-8}mbar$, $\theta = -16^0$.
  - Al : $5nm$ @ $0.6nm/s$, $(I = 550mA)$, $P = 1.10^{-7}mbar$, $\theta = -16^0$.

Current phase relation measurement samples

Choice of materials The current phase relation samples are done in a single lift-off step. The deposited sequence of materials is thus critical. The nanotube contacts are done using a thin layer of Palladium followed by a thick layer of Aluminum. The Pd thickness and quality is critical. Too thin the film is not continuous, too thick superconductivity is suppressed. It must also be free of magnetic impurities and deposited as fast as possible to avoid contamination. Josephson junctions are realized by 2 angle evaporations and an oxidation. The optimized conditions are:

- E-Gun evaporator :
  - Pd : $4nm$ @ $0.2nm/s$, $(I = 130mA)$, $P = 2.10^{-7}mbar$, $\theta = +13^0$.
  - Al : $80nm$ @ $0.7nm/s$, $(I = 400mA)$, $P = 3.10^{-7}mbar$, $\theta = +16^0$.
  - Oxidation : Oxygen O_2 at $P = 10mbar$ for 10 minutes.
  - Al : $100nm$ @ $0.9nm/s$, $(I = 400mA)$, $P = 3.10^{-7}mbar$, $\theta = -16^0$.
- Joule evaporator :
  - Pd : $4nm$ @ $0.5nm/s$, $(I = 267A)$, $P = 3.10^{-6}mbar$, $\theta = +13^0$.
  - Al : $70nm$ @ $1.5nm/s$, $(I = 240A)$, $P = 5.10^{-6}mbar$, $\theta = +16^0$.
  - Oxidation : Oxygen O_2 at $P = 3.10^{-1}mbar$ for 10 minutes.
  - Al : $120nm$ @ $1.2nm/s$, $(I = 240A)$, $P = 9.10^{-6}mbar$, $\theta = -16^0$.

Geometrical dimensions of the assymetric SQUID loop The geometrical dimensions of the assymetric SQUID loop and the big Josephson junctions have been choosen to fulfill several criteria: - Critical current assymetry ≈ 10 - Negligible inductance - Sufficient precision of the applied flux - Negligible distorsion of the current phase measurement due to magnetic flux through the big junctions. The optimized dimensions are (see also figure A.4):

- Loop size $\approx 8 \times 12\mu m^2$
- Junctions size $\approx 2000 \times 200nm^2$

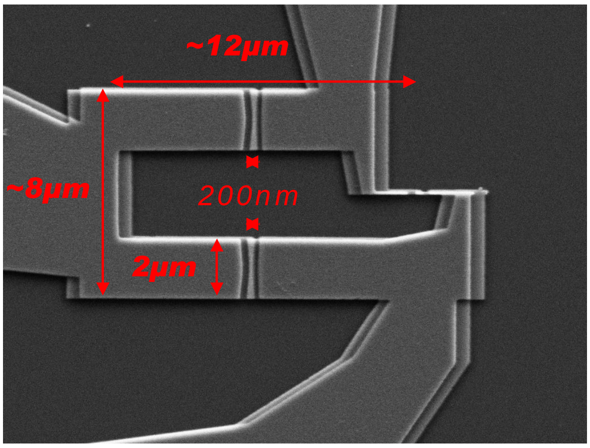

Figure A.4: Typical dimensions chosen for the SQUID loop. Here is shown a SEM picture of the device used to measure the current phase relation of the small Josephson junction.

Appendix B

Circuit characterization by external high frequency irradiation

We characterize the dc response of the SIS noise detector submitted to an external radio-frequency irradiation via a local antenna. By first neglecting the source junction, on which no bias is applied, we highlight photo-assisted tunneling processes [120] (section B.1). Depending on the bias region of interest, the signature is either the appearence of current steps or current peaks. Steps appear nearby voltages $V_D = \pm 2\Delta/e$ and are due to inelastic tunneling of quasiparticles. Peaks appear in the subgap region, nearby existing peaks due to the resonant environment and are due to inelastic tunneling of Cooper-pairs [113]. We compare these experimental findings to theoretical expectations.

We then theoretically analyse the source/detector interaction in presence of HF excitation. The mixing theory [117] allows to define methods to measure the finite frequency complex admittance of the source junction (section B.2).

B.1 SIS junction response to external irradiation

Here we study the dc response of a SIS junction in a resonant environment to an external high frequency activation.

B.1.1 Quasiparticles tunneling

In the vicinity of the quasiparticles branch, a SIS junction under external irradiation exhibits photon-assisted tunneling current. The theory of this effect was done by Tien and Gordon (1963) [120]. This current adds to the dc $I(V)$ characteristic of the sample leading to current steps or peaks in the $I(V)$ at voltages $|V_D| = 2\Delta/e \pm h\nu'/e$ in the differential conductance dI_D/dV_D.

In order to measure this signature, we first minimize the supercurrent flowing into the detector by applying a magnetic flux through the loop of the SIS junction which has a

SQUID geometry. The source junction is unbiased and the derivative of the $I_D(V_D)$ characteristic under external irradiation dI_D/dV_D is measured with a lock-in amplifier technique. Results of these measurements are shown in figure B.1 for two different excitation powers of the antenna and frequency $\nu' = 18.71GHz \neq \nu_n$[1]. What is observed is the presence of additional peaks around 2Δ. These peaks take place at $V_D = 2\Delta/e \pm h\nu'/e$ and grow with HF power (only one single frequency is shown for simplicity). It is consistent with theoretical predictions [120] where the current I_{AB} through the junction follows:

$$I_D(V_D) = C \sum_{n=-\infty}^{\infty} J_n^2(\alpha) \int_{-\infty}^{\infty} [f(E - eV_D) - f(E + nh\nu')] \\ \rho_A(E - eV_D)\rho_B(E + nh\nu)dE \tag{B.1}$$

where C is a proportionality constant, $J_n(\alpha)$ is the Bessel function of order n and $\alpha = eV_{ac}/h\nu$. V_D is the applied dc voltage accross the junction, the f's are Fermi factors taken at different energies and ρ_a and ρ_b are respectively, superconducting densities of states of superconductors A and B. Since the ac excitation is small, $\alpha << 1$. By linearising Bessel functions the $I(V)$ characteristic is approximated by:

$$I_D(V_D) \cong \frac{1}{4}\left(\frac{eV_{ac}}{h\nu'}\right)^2 \left[I_{QP}(V_D + h\nu'/e) + I_{QP}(V_D - h\nu'/e) - 2I_{QP}(V_D)\right]. \tag{B.2}$$

The data show that experimental peaks at $V_D = 2\Delta/e + h\nu'/e$ are strongly attenuated compared to the ones at $V_D = 2\Delta/e - h\nu'/e$ which is not expected by theory. We explain this discrepancy by a possible mixing with quasiparticles tunneling at frequency $\nu = \nu_1 - \nu' \approx 11.5GHz$ due to the presence of the resonator. We do not discuss further this phenomenon. We choose to fit peaks in $V_D = 2\Delta/e - h\nu'/e$ to deduce V_{ac} using equation B.2. This is shown in figure B.1. For $\nu' = 18.71GHz$ and injected power $P_1 = -10dBm$ we find $V_{ac1} = 2.01\mu V$ whereas for $P_2 = -5dBm$, $V_{ac2} = 3.43\mu V$. These values are consistent with the power ratio taking into account the definition of dBm[2].

B.1.2 Cooper pairs tunneling

In the following, the detector supercurrent is maximized and the source junction is not polarized. We measure the $I_D(V_D)$ characteristic of the detector under external HF excitation in the subgap domain. Without irradiation, this region is known to exhibit peaks at

---

[1] The ν_n's are the resonant frequency of the resonator according to the first part of this thesis (part I)

[2] dBm (sometimes $dBmW$) is an abbreviation for the power ratio in decibels (dB) of the measured power referenced to one milliwatt (mW). Zero dBm equals one milliwatt. By expressing x the power in Watts and P in dBm, the link between them is: $x = 10^{\frac{P-30}{10}}$. As the power is proportional to the voltage V_{ac} squared, one has the ratio $\frac{V_{ac1}}{V_{ac2}} = 10^{\frac{P_1-P_2}{20}}$. Performing the numerical application for $P_1 = -10dBm$ and $P_2 = -5dBm$ we get $\frac{V_{ac1}}{V_{ac2}} = 0.56$. Fits to experimental data gives $\frac{V_{ac1}}{V_{ac2}} = 0.586$ which is in agreement with the injected power

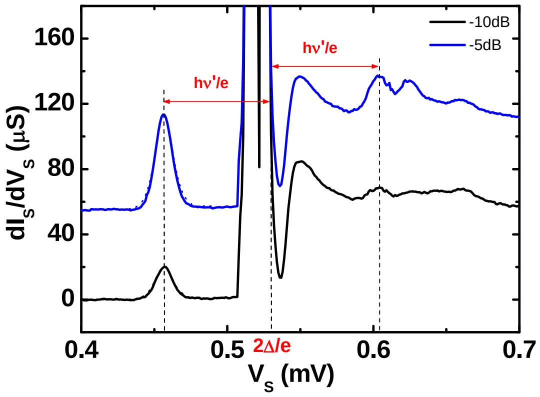

Figure B.1: Full lines : Derivative of the I(V) characteristic of the source close to the superconducting gap under HF irradiation ($\nu' = 18.71 GHz$) for two powers $P = -5dBm$ and $P = -10dBm$. Peaks appearing at $V_D = 2\Delta/e \pm h\nu'/e$ grow continuously with power. Dotted lines : Fit to experimental data using equation B.2 to extract V_{ac}.

$V_n = h\nu_n/2e$ with ν_n the resonance frequencies of the resonator. These peaks are related to the resistive part of the resonant environment. We here show that the external irradiation changes the global shape of these peaks and that we can theoretically understand these changes.

Experimental results

We show in figure B.2 the results of such measurements at the irradiation frequency $\nu' = 18.71 GHz$ for the two powers $P = -10dBm$ and $P = -5dBm$. At very low HF power, no changes are observed. When the power is increased, small kinks grow at $V_D = h\nu_n/e \pm h\nu'/e$ and the main central peak at $V_D = h\nu_n/e$ is reduced proportionally to the HF power. These changes are however quite difficult to observe in the dc $I(V)$ characteristics. That is why we also show the dI_D/dV_D curves which are easier to interprete. We now theoretically explain this behaviour.

Theoretical understanding

The framework of the following calculations is inspired by Shapiro [202]. Under external HF irradiation, the voltage accross the junction is the sum of the dc voltage V_{DC} applied to the junction and the ac voltage created by HF at frequency $\nu_{rf} = \omega_{rf}/2\pi$, $V_{ac} sin(\omega_{rf}.t)$. One then rewrites the Josephson equations:

$$\left\{ \begin{array}{rcl} V & = & V_{DC} + V_{ac} sin(\omega_{rf}.t) \\ \frac{d\phi}{dt} & = & \frac{2eV}{\hbar} \\ I & = & I_C sin\phi \end{array} \right. \tag{B.3}$$

By using these equations we obtain the current flowing into the junction :

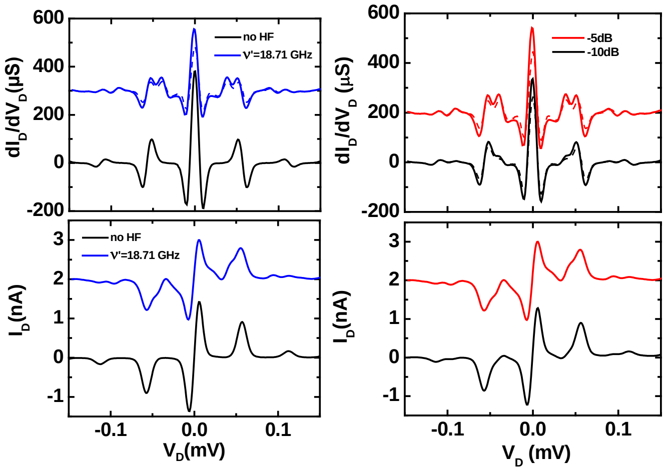

Figure B.2: (a) Measured (full lines) and fitted (dashed lines) subgap dI_D/dV_D characteristic of the SIS detector in a resonant environment with and without external high frequency irradiation at $\nu' = 18.71$ GHz. Extra peaks appear under ac excitation at positions fixed by the frequency of the external irradiation. (b) $I_D(V_D)$ characteristic of the source in the same conditions. Extra kinks appear under ac excitation.

$$I = I_C sin(\frac{2eV_{DC}}{\hbar}t - \frac{2eV_{ac}}{\hbar\omega_{rf}}cos\omega_{rf}t + \gamma_0) \tag{B.4}$$

with γ_0 an integration constant. Therefore by using the Jacobi-Anger expansion of the sine of a cosine we can rewrite this current as :

$$I = I_C \sum_{n=-\infty}^{+\infty} (-1)^n J_n(\frac{2eV_{ac}}{\hbar\omega_{rf}})sin(\gamma_0 + \omega t - n\omega_{rf}t) \tag{B.5}$$

with $\omega = 2eV_{DC}/\hbar$. This current is time dependent excepted if $\omega = n.\omega_{rf}$ with n an integer number. We deduce from this the expression of the dc current flowing through the junction:

$$I_{DC} = \frac{I_C^2}{2V_{DC}} \sum_{n=-\infty}^{+\infty} J_n^2(\frac{2eV_{ac}}{\hbar\omega_{rf}})Re[Z(\frac{2eV_{DC}}{\hbar} - \omega_n)]. \tag{B.6}$$

In the limit of small ac excitation $\frac{2eV_{ac}}{\hbar\omega_{rf}} << 1$, one can linearize Bessel function J_0 to second order and J_1 to first order. Identifying $I_{JJAC}(V) = 1/(2V).Re[Z(2eV/\hbar)].I_C^2$, we obtain a simplified expression for the dc current flowing into the junction:

$$I_{DC} = \left(1 - \frac{1}{2}(\frac{2eV_{ac}}{\hbar\omega_{rf}})^2\right) I_{JJAC}(V) + \left(\frac{eV_{ac}}{\hbar\omega_{rf}}\right)^2 [I_{JJAC}(V - \hbar\omega_{rf}/2e) + I_{JJAC}(V + \hbar\omega_{rf}/2e)]\,. \tag{B.7}$$

It shows that by irradiating the Josephson junction, the subgap $I(V)$ characteristic is a superimposing of the renormalized subgap $I(V)$ curve without irradiation with the same curves shifted from $\pm h\nu_{rf}/2e$ normalized to ac power excitation.

Comparison theory and experiment

We fit the data shown in figure B.2 with formula B.7. V_{ac} is the adjustable parameter. Peaks positions are reproduced by frequency under study and we obtain HF powers $V_{ac} = 2.1\mu V$ at $P = -10dBm$ and $V_{ac} = 3.4\mu V$ at $P = -10dBm$. It is consistent with values obtained in subsection B.1.1 (respectively 2.01 and $3.43\mu V$).

B.1.3 Conclusions

In this section we have presented the detector response to an external high frequency irradiation. Photo-assisted processes were clearly highlighten, both concerning quasiparticles and Cooper pairs tunneling. In the following, we theoretically study the source/detector interaction under HF irradiation.

B.2 Source/detector interaction in presence of HF excitation

Here we theoretically address the source/detector interaction in presence of an external high frequency drive at frequency ν_0.

B.2.1 Model

AC irradiation generates harmonic voltage fluctuations in the circuit. The ac currents and voltages appearing into the sample are modified as shown in figure B.3. In particular, fluctuations induced by antenna takes the form $V_{LO}(t) = V_{L0} cos\omega_0 t$ with V_{LO} the amplitude of the local voltage variation and $\omega_0 = 2\pi\nu_0$ its pulsation. This signal is equally present accross the 2 junctions. It follows the ac current $i_S(t)$ flowing through the source due to this excitation is related to its admittance Y_S and reads : $i_S(t) = Y_S.V_{LO}(t)$. This oscillating current couples to the detector through the resonator leading to excess voltage fluctuations appearing accross the detector: $Z_t i_s(t) = Z_t.Y_S.V_{LO}(t)$ with Z_t the transimpedance. The reference signal $V_{LO}(t)$ and $Z_t.Y_S.V_{LO}(t)$ are mixed by the detector. As Z_t and Y_S are complex functions, one needs to carefully treat this mixing. This is done in the following. Note that what is said for the detector is completely symmetric with respect to a source/detector exchange.

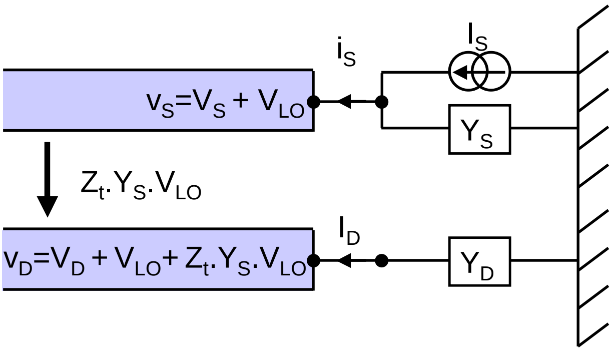

Figure B.3: Current and voltages appearing into the circuit under external HF irradiation. The principle of the ac conductance measurement is to mix at the detector level, the reference signal $V_{LO}(t)$ to the signal coming from the source at the same frequency $v_{sig}(t) = Z_t.Y_S.V_{LO}(t)$.

B.2.2 Mixing theory applied to the detection scheme

A SIS junction is known to be a quantum mixer [117]. Let us suppose the voltage applied to this junction is the sum of a dc voltage and two time dependent voltages so that $V(t) = V_0 + V_{LO}(t) + v_{sig}(t)$. V_0 is the dc component, $V_{LO}(t)$ the local oscillator term and $v_{sig}(t)$ the voltage coming from an external source. These last two terms are defined as :

$$V_{LO}(t) = V_{LO}cos(\omega_0 t) \tag{B.8}$$

$$v_{sig}(t) = Re\left[\sum_{m'=-\infty}^{+\infty} v_{m'}e^{i\omega_{m'}t}\right] \tag{B.9}$$

where V_{LO} and ω_0 are respectively the amplitude and the driven frequency of the local oscillation. $v_{m'}$ and $\omega_{m'} = \omega_0 + m'\omega$ are respectively the amplitude and the driven frequency of the external signal.

Application - In the experiment $v_{sig}(t) = Re\left[Z_t(\omega_0).Y_S(\omega_0, V_S).V_{LO}e^{i\omega_0 t}\right]$ so that $m' = 0$ and $v_0 = Z_t(\omega_0).Y_S(\omega_0, V_S).V_{LO}$.

From a general point of view, with the same notations the current flowing through the junction reads

$$i_{sig}(t) = Re\left[\sum_{m=-\infty}^{+\infty} i_m e^{i\omega_m t}\right] \tag{B.10}$$

with i_m the amplitude of the current flowing into the junction at frequency ω_m. By assuming small signals, voltage and current components are linearly related by an admittance matrix

$$i_m = \sum_{m'} Y_{mm'}v_{m'} \tag{B.11}$$

.

The values of the matrix elements are related to the strength of the local oscillator and the nonlinear dc $I(V)$ characteristic of the SIS junction. These elements are complex so that $Y_{mm'} = G_{mm'} + iB_{mm'}$.

Application - Experimentally, one only measures the dc component of the current and $i_{sig}(t)$ must be time independent. This condition is fulfilled when $\omega_m = \omega_0 + m\omega = 0$. As $\omega = \omega_0$, we obtain that only $m = -1$ satisfies the condition. Finally, only $m = -1$ and $m' = 0$ becomes relevant and the measurable dc current is $i_{sig,dc} = Re\,[i_{-1}]$ with $i_{-1} = \sum_{m'} Y_{-1,m'} v_{m'} = Y_{-1,0} v_0 = Y_{-1,0} Z_t(\omega_0).Y_S(\omega_0, V_S).V_{LO}$. It can be written as :

$$\boxed{i_{sig,dc} = Re\,[(G_{-1,0}(V_D, \omega_0) + iB_{-1,0}(V_D, \omega_0))Z_t(\omega_0).Y_S(\omega_0, V_S).V_{LO}]\,.} \tag{B.12}$$

At this stage, we need to calculate $G_{-1,0}$ and $B_{-1,0}$.

The general form for $G_{mm'}$ and $B_{mm'}$ reads [117]:

$$\begin{aligned} G_{mm'} &= \tfrac{e}{2\hbar\omega_{m'}} \textstyle\sum_{n,n'=-\infty}^{+\infty} J_n(\alpha) J_{n'}(\alpha) \delta_{m-m',n'-n} \\ &\times[[I_{QP}(V_0 + n'\hbar\omega/e + \hbar\omega_{m'}/e) - I_{QP}(V_0 + n'\hbar\omega/e)] \\ &+[I_{QP}(V_0 + n\hbar\omega/e) - I_{QP}(V_0 + n\hbar\omega/e - \hbar\omega_{m'}/e)]] \end{aligned} \tag{B.13}$$

$$\begin{aligned} B_{mm'} &= \tfrac{e}{2\hbar\omega_{m'}} \textstyle\sum_{n,n'=-\infty}^{+\infty} J_n(\alpha) J_{n'}(\alpha) \delta_{m-m',n'-n} \\ &\times[[I_{KK}(V_0 + n'\hbar\omega/e + \hbar\omega_{m'}/e) - I_{KK}(V_0 + n'\hbar\omega/e)] \\ &+[I_{KK}(V_0 + n\hbar\omega/e) - I_{KK}(V_0 + n\hbar\omega/e - \hbar\omega_{m'}/e)]] \end{aligned} \tag{B.14}$$

$$\tag{B.15}$$

with $\alpha = eV_{LO}/\hbar\omega_0$, $J_n(\alpha)$ the Bessel function of first kind to n^{th} order and $\delta_{m-m',n'-n}$ the kronecker delta. All other notations are the same than in previous parts of this thesis and the kronecker formalism means $n' - n = m - m'$

Application - Experimentally one has $m = -1$, $m' = 0$ and thus $n' = n - 1$. To calculate analytically $G_{-1,0}$ and $B_{-1,0}$ the infinite sum over n and n' needs to be simplified. This is done by assuming that only transitions from eV to $eV \pm \hbar\omega_0$ have significant probabilities to occur and that transitions of higher energies are strongly suppressed. This assumption is known to be valid in the small excitation range $eV_{LO}/\hbar\omega_0 << 1$. Therefore, by using properties of the Bessel functions and the fact that only transitions from eV to $eV \pm \hbar\omega_0$ are possible, it appears two terms in the sum over n and n' which are ($n = 1$, $n' = 0$) and ($n = 0$, $n' = -1$). It turns out that:

$$G_{-1,0} = 2 \times \frac{e}{2\hbar\omega_0} J_0(\alpha) J_1(\alpha)[I_{QP}(V_0 + \hbar\omega_0/e) + I_{QP}(V_0 - \hbar\omega_0/e) - 2I_{QP}(V_0)] \tag{B.16}$$

$$B_{-1,0} = 2 \times \frac{e}{2\hbar\omega_0} J_0(\alpha) J_1(\alpha)[I_{KK}(V_0 + \hbar\omega_0/e) + I_{KK}(V_0 - \hbar\omega_0/e) - 2I_{KK}(V_0)] \tag{B.17}$$

which simplifies in the low V_{LO} limit to

$$G_{-1,0} = \left(\frac{e}{\hbar\omega_0}\right)^2 \frac{V_{LO}}{2}[I_{QP}(V_0 + \hbar\omega_0/e) + I_{QP}(V_0 - \hbar\omega_0/e) - 2I_{QP}(V_0)] \qquad \text{(B.18)}$$

$$B_{-1,0} = \left(\frac{e}{\hbar\omega_0}\right)^2 \frac{V_{LO}}{2}[I_{KK}(V_0 + \hbar\omega_0/e) + I_{KK}(V_0 - \hbar\omega_0/e) - 2I_{KK}(V_0)] \qquad \text{(B.19)}$$

B.2.3 Proposal for finite frequency admittance measurements

We can use the theoretical prediction B.12 to measure the in-phase and out-of-phase components of the admittance of the source. To do so we need to detail the precise shapes of $Z_t(\nu_0)$, $G_{-1,0}(V_D, \nu_0)$ and $B_{-1,0}(V_D, \nu_0)$. This is done in the following. From their analysis, proposals are made to extract the admittance components of the source junction. These proposals are irradiation frequency dependent. Hereafter we describe two limits: 1- The irradiation frequency is equal to the resonant frequency of the coupling circuit ($\nu_0 = \nu_1$); 2- The irradiation frequency is far from the resonant frequency of the coupling circuit ($\nu_0 \neq \nu_1$).

Irradiation frequency matches a resonant mode : $\nu_0 = \nu_1$

The real Z_t' and imaginary Z_t'' parts of the complex transimpedance $Z_t = Z_t' + iZ_t''$ are shown in figure B.4. At the resonant point shown by a full green vertical arrow, the imaginary part Z_t'' is strictly 0 while the real part Z_t' is maximum. The transimpedance is then purely real.

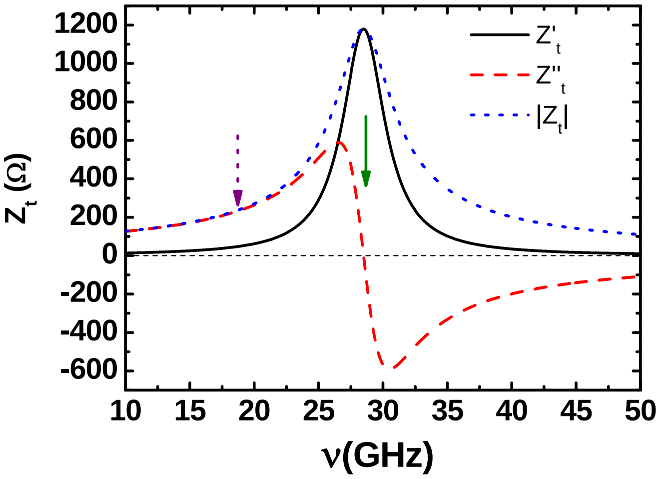

Figure B.4: Calculated modulus $|Z_t|$, real Z_t' and imaginary Z_t'' components of the complex transimpedance around the first resonant frequency of the coupling circuit.

Injecting this real quantity in equation B.12 simplifies the analysis. At this stage, the dc signal is

$$i_{sig,dc} = Re\left[(G_{-1,0}(V_D,\omega_0) + iB_{-1,0}(V_D,\omega_0))Z'_t(\omega_0).Y_S(\omega_0,V_S).V_{LO}\right]. \tag{B.20}$$

We have plotted in figure B.5 the bias dependence at frequency ν_0 of $G_{-1,0}$ and $B_{-1,0}$. It turns out their relative values strongly depend on V_D. We use this criteria to extract methods to independently measure $Re[Y_S]$ or $Im[Y_S]$.

$\mathbf{Re[Y_S(V_S)]}$ extraction We here propose to measure the bias dependence of the real part of the source admittance at the irradiation frequency. To do so, we need to fix the detector voltage at $V_D = V'_{D1}$ as shown in figure B.5. In this particular case $G_{-1,0}$ is finite while $B_{-1,0}$ is zero. It follows that the dc current measured through the detector simplifies to

$$i_{sig,dc} = Re\left[G_{-1,0}(V'_{D1},\omega_0).Z'_t(\omega_0).Y_S(\omega_0,V_S).V_{LO}\right]. \tag{B.21}$$

As $Y_S(\omega_0,V_S) = Re[Y_S(\omega_0,V_S)] + iIm[Y_S(\omega_0,V_S)]$, the real part of the previous expression is strictly proportional to $Re[Y_S(\omega_0,V_S)]$. In those conditions, recording the dc current through the detector as a function of the source bias is a direct measure of the in-phase component of the source admittance and one has:

$$Re[Y_S(\omega_0,V_S)] = \frac{i_{sig,dc}(V_S)}{G_{-1,0}(V'_{D1},\omega_0).Z'_t(\omega_0).V_{LO}}. \tag{B.22}$$

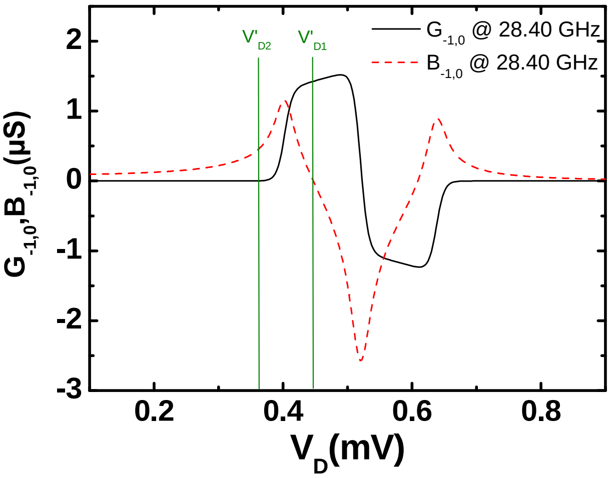

Figure B.5: Calculated voltage bias dependence of $G_{-1,0}$ and $B_{-1,0}$ using a fit to the experimental I(V) characteristic of the detector, for $V_{LO} = 2\mu V$ and for frequency $\nu_0 = \omega_0/2\pi = 28.4$ GHz.

Im[$\mathbf{Y_S}$($\mathbf{V_S}$)] extraction We now propose to measure the imaginary part of the source admittance. To do so, we propose to fix the detector voltage at $V_D = V'_{D2}$ as shown in figure B.5. Now $G_{-1,0}$ is zero while $B_{-1,0}$ is finite. It follows the dc current measured through the detector simplifies to

$$i_{sig,dc} = Re\left[iB_{-1,0}(V'_{D2}, \omega_0).Z'_t(\omega_0).Y_S(\omega_0, V_S).V_{LO}\right]. \tag{B.23}$$

For the same reasons as previously, one now measures a quantity proportional to $Im[Y_S(\omega_0, V_S)]$, the out-of-phase component of the source admittance and one has :

$$Im[Y_S(\omega_0, V_S)] = \frac{-i_{sig,dc}(V_S)}{B_{-1,0}(V'_{D2}, \omega_0).Z'_t(\omega_0).V_{LO}}. \tag{B.24}$$

Irradiation frequency is far from a resonant mode : $\nu_0 \neq \nu_1$

By irradiating far from the resonant frequency, it turns out that the imaginary part of the transimpedance Z''_t is much larger than the real part Z'_t. This is shown in figure B.4 by a dashed purple vertical arrow. In the following, we will assume the transimpedance is purely imaginary. The same analysis as in the previous paragraphs allows to propose a way to measure the admittance components of the source.

Re[$\mathbf{Y_S}$($\mathbf{V_S}$)] extraction Theoretical expectations for $G_{-1,0}$ and $B_{-1,0}$ are shown in figure B.6 for an out-of-resonance excitation frequency. From those curves and for the same reasons as in the previous paragraphs, we propose that the detector bias V'_{D3} shown in this figure allows to probe $Re[Y_S(V_S)]$. It is related to the measured dc current as :

$$Re[Y_S(\omega_0, V_S)] = \frac{-i_{sig,dc}(V_S)}{B_{-1,0}(V'_{D3}, \omega_0).Z''_t(\omega_0).V_{LO}}. \tag{B.25}$$

Im[$\mathbf{Y_S}$($\mathbf{V_S}$)] extraction Using detector bias V'_{D4} as shown in figure B.6 would allow to extract $Im[Y_S(V_S)]$. It is related to the measured dc current as :

$$Im[Y_S(\omega_0, V_S)] = \frac{-i_{sig,dc}(V_S)}{G_{-1,0}(V'_{D4}, \omega_0).Z''_t(\omega_0).V_{LO}}. \tag{B.26}$$

B.2.4 Conclusions and limitations

In this section, we have presented a theoretical procedure to independently measure the real and imaginary components of the source junction admittance at the irradiation frequency. Whereas those methods seem straightforward, they rely on several approximations. As an example, for the *on-resonance* irradiation, we have completely neglected the imaginary part of the transimpedance. In the experiment, this would require a perfect knowledge of the resonance frequency and the irradiation frequency. Finally, the experimental precision is not good enough to perfectly fulfill this assumption. It is then more likely to measure a

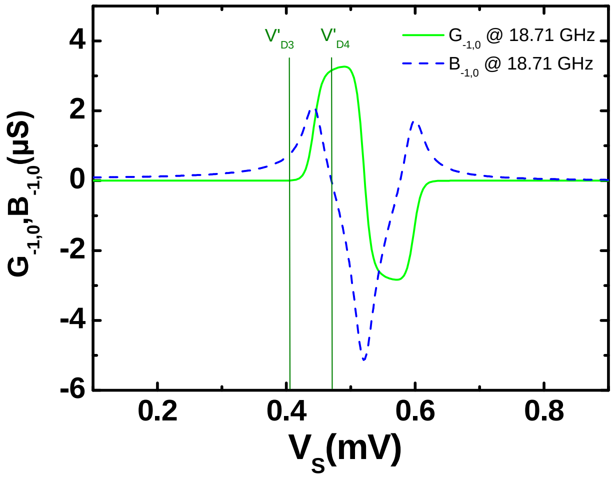

Figure B.6: Calculated voltage bias dependence of $G_{-1,0}$ and $B_{-1,0}$ using a fit to the experimental I(V) characteristic of the detector, for $V_{LO} = 2\mu V$ and for frequency $\nu_0 = \omega_0/2\pi = 18.71$ GHz.

combination of $Re[Y_S]$ and $Im[Y_S]$. In the *out-of-resonance* irradiation case, limitations on the relative amplitudes of Z'_t and Z''_t are of great importance. One has to fulfill the criteria $Z''_t >> Z'_t$. This is true only in a small frequency range as can be seen in figure B.4.

Another issue of the technique is that it necessarily needs to bias the source. Emission noise is at some point generated and leads to an additional photo-assisted dc current flowing into the detector. One therefore needs to discriminate the contributions of noise and admittance.

A summary of the proposed experimental conditions are shown in tables B.1 and B.2. Note that any detector positions proposed here could be replaced by their symmetric ones with respect to the irradiation frequency.

This proposal will need to be experimentally tested.

Condition 1	$\nu_0 = \nu_1 = 28.4GHz$	$\nu_0 = \nu_1 = 28.4GHz$
Condition 2	$V_D = V'_{D1}$	$V_D = V'_{D2}$
Measured quantities	$Re[Y_S(V_S, \nu_0)]$	$Im[Y_S(V_S, \nu_0)]$
Extraction from DC signal	$\frac{i_{sig,dc}}{G_{-1,0}(V'_{D1},\nu_0).Z'_t(\nu_0).V_{LO}}$	$\frac{-i_{sig,dc}}{B_{-1,0}(V'_{D2},\nu_0).Z'_t(\nu_0).V_{LO}}$

Table B.1: Summary of the experimental conditions proposed to measure admittance components of the source junction at the resonant frequencies of the coupling circuit.

Condition 1	$\nu_0 \neq \nu_1$	$\nu_0 \neq \nu_1$
Condition 2	$V_D = V'_{D3}$	$V_D = V'_{D4}$
Measured quantities	$Re[Y_S(V_S, \nu_0)]$	$Im[Y_S(V_S, \nu_0)]$
Extraction from DC signal	$\frac{-i_{sig,dc}}{B_{-1,0}(V'_{D3},\nu_0).Z''_t(\nu_0).V_{LO}}$	$\frac{-i_{sig,dc}}{G_{-1,0}(V'_{D4},\nu_0).Z''_t(\nu_0).V_{LO}}$

Table B.2: Summary of the experimental conditions proposed to measure admittance components of the source junction far from the resonant frequencies of the coupling circuit.

B.3 Conclusion

In this chapter, we have studied the effect of external high frequency irradiation on the device under study. The effects on quasiparticles and Cooper-pairs tunneling into the SIS detector were highlighten. The source/detector interaction under HF signal was studied theoretically. Proposals to access the voltage dependence of the quantum conductance and susceptance were made.

Appendix C

Switching histograms, effective phase temperature and Shapiro steps

C.1 Switching histograms

We have represented in figure C.1 several switching histogramms of the SQUID obtained by accumulating 8000 switching events at different ramp frequencies. We observe the higher the frequency, the higher the switching current. This is quite well explained within the $RCSJ$ model [113]. Indeed at high sweeping frequency, the time left to the particle to thermally escape the well is small so that the switching current will approach the critical current. The same interpretation explains that the width of the histogram gets wider with frequency. We finally choose to operate at $\nu = 414Hz$ because it is fast enough to accumulate enough events in a reasonable time and that the switching histogram remains assymetric. Let us notice the switching histograms can vary substantially by polarizing the SQUID in the other way round. This effect is related to some differences in between the two junctions in series. We do not address this particularity here. The experiment was however carried out using the cleanest condition.

C.2 Effective phase temperature

In figure C.2 is represented the normalized switching histogram at frequency $\nu = 414Hz$ of the SQUID. We have fitted this histogram with the escape temperature T_{Esc} being the only adjustable parameter. It turns out $T_{Esc} = 231mK$ gives the more accurate fit. It is much higher than the phonon temperature $T_{Phonons} = 18mK$. Note than the crossover temperature between the thermal regime and the macroscopic quantum tunneling (MQT) regime is, in our system, $T_{cross} = \hbar\omega_P/2\pi k_B = 17.8mK$ which is smaller than the base temperature of our dilution fridge.

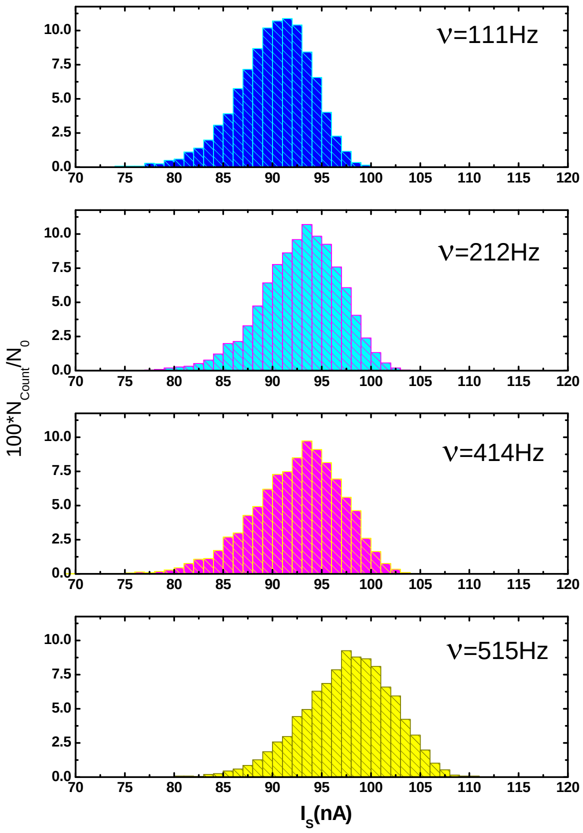

Figure C.1: Switching histograms of the two serial junctions obtained at different sweeping frequency.

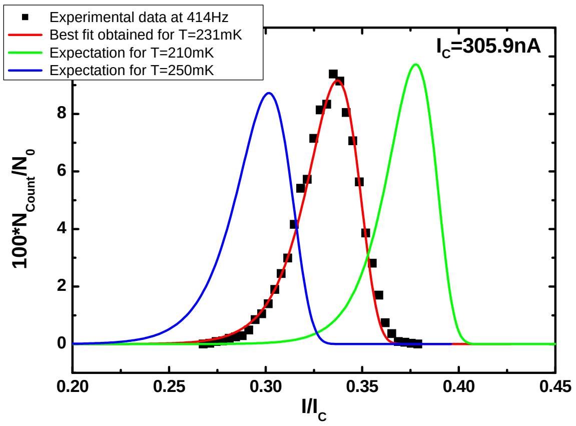

Figure C.2: Fitting of the normalized switching histogram at 414Hz. We obtain the effective temperature of the phase $T_{Esc} = 231mK$.

C.3 Shapiro steps

Under ac excitation, the supercurrent branch is known to exhibit step like features named Shapiro steps [202]. These steps occur at fixed values of the voltage $V_n = nh\nu/2e$ given by the excitation frequency ν and the integer number n. The highest the power, the larger is the number of visible steps. We show in figure C.3a and b the evolution of the supercurrent branch of the SQUID under ac excitation. Steps effectively appear at well defined voltages corresponding to the high frequency excitation: $\Delta V = h\nu/2e = 8.1\mu V$. Stochastic jumps of higher amplitude are also visible. They are supposingly due to the combination of thermally and resonantly (ac excitation) activated processes and do not change the plateaus positions.

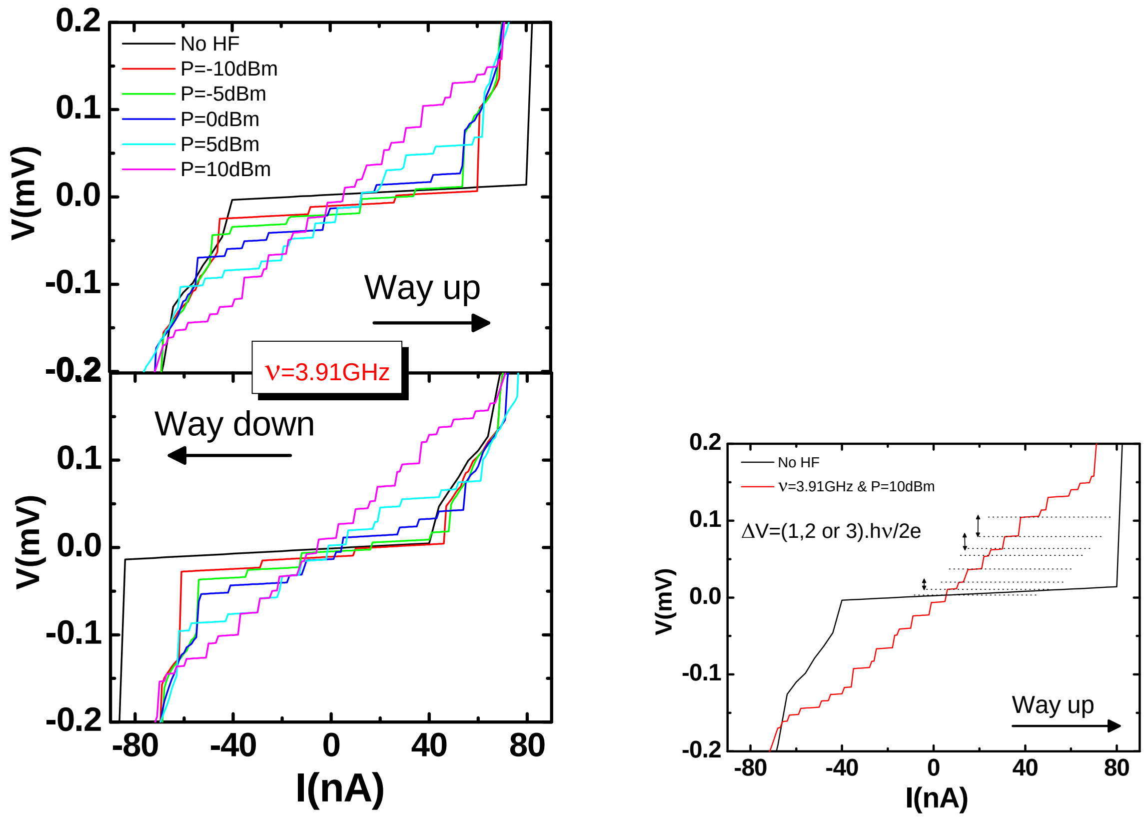

Figure C.3: (a)Ways up and down of the $V(I)$ characteristics of the SQUID subjected to external irradiation ($\nu = 3.91GHz$). The highest the power, the highest the number of Shapiro steps. Stochastic jumps appear due to thermally activated processes. (b) Comparison of the $V(I)$ characteristics without irradiation and under strong irradiation at $\nu = 3.91GHz$ and $P = +10dBm$. The Shapiro steps appear at voltages which are multiple integers of $h\nu/2e = 8.1\mu V$.